The dynamics of a horizontal cylinder oscillating as a wave energy converter about an off-centred axis.

Jorge A. Azevedo Lucas

A thesis submitted for the degree of Doctor of Philosophy.
The University of Edinburgh.
April 2011

Abstract

The hydrodynamic properties of a horizontal cylinder which is free to pitch about an off-centred axis are studied and used to derive the equations of motion of a wave energy converter which extracts energy from incoming sea waves with a linear power-take-off mechanism.

The present work follows from a recent study which compared the performance of an off-centred cylinder with those of the Edinburgh Duck wave energy converter. The small decrease in performance found is offset by a reduction in the likely costs associated with the manufacturing of the cylindrical cam compared with those of the asymmetric profile.

As part of the survivability strategy in very energetic seas-states it had been planned to completely submerge the device so as to reduce the mooring forces. However, experiments with scale models show that a good absorption capacity is retained even when fully-submerged. The hydrodynamic properties of a horizontal cylinder that pierces the free-surface and of one that is fully submerged are therefore of central concern in this study. These properties are well known for the case of very long cylinders but they are now found for cylinders with different widths, drafts, submergence levels and water-depths. The hydrodynamic forces and moments at the off-centred axis are, furthermore, derived through the application of transformation formulae.

The equation of motion of the off-centred cylinder is derived for one degree of freedom and its performance as a wave energy converter is analysed. A relationship which relates the resonance of the device with the location of the off-centred axis and its mass distribution is derived and used to optimize the design for average sea conditions attained at a real location. Design cases associated with three diameters of the cylinder are looked into detail for both a fully-submerged and free-surface piercing cylinder.

The one degree of freedom model is extended to include a multi-body which has three degrees of freedom in order to describe the dynamics of a proposed wave powered desalination system based on a cylindrical Duck device. This mathematical model is derived through linearised Lagrangian equations of motion in which the hydrodynamic forces are included as generalised external forces. The advantage of such approach is to reduce the number of equations associated with multi-body systems by removing the reaction forces of holomonic constraints from the system of equations to solve.

This model is validated through experiments with a scale model performed in the curved tank of the University of Edinburgh with both regular waves and mixed seas.

Declaration of originality

I hereby declare that this thesis has been composed by myself and that except where stated, the work contained is my own.

I also declare that the work contained in this thesis has not been submitted for any other degree or professional qualification except as specified.

Jorge Lucas

Acknowledgements

The present dissertation contains much of the work I've been caring on during the last four years in the Institute for Energy Systems (IES) of the University of Edinburgh. My involvement in wave energy began with the European training network program in wave energy: 'WAVETRAIN'. I was hosted in the IES as a fellow of such program during one year under the supervision of professor Stephen Salter and Jamie Taylor. I would like first to thank them for giving me such great opportunity and direction, and for granting me always during these years constant availability, good guidance and knowledge. With the same order of importance I would like to thank my supervisor Ian Bryden who made this work possible and supported me in all aspects.

I would also like thank and acknowledge the contributions of João Cruz and Remy Pascal with whom I collaborated. The most visible outcome of these collaborations is the construction of the scale model of the cylindrical desalination Duck and the articles published in proceedings of recognized international conferences .

The list of thanks should be extended to all IES colleagues, for their contribution in either formal or informal discussions. In particular I would like to thank my office mates and friends: Jamie Taylor, Grégory Payne, Gareth Gretton and Remy Pascal for the wonderful working environment and all the good moments shared. A special thank should be given to Grégory Payne who helped me and initiated me in the wonders of WAMIT, and David Forehand who helped me with the physical description of the dynamics of a triple pendulum.

In a more personal level, I would like to thank my parents and brother who were always present and provided me with the best support.

Finally, I wish to extend this list to include some of my good friends which made my staying in Edinburgh very pleasant and fruitful: Vera Correia, Beatriz Viçoso, Filipa Cavaco e Laurent Matteau, Joana Gafeira, Nuno Ferreira, Marian Vermote, João Alpedrinha, Bruno Martins, Vanessa Cristão, Cristina Nunes-Fonseca, Cláudia Bicho, Susana Ribeiro, David Martins, Pedro Vale, Ricardo Almeida e Ana Sousa, Rita Covas e Martim Melo, Ricardo Ramiro, Francesca Filiaci, Giulia Blasoni and Martyna Pakuła.

Contents

List of Figures

List of Tables

About notation.

In the present work, the representation of the different physical quantities accounted in the text was chosen such to avoid repetition of symbols. However in few cases, because of general and wide use of some representations, an overlap in the notation might occur. In such cases, any ambiguity is clarified by stating in the text the meaning of such quantities. Attention is drawn to the use of the letter 'H' used in this work to represent a draft. Confusion might occur as this letter is frequently associated with the height of a wave. For this reason, it is intentionally avoided to relate to this quantity and when such is represented as twice the wave amplitude ($2a$).

In general, quantities or variables which have a real value are represented by a plain letter. Greek alphabet letters are also used. For example, the wave length of a wave is represented by λ.

Vectors are represented by an upper arrow. For example, the displacement vector of a floating body is represented by $\vec{\xi}$. Matrices and tensors are represented by bold case letters. For example, the added mass matrix is represented by $\mathbf{A}$. The components of vectors, matrices or tensors are represented by the same letter with subscripts referring to its position.

The complex conjugate value of a complex variable is represented by a superscript 'asterisk' ('*'). A superscript 'dagger' ('†') is used to represent the complex conjugate transpose.

The absolute value of a variable is represented by two vertical bars around it. For example the absolute value of the excitation wave force vector is represented by $|\vec{X}|$.

Partial time derivatives are represented by the common notation: $\frac{\partial}{\partial t}$. The total time derivative of a quantity or variable is represented by either $\frac{d}{dt}$ or by a upper dot. For example the acceleration the centre of mass of a body is represented by either $\vec{a} = \frac{d\vec{u}}{dt} = \dot{\vec{u}} = \ddot{\vec{\xi}}$.

Time averaged values are represented with an over-bar. For example the average wave power per unit crest length is represented by $\overline{P_w}$.

Unless stated otherwise, in an inertial frame of reference a Cartesian right-handed coordinate system is chosen such that component 3 is vertical pointing upwards and component 1 is horizontal in the plane of view pointing to the right.

The waterplane area and moments associated with a floating structure are represented in this work by:

$$S_{ij} = \iint_{S_0} x_1^i x_2^j \, dx_1 \, dx_2 \tag{1}$$

thus:

$$S_{00} = \iint_{S_0} dx_1 \, dx_2 \tag{2a}$$

$$S_{10} = \iint_{S_0} x_1 \, dx_1 \, dx_2 \tag{2b}$$

$$S_{01} = \iint_{S_0} x_2 \, dx_1 \, dx_2 \tag{2c}$$

$$S_{11} = \iint_{S_0} x_1 \, x_2 \, dx_1 \, dx_2 \tag{2d}$$

$$S_{20} = \iint_{S_0} x_1^2, \, dx_1 \, dx_2 \tag{2e}$$

$$S_{02} = \iint_{S_0} x_2^2, \, dx_1 \, dx_2 \tag{2f}$$

Indicial notation and summation convention.

Indicial notation is used to represent explicitly the values of elements or components of matrices or vectors. For example, the dot product of two vectors $\vec{a}$ and $\vec{b}$ is represented in indicial notation as:

$$\vec{a} \cdot \vec{b} = a_1 \, b_1 + a_2 \, b_2 + a_3 \, b_3 = \sum_{k=1}^{3} a_k \, b_k$$

Where stated in this work, the *summation convention* is used. This notation is more compact and assumes that the quantities which have repeated indexes are summed over. In this notation, the summation symbol '$\sum$' is not represented. For example, the dot product of two vectors $\vec{a}$ and $\vec{b}$ is represented by:

$$\vec{a} \cdot \vec{b} = a_k \, b_k$$

To represent the external product between two vectors in indicial notation is convenient to introduce the permutation symbol, also known by Levi-Civita or antisymmetric symbol ε_{ijk}.

It is defined as:

- every indice as the values 1, 2 or 3;

- the symbol changes signal with the exchange of any two indices (odd permutation of 1,2,3);
- the symbol is zero when any of the symbols are equal.

The sign convention can be remembered by making the numbers 1,2,3 into a circle. Then any even permutation will be in cyclic order (CW) and a odd permutation in acyclic order (ACW). Examples:

- $\varepsilon_{123} = \varepsilon_{231} = \varepsilon_{312} = 1$
- $\varepsilon_{132} = \varepsilon_{213} = \varepsilon_{321} = -1$
- $\varepsilon_{ijk} = -\varepsilon_{jik} = -\varepsilon_{kji} = -\varepsilon_{ikj}$

Using this compact notation, every component of the external product of two vectors can be expressed as:

$$(\vec{u} \times \vec{v})_i = \sum_{jk} \varepsilon_{ijk} u_j v_k$$

with i, j, k = 1, 2, 3. If the summation convention is used, the summation symbol is not represented, and it gives instead:

$$(\vec{u} \times \vec{v})_i = \varepsilon_{ijk} u_j v_k$$

Expanding the above formula for the first component of the external product vector between $\vec{u}$ and $\vec{v}$, it gives:

$$(\vec{u} \times \vec{v})_1 = \sum_{jk} \varepsilon_{1jk} u_j v_k = \varepsilon_{123} u_2 v_3 + \varepsilon_{132} u_3 v_2 = u_2 v_3 - u_3 v_2$$

The Kronecker delta, δ_{ij} is defined as:

- every indice can as the values 1,2 or 3
- $\delta_{ij} = 0$, if $i = j$
- $\delta_{ij} = 1$, if $i \neq j$

The relation between the antisymmetric symbol and the Kronecker delta, also known by the $\varepsilon - \delta$ identity is given by:

$$\varepsilon_{ijk}\varepsilon_{irs} = \delta_{jr}\delta_{ks} - \delta_{js}\delta_{kr} \tag{3}$$

Nomenclature.

$\forall$	Displaced volume of water.
α_0	Angle between the horizontal plane and the plane that contains the off-centred axis and the central axis of a horizontal cylinder.
β	Angle of an incident regular wave.
$\vec{\Theta}$	Complex amplitude the relative angles vector ($\vec{\theta}$).
$\vec{\theta}$	Relative angles vector ($[\theta_1, \theta_2, \theta_3]$).
θ	Angle between the centre of the cylinder and the vertical.
θ_1	Relative angle between the rigid struts and the vertical.
θ_2	Relative angle between the rigid struts and the hull.
θ_3	Relative angle between the hull and water pendulum.
γ	Surface tension.
$\Delta\theta$	Angular displacement.
$\Delta\hat{p}$	Normalised pressure difference across the pneumatic damper.
Δp	Pressure difference across the pneumatic damper.
Δp_{rms}	Root mean square of the pressure across the pneumatic damper.
$\delta\vec{r}$	Virtual displacement vector.
δX	Standard error or uncertainty in the quantity 'X'.
δW	Virtual work.
ε	Bending strain.
ε_{ikj}	Antisymmetric or Levi-Civita symbol.
η	Free-surface elevation.
η_{rms}	Free-surface elevation root mean square.
λ	Wavelength of a regular wave.
λ_d	Deep water wavelength of a regular wave.
μ	Viscosity of the fluid.
ν	Kinematic viscosity of the fluid.
$\vec{\xi}$	Displacement vector associated with floating body.
$\hat{\vec{\xi}}$	Complex amplitude of the displacement vector.
ξ_k	Components of the displacement vector: ($k = 1, ..., 6$) correspond to the modes of motion surge, sway, heave, roll, pitch and yaw.
ρ	Density of the fluid.
$\vec{\sigma}$	Position of the source of strength 4π.
σ_X	standard deviation of the random variable 'X'.
τ	Torque.
ϕ	Velocity potential.
ϕ_0	Velocity potential associated with an incident wave.
ϕ_R	Velocity potential associated with a radiated wave.
ϕ_S	Velocity potential associated with a scattered/diffracted wave.
ϕ_X	Diffracted velocity potential ($\phi_0 + \phi_S$).

Υ	Phase delay.
$\vec{\Omega}$	Angular velocity vector associated with a (floating) body.
ω	Angular frequency of a regular wave.
$\mathbf{A}$	Added mass matrix.
A	Added mass associated with a one degree of freedom system.
a	Amplitude of an incident regular wave.
$a^{+/-}$	Far-field amplitude of a radiated regular wave at $+/-\infty$.
$\mathbf{A}_\theta$	Generalised added mass matrix.
$\mathbf{B}$	Hydrodynamic damping matrix.
B	Hydrodynamic damping associated with a one degree of freedom system.
$\vec{b}$	Base vectors associated with the body fixed coordinate system of a non-inertial frame of reference that is fixed with the body.
$\mathbf{B}_\theta$	Generalised hydrodynamic damping matrix.
$\mathbf{B}^E$	External damping matrix.
$\mathscr{C}$	Centre of the horizontal cylinder.
$\mathbf{C}$	Hydrostatic stiffness matrix.
C	Hydrostatic stiffness associated with a one degree-of-freedom system.
$\mathbf{C}_\theta$	Generalised hydrostatic stiffness matrix.
$\mathbf{C}^E$	External Stiffness matrix.
c_g	Group velocity of a regular wave or wave-train.
$C\vec{W}$	Vector from the centre of the cylinder to the centre of mass of the inner water pendulum.
CW	Capture width.
$(CW)_{max}$	Maximum capture width.
D	Diameter of the horizontal cylinder.
d	Vertical distance from the axis of rotation to the pneumatic damper horizontal centre line.
$\overline{E}$	Average energy density of a wave per unit area.
$\vec{e}$	Base vectors associated with an inertial frame of reference.
$\hat{F}$	Normalised mooring force.
$\vec{f}$	External force vector applied to a system (time domain).
$\vec{f}_A$	Hydrodynamic added mass force.
$\vec{f}_B$	Hydrodynamic damping force.
$\vec{f}_C$	Hydrostatic stiffness force.
f_c	Clock frequency of the tank.
$\vec{F}_d$	Control force of the power-take-off.
$\vec{f}_h$	Hydrodynamic force.
F_{max}^{sea}	Maximum mooring force measured in a mixed sea.
$\hat{F}_{peak}^{sea}$	Normalised amplitude of the maximum resultant mooring force for a mixed sea.
f_p	Peak frequency associated with a spectra.
$\vec{F}_R$	Complex amplitude of the radiation force vector.
$\vec{f}_R$	Hydrodynamic radiation force.
F_{rd}	Froude number.
F_{rms}	'RMS' Value of the resultant mooring force.
$\hat{F}_{rms}^{sea}$	Normalised amplitude of the root mean square of the resultant mooring force for a mixed sea.
$\vec{f}_X$	Hydrodynamic excitation force.

g	Gravity constant.
$G(\vec{x};\vec{\sigma})$	Green function.
$\mathscr{H}$	Centre of mass of the cylinder (hull) (in a planar section).
H	Draft of the horizontal cylinder measured from the bottom of the cylinder to the free-surface.
H_{m_0}	Significant wave height.
$\mathbf{I}$	Principal moment of inertia of a body.
i	Imaginary number defined by $i^2 = -1$.
I_H	Principal moment of inertia of the cylinder (hull) and parallel to its main axis.
I_W	Principal moment of inertia of the water pendulum parallel to its main axis.
$\mathbf{J}$	Moment of inertia of a body relative to a point.
J	Moment of inertia at the off-centred axis of the cylinder and parallel to its main axis.
J_0	Bessel function of zero order.
J_H	Moment of inertia of the cylinder (hull) at the off-centred axis and parallel to its main axis.
J_W	Moment of inertia of the water pendulum at the off-centred axis and parallel to its main axis.
$\mathscr{L}$	Lagrangian of a system.
$\vec{L}$	Angular momentum vector.
L	Length scale.
l_0	Distance from the off-centred axis to the centre of the cylinder.
l_1	Distance from the mooring attachment point to the off-centred axis of the cylinder.
l_2	Distance from the off-centred axis of the cylinder to the centre of mass of the hull cylinder.
l_3	Distance from the centre of the cylinder to the centre of mass of the inner water pendulum.
$\mathbf{K}$	Control matrix of a linear power-take-off.
K	Control term of the linear power-take-off.
k_0	Pneumatic damping (calibration constant).
K_0	Mechanical damping (calibration constant).
k	Wave number of a regular wave.
$\vec{m}$	External moment (or torque) applied to a system (time domain).
m	Total mass of a system.
m_j	Spectral moment of j order.
$\vec{m}_A$	Hydrodynamic added mass moment.
$\vec{m}_B$	Hydrodynamic damping moment.
$\vec{m}_C$	Hydrostatic stiffness moment.
m_d	Control torque of the power-take-off.
$\vec{m}_h$	Hydrodynamic moment.
m_H	Mass of the hull cylinder.
m_W	Mass of the water inside the hull (inner water-pendulum).
$\vec{m}_R$	Hydrodynamic radiation moment.
$\vec{m}_X$	Hydrodynamic excitation force moment.
$\vec{n}$	Normal vector to the body surface (positive when pointing out of the fluid volume).
N	Number of measurements.
n_f	Number of fronts.
$\vec{p}$	Linear momentum vector associated with a rigid body.
p	Pressure.
$\overline{P_{abs}}$	Average absorbed power.

P_{abs}	Instantaneous absorbed power.
$\overline{P_{abs}^{sea}}$	Average absorbed power in a mixed sea.
$\overline{P_{max}}$	Maximum average absorbed power.
$\overline{P_w}$	Average power in a wave per unit crest length.
$\overline{P_w^{sea}}$	Average wave power per unit crest length for a mixed sea.
$\vec{Q}$	Generalised force vector of a system.
Q	Air-flow rate.
$\vec{q}$	Generalised coordinate vector of a system.
$\dot{\vec{q}}$	Generalised velocity vector of a system.
$\ddot{\vec{q}}$	Generalised acceleration vector of a system.
Q_θ	Generalised force of the system.
Q_A	Generalised added mass component of the radiation force.
Q_B	Generalised hydrodynamic damping component of the radiation force.
Q_C	Generalised hydrostatic stiffness force.
Q_h	Generalised hydrodynamic force.
Q_X	Generalised wave excitation force.
$\mathscr{R}$	Off-centred axis of oscillation of the horizontal cylinder (in a planar section).
R	Reflection coefficient.
$\vec{r}$	Position vector.
r	r-number of the tank.
$\vec{r}_b$	Position vector of the centre of buoyancy (x_b, y_b, z_b).
$\overrightarrow{RC}$	Vector from the off-centred axis to the centre of the cylinder.
RCW	Relative capture width.
$(RCW)_{sea}$	Relative capture width associated with a mixed seas.
R_e	Reynolds number.
$\vec{r}_g$	Position vector of the centre of mass (x_g, y_g, z_g).
$\overrightarrow{RH}$	Vector from the off-centred axis to the centre of mass of the cylinder.
$\vec{r}_H$	Position vector of the centre of mass of the cylinder in the inertial reference frame.
$\vec{r}_R$	Position vector of the off-centred axis of the cylinder in the inertial reference frame.
$rtime$	Repeat time of the tank.
$\vec{r}_W$	Position vector of centre of mass of the inner water pendulum in the inertial reference frame.
S_{ij}	Water-plane area and moments.
S_b	Wet surface of a (floating) body.
S_d	Bulkhead area of the pneumatic damper.
$S(f)$	Wave spectra.
sf	Scale factor.
s_X	Experimental standard deviation associated with the measurement of variable 'X'.
$\mathscr{T}$	Total kinetic energy of a system.
T	Wave period of an incident wave.
T_e	Energy Period ($T_e = m_{-1}/m_0$)
$.\mathscr{T}_r$	Rotational kinetic energy of a system.
$\mathscr{T}_{tr}$	Translational kinetic energy of a system.
$\vec{U}$	Complex velocity vector of a body.
$\vec{u}$	Velocity vector of a body (in time domain).

$\dot{\vec{u}}$	Acceleration vector of a body (in time domain).
$\vec{U}_\theta$	Generalised velocity vector.
$\vec{U}_O$	Optimum velocity of a device such to achieve $\overline{P_{max}}$.
$\mathcal{V}$	Potential energy of a system.
$\vec{v}$	Velocity vector associated with the fluid.
v_b	Velocity of decent of the bell of the damper calibration rig.
V_p	Volume of air in one partition.
W	Width of the horizontal cylinder.
X	Complex amplitude of the wave excitation force associated with one degree of freedom system.
$\vec{X}$	Wave excitation force and moment vector (6 component).
$\overline{X}$	Mean value associated with variable 'X'.
$\vec{X}_\theta$	Generalised excitation force vector.
X_{rms}	Root mean square associated with variable 'X' .
$\mathbf{Z}$	Radiation impedance matrix.
Z	Radiation impedance associated with a one-degree of freedom system.
$\mathbf{Z}_\theta$	Generalised radiation impedance vector.
z_0	Water depth.
z_b	Vertical position of the centre of buoyancy.
z_g	Vertical distance of the centre of mass.
Z_b	Vertical position of the centre of buoyancy measured from the centre of the cylinder.
Z_B	Vertical position of the centre of mass of the Ballast measured from the centre of the cylinder.
Z_g	Vertical distance of the centre of mass measured from the centre of the cylinder.

Acronyms and abbreviations

2D	Two Dimensional.
3D	Three Dimensional.
AWS	Archimedes Wave Swing.
BC	Boundary Condition.
BEM	Boundary Element Method.
COB	Centre Of Buoyancy.
COM	Centre Of Mass.
DBC	Dynamic Boundary Condition.
DLL	Dynamic Link Library.
EWPG	Edinburgh Wave Power Group.
IPS	Interproject Service AB.
IST	Instituto Superior Técnico
KBC	Kinematic Boundary Condition.
MIT	Massachusetts Institute of Technology
OPEC	Organization of the Petroleum Exporting Countries.
OWC	Oscillating Water Column
RAO	Response Amplitude Operator
RCW	Relative Capture Width
RMS	Root Mean Square
UK	United Kingdom
WAMIT	Wave Analysis MIT
WEC	Wave Energy Converter

Chapter 1
Introduction

The present work is concerned with the study of a new design for the solo Duck wave energy converter (WEC) which has been recently considered at the University of Edinburgh. The key innovation is the modification of the asymmetric profile of the cam shape to a circular horizontal cylinder which oscillates with the same nodding motion around of an off-centred axis. The initial studies from a hydrodynamic numerical model showed that a good performance was still achievable and that it was worthwhile to pursue this direction. The immediate advantages of this design are associated with the cost reduction of manufacturing and assembly for a full scale prototype.

Figure 1.1 shows a schematic drawing of the cylindrical Duck at operation in the sea. The dimensions are of 12 m in diameter by 30 m in length ($W/D = 2.5$) and it is designed to operate at a water depth of about 50 m ($z_0/D \approx 4$). The off-centred cylinder pierces the free surface at a certain draft and is connected to the sea floor through post-tensioned concrete tubes. An universal joint connects these tube struts to the sea-floor allowing swing rotations about the vertical axis such to align the device automatically to the predominant direction of the incident waves and swell. Some details of the design, installation and operation are described in Salter et al. [2007].

A version of the Duck which could produce fresh water instead of electricity is looked at in detail. The desalination Duck uses the direct action of its motion in the sea waves to drive a thermal process based on vapour-compression. This version of the Duck is convenient to study because the desalination process involves a pressure across the thermal heat exchanger that is proportional to the angular velocity of the device. As a consequence, an almost ideal linear damping is obtained which is suitable for the mathematical models in the frequency domain that are developed in the present work.

As part of the survivability strategy, it was thought to fully submerge the device and seek refuge at the sea floor from storms or very energetic sea states. This could be achieved at prototype scale by letting sea water enter inside the rigid struts in a controlled way such as to counter balance the buoyancy force of the cylinder. The tests performed with a scale model in a three dimensional wave basin showed that the device is still a good

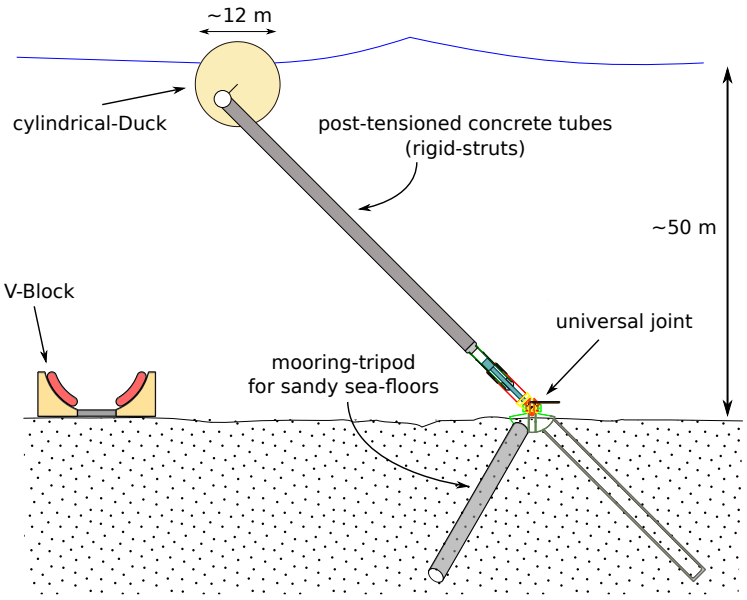

Figure 1.1: *The cylindrical Duck in operation at sea. Drawing from Salter et al. [2007] where a proposal to moor the device in a sandy sea-floor is presented. It uses a tripod anchor that is sunk into the sand by using controlled water-jetting and is retained by suction. The V-block shown is part of the proposed installation process.*

wave energy absorber when totally submerged at a certain level with the advantage of lowering the mooring forces by more than half [Lucas et al., 2008].

Such performance is not surprising and indeed it resembles the operation of a wave energy converter known as the 'Bristol cylinder', proposed by David Evans [Evans, 1976, Evans et al., 1979]. This device, pictured in Figure 1.2, is a long cylinder which is totally submerged and connected to the sea floor through external hydraulic rams. These control its motion, and wave energy is absorbed by allowing the cylinder to move in small orbits with uniform circular motion.

The main idea behind this concept is a well known property of submerged long cylinders. Since Ursell [1950a,b] it is known that a fully-submerged cylinder with its centre moving with uniform velocity in a circle of small radius produces uni-directional waves on the free surface above it. This peculiar property is found at all frequencies and Evans et al. [1979] showed that there is a particular circular motion of the cylinder that is capable of absorbing completely an incident regular wave train of any frequency.

As a consequence of geometric symmetry, a cylinder whose centre moves in a circular orbit at uniform velocity is dynamically indistinguishable from one which rotates with equivalent angular velocity around an off-centred axis. Figure 1.3 attempts to represent this observation.

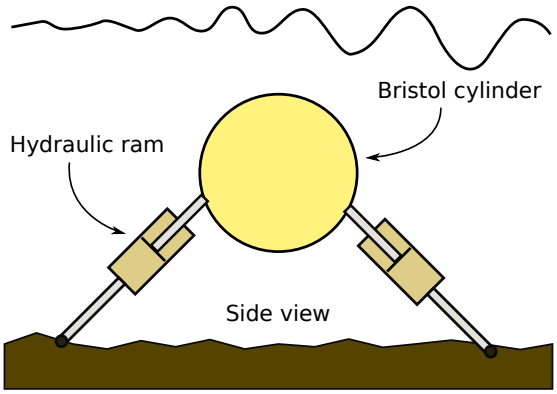

Figure 1.2: *Schematic drawing of the Bristol cylinder in operation at sea.*

It should be emphasised however that in spite of the geometrical similarity between the two fully-submerged devices, the cylindrical Duck and the Bristol cylinder absorb wave energy in different ways. Whereas the second rotates continuously with its centre in a circular orbit, the first nods with oscillatory motion around its off-centred axis.

Thus the properties of a horizontal cylinder piercing the free surface and fully-submerged are of central concern in the present work. Section 2.3 reviews aspects of such properties as reported by other authors. Section 4.2 extends those results by considering additional variables such as the width of the cylinder and the water depth. Furthermore, in Section 4.3, these are widen to include the case of a cylinder with an off-centred axis through the use of transformation formulas which establish the relationship between the hydrodynamic forces and moments at the centre of the cylinder to those at the off-centred location. All hydrodynamic forces are computed with a commercial software called *WAMIT* which is described in Section 4.1.

The equation of motion of the off-centred cylinder is derived for one degree of freedom system and its performance as a wave energy converter is analysed through Sections 4.4 and 4.5. The design is optimised for the sea conditions at a real location, by taking into

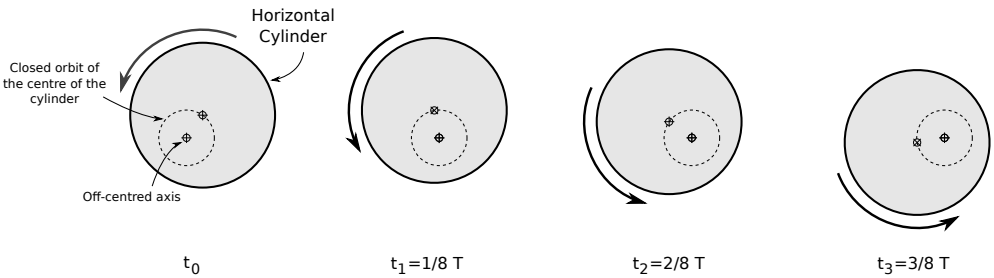

Figure 1.3: *Motion of an off-centred horizontal cylinder. Geometric similarity between a cylinder moving its centre with uniform circular motion in a circular orbit and a cylinder rotating with uniform angular velocity around an off-centred axis.*

account the hydrodynamic forces computed for the different configurations of cylinders with a width to diameter ratio (W/D) of 2.5 in deep water. Design cases associated with three diameters of the cylinder are looked into detail for the fully-submerged and free-surface piercing cylinder. Different control strategies are considered with focus on pure damping control. It is shown how the inertia can be adjusted to make the device resonate at a certain wavelength through a careful distribution of mass and a relationship between the location of the off-centred axis and mass redistribution to achieve a maximum performance is given. The section concludes with the computation of the forces at the attachment point for the design cases considered.

Chapter 3 and 5 deal with the application of the off-centred cylinder to the desalination Duck. In Chapter 3 the experimental methodology and results associated with the tank tests performed with a 1:33 scale model of the desalination Duck are presented, and these results are then used to validate the mathematical model developed in Chapter 5.

Among the difficulties associated with the experimental testing was the design of a linear pneumatic damper used to substitute the desalination unit of the full scale machine. Some of the initial results presented in Lucas et al. [2007, 2008] had to be considered unreliable as they were based on experiments which were subsequently found to have used a damper of unstable calibration. After those experiments it was found that the properties of the material used in the pneumatic damper changed with the entrapment of small amounts of stray water from the inner water pendulum during large motions of the scale model. The linear damper was redesigned with a new material having a stable linear air flow to pressure characteristics. This design was based on thin stainless steel shims with slit cuts such as to control its stiffness during the passage of the required air flow. The details of the design and calibration of this damper are presented in Section 3.2. The results from the experimental tests performed with regular and mixed seas are presented in Section 3.4.

The dynamics of the desalination Duck is described by a semi-analytic model presented in Section 5.3. This model includes the hydrodynamic forces computed for the horizontal cylinder in Section 4.2 and takes into account the influence of the mooring attachment and the water-pendulum inside the hull of the desalination Duck. This model is developed following a Lagrangian approach to describe the dynamics of the system, a convenient approach for multi-interacting bodies. This description requires the definition of independent variables associated with the motion which are referred to as generalised coordinates. All external forces, including the hydrodynamic forces, are consequently expressed within this framework. The constraint forces, however,

do not need to be included. Along with the reduction of the number of equations needed to describe the motion, these constitute the main advantages for using such formulation. To illustrate the procedure, the dynamics of a simpler model with just one degree-of-freedom are derived in Section 5.2. Validation of these models with experiments are presented in Sections 5.2.1 and 5.3.1.

1.1 Some facts about wave energy

Sea and ocean waves are the result of the transfer of energy from the atmosphere to the top layer of water. In general it is known that waves are associated with winds or atmospheric pressure gradients and it is clear from laboratory experiments that high wind speeds create both gravity and surface-tension waves [Wiegel, 1964].

It is common to distinguish between waves which are under the influence of local winds, which have an irregular character and direction of propagation, from those which have been generated far away in a remote storm and which are smoother in appearance and propagate predominantly in only one direction. The first are commonly called *wind waves*, whilst the latter are known as *swell*.

In deep water, the waves after being created in the oceans, travel very long distances with little energy losses. Thus when compared with other renewable energy sources, the resource available in the ocean waves present a high energy density and can be forecast with some anticipation.

If the propagation of a wave is followed by an observer moving with a velocity equal to the wavelength of the wave divided by its period, the wave will appear to him as if not moving. This velocity is known as the *phase velocity* of the wave.

The nature of the water waves is dispersive. This means that waves of different wavelengths propagate with different phase velocities. In deep water, longer waves travel faster than short waves. In deep water, when waves travel together in a wave-train group, the component wave periods tend to segregate in such way that the longest waves lead the main body of waves and the shortest waves lag behind. Linear wave theory shows that in deep water, the *velocity of the group* is half of that of the phase velocity.

The *mean energy density per unit area* is proportional to the square of the wave amplitude ($\overline{E} = \frac{1}{2}\rho g a^2$) and with equal contributions from the kinetic and potential energy enclosed in a vertical column of the same area. The *mean energy flux rate* is shown to be equal to the mean energy density multiplied by the group velocity ($\overline{P_w} = \overline{E}\, c_g$).

It is estimated that the available wave energy resource for the north-Atlantic is of the order of 290 GW [Clément et al., 2002]. The long term annual average wave-power in the north-west Atlantic ranges from about 25 kW/m on the Canary Islands to about 75 kW/m over the west coasts of Ireland and Scotland. Taking into account the North-sea, which has an annual average power level between 10 to 21 kW/m and the Mediterranean basin which has lower levels between 4 and 11 kW/m (with the best resource in the Aegean sea), the total wave energy resource for Europe is of about 320 GW.

The total energy consumption in the world in 1991 given by World Resources Institute (WRI) [2005] is equal to 8.7×10^9 toe (metric tones of equivalent oil). This value converts to about 1.01×10^5 TWh, giving an average power consumption rate of 11.6 TW. For the year of 2001 this increases to 13.3 TW and has been estimated to be about 15 TW in 2008. The main sources of energy come from fossil fuels: oil (36.8%), gas (26.0%) and coal (25.2%). These numbers give notice of the increasing dependence on energy of modern societies and the enormous pressure and challenges ahead if environmental sustainability is to be pursued. The same source reports that the electrical energy consumption in Europe is about 5.6 MWh per capita which gives 463 GW average power consumption rate (European population of 7.25×10^8).

It is clear then that even if only a fraction of the total deep-water wave energy resource was to be harvested, it could provide a significant contribution to energy demand and sustainability in European countries.

1.2 On the history of wave-power

Many different mechanisms and concepts have been proposed to harvest the energy from sea waves. The first known patent of such a device is attributed to Girard & fills, de Paris and dates from 1799. The first British patent dates from 1855, and by 1973 Leishman and Scobie [1976] were able to document 340 patents in Britain alone [Clément et al., 2002]. Falcão [2010] recognises more than 1000 patents that had been registered around the world by 1980. A source of regularly updated information on the status of development of wave energy is given in the annual reports on ocean energy from the International Energy Agency. Annex 9 of the 2008 report [AEA Energy & Environment and Sustainable Energy Ireland, 2006] gives a list of a total of 80 different concepts under development during that year.

The above numbers testify to the wide interest in wave energy but also to the difficulties, problems and different conceptual solutions that have been proposed to harvest this

energy. Until today, the commercial feasibility for such devices is still to be proven. Nevertheless, several concepts have reached the prototype scale and have been tested and demonstrated in real seas.

It is of common to attribute the pioneering work of Yoshio Masuda in the 1940 as the start of the development of modern wave energy. He engineered a navigation buoy powered by wave energy that reached commercial implementation in 1965. However, it was not until the so-called energy crisis of 1973 and the work by Salter [1974] that general interest was raised and intensive research pursued.

It is not the intention of present work to give an extensive review of the different technologies available and proposed to date. Due to the enormous number of different technologies and concepts available it is difficult even to classify them into a simple set of categories. Different authors have used different classifications depending on the selection criteria. The classical terminology applied to a wave energy converter distinguishes three main categories: *point absorber*, *terminator* and *attenuator*. It is applied mainly to oscillating bodies and provides information on the principle of operation and absorption geometry.

Falcão [2010] gives a review which focuses on the different proposed concepts and power-take-off technologies. He provides a classification which is mostly based on the working principle and is more appropriate to describe the concepts that are been developed today. This classification is reproduced in Figure 1.4 and information on some of the devices can be found in the web-pages which are listed in Figure 1.5.

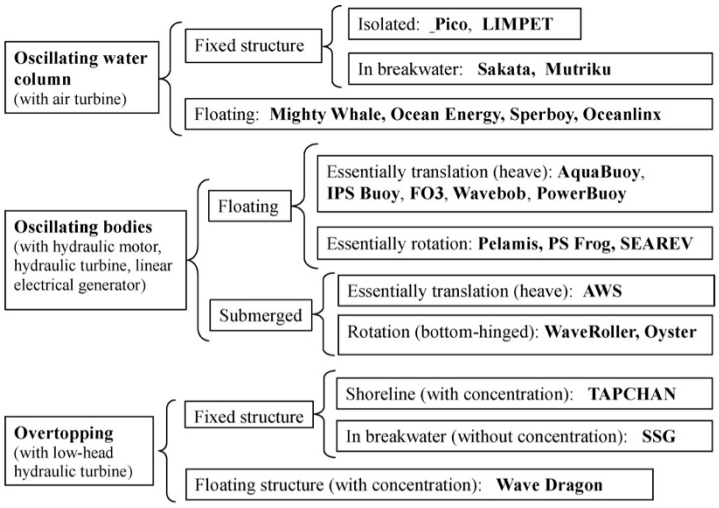

Figure 1.4: *Classification based on the working principle of wave energy-converter devices. Reproduced from Falcão [2010].*

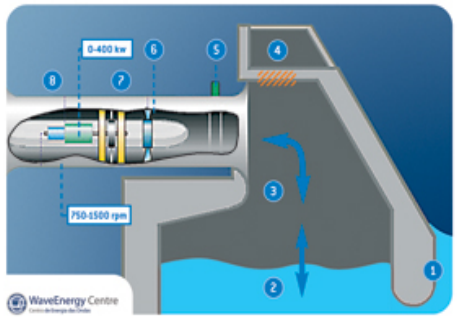

Oscillating Water Column (OWC)

Fixed structure:
Pico OWC (http://www.pico-owc.net/)

In breakwater:
Sakata OWC

Floating structure:
Oceanlinx (http://www.oceanlinx.com)

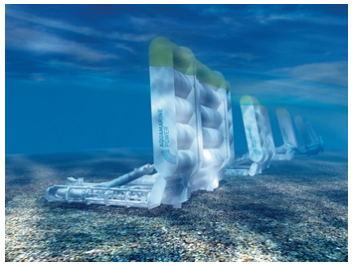

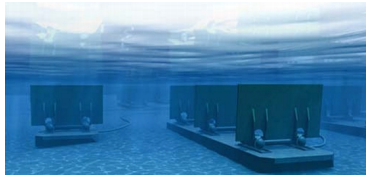

Submerged Oscillating Bodies:

Oyster (http://www.aquamarinepower.com)

WaveRoller (http://www.aw-energy.com/)

AWS (http://www.awsocean.com/)

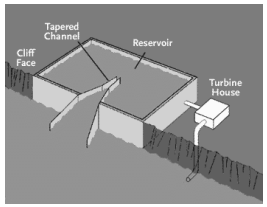

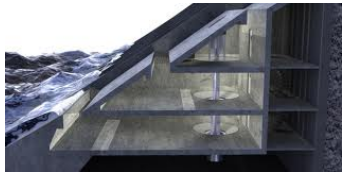

Overtoping:

WaveDragon (http://www.wavedragon.net)

TAPCHAN

WaveSSG (http://www.waveenergy.no)

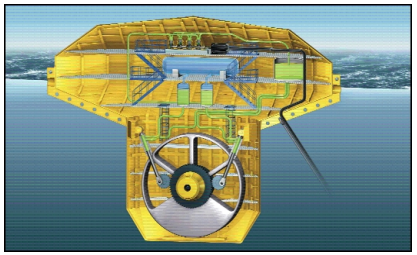

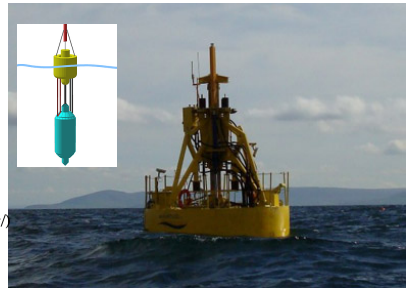

Floating Oscillating Bodies:

Pelamis (http://www.pelamiswave.com)

SeaRev (http://fr.wikipedia.org/wiki/Searev/)

WaveBob (http://www.wavebob.com/)

Figure 1.5: *Examples of wave energy-converters.*

Chapter 2
Background review

The topic of wave energy conversion and utilisation has been mostly developed over the last forty years and can be followed most closely through the regular international conference proceedings since 1976. The first at Canterbury, then Heathrow (1978) and Edinburgh (1979). The First symposium on Wave Energy Utilisation took place in Gothenborgh (Sweden) in 1979 and the second in Trondheim (Norway) in 1982. Very relevant as well was the international Union of Theoretical and Applied Mechanics (IUTAM) symposium that took place in Lisbon in 1980. Finally, since 1993 the biannual European Wave (and Tidal) Energy conferences of Edinburgh, UK (1993); Lisbon, Portugal (1995); Patras, Greece (1998); Aalborg, Denmark (2000); Cork, Ireland (2003); Glasgow, UK (2005); Porto, Portugal (2007) and Uppsala, Sweden (2009).

Some reviews which summarise the most important achievements can be found in journal papers, books and reports. One of most recent is given by Falcão [2010] which reviews the various technological concepts developed during these years. Salter [1989] reviews the topic in 1988 in a period where major achievements had already been obtained but society interest and the number of financed projects had declined sharply in the UK. Clément et al. [2002] provides an overview of state of the art and perspectives wave energy on the European countries at the start of the decade following a renewed interest in the field, mainly due to the financing framework programs provided by the European Commission. A more theoretical review which is focused mostly on the principles and mathematical description of wave energy extraction is given by Falnes [2007] and Evans [1981].

Comprehensive overviews at the state of the art of wave energy which focus on both the theoretical aspects and the technical implementations of different technologies can be found in a book edited by Cruz [2008] and on a report produced for The UK Department of Trade by Thorpe [1999]. Count and Jefferys [1980] provides a collection of papers which reviews and focus important technical aspects still very relevant today on the wave energy absorption. Falnes [2002] is seen by many as the reference book for a complete theoretical background on wave power absorption by oscillating systems.

Many of the topics of interest in wave energy are shared by off-shore structures, boats and barges. The hydrodynamics of off-shore structures and in particular the motion and interaction of floating bodies in waves can be found in many books of which Newman [1977], Faltinsen [1990], Sarpkaya and Isaacson [1981], Mei [1989] and Wiegel [1964] are notable examples. Of importance on this topic is the review given by Wehausen [1971]. An extensive review on the mathematical theory of surface waves can be found for example on Wehausen and Laitone [1960] and Lamb [1975].

2.1 The Edinburgh Duck wave energy converter

In 1974 Salter described his invention at the University of Edinburgh of a promising new wave energy converter [Salter, 1974]. By the early nineteen-eighties this device, which is now generally referred to as the Edinburgh Duck, had been extensively studied. Its conceptual development and evolution of design is well documented in many publications and reports of his Edinburgh Wave Power Group. A brief overview of the work performed there in the last forty years is given by Salter [2008].

2.1.1 The Duck

The energy crisis of 1973 and the steep increase of oil prices caused by the OPEC embargo into some of the leading western economies set the stage for the intensification of research into alternative sources of energy that could secure future energy availability.

In this context, Salter [1974] presented a paper in which he proposed to harvest large amounts of energy from ocean waves. He drew attention to the high power densities transported by the waves, which could reach average annual values as high as 77 kW/m in locations based in the northern Atlantic close to the north-western coast of the UK. Salter proposed a machine, the Duck, which would be able to convert to mechanical work the energy from the waves and he reported experiments with scale models in which he had obtained efficiencies as high as 80% for wavelengths of about eight times the diameter of the device.

The original design of the Duck was based on the efficient hydrodynamic shape that is shown in Figure 2.1, which was able to rotate about an axis parallel to the incident waves.

Many Ducks would be laid in ‘terminator’ arrays across the prevailing wave direction and energy would be captured from their movements relative to a common cylindrical

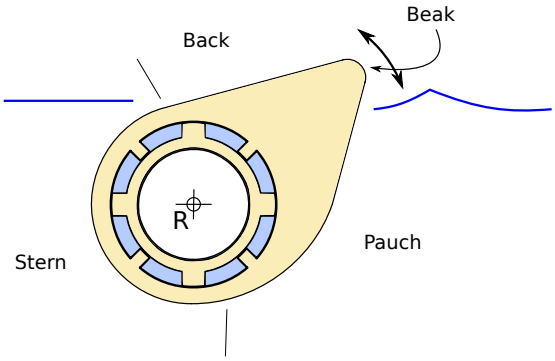

Figure 2.1: *Duck profile (adapted from Salter [1974]) showing early spline-pump power-take-off concept.*

'spine'. By averaging the reactions from differently-phased Duck motions, the relatively stationary and torsionally-stiff spine would thus provide a common source of reaction for the many separate electricity generating systems. A contemporary artist's impression of a Duck wave-farm is shown in Figure 2.2.

To relieve excessive heave and surge bending moments, the spine for a complete Duck power station evolved over a number of years into an articulating linear array of separate closed tubes that were inter-connected by active two degree-of-freedom joints. During experimental studies it was found that useful additional wave energy could be captured from the movements of these joints Salter [1980]. Typical dimensions for a single 2 MW Duck, designed to match the North Atlantic conditions, were 10 to 15 m stern diameter and 30 to 45 m wide. Some references to the Duck's articulated-spine are evident in the recent sea-going machines built by Pelamis Wave Power.

Early Duck designs were driven by the UK wave energy program which required the development of 2 GW power station concepts and so part of the philosophy behind the spine-mounted terminator concept was to maximise the use of sea-space. Because the

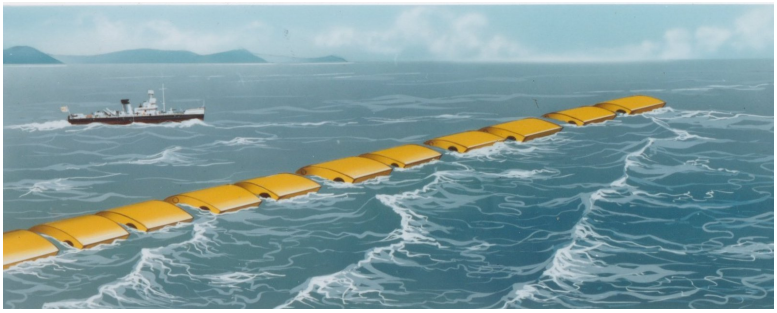

Figure 2.2: *An early artist's impression of a Duck string (ETSU artist).*

reaction-forces required for the power generation were provided for within the complete floating system, Duck-strings could be 'slack-moored' so that the seabed attachments would be required only to provide against mean drift forces.

Until the closure of the UK wave energy program in 1982, the Edinburgh Duck was the object of intensive experimental research described in the wave power-group annual reports [Salter et al., 1975, Jeffrey et al., 1976, 1978a,b,c]. Innumerable tank tests with small scale models were performed during these years, and these led to consistent improvements in the design and in the achieved performances. The work of the wave power group at Edinburgh is also relevant on the development of pioneering small-scale experimental techniques and facilities of which the absorbing wave-makers with force feed-back and the wide-tank are a mere examples. [Salter, 1981]. The results from the tank tests also inspired early theoretical work on the theory of energy absorption (for example Evans [1976]) and the information collected then is still very valuable today as a source of experimental data which can be useful to validate theoretical mathematical models based on more sophisticated mathematical assumptions.

The most important results obtained during the Duck tank tests and also the evolution of the full scale concepts which propose sophisticated solutions for very challenging engineering problems can be followed through several journal and conference proceedings publications: Salter et al. [1976], Salter [1976, 1979, 1980, 1982, 1985b].

The full scale design was assessed several times by independent consultants and continuous improvements were made by the wave power group to address identified problems and decrease costs. The report by Thorpe [1999] describe three major full scale designs assessments for the Duck performed in 1983, 1991 and 1998. The corrections and improvements in the consecutive designs led to reductions of about 70% on the generation costs between the consecutive stages, putting the final estimated price of electricity generation at 5.3 p/kWh (at 8% discount rate). The 1998 design had major modifications and the reader is referred to this report and also Salter [1993] more for details.

Among the first attempts to produce mathematical models that were able to give realistic descriptions of the dynamics and predict correctly the efficiencies found experimentally for the Edinburgh Duck are given by Count [1978] and Mynett et al. [1979].

Count [1978] extends the two dimensional source distribution method given by Ursell [1950a,b] to apply it to an asymmetric floating body. With the hydrodynamic forces solved for the shape of the Duck, it considers the dynamic equations for one and for

multiple degrees of freedom with a linear power take off, obtaining a good agreement with experiments for the estimated performance curves. In this paper Count also compares the two-dimensional performances of the Edinburgh Duck with a two-pontoon system of semi-elliptical cross section hinged in the middle, and concludes that both are comparable at appropriate scales, having an almost identical performance, if only fixed damping is applied. He also concludes that a 10 m Duck has an excellent performance over typical sea states if a 'reactive' loading power take off is used, and that the diameter should be increased to 15 m for comparable performance if fixed damping is used instead. Also for a non-optimised geometry he found a decrease in performance if the system was not restrained and free to move also in surge and heave.

Mynett et al. [1979] uses a numerical method based on the linear potential theory to study the performance of the Edinburgh Duck. The method is based on hybrid elements and uses a finite element approximation near the body and an analytical representation in the remaining domain. By parametrising the geometry, it performs a series of investigations of the impact of variation of the geometry on the performance, concluding that less asymmetric profiles have little impact on the optimal performance. It also concludes that the water depth affects only in minor ways, the hydrodynamic coefficients and optimum performance, and that performance drops with increasing freedom in heave and surge.

The remarks on the drop of performance for devices moving freely in more than one degree of freedom should be taken carefully and complemented with the experimental results reported in Jeffrey et al. [1978a]. These experiments were carried out using different values of compliance for heave and surge modes of motion and it was found an increase in performance when certain values of compliance were used comparing with the one degree of freedom case.

2.1.2 The solo Duck

During the nineteen-eighties, a float-alone 2 MW solo Duck was studied [Salter, 1989]. It offered a possible route to the kind of experience in design, construction and operation of sea-going systems that would be helpful in the development of 2 GW multi-Duck systems. In contrast to the slack-moored Duck-string, the spine-less solo Duck shown in in Figure 2.3 (one of several possible configurations) would be connected by a tension-leg arrangement to piled seabed attachments that would also provide reaction forces for its power-take-off system.

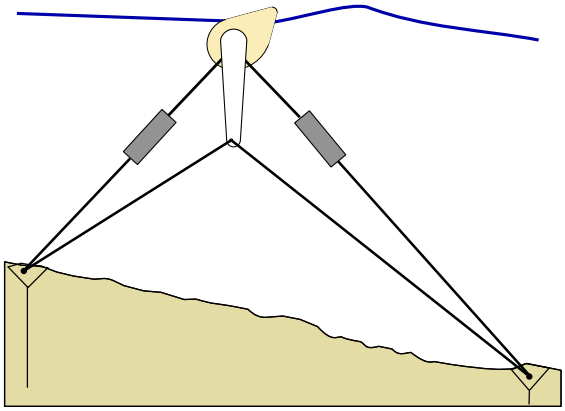

Figure 2.3: *A solo Duck with tension-leg moorings and piled seabed attachments from Salter [1989]. In this particular arrangement, the hanging arm and the lower lines provide torque reaction for the Duck power-take-off system whilst the boxes in the upper lines contain hydraulic mechanisms for yielding and elasticity control.*

Tank experiments with a solo Duck, however, subsequently showed that it would be hard to prevent unacceptable snatching of its tension-leg cables. In steep waves these would at times go completely slack, and then violently tighten again when the hydrodynamic loads reversed again [Salter et al., 2007].

The tension-leg cables of the solo Duck design were therefore replaced by post-tensioned concrete tubes, referred to as *struts*. Compared with the unavoidable stress-reversals of the steel cables within the tension-leg system, the steel bars within the struts would remain always in tension and would therefore be protected against fatigue. The struts of the solo Duck would be connected by a universal-joint to the seabed attachments to give the machine the freedom to automatically align with the predominant direction of the incident waves and swell. Details of this design can be found at Salter et al. [2007].

Extensive tank tests with a 1:100 scale model of the solo Duck are reported in Skyner [1987]. By using a rig developed in the early years of the wave power-group, known as the heave-surge-pitch rig, Skyner was able to measure the radiation impedance associated with the solo Duck. This rig proved to be the ideal tool for these measurements as it provided the means to perform the adequate controlled motions and force measurements necessary to estimate this hydrodynamic quantity. By using the radiation impedance, Skyner was able to predict the power-take-off characteristics which would give maximum performances in regular waves and mixed seas and also to obtain estimations for full-scale Ducks.

Nebel [1992a] described a method to perform a complex-conjugate synthesiser control in regular waves by implementing a pseudo complex conjugate controller which was able

to simulate optimum control over a wide frequency bandwidth, obtaining even higher efficiencies.

Pizer [1992, 1993b] used a three dimensional numerical method to compute the hydrodynamic forces of the solo Duck and estimated performances for different geometries and operating conditions. The numerical method was based on the technique described by Garrison and Chow [1972]. It is a linear wave-theory three-dimensional low-order method, based on the distribution of pulsating Green function sources over the surface of the body which interact with the fluid. A mesh of triangular or quadrilateral facets is used to describe the velocity potential, and compute the hydrodynamic coefficients of the submerged structure. The method is validated with known analytical results and experiments from Skyner [1987]. Pizer computes the performance associated with a solo Duck under motion constrains for head-on waves and waves at a 40° angle, for cases in which the device is operated with three and six degrees of freedom. In the report, Pizer [1994], the study is extended to an increased number of different geometries and for cases in which the power-take-off controller operates with pure damping.

2.1.3 The desalination Duck

A version of the Duck which uses wave induced motions to directly drive a desalination vapour compression process had started to be developed in the mid eighties [Salter, 1985a, 2005, Salter et al., 2007].

It is known that globally the consumption of fresh water is growing at a faster rate than the population growth. The records presented by FAO show that since 1900 to 1995 the global fresh water consumption had increased by about six times which is twice the rate of population growth [IWMI, 2006]. The same source estimates that about 7% of the total theoretical available fresh water is already being extracted from the planet. This an estimate of the total resources and does not reflect the actual available resources and the non homogeneous distribution of fresh water around the globe. From these arguments it can be concluded that fresh water is already a scarce resource especially in regions in the Middle East, North-Africa, West of North America, North of China, South of India and South East of Australia [IWMI, 2006].

It is thus expected that fresh water production through desalination processes will increase in the future. The global capacity in 2005 was of about 32 000 000 m^3/day

and is estimated to grow at a rate of about 1% per year which is still lower than the rate of demand which is of about 3% [IWMI, 2006].

All desalination processes are energy intensive and thus its costs are a major drawback. The use of renewable energy sources to fetch the energy required to drive the process is seen as desirable to decrease associated costs but examples of large scale plants are still to this day scarce and mostly associated with solar or wind energy. The use of the energy from sea waves for the production of fresh water was first reported to have been successfully accomplished by the DELBOY project which used oscillating buoys to drive pistons pumps to fed sea water to reverse osmosis modules [Hicks et al., 1989]. A review of the resource assessment and the technologies developed to drive a desalination process with wave energy is given by Davies [2005]. These are mostly based on the reverse osmosis principle which uses pressurised sea water, forced to pass through a permeable membrane which retains the salts. In this technology, small leakages of salted water are common to occur and these membranes are designed to just meet the World Health Organisation requirements for total dissolved solids below 500 parts per million [Salter, 2005].

The alternative desalination process proposed by Salter [1985a] uses the wave driven motions of the Duck to drive a thermal distillation process known as vapour-compression desalination. Like any other distillation process the vapour-compression produces almost pure water with total dissolved solids between 0 to 25 parts per million.

A schematic diagram to describe the vapour-compression principle is given in Figure 2.4. The sea water is initially filtered and pre-heated to a feed temperature (T_f) in a multi-flow heat exchanger and introduced into the evaporator where the temperature is further increased to boiling temperature (T_1). The energy (latent heat) required to increase the temperature of the feed is provided by the saturated steam which condenses on the other side of the heat-exchanger. On the feed side, the vapour which is at pressure P_1 has a saturation temperature equal to $T_{v1} = T_1 - \epsilon$ where ϵ is the boiling point elevation (which increases with the total dissolved solids). The mechanical turbo-compressor sucks the steam vapour and discharges it as super-heated vapour at a pressure P_2 to the other side of the thermal heat exchanger. The super-heated vapour loses its energy (latent heat) by cooling to saturation temperature T_2 and condenses to form the product distillate (fresh-water). The non-evaporated feed in the evaporator forms the brine blow-down and both the product distillate at T_2 and brine at T_1 are used to pre-heat the feed in the multi-flow heat exchanger. The main energy used in this process is the mechanical work required to drive the turbo-compressor.

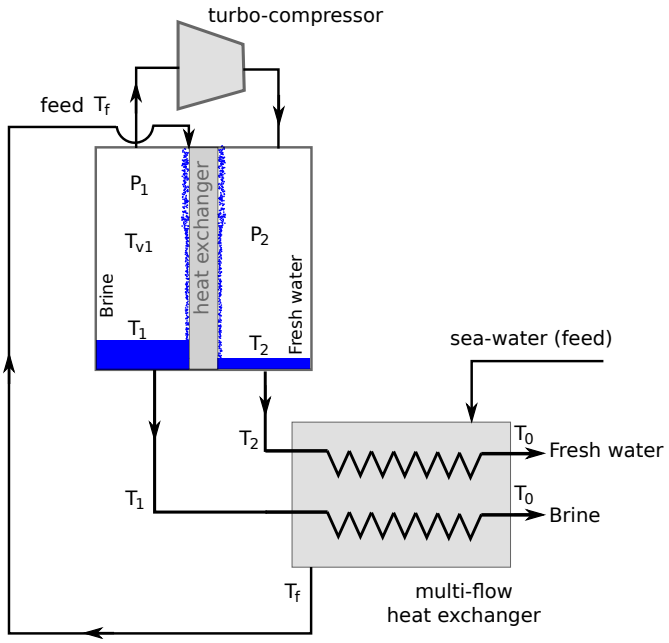

Figure 2.4: *Schematic diagram of the vapour compression distillation process.*

In the desalination Duck, which is sketched in Figure 2.5, instead of the turbo-compressor used in most vapour compression systems, the pumping action is provided directly by the motion of the Duck in waves. The body of the Duck is partially filled with warm water and a central partition divides the remaining interior into two separate steam compartments. The thermal heat-exchanger is located in this central partition and is designed to be folded in a series of clamped U-shapes, such to provide the separation surface for the process. Brine is recirculated on one side whereas on the other side, steam condenses into fresh water which is collected as final product.

The water inside the Duck is heated at factory before deployment to almost boiling temperature and kept warm during operation mainly due to the thermal isolation provided by the foam concrete with one meter thickness placed around the cylinder hull. Assuming a thermal conductivity of the foam concrete of 0.1 W/mK, it is expected a temperature fall of less than 4 K over a month if all energy flows were stopped. During operation, heat is constantly generated by the work produced in compressing the steam and by all internal flow losses [Salter et al., 2007].

While the Duck undergoes its wave-driven alternating rotations, the surface of the inner water tends to stay relatively horizontal and so the system forms an enormous, positive displacement double acting pump with no sliding seals or accurate machined parts and

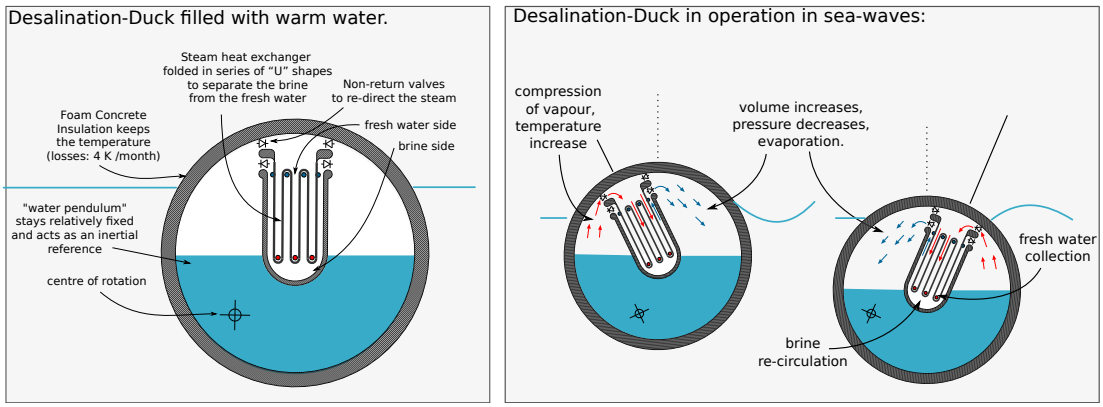

Figure 2.5: *Schematic section of the desalination Duck*

very low internal losses. The torque opposing the wave motion of the Duck is proportional to the pressure across the partition which, being proportional to the angular velocity, provides something like the ideal linear damping.

The sea water feed is first filtered and then pre-heated by the thermal inertia of the Duck to almost boiling temperature. Its temperature is further increased when the feed water falls downwards along the surface of the heat-exchanger and is evaporated by the reduction of pressure in the suction chamber, drawing latent heat from the heat-exchanger. On the next stroke, compression occurs and warms the vapour. The warm pressurised vapour is then fed to the other side of the heat-exchanger where condensation occurs with release of the latent heat. By sequencing the non-return valves shown in Figure 2.5 the vapour is directed alternately through the compression and suction sides of the heat-exchanger. The boiling temperature of brine increases with the percentage of dissolved solids and so places a practical limit for its concentration and number of recirculation cycles. The thermal energy of the products (brine and fresh-water) is then recycled to preheat the sea-water feed for a new cycle of vapour-compression.

2.2 Bristol cylinder

The device proposed by David Evans known as the Bristol cylinder was conceived from purely theoretical considerations based on properties of submerged cylinders known since Ogilvie [1963].

A two dimensional fully-submerged cylinder is able to generate waves in the free surface propagating in only one direction when the cylinder moves in such way that its centre describes a circle with uniform circular motion. Heave oscillations of the cylinder produce waves of equal amplitude and phase radiating to infinity to either side, whereas surge oscillations produce waves of equal amplitude but of opposite phase. Through a suitable combination of the amplitudes and phases of these vertical and horizontal motions is possible to cancel the wave at one side completely and thus radiate a wave in only one direction. Reversing the sign of the time coordinate shows that there exists a motion of the cylinder which is able to absorb 100% of a given incident wave. This result remains valid for all depths of submergence and all frequencies showing that a cylinder satisfies the criteria of a good wave absorber [Evans, 1976].

Another important property of submerged cylinders is that no incident energy is reflected from a fixed submerged cylinder [Dean, 1948, Ursell, 1950a,b]. The zero reflection implies that the mean second-order horizontal forces are smaller and also enables cylinders to be placed one behind the other so that the second can pick up any energy lost by the first. Evans [1980] show how such idea could improve the performance by showing the theoretical curve of two cylinders tuned to different frequencies ensuring 100% absorption at these frequencies achieving high efficiencies over wide frequency band.

Evans's work is very broad and is devoted mainly to the theory of wave absorption by oscillating bodies. Most of the theoretical work developed by his group related with the Bristol cylinder can be found at Evans [1976, 1979, 1980, 1985], Evans and Linton [1993].

Performance curves for a fully-submerged cylinder constrained by a damper-spring power-take-off to move only in horizontal and vertical direction can be found in Evans [1976] as an application for his pioneering work on the theory on of wave absorption by oscillating bodies.

Evans was able to predict successfully the performance curves for his device before performing experiments on the heave-surge-pitch rig at the University of Edinburgh [Evans et al., 1979]. A very good agreement with theory was found for the small incident waves and the theoretical maximum of 100% absorption predicted by the theory was achieved for appropriate values of spring and damping constants and also the broad bandwidth predicted by the theory was confirmed.

2.3 Hydrodynamic properties of horizontal cylinders

It was not before 1976 that Evans [1976] presented for the first time a rigorous theory on the wave absorption by oscillating bodies which was able to explain the experimental high efficiencies obtained by Salter [1974]. In his paper, Evans applied his theory to fully and half submerged horizontal cylinders restrained by a spring-damper power-take-off system which allowed only oscillations of the cylinder in one or two modes of operation (surge and heave), obtaining the corresponding efficiency curves. By using far-field arguments, he first derived an expression which gives the maximum two-dimensional efficiency in terms of the amplitude of the waves radiated at both extremes of infinity showing that for one mode of operation a maximum efficiency of 50% would be reached and that it would be possible to obtain 100% if the oscillations would generate waves in only one direction.

The main reason pointed out by Evans for not predicting the performance of the Edinburgh Duck was the lack of knowledge of the hydrodynamic coefficients associated with asymmetric cam shapes as the Duck. These coefficients are fundamental to estimate the linear hydrodynamic forces associated with the interaction of a particular large structure with the waves. The main difficulty to describe the dynamics of these off-shore structures lies in the estimation of these quantities, which depend essentially on the shape of the structure and on its frequency of oscillation (see Section 4.1.3 for a brief overview on these relationships). Therefore, he used known period dependent values of these coefficients for a fully and half-submerged cylinder estimated from curves given by Frank [1967].

In subsequent work, Evans et al. [1979] considered two-dimensional analytical solutions derived for forced oscillations of a submerged cylinder derived initially by Ursell [1950a,b] and extended by Ogilvie [1963]. The method represented the velocity potential by a sum of source functions and multi-poles placed at the origin with strength determined so as to satisfy the boundary conditions on the body and so the solution is obtained by determining the coefficients in the multi-pole series by solving approximately an infinite set of linear equations.

Plots of the added mass and hydrodynamic damping coefficients used by Evans are found at Figures 1 and 2 of McIver and Evans [1984] as an example of the negative values of added mass that can occur for a range of oscillating periods when the depth of submergence of the cylinder is sufficiently small compared its diameter. Added mass is related with the mean kinetic and potential energy of the fluid and negative values

occurs when the oscillating body produces a fluid motion where the mean potential energy exceeds the mean kinetic energy.

A more detailed study of these coefficients for horizontal cylinders near or penetrating the free-surface is given by Greenhow and Ahn [1988]. The limit problems at high and low frequency of oscillation were studied in a previous paper by the same principal author [Greenhow and Yanbao, 1987] in which he reviews analytical results for the asymptotic limits for the added masses of horizontal cylinders near or penetrating the free-surface.

Greenhow and Ahn [1988] used a standard numerical source-sink program to compute the non-dimensional frequency dependence of these quantities, which are reproduced below for reference as Figures 2.6 and 2.7 for different submergence levels and drafts of two-dimensional horizontal cylinder fully-submerged and piercing the free surface.

For the fully-submerged case Ogilvie [1963] shows that both the hydrodynamic coefficients are equal in heave (vertical) and surge (horizontal) modes at all frequencies. Using the asymptotic approximations, Greenhow and Ahn [1988] shows that when fully-submerged, the asymptotic approximations give a zero value for the hydrodynamic damping at both lower and higher frequency limits, and the added mass shows variation with depth of submergence, specially in the low frequency case. When the cylinder breaks the surface surge, added mass remains continuous but with a discontinuity in the derivative. The heave added mass becomes logarithmically infinite as a consequence of source like potential shown by non-vanishing damping.

Greenhow observes that the rapid variations of added mass and damping can be understood physically in terms of resonance as the waves generated at the top of the cylinder are strongly reflected by the sudden occurrence of deep water at the cylinder edge forming standing waves above the cylinder and causing a rapid drop in the wave radiation damping.

By using the Kramers-Kroning relations which relate the added mass to the hydrodynamic damping, Greenhow justifies the occurrence of negative added mass just after the peak in the hydrodynamic damping by the rapid drop of this quantity.

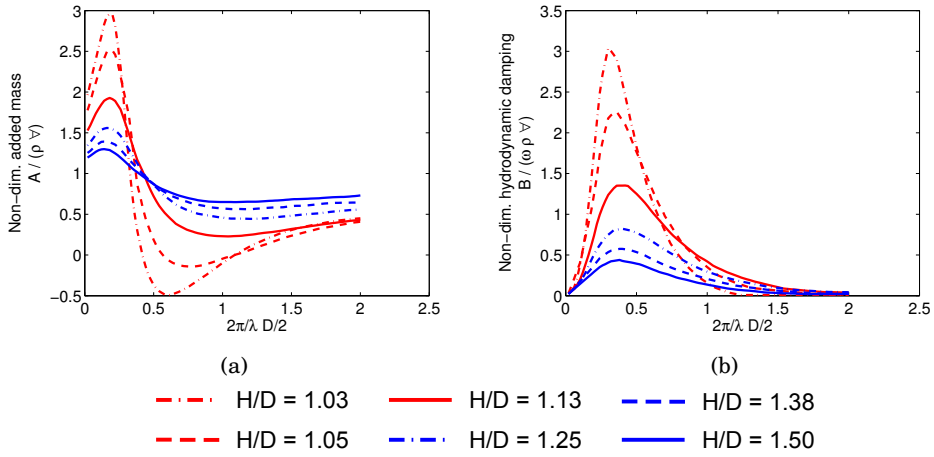

Figure 2.6: *(a) Added mass and (b) hydrodynamic damping, for a fully submerged long horizontal cylinder. Variation with non-dimensional frequency* $\frac{kD}{2} = \frac{2\pi}{\lambda}\frac{D}{2}$. *H is the draft measured from the bottom of the cylinder to the free-surface. Data from Greenhow and Ahn [1988].*

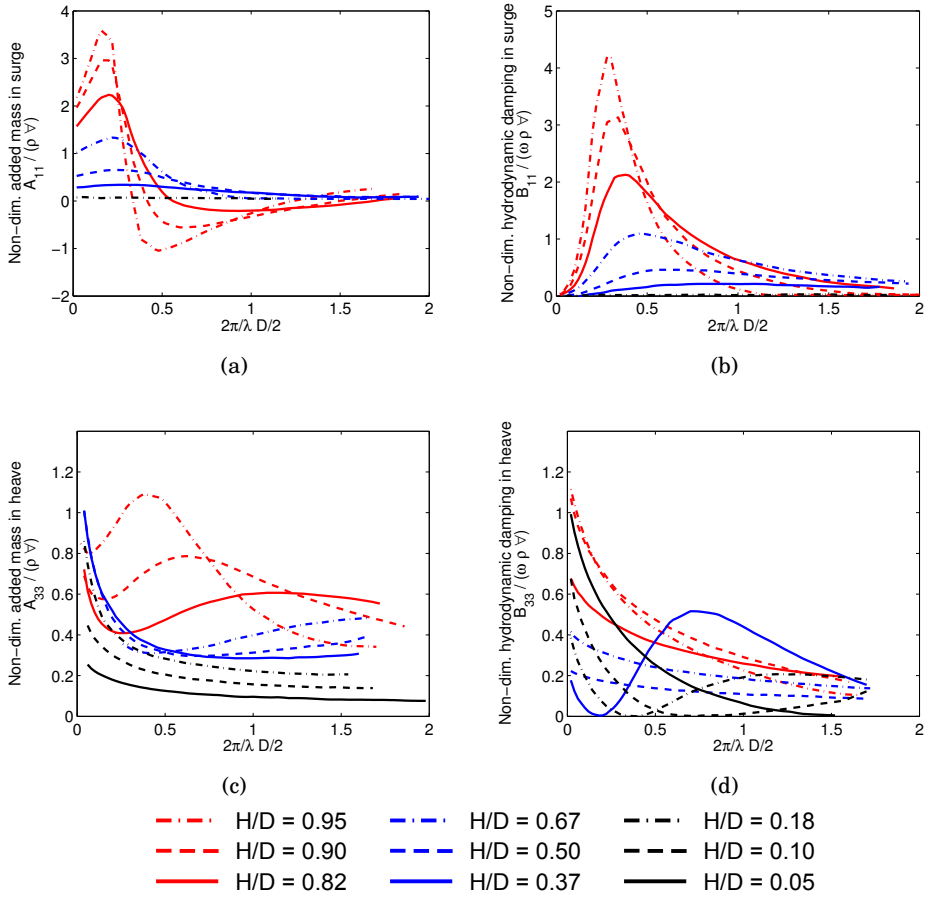

Figure 2.7: *(a) Added mass and (b) hydrodynamic damping in heave and (c) added mass and (b) hydrodynamic damping in surge for a cylinder piercing the free-surface. Variation with non-dimensional frequency* $\frac{kD}{2} = \frac{2\pi}{\lambda}\frac{D}{2}$. *H is the draft measured from the bottom of the cylinder to the free-surface. Data from Greenhow and Ahn [1988].*

2.4 Description and interpretation of previous research work from offset cylinders

The initial studies on the hydrodynamics of the cylindrical Duck were presented in Cruz and Salter [2006]. As such, the hydrodynamic forces associated with an off-centred horizontal cylinder piercing the water surface were studied in some detail. Cruz [2009] provides a further extension of this work.

These forces were computed through the use of a commercial Boundary Element Method (BEM) software called *WAMIT*, based on linear potential flow theory which is described in some detail in Section 4.1 of the present work.

These initial studies were aimed primarily at evaluating the influences of the off-centred axis and draft of the cylinder on the motions and performance such to identify the best configurations to achieve the best energy absorption performance. A total of forty different configurations were investigated.

The influence of the rigid struts (see Figure 1.1) and damping were included in the *WAMIT* model through the use of an external stiffness and damping matrix (see (4.18b) in Section 4.1 for more details). The motion responses in the three degrees-of-freedom (surge, heave and pitch) were obtained from *WAMIT*, and performance was computed by assuming that only one mode of operation (pitch) would capture wave energy.

It was found that the hydrodynamic forces are strongly dependent on the configuration chosen and thus by choosing an appropriate draft and location for the off-centred axis, the performance of the cylindrical Duck could be adjusted to be comparable with that of a 'classic' solo Duck with the same control function. Cruz concluded that the location of the off-centred axis influences the resonance peak both in position and amplitude. As both the submerged volume of the cylinder and distance of the off-centred axis to the centre increases, it broadens period performance bandwidth. He also observes that it could be beneficial to actively control both parameters in a full scale application to match varying sea states.

As part of the validation process of the *WAMIT* numerical model, Cruz performed comparisons with the 'classic' solo Duck using results obtained by Pizer [1994] and with the the experimental measurements in regular waves performed by Skyner [1987].

Figure 2.8(a) reproduces the results obtained by Cruz. These compare the theoretical performances obtained using a complex conjugate control for the cylindrical Duck

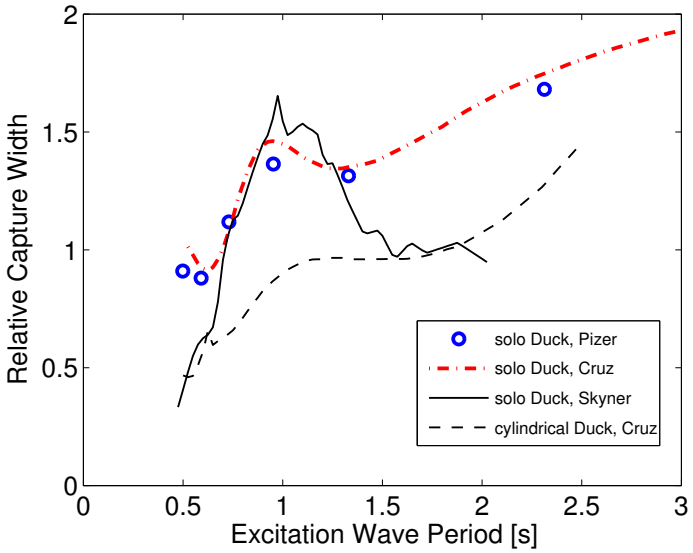

(a)

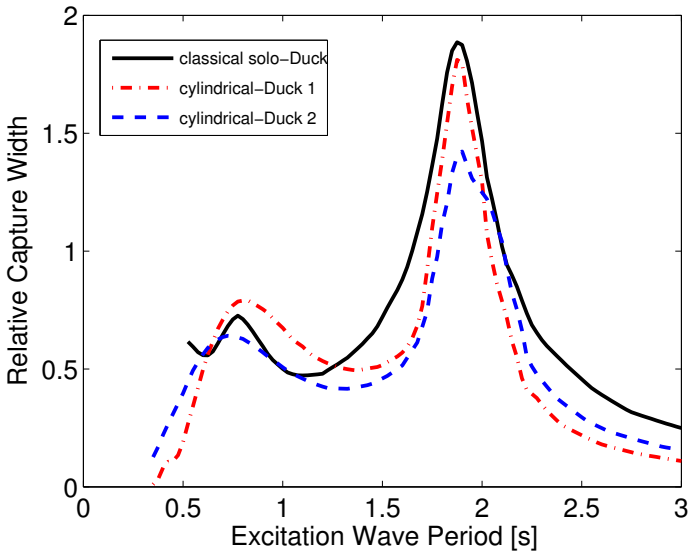

(b)

Figure 2.8: *(a) Comparison of performances in regular waves obtained for the 'classic' solo Duck using a complex conjugate control strategy. The 'thick' curve was obtained using a WAMIT hydrodynamic model (Cruz [2009]) and the circles were obtained using a low-order custom made hydrodynamic code (Pizer [1994]). The 'thin' curve corresponds to tank measurements by Skyner [1987] which used frequency-specific mixes of spring and damping in pitch and spring in heave and surge to obtain the maximum pitch performance for the 'classic' solo Duck. (b) Performance comparison in regular waves between the 'classic' solo Duck and cylindrical version for two different locations of the axis of oscillation. The three curves where obtained through WAMIT hydrodynamic model present by Cruz [2009] using an optimum damping control strategy.*

with those obtained for the 'classic' Duck with the same control. The experimental performances measured in regular waves by Skyner [1987] through the use of optimum values of spring and damping are also included for reference.

Figure 2.8(b) reproduces the performances for the cylindrical Duck and 'classic' solo Duck when an optimum damping control strategy is used. The two curves associated with cylindrical Duck correspond to different locations of the off-centred axis and were scaled using a Froude similarity law (see Section 3) such to place the peaks at the same resonance period as the observed for the 'classic' solo Duck.

Preliminary comparisons with a physical scale model were performed in the Edinburgh tank, and measurements for the motion responses were performed for two cases in which the damping mechanism was either taken into account or not. In general, a good agreement was found between the hydrodynamic model and experiments, with the best correlation for the pitch motion.

To access and decouple the influence of the inner water pendulum, the mass provided by the inner water-pendulum was substituted by static ballast consisting of sand bags evenly distributed. With this arrangement the inertia of the system stayed constant during the measurements avoiding any slamming effects from the inner water. As expected a better correlation with the numerical model was obtained. For the case with the inner water pendulum, Cruz identified considerable differences in the results around the second resonance peak, suggesting that the influence of the parametric change of the centre of gravity and inertia were significant and were not represented accurately in his numerical model.

To account for this and to decouple the effect between the inner water pendulum and the outer cylindrical shell, Cruz implemented a two body approach within *WAMIT*. This can be accomplished by defining in the equation of motion with 12 by 12 matrix quantities (6 by 6 for each body) for the inertia, external damping and spring, and restrict the modes of motion to the ones of interest (in this specific case, only pitch for the water pendulum). This procedure is not detailed in Cruz [2009], being pointed out that differences found between the different numerical models seemed negligible for the majority of frequencies tested. It is also proposed to study in future work the influence of the inner water pendulum motion by using a more recent version of WAMIT code which allows the inclusion of internal tanks or by using a different code like *AQUADYNE* coupled with *CUVE* .

A different approach to solve the multi-body problem is considered within the present work which is described in Section 5.3. The equations of motion are solved analytically for the cylindrical shell and water pendulum using generalised coordinates and Lagrange dynamics with the hydrodynamic forces and power-take-off included as external generalised forces. The equations are linearised and considered in the frequency domain. This method decouples clearly the influence of inner water pendulum.

Cruz also presented preliminary results for the tank measurements obtained with a linear damper. The desalination unit in the scale model was substituted by a linear pneumatic damping system designed to impose a torque proportional to the angular velocity of the device. However, this first damper presented many problems related with air-leakages and calibration and as such these preliminary results should be considered with some care. In the present work, in Section 3.4, most of the experiments are re-evaluated by using later dampers which were redesigned so to present a stable characteristics and calibration over time.

2.5 Wave power absorption theory

A brief summary of wave power absorption theory that is of some importance for the present work is given bellow. This theory is developed under the assumptions of linear potential flow with the motions of the devices taken as being sufficiently small. Further details on these assumptions are presented in Section 4.1.1 within the context of a software known as *WAMIT* used to compute the hydrodynamic coefficients of the horizontal cylinders and which is based on this theory.

The *mean absorbed power* by a body oscillating in one single mode of motion is shown to be (see for example Evans [1980]):

$$\overline{P_{abs}} = \frac{1}{8}\frac{|X|^2}{B} - \frac{1}{2}\left|U - \frac{1}{2}\frac{X}{B}\right|^2 B \tag{2.1a}$$

where X, B and U are the complex amplitudes of the incident wave excitation force, hydrodynamic damping and velocity of the oscillating body respectively. It is shown that in general $B > 0$, so the *maximum mean absorbed power* is:

$$\overline{P_{max}} = \frac{1}{8}\frac{|X|^2}{B} \tag{2.1b}$$

achieved when the second term of (2.1a) is zero, which occurs when the velocity of the device is in phase with the excitation force and the amplitude of the optimum velocity is:

$$U_O = \frac{1}{2}\frac{X}{B} \tag{2.1c}$$

If power is extracted through a linear power-take-off mechanism such that force is proportional to velocity, $F_d = -KU$ and substituting into the one degree-of-freedom equation of motion, the *mean absorbed power* by the device can be written alternatively to (2.1a) as (see Evans [1985], Evans and Linton [1993]):

$$\overline{P_{abs}} = \frac{1}{4}\left(K + K^*\right)|U|^2 = \frac{1}{8}\frac{|X|^2}{B}\left(1 - \frac{|K - Z^*|^2}{|K + Z|^2}\right) \tag{2.1d}$$

The *maximum mean absorbed power* given by expression (2.1b) is achieved when the power-take-off constant of the linear controller is equal to the complex conjugate of the radiation impedance, i.e.:

$$K = Z^* = B + i\,\omega\left(J + A - \frac{C}{\omega^2}\right) \tag{2.1e}$$

where J is the moment of inertia (or the inertial mass) of the device, A the hydrodynamic added mass and C the hydrostatic stiffness.

It should be noted that as defined, the linear power-take-off constant K is a complex number and the maximum value of mean absorbed power is achieved only if the above condition (2.1e) is satisfied for every incident wave. This type of control is commonly known as *complex conjugate control*. It gives a useful maximum performance limit but is of limited practical interest as no physical implementation is known to date.

If the power-take-off force consists instead of a *pure value of damping*, K is a real number and it is shown that the mean absorbed power by the device is given by the expression (Evans and Linton [1993]):

$$\overline{P_{abs}} = \frac{1}{4}\frac{|X|^2}{(B + |Z|)}\left(1 - \frac{(K - |Z|)^2}{|K + Z|^2}\right) \tag{2.2a}$$

For this case the *maximum* value of the mean absorbed power is achieved when the control constant is equal to the absolute value of the radiation impedance, i.e.:

$$K = |Z| = \sqrt{B^2 + \omega^2\left(J + A - \frac{C}{\omega^2}\right)^2} \tag{2.2b}$$

and is equal to:

$$\overline{P_{max}} = \frac{1}{4}\frac{|X|^2}{(B+|Z|)} \tag{2.2c}$$

By introducing an expression which relates the hydrodynamic damping (B) with the excitation force (X) (Haskind relation), and substituting into (2.1b) and dividing by the average power in the incident wave-train per unit crest length ($\overline{P_w}$), an expression for the maximum performance is obtained (see Evans [1980]):

$$(CW)_{max} = \frac{\overline{P_{max}}}{\overline{P_w}} = \lambda \frac{\left|X(\beta)\right|^2}{\int_0^{2\pi} |X(\theta)|^2 \, d\theta} \tag{2.3a}$$

This quantity (CW) is known to the wave energy community as the *capture width*. It represents an equivalent frontage length upon which the device is able to absorb all the incident wave power. It has dimensions of length and for some cases it is known to reach values greater than the actual length of the device.

It is also common to express CW as non-dimensional by dividing it by the frontage width of the device (W). This quantity is commonly referred as *relative capture width* and is given as:

$$RCW = \frac{CW}{W} = \frac{\overline{P_{abs}}}{\overline{P_w} W} \tag{2.3b}$$

Maximum limit values for the special cases of devices which are *axi-symmetric*, i.e. those which have a vertical axis of revolution and which move in only one degree of freedom are known and were derived independently and almost simultaneously by Budal and Falnes [1975], Evans [1976] and Newman [1976].

For the special case of an *axi-symmetric body moving only in heave*, the oscillations are independent on the direction of the incident wave and so $|X(\theta)|^2$ in (2.3a) can be taken out of the integral, evaluating to 2π and $CW_3^{max} = \lambda/2\pi$.

Writing (2.3a) in terms of the far-field functions an equivalent expression is obtained:

$$CW_{max} = \frac{\overline{P_{max}}}{\overline{P_w}} = \lambda \frac{\left|f(\beta)\right|^2}{\int_0^{2\pi} |f(\theta)|^2 \, d\theta} \tag{2.3c}$$

This expression permits to understand the fundamental concept that a good wave energy absorber as the ability when making waves to concentrate the propagating wave energy along a narrow sector rather than distributing the energy along all angles. This would minimise the value of the integral in (2.3c), maximising the value of the capture width.

The two-dimensional equivalent of the above expression has the amplitudes of the radiated waves in the infinity appearing explicitly (a^+ at $+\infty$ and a^- at $-\infty$) and was given by Evans [1976]:

$$E_{max} = \frac{\overline{P_{max}}}{\overline{P_w}} = \frac{|a^+|^2}{\left(|a^+|^2 + |a^-|^2\right)} \tag{2.3d}$$

The above expression emphasises the importance for a good wave absorption device to be a good wave-maker with the ability to generate waves in only one direction. In such case, a maximum efficiency equal to one would be possible to be achieved: $E_{max} = 1 \Leftarrow |a^-| = 0$.

This expression also justifies the conceptual design of the Duck by Salter which since the earliest designs was made in such way to not generate waves to the rear.

An extension of the above expressions to devices that *absorb energy in more than one mode of operation* can be found in Evans [1980], Falnes [1980].

The velocity of the device is given as a vector of n components that characterise its motion: $\vec{U} = [U_1, U_2, ..., U_i, ..., U_n]^T$. The control force ($\vec{F}_d$) and the wave excitation force ($\vec{X}$) are also vectors with n components associated with each mode of motion whilst **Z**, **A**, **B**, **C** and **J** are $n \times n$ matrices.

The mean absorbed power is then given by the expression:

$$\begin{aligned} \overline{P_{abs}} &= \frac{1}{4}\left(\vec{U}^\dagger \vec{X} + \vec{X}^\dagger \vec{U}\right) - \frac{1}{2}\vec{U}^\dagger \mathbf{B} \vec{U} \\ &= \frac{1}{8}\vec{X}^\dagger \mathbf{B}^{-1} \vec{X} - \frac{1}{2}\left(\vec{U} - \frac{1}{2}\mathbf{B}^{-1}\vec{X}\right)^\dagger \mathbf{B}\left(\vec{U} - \frac{1}{2}\mathbf{B}^{-1}\vec{X}\right) \end{aligned} \tag{2.4a}$$

The last expression in (2.4a) is obtained provided that $\mathbf{B}^{-1}$ exists (i.e. $\det\mathbf{B} \neq 0$). The dagger superscript symbol (†) represents the complex conjugate transpose (also known as Hermitian transpose or adjoint matrix).

The *maximum absorbed power* for a device in *multi-mode operation* is then given by an expression which is in appearance very similar to (2.1b):

$$\overline{P_{max}} = \frac{1}{8}\vec{X}^\dagger \mathbf{B}^{-1} \vec{X} \tag{2.4b}$$

which is achieved when the velocity of the device is equal to:

$$\vec{U}_O = \frac{1}{2}\mathbf{B}^{-1}\vec{X} \tag{2.4c}$$

If the control force is linear such that $\vec{F}_d = -\mathbf{K}\vec{U}$ with **K** a $n \times n$ matrix and such that the equation of motion in the frequency domain can be written as $(\mathbf{K} + \mathbf{Z})\vec{U} = \vec{X}$, the

condition for the optimum velocity, given by (2.4c) is achieved provided that $\mathbf{K} = \mathbf{Z}^{\dagger}$ (note that: $\left(\mathbf{Z}^{\dagger} + \mathbf{Z}\right) = \mathbf{B}$).

A theory which considers the power absorbed by a device from a lower number of absorption modes than the number of motion modes can be found in Count and Jefferys [1980], Evans [1985], Evans and Linton [1993]. In this theory it is assumed that only m ($\leq n$) velocity components of the device ($\vec{U}$) can be controlled, and thus the control force is written as:

$$\vec{F}_d = -\mathbf{R}\mathbf{K}\mathbf{R}^T\vec{U} \tag{2.5a}$$

with $\mathbf{K}$ a $m \times m$ matrix, and $\mathbf{R}$ a $n \times m$ for which the diagonal components are equal to one and all other components equal to zero: $R_{ij} = \delta_{ij}$, with the Kronecker delta $\delta_{ij} = 1$ if $i = j$ and $\delta_{ij} = 0$ otherwise.

The *mean absorbed power* is then given by:

$$\overline{P_{abs}} = -\frac{1}{2}Re\left\{\vec{F}_d^{\dagger}\vec{U}\right\} = \frac{1}{4}\vec{U}^{\dagger}\mathbf{R}^T\left(\mathbf{K} + \mathbf{K}^{\dagger}\right)\mathbf{R}\vec{U} \tag{2.5b}$$

where the velocity of the device ($\vec{U}$) satisfies the equation of motion in the frequency domain:

$$\left(\mathbf{R}\mathbf{K}\mathbf{R}^T + \mathbf{Z}\right)\vec{U} = \vec{X} \tag{2.6}$$

and it is shown that the *maximum mean absorbed power* is achieved when the power-take-off matrix is equal to:

$$\mathbf{K} = \left(\mathbf{R}^T\left(\mathbf{Z}^{\dagger}\right)^{-1}\mathbf{R}\right)^{-1} \tag{2.7}$$

The above expressions assume the occurrence of small harmonic sinusoidal waves and motions and as such are of limited importance. The stochastic nature of a real sea state imposes that to apply the above mathematical framework the principle of superposition must be assumed.

The total mean wave power per unit crest length associated with an unidirectional random wave-train is given by (Tucker and Pitt [2001]):

$$\overline{P_w^{sea}} = \rho g \int_0^{\infty} S(\omega)\, c_g\, d\omega \tag{2.8}$$

where $S(\omega)d\omega$ is the energy contribution from waves with frequencies between ω and $\omega + d\omega$ and c_g is the group velocity associated with the wave-train.

For deep water, the group velocity is half of the phase velocity: $c_g = \frac{1}{2}\frac{\omega}{k}$ with $\omega^2 = g\,k$.

Considering also the energy contribution from the waves incident upon different directions (β) in a real sea, the total mean wave power per unit circle area in deep water is given by:

$$\overline{P_w^{sea}} = \frac{1}{2}\rho g^2 \int_0^{\infty}\int_{-\pi}^{+\pi} S(\omega,\beta)\,\omega^{-1}\,d\beta\,d\omega = \frac{1}{64\pi}\rho g^2 H_{m_0}^2 T_e \tag{2.9}$$

where H_{m_0} and T_e are the significant wave height and energy period defined respectively as: $H_{m_0} = 4\sqrt{m_0}$ and $T_e = m_{-1}/m_0$, where m_i are the spectral moments of ith order given by $m_i = \int_0^{\infty} S(f,\theta) f^i\,d\theta\,df$.

The *total mean power absorbed* by an isolated device is given by:

$$\overline{P_{abs}^{sea}} = \frac{1}{2}\rho g^2 \int_0^{\infty}\int_{-\pi}^{+\pi} S(\omega,\beta)\,\omega^{-1}\,CW\,d\beta\,d\omega \tag{2.10}$$

The relative capture width associated with the performance of a device in a mixed sea is given by analogy with (2.3b) with the correspondent average absorbed power and average power per unit front length associated with the mixed sea,i.e.:

$$RCW_{sea} = \frac{\overline{P_{abs}^{sea}}}{\overline{P_w^{sea}}\,W} \tag{2.11}$$

One of most commonly used spectra that has been employed to describe ocean waves has a distribution known as *Pierson-Moskowitz* and assumes steady wind conditions over a large area of the ocean and over a long time interval so that waves come into equilibrium with wind and the sea is said to be fully developed. This spectra are described by one parameter, the wind speed. Another spectra that are commonly used and are essentially of the same form, uses two parameters: the significant wave height (H_{m_0}) and peak frequency (f_p). This spectra are known as *Bretschneider* and are given by the following formula:

$$S(f) = \frac{5H_{m_0}^2}{16 f_p}\,\frac{1}{(f/f_p)^5}\,\exp\left(-\frac{5}{4}\left(\frac{f}{f_p}\right)^{-4}\right) \tag{2.12}$$

Chapter 3
Experimental methodology

At the early stages of conceptualisation and development of a wave energy converter it is of fundamental importance to proceed with experiments which take place in the controlled environment of a laboratory. These experiments are very valuable to verify and identify possible flaws in the modelling process and to uncover mistakes which could lead to disaster if only detected at prototype scale.

The use of a wave-tank basin to test scale models is thus crucial and a very important tool at the disposal of the designer. The design process should be iterative and the results of those tests integrated into concept development from the earliest stages.

The ultimate objective of tank testing is to reproduce as close as possible in the controlled environment of a laboratory the conditions found at full scale seas.

Tank tests are also important to validate and verify the mathematical models which represent the dynamic behaviour of a device and which are fundamental during all design procedure. Nevertheless, these models are inherently idealisations of the conditions found in real seas and experimental tank tests become even more valuable when the mathematical models are inadequate to represent these real phenomena.

The validity of the extrapolation of results obtained with scale models to prototype scale is only ensured when there is conservation of dynamic similarity between the scales and this condition occurs whenever the relative ratio of the dominant forces is preserved [Newman, 1977].

Two important non-dimensional numbers associated with fluid dynamics problems are the *Froude* and *Reynolds numbers*. These reflect the relative weight of the inertial to the gravitational and viscous forces and are given respectively by:

$$F_{rd} = \frac{U}{\sqrt{gL}} \quad \sim \quad \frac{\text{Inertial}}{\text{Gravitational}} = \frac{\rho U^2 L^2}{\rho g L^3} = \frac{U^2}{gL}$$
$$R_e = \frac{UL}{\nu} \quad \sim \quad \frac{\text{Inertial}}{\text{Gravitational}} = \frac{\rho U^2 L^2}{\rho g L^3} = \frac{U^2}{gL}$$

where ρ, μ and U are respectively the density, viscosity and velocity of the fluid, g the acceleration of gravity, L a characteristic length associated with the problem and $\nu = \mu/\rho$ the kinematic viscosity of the fluid.

Dynamic similarity is thus guaranteed only if both of these numbers are kept constant for both scale model and prototype. Unfortunately the ratio between them, proportional to the ratio of gravitational to viscous forces is incompatible for most geometrical scales due to the limitations of the range of the kinematic viscosities of real fluids. Indeed:

$$\frac{R_e}{F_{rd}} = \frac{\sqrt{g}L\sqrt{L}}{\nu} \quad \sim \quad \frac{\text{Inertial/Viscous}}{\text{Inertial/Gravitational}} = \frac{\text{Gravitational}}{\text{Viscous}}$$

To illustrate this argument and for example, if the length scale between prototype to scale model is 1/100, and if the kinematic viscosity of water (at 20°C) is equal to $\nu = 1.0 \times 10^{-6}$ m^2/s, it would require ν to decrease by a corresponding amount of three orders of magnitude ($100\sqrt{100} = 1000$).

Because of the small values of the kinematic viscosity of water (ν), viscous forces are only dominant for very small length scales and can be ignored for most of problems involving wave tank testing. For a typical wave tank experiment in which the length scale of a physical model is equal to 100 mm, and is excited by a small regular wave of period equal to $T = 1$ s and amplitude of $A = 10$ mm, the fluid velocity is $U = \omega A = 2\pi \times 1 \times 0.01 = 0.063$ m/s. Thus, the corresponding Reynolds number is equal to $Re = \frac{UL}{\nu} = 6300$, and the Froude number to $F_{rd} = \frac{U}{\sqrt{gL}} = 0.064$, denoting an absolute dominance of the inertial and gravitational forces relative to the viscous forces.

For large structures, when the diffraction regime applies ($L/\lambda > 1/5 = 0.2$), Sarpkaya and Isaacson [1981, §6.0] argue that the fluid particle displacements relatively to the length scale (L) become sufficiently small so as the effects of flow separation are minimal and localised. In such case flow separation should not occur and the effects of viscosity are confined to the boundary layers. It is then also appropriate to treat the flow as irrotational and apply the potential flow theory.

These arguments justify the dominance of the inertial and gravitational forces relative to the viscous forces and as such in order to derive full scale results from scale model testing it is in general sufficient to consider the *Froude similarity law*.

The constancy of the *Froude number* at both model and prototype scale provides a relationship between the scale factors which can be used to derive prototype values from measurements at model scale. Defining the scale of a quantity x as the ratio of

the value of that quantity in the physical model to that of the prototype: $k_x = x_m/x_p$. The constancy of the Froude number implies that the scale of velocities is equal to the square root of the scale of lengths: $k_U = (k_L)^{1/2}$. Table B.1 in Appendix B presents some scale factors obtained through the assumption of Froude similarity law and which relate the results obtained with a scale model to the expected values at full scale.

The present chapter presents a description of the experimental tests performed with a scale model of the desalination Duck wave-energy converter in the curved-tank of the University of Edinburgh. The first sections describe briefly this three dimensional wave-basin facility and also the working area in which the measurements were performed.

The scale model of the desalination Duck was initially built to validate the hydrodynamic model developed by Cruz and Salter [2006]. This study considered a selection of sub-optimal sets of configurations for experimental validation and also some preliminary tank test measurements for the response amplitude operator, which showed a general good agreement with the hydrodynamic model. Lucas et al. [2007] and Lucas et al. [2008] extended the experimental results including the measurements of performance and mooring forces in monochromatic and polychromatic seas and also for configurations in which the model was totally submerged. After these studies were performed, it was observed that the air-damper used inside the scale model was vulnerable to water spills from the inner water-pendulum and that this had a dramatic impact on its calibration characteristics and so those results should be treated with care.

The scale model is briefly described in Section 3.2 with some detail of the re-design of the air-damper to solve the water-spill problem and of its subsequent calibration.

Section 3.3 describes the instrumentation and calibration procedures used for the measurements. These use specifically designed force sensor and conditioning circuit for a pressure sensor. This section also describes the procedures used to measure the waves with conductivity wave-gauges and the video tracking system used to record the motion of the scale model.

The final section present the results obtained with the scale model for monochromatic and polychromatic waves.

3.1 The Edinburgh curved-tank

The curved-tank of the University of Edinburgh is an experimental facility designed primarily for wave energy. It has a nominal water depth of 1.2 m and is fitted with 48 absorbing wave-makers hinged at half of the depth and disposed in a unique configuration around a quarter circle with 9 m radius. This new tank was commissioned in 2003 and is the successor to the old 'wide-tank' which was demolished in 2001 as a consequence of the completion of a long-delayed building project at the University of Edinburgh [Taylor et al., 2003].

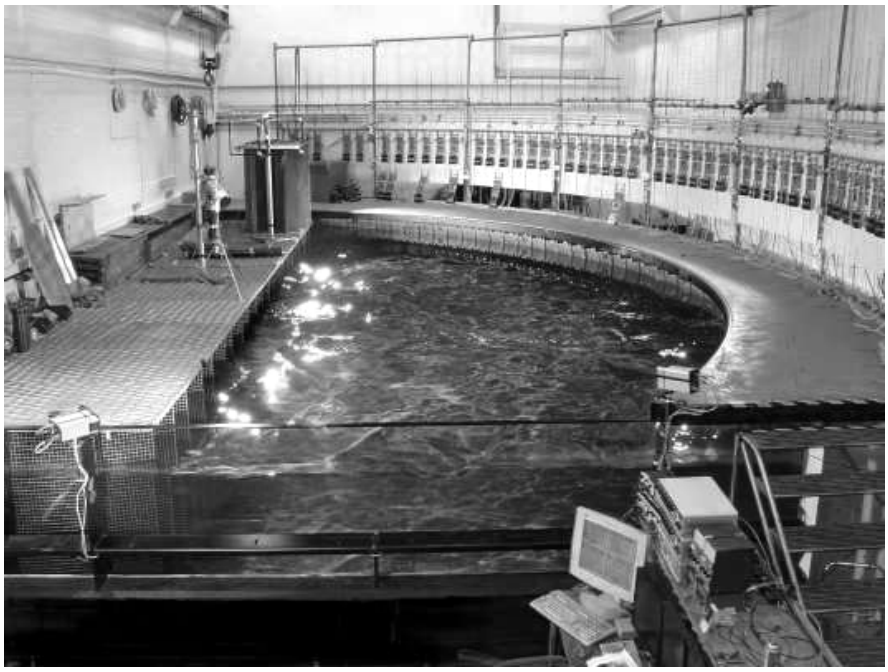

Figure 3.1: *The Edinburgh curved-tank. Note the Qualisys video cameras at the left at the start of the beach walkway and the right at the near inner end of the curved walkway (see Section 3.3.2).(Photo from Taylor et al. [2003])*

This new facility should be apprised in the context of the old wave basin built in 1977 with the dimensions of 28 m by 11 m and with the same nominal depth. It was the first tank with the capacity to generate multi-directional long-crested seas to be built specifically for wave energy and was designed to test Duck-strings at scales down to 1/150. It was fitted with 89 force-control absorbing wave-makers placed along the longest side and as originally commissioned, it could use up to 70 sinusoidal wave-fronts superimposed on one another to synthesise multi-directional seas [Salter, 1981].

The area available at the University of Edinburgh to rebuilt the wave-tank was much smaller than the area of the wide-tank and the curved shape was chosen as the best

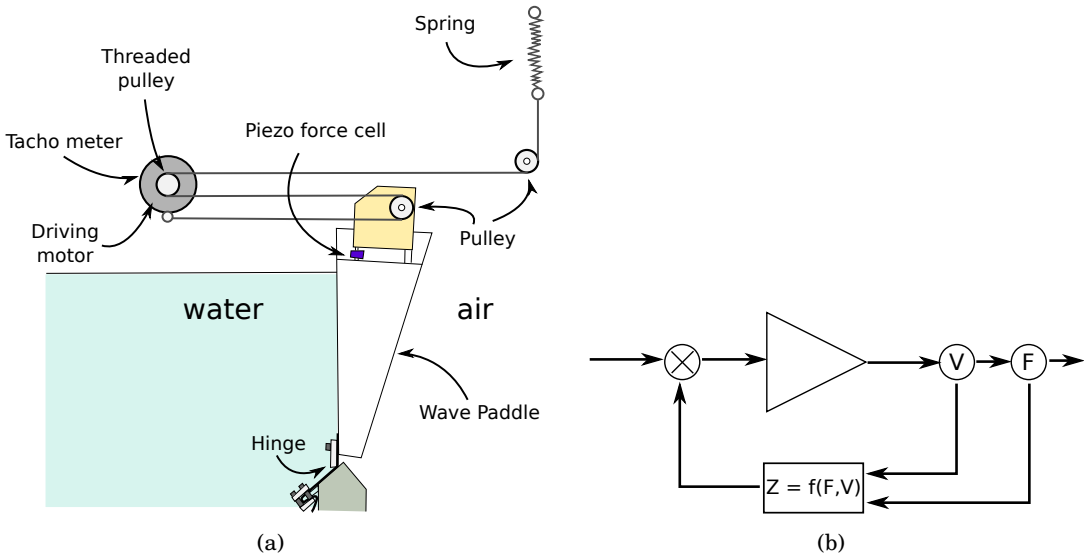

Figure 3.2: *(a) Schematic drawing of a wave-maker with force-control feedback. (b) Schematic of the control-loop.*

compromise to maximise the angular spread. Nevertheless, it should be pointed out that this solution presented a very significant reduction in fetch between the wave-makers and beaches when compared with the wide-tank. The quarter-circle shape was also intended as a pre-test and first step towards the design of a fully circular tank with its perimeter entirely consisting of absorbing wave-makers and which would included multi-directional currents [Salter, 2001]. As a requirement for the design of the new tank it was intended to keep the user friendliness, functionality and intimacy of the old wide-tank and build it within an available budget, which meant the reuse of much of the equipment and components of the old wide-tank.

The curved-tank was built and commissioned by Edinburgh Designs Ltd. A detailed description of the main features of the curved-tank can be found in Taylor et al. [2003] and Payne [2005]. Figure 3.1 shows the tank during the generation of a multi-directional sea.

An indispensable feature of the Edinburgh wave tanks is the use of *absorbing wave-makers* with *force-control feedback* technology, as shown in Figure 3.2.

Since the first wave-energy experiments with the Duck in the early seventies it was clear that it was necessary to produce clean and repeatable waves in the laboratory. If there was no active wave-maker absorption technology, waves reflected by the scale models bounced backward and forward between model and wave-paddles, mutually interfering

and building up standing wave patterns. This made it difficult to measure the energy content of the incident waves and to calculate the efficiency of the device under test.

The development and design of efficient absorbing wave-makers was a priority from the early days of wave energy studies at the University of Edinburgh and owes much of its developing effort to the need to develop systematic methodologies for testing wave energy scale models.

The absorbing wave-makers at the University of Edinburgh were developed through an intuitive and experimental approach and it was clear from the outset that the force feedback provided better wave quality than position or wave amplitude feedback.

The absorption technique was based on the measurement of force and velocity signals at the wave-paddle and the feedback of those into a controller in such a way to ensure that the motion of the wave-paddle was able to transmit the right amount of energy to the water at each frequency. Salter [1981] argues that is "better to leave the waves to decide for themselves which order of Stoke's corrections is appropriate" than to try to enforce a particular shape.

The force-feedback concept only works properly if the back of the wave-paddle is dry during operation. That ensures that the force measurements at the front are not disturbed by sloshing water at the back and ensures that the right amount of energy is transmitted to the front of the wave-paddle where waves are created.

Until recently it could be argued that it was a question of personal experience or subjective interpretation to acknowledge that force-control feedback generates waves with better quality than the systems which use position-control feedback. Such systems are more widespread and a review on absorbing wave-makers can be found at Schäffer and Klopman [2000]. The position-control technique relies on the measurement of wave amplitude with the feedback loop aiming to control the motion of the wave-maker to enforce an expected amplitude of the generated wave. The amplitude of the wave is normally measured with a wave-probe placed at the front of the wave-paddle and so to work properly this gauges should be properly clean and calibrated at all times, a non-trivial requirement. It should be pointed out also that because the position signal is obtained from the integration of the wave amplitude measurements, some slow drift is expected to occur requiring a frequent reset of the position of the wave-paddle. In some cases the gauges are placed at some distance from the wave-paddle introducing frequency variable phase lag in the measured signal. Also the occurrence of evanescent modes of

waves close to the wave-paddles where the gauges are placed introduce difficulties in the use of this technique.

Recently Spinneken and Swan [2009a,b] have presented a second order theory for wave-making using force-control feedback which justifies with experimental measurements using monochromatic waves the lesser spurious harmonic content introduced by this absorbing technique when compared with position-control feedback.

Many details on the design and manufacturing of the wave-maker system developed at Edinburgh can be found in Salter [1981]. The wave-paddle is hinged at the bottom and covered with a waterproof membrane with gussets to allow relative movement between adjacent paddles. It is made as a wedge sloped box of aluminium alloy driven by a low-inertia printed armature motor through a multi-strand stainless steel wire that is wrapped around a screw threaded pulley on the motor shaft. The hydrostatic force from the wet side is balanced by a spring which sets the wave-paddle into its equilibrium position. The force between paddle and motor is measured at the front of the paddle through a piezoelectric load cell and the velocity is derived from a tachometer coupled to the rear shaft of the driving motor. A schematic of the control loop is also presented in Figure 3.2(b).

In the curved-tank each wave-maker is addressed individually by the system controller during the creation of the target sea via a time division multiplex system that operates at 32 Hz.

The generation of directional waves by multiple wave-makers can be understood through the principle of Huygens as illustrated in Figure 3.3 for a linear array of wave-makers. The desired direction of propagation of the wave is obtained by shifting the time response of each wave-maker in the array by a certain delay (Υ) proportional to sine of the angle (α). For the special geometry of the curved-tank, the motion of all wave-makers with no phase delay generates a curved wave that propagates towards the centre of the wave-makers arc. To produce a strait wave propagating at 0° the wave-makers must move with a certain delay (Υ) between them in a snake like motion.

Mixed seas in the curved-tank are generated by superimposing different 'wave-fronts'. A wave-front is defined by four parameters: amplitude, frequency, angular direction and phase. To produce a mixed sea in the curved tank, the random phase method is used. This method is deterministic and ensures that during different runs repeatable conditions occur. This is an important and desirable characteristic of wave generation for wave energy development.

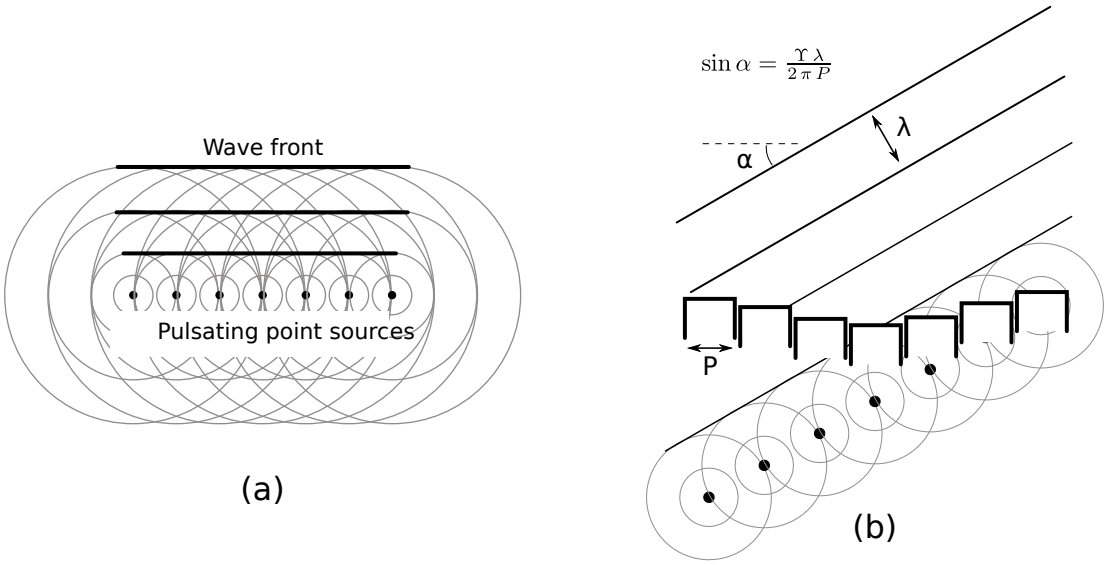

Figure 3.3: *Illustration of the Huygens principle.*

In the random phase method, the wave energy density spectrum of the desired sea is discretised into a certain number (N) of components or wave fronts. The desired amplitude of each wave front is related with the displacement of the wave-paddle by a certain stroke so a discrete paddle displacement energy spectrum is obtained. Then N associated complex-Fourier coefficients are calculated by choosing random phases between 0 and 2π, and the wave-paddle stroke time series signals are obtained through an inverse discrete Fourier transform.

The Edinburgh wave power group and later Edinburgh Designs Ltd. developed a higher level programming language and compiler ('WAVE' and 'OCEAN') to use in wave tanks [Rogers and King, 1997]. The creation of specific sea-states is then possible by specifying the input parameters associated with a specific wave function. For example, a single wave-front requires four parameters to be specified: amplitude, frequency, phase and direction of propagation. A mixed sea-state like a Bretschneider requires two input parameters: the peak frequency and spectral variance, and directional properties can be introduced by combining the mixed sea function with angle modifier functions.

The curved-tank has an experimentally determined *transfer function* which relates each wave-front and propagation direction to a gain factor and phase.

A important parameter related with the wave generation process is the repeat number or r-number (r). It specifies the number of wave fronts available for the generation of the sea-state and which is equal to $n_f = 2^r$. The frequency associated with a certain front is thus a multiple of the clock-frequency ($f_c = 32$Hz) and the total number of fronts divided

by the clock-frequency defines the period of the sea state, that is the time interval which the sea state is repeated. This number is known as the repeat time and is given by: $rtime = 2^r/f_c$. The 'OCEAN' manual recommends the use of an r-number between 6 and 16. For example, if the r-number is equal to $r = 11$, the number of available wave-fronts is $n_f = 2^{11} = 2048$, with each frequency given by $f = n/f_c$ and a repeat time equal to $rtime = n_f/f_c = 2048/32 = 64$ s. The specification of large r-numbers require large availability of memory to generate the wave data and that was a serious limiting factor during the pioneering work of the wide-tank when computers did not have enough power.

It is also important to refer and describe the passive absorbing elements placed within the tank to diminish the reflection of waves from the boundary walls. The beaches are placed along the tank wall opposite to the wave-makers. In plan view, these are wedge shaped steel cages that are filled with increasing densities of a geotextile material (Tensamat) and blocks of polyester skeletal foam. Details on the beaches and its construction can be found in Taylor et al. [2003], Plu [2003] and Payne [2005].

The remaining wall consists of a large glass window which allows the inside of the tank to be directly observed from the control area (see Figure 3.1). This feature is very helpful particularly during the early stages of development of a wave-energy converter. However, a drawback is that its surface is also reflective to waves and contributes to spurious waves that may not be desired in the tests. Despite this reflective wall, the settling time of the tank remains short, usually being less than 30 s allowing a quick repetition of tests.

3.1.1 Characterisation of the working area

The Edinburgh curved-tank presents a unique geometric configuration and since it was deployed in 2003 various studies have been performed to evaluate and characterise the generated wave field.

The first studies were performed by Plu [2003] and confirmed that the good repeatability of the earlier wide-tank was maintained. A first attempt at measuring the reflection coefficient from the new beaches using a two probe technique was inconclusive as very significant differences were found in the estimation of the wave amplitude at different positions of the gauges. Instead, Plu evaluated the transmission coefficient from the beaches, for eight different regular wave frequencies, by measuring the free-surface elevation root-mean-square signal (η_{rms}) before and after them at two locations: close to the glass and near to the working area. The results showed that the new beaches had in general better absorption characteristics than the beaches on the old-wide-tank,

specially for the long waves. Reflections from the glass window and their interference with the wave field were also early identified. Specifically, these were quite evident in maps which recorded the η_{rms} in an area of 1.88×3.5 m^2 (wide x long), for two wave frequencies, and which showed a hill-valley like pattern distributed along a diagonal line at a certain angle with the propagation direction of the waves. These results were interpreted as a standing wave pattern due to the interferences from reflected waves which included those coming from the glass.

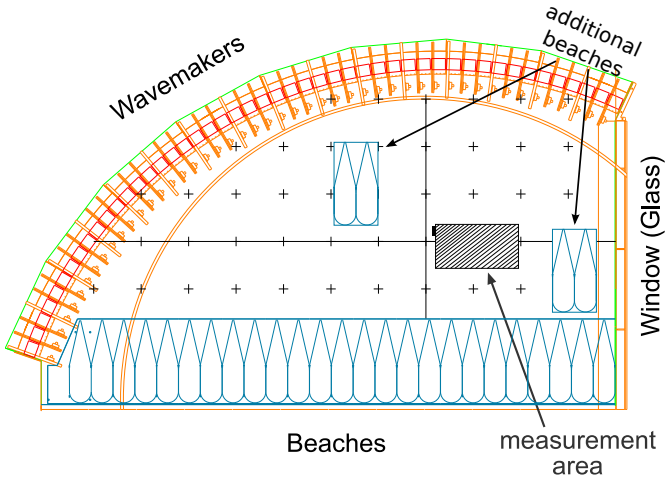

Figure 3.4: *Top view schematics of the curved-tank.*

Cruz et al. [2006] and Cruz [2009] performed a more accurate and detailed study of the wave field in the curved-tank by mapping η_{rms} over a larger area equal to 6×2 meter with increased spacial resolution. A total of seven wave-probes suspended from a metal frame were positioned at eight distinct locations to measure the waves at three different frequencies (0.75, 1.0 and 1.25 Hz), with three different amplitudes and three distinct propagation directions (-30, 0,+30°). As in Plu [2003] standing waves patterns were found with peaks and troughs separated by roughly a quarter of the wavelength disposed along a diagonal line to the propagation direction suggesting strong interference from the glass window.

The results are partially reproduced in Table 3.1, showing that the measurements associated with the free surface elevation of the oblique waves have larger relative dispersion ($s_\eta/\overline{\eta_{rms}}$) than the direct incident waves. Cruz [2009] also measured the reflection coefficient for waves directly incident on the beaches for the same area. A two probe method described by Goda and Suzuki [1976] was used and it was found to be lower than 10% for the frequency interval between 0.750 Hz to 1.25 Hz. Nevertheless

dir. (°)	freq. (Hz)	$\overline{\eta_{rm}}$ (mm)	s_η (mm)	$\delta\eta_{rms}$ (mm)	$s_\eta/\overline{\eta_{rms}}$ (%)	$\delta\eta_{rms}/\overline{\eta_{rms}}$ (%)	$\overline{R}$ (%)	s_R (%)	δR (%)	$s_R/\overline{R}$ (%)	$\delta R/\overline{R}$ (%)
0	0.75	26	1.4	0.3	5.4	1.1	5.2	2.80	0.40	53.85	7.77
	1.00	29	1.9	0.4	6.5	1.3	4.0	1.88	0.27	46.53	6.72
	1.50	30	2.9	0.6	9.8	2.0	9.1	4.07	0.59	44.53	6.43
-30	0.75	24	6.2	1.3	26.4	5.4					
	1.00	25	7.6	1.6	30.3	6.2					
	1.50	25	5.1	1.0	20.4	4.2					
+30	0.75	28	6.4	1.3	23.1	4.7					
	1.00	31	6.4	1.3	20.7	4.2					
	1.50	31	10.3	2.1	32.9	6.7					

Table 3.1: *Variation of η_{rms} for an area of 6 by 2 m and reflection coefficient obtained with a two probe technique described by Goda and Suzuki [1976] (from Cruz [2009]).*

$\overline{\eta_{rm}}$: average value of the measured free-surface wave elevation root mean square;
s_η: sample standard deviation of η_{rms};
$\delta\eta_{rms}$: standard error or uncertainty in the measurement of η_{rms} ($\delta\eta_{rms} = s_\eta/\sqrt{N}$ with N the number of measurements).
$\overline{R}$: average measured value of the reflection coefficient;
s_R: sample standard deviation of reflection coefficient;
δR: standard error or uncertainty in the measurement of the reflection coefficient.

it should be pointed out that these results present a large relative dispersion ($s_R/\overline{R}$) of about 50%.

Within the present work in order to improve the quality of the wave field in the tank area selected for the experiments, three specific measures were carried out:

1) Two additional beaches were placed inside the tank as shown in Figure 3.4 aiming to decrease the influence of the reflections from the observation window and of cross waves in the tank.

2) The six furthermost wave-making paddles which face the observation window (numbers 39 to 44) were excluded from producing waves, and used only as active absorbers.

3) The transfer function of the tank was modified so as to optimise the wave field in the working area.

The tank transfer function (TTF) is characterised by a set of gain values which establish the relationship between the input signal at the wave-makers and the amplitude of the waves in the tank for each direction of propagation. The gains of the transfer function, were corrected for direct incident waves at each frequency, by comparing a nominal target amplitude of the waves (10 mm) with the measured incident wave amplitude.

To account with the reflected waves, the incident waves were measured by using a standard reflection analysis method described by Mansard and Funke [1980]. This

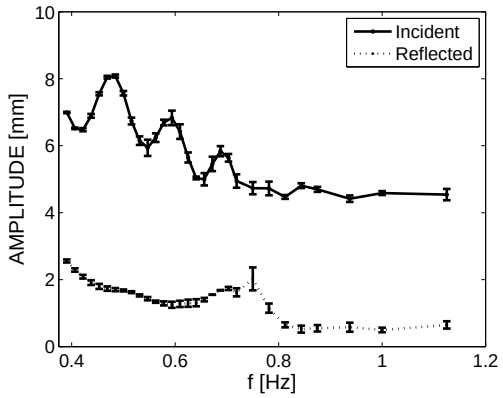

Figure 3.5: *Measured incident and reflected regular waves.*

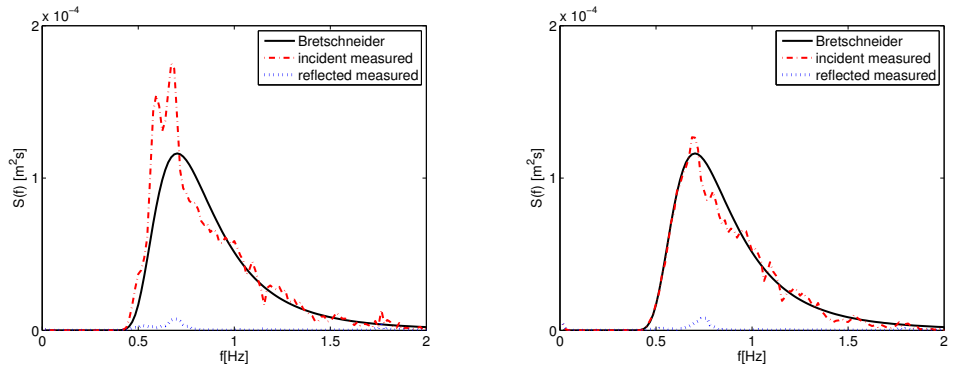

(a) (b)

Figure 3.6: *Comparison of measured spectral densities of a Bretschneider spectrum for the incident and reflected spectrum (broken lines) with the expected theoretical spectrum (continuous line). a) Using the pre-existing tank transfer function, b) using a tank transfer function optimised for the area where the experiments take place (see Table 3.2 for the spectral parameters).*

method considers three point measurements and takes into account the effects of noise on the wave elevation signals. In this method, the amplitudes of the incident and reflected waves are obtained through the minimisation of error using a least squares fit procedure. Special attention was given to the spacing between the probes in order to improve the accuracy and to avoid the singularities associated with the method.

A total of thirty directly incident waves with different frequencies and amplitudes between 5 and 10 mm were measured in at least two different spacial locations of the working area with two lines of wave gauges giving at least four measurements available to estimate the incident and reflected wave amplitudes and the associated uncertainty.

The results are shown in Figure 3.5. The error bars represent the standard error or uncertainty associated with the measurement (δX). These are defined as the

Bretschneider Spectrum	m_0 (m^2)	f_p (Hz)	T_e (s)
Target	5.6E-05	0.703	1.24
with default TTF	6.2E-05	–	1.30
with optimised TTF	5.3E-05	–	1.32

Table 3.2: *Target and measured spectral parameters for the spectra reproduced in Figure 3.6.*

experimental standard deviation (s_X) divided by the square root of the number of measurements (N), i.e: $\delta X = s_X/\sqrt{N}$, where $s_X = \sqrt{\frac{N}{N-1}}\sigma_X$, with σ_X the sample standard deviation.

The positive effect of the optimisation of the transfer function of the tank can be appreciated in Figure 3.6 and Table 3.2 in which a target theoretical Bretschneider spectrum given by Equation (2.12) is compared with the measured spectrum before and after the set up of the optimised transfer function of the tank.

Using the same reflection analysis technique, the *reflection coefficient* was measured at four locations in the measurements area, for waves of six different periods and of different amplitudes, incident at zero degree. This quantity is defined by the ratio of the reflected by the incident wave amplitude and the plots in Figure 3.7 show its variation against the steepness of the incident wave ($2a/\lambda$) for different wave periods.

As expected the value of the reflection coefficient increases for the lower steepnesses and its value is lower than 10% for the shortest measured waves (of $T = 1.0, 0.8$ and 0.7 s). For the longer waves it increases considerably but still is lower than about 15% for a steepness higher than 0.02. The wave with period equal to 1.3 s showed the higher reflection coefficient value whereas the wave with period equal to 0.8 the lowest.

Figure 3.8 shows that the amplitude of the incident wave can also be estimated through the average value of η_{rms}, if a sufficient number of measurements at different locations of the measurement area are taken into consideration. The differences found between the incident wave amplitudes obtained by averaging the η_{rms} and through the reflection analysis method are in general less than 2% for the shortest waves ($T = 1.0, 0.8$ and 0.7 s) and lower than 5% for the longest waves.

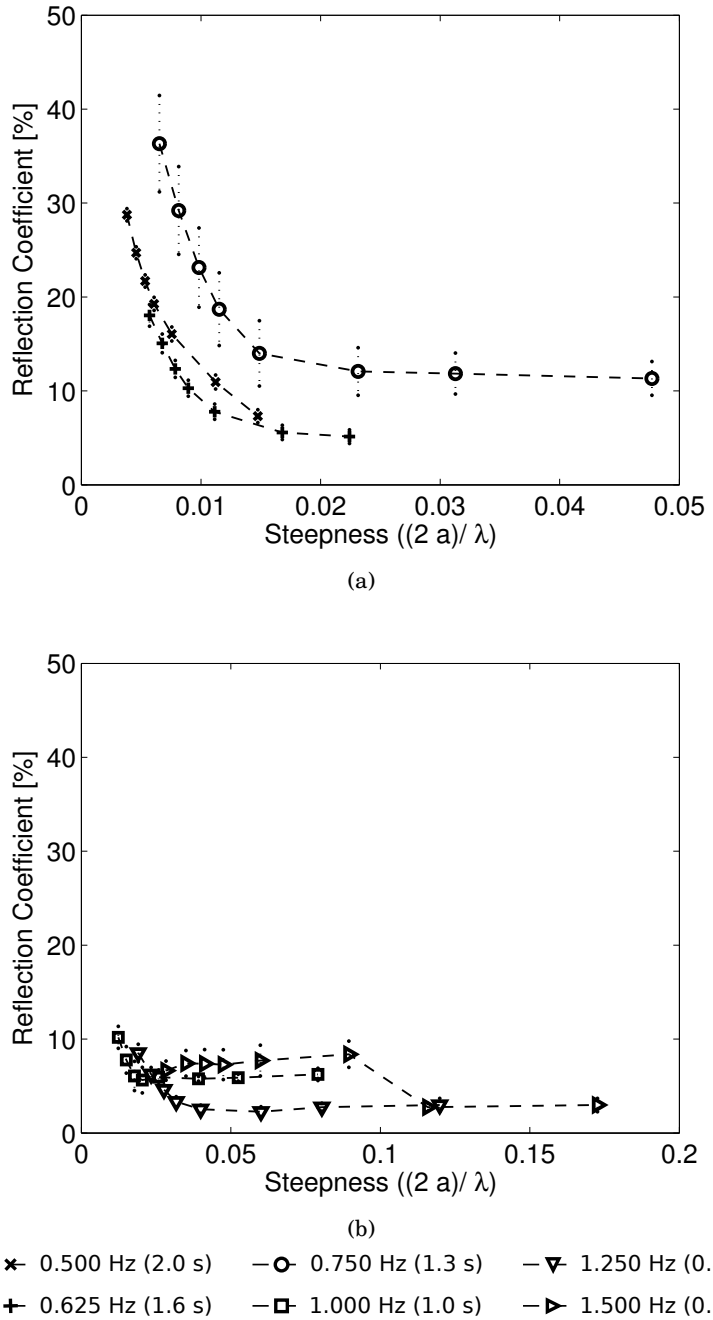

Figure 3.7: *Reflection coefficient versus the steepness of the incident wave in the test area. The reflection coefficient was estimated through the Mansard and Funke [1980] method for a total of eight measurements in different locations: (a) longer waves, (b) shorter waves.* ***NB:*** *The error bars are the standard errors or uncertainty in the measurement computed as:* $\left(\delta R/\overline{R}\right)^2 = (\delta a_i/\overline{a_i})^2 + (\delta a_r/\overline{a_r})^2$.

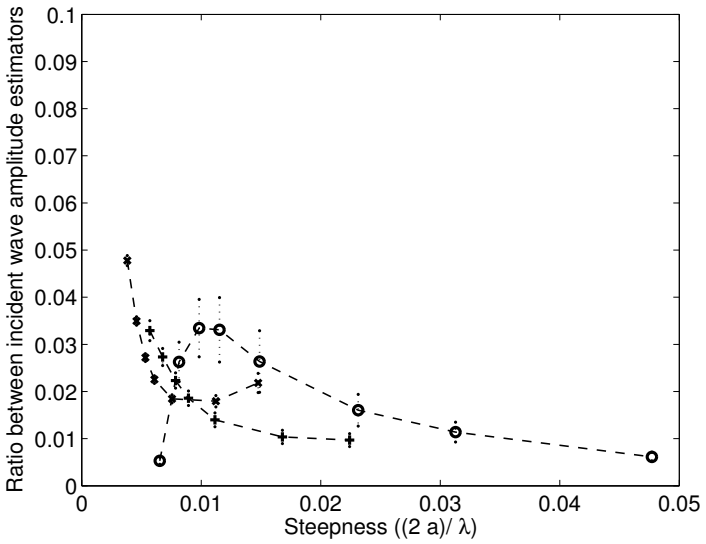

(a)

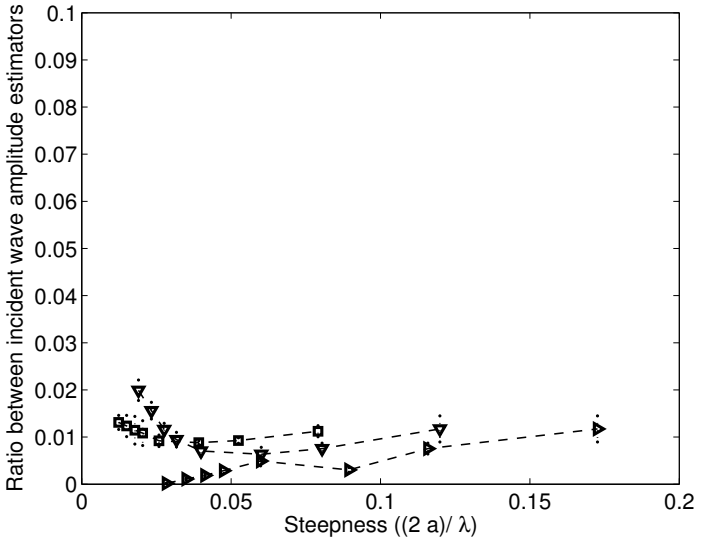

(b)

0.500 Hz (2.0 s) 0.750 Hz (1.3 s) 1.250 Hz (0.8 s)
0.625 Hz (1.6 s) 1.000 Hz (1.0 s) 1.500 Hz (0.7 s)

.

Figure 3.8: *Ratio between the estimations of the incident wave amplitude using the average value of η_{rms} with twenty four measurements at different locations and the average of four measurements of the incident wave amplitude through the reflection analysis method given by Mansard and Funke [1980]:* $|1-\sqrt{2}\overline{\eta_{rms}}/\overline{a_i}|$

3.2 The physical model

A physical model of the cylindrical desalination Duck was built to validate the preliminary numerical results obtained by Cruz and Salter [2006]. The diameter and width of the cylinder are equal to 0.364 m and 0.643 m respectively and so the scale of the model is 1:33 based on a full scale cylinder with 12 m diameter.

The main structural components are made of clear acrylic material to allow a direct visualisation of the inner mass of water and to confirm that it was working and behaving as a positive displacement double acting pump. A fish-eye view of the model during the tank tests is shown in Figure 3.9. Figure 3.10 presents three distinct views of the solid model 3D drawing.

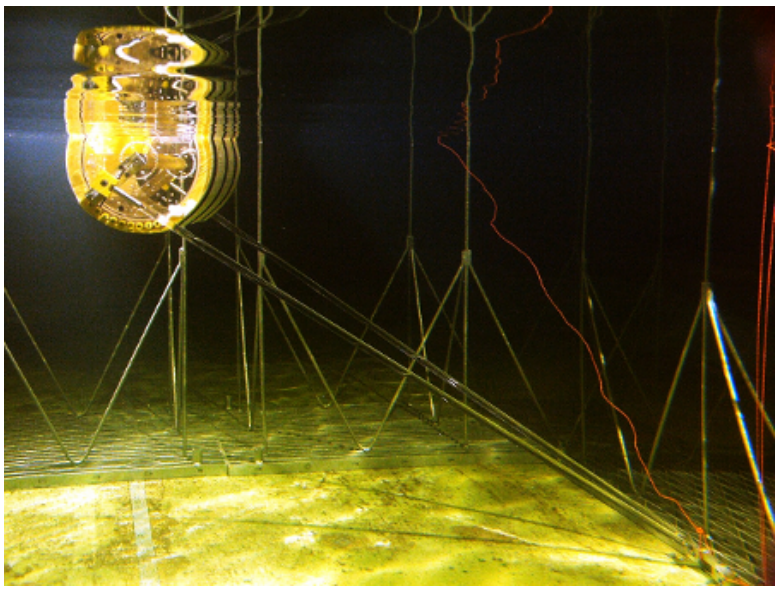

Figure 3.9: *Fish-eye view of the 1:33 scale cylindrical Duck model with offset axis under test in the curved-tank at the University of Edinburgh.*

The philosophy behind the design aimed to provide flexibility and easy access to the test parameters such that it would be possible to change them quickly and reconfigure the geometry and damping during the experiments.

The location of the off-centred axis of oscillation can be changed through a mechanism that has an array of tapped holes to allow angular and radial variation of the attachment point of the rigid struts mooring system.

The model is connected to the mooring system through two rigid struts shaped as a 'V' yoke. The mooring system is fixed to the tank floor. The lower end of the 'V' has a modified universal joint that allows the system to yaw and thus follow changing tank sea-states.

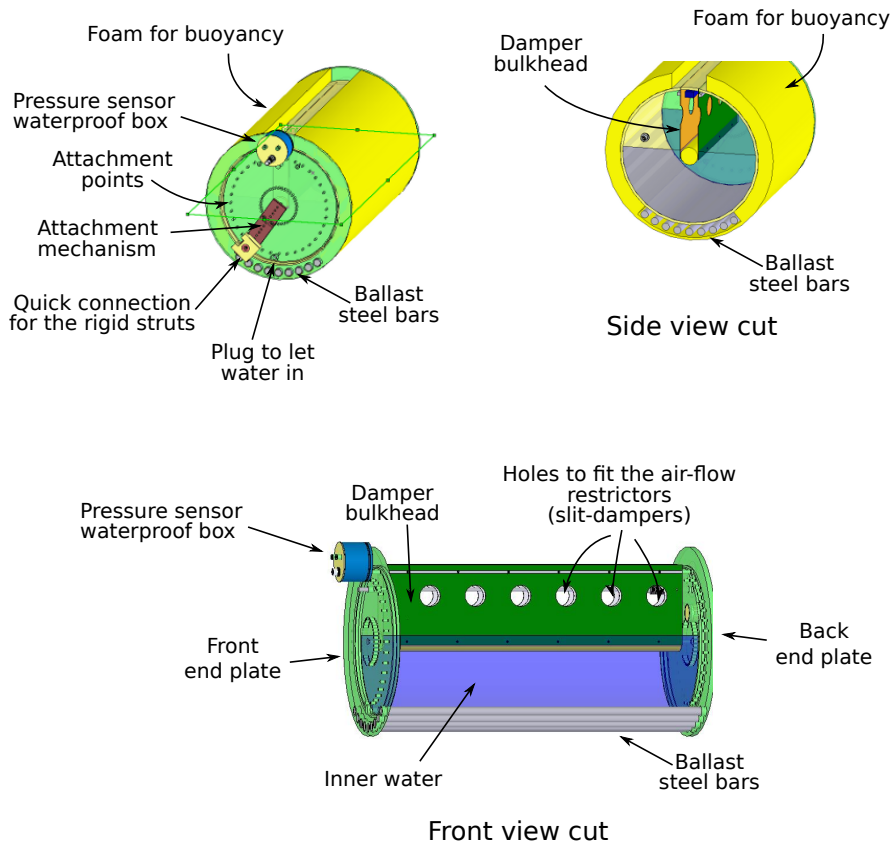

Figure 3.10: *Three distinct views of the cylindrical desalination Duck created with SolidWorks.*

The other two ends of the 'V' are connected to the off-centred-axis of the cylinder through the mechanism shown in Figure 3.10.

The mass and consequently the submerged volume can be adjusted by combining different arrangements of ballast and by adjusting the water level inside the scale model. The ballast consists of a variable number of steel rods parallel to the axis located at the lower end of the cylinder (see Figure 3.10). The amount of water that gets inside the model is controlled by opening and closing a plug entrance located at the lower end of the front end-plate (Figure 3.10). The correct operation of the unit requires the inner water level to reach the partition air-damper. By varying the amount of water inside the model and the number and location of the ballast bars it is possible to also obtain small variations of the total inertia.

The steam desalination unit of the proposed full-scale device is represented in the tank model by an air-damper, designed to impose a pressure difference across the central partition that would be proportional to the angular velocity of the cylindrical Duck.

The initial damper design used a pre-calibrated synthetic felt material which was fitted into the partition. The particular material was provided by the Instituto

Superior Técnico of Lisbon (IST) and was chosen because of the known relatively linear relationship between the pressure differential across it and the flow through it. Previous studies used a similar material when working with oscillating water column models [Delauré and Lewis, 2003]. The pressure flow characteristics in the damper could then adjusted by controlling the area of felt material exposed to the air flow through a mechanical mechanism.

It was subsequently found that the calibrated characteristics of the felt was only valid whilst this material was dry, and that very small quantities of entrained water would greatly change it. Figure 3.11 shows the results of some experimental measurements for the flow rate against pressure differential across this material. Small samples of about 40 mm diameter were fitted in a rig which provided constant flow rate to one side of the test samples and pressure was measured across it. The plot show the measurements for a single and two superimposed layers of felt material and also the change in the characteristics when one layer was wetted with only 2 mL of water.

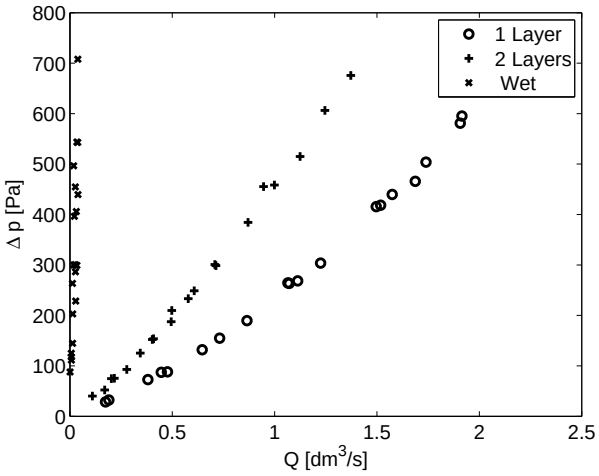

Figure 3.11: *Flow rate vs pressure characteristics for the felt material used in the air damper during the first tests.*

The drastic change in the slope of the calibration curve for the wetted felt degraded the confidence in the calibration for the air-damper used during the first tank measurements. Small amounts of water are seen likely to spill from the inner water-pendulum to the air-damper either during the set-up before the tests or during the tests themselves when large angular amplitude responses are obtained.

The initial efforts to solve this problem were focused on the search for a different material technique that would be suited for the air-damper and which could maintain an approximate linear characteristics.

3.2.1 Design of the linear air-damper

The initial design of the linear air damper was modified to accommodate the changes which were needed to solve the problem of the inadequate felt material.

The new material to fit into the air-damper was required to present a linear air flow rate versus pressure characteristic and which was stable over time.

The work by Minns [Minns, 2008, Duckers et al., 2008] greatly influenced the search for this material. To model the characteristics of Wells turbine within a scale model of an oscillating water column device, in tank tests, he used 'slit-rubber simulators' and found that this material was able to impose the desired linear relationship between the air flow rate and pressure.

The 'slit-rubber simulators' used by Minns, are shown at the centre of Figure 3.12 in the assembled oscillating-water-column scale model. These are composed of a circular rubber sheet with a 2 mm thickness and with a cross cut at its centre which can be of different lengths. Both the thickness and slit-cut lengths influence the stiffness of the material and its ability to resist the passage of air. Throughout a suitable combination of these two parameters it is possible to obtain the desired linear relationship between the air flow rate and pressure.

Figure 3.12: *Slit-rubber Wells turbine simulators used by Minns [2008].*

One of the problems identified by Minns was the occurrence of stiction along the rubber slits as a minimum pressure is needed to open the slits to the passage of the air flow. This effect could be observed in the measurement for the flow characteristics of the material at very low flow rates.

The solution found to minimise the occurrence of stiction was to decrease the area of contact between the slits. Thinner materials with only three cuts instead of the cross

profile were found to perform better. Also rubber was not thought to be a material able to provide the stability required.

To gain some understanding of the processes and improve the design associated with the slits, the initial experiments used polyester film (as used for overhead slide projectors) as the base material. The profiles were drawn with CAD software and printed into the transparencies. These were then cut with a knife and conveniently deburred. The advantage of this procedure was its rapidly. This allowed a systematic study and understanding of the design of the slits, even though the polyester film was not deemed stable enough to be used as the final material.

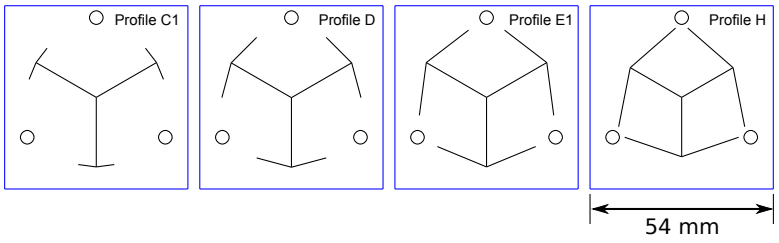

(a)

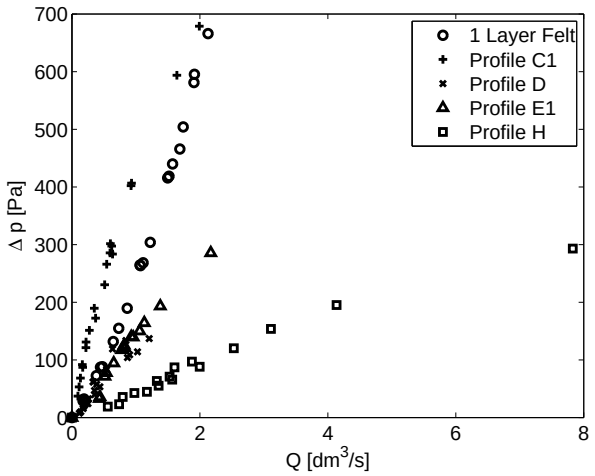

(b)

Figure 3.13: *(a) Profiles of the polyester film damper (b) Pressure against air flow rate characteristics.*

Some curves for the flow rate versus pressure associated with different slit profiles alongside with the 'felt' material used during the initial tank tests are shown in Figure 3.13.

The measurements of the pressure against air flow rate show an almost linear relationship for the slit-cut flow restrictors with the slope dependent on the specific profile.

Although the linearity was gratifying, it was found that the handmade slit-dampers showed a poor repeatability of the calibration characteristics. The final design was therefore based on a thin stainless steel shim material with a thickness of 0.05 mm and with the slit profiles cut chemically by a photo-etching process. These were provided by the company Tecan Ltd.

This process allows very precise and clean cuts. It consists of the masking of the stainless steel with a dry film of photo-resist. Then it is exposed to light with the slit profiles artwork to develop into the thin layer of photo-resist. The image is then etched with a chemical solution. An image of the final product is presented in Figure 3.14(a) and its drawing reproduced in Figure F.1 of Appendix F.

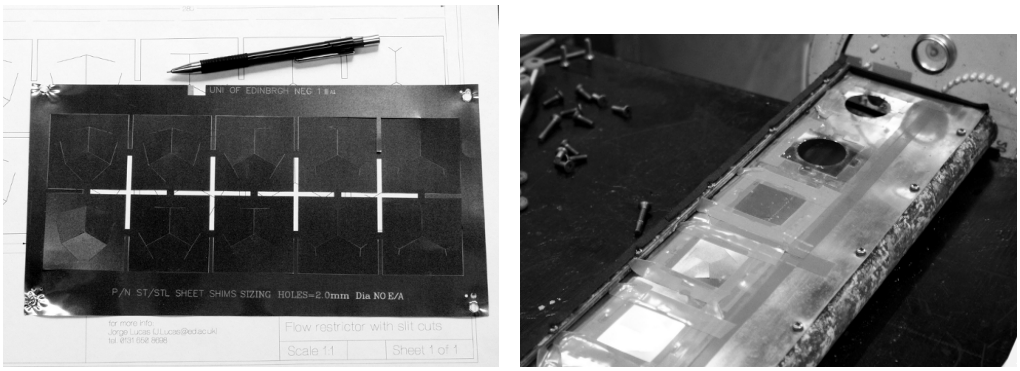

(a) (b)

Figure 3.14: *a) Final photo-etched slit stainless steel shims. b) Scale model damper bulkhead with fitted slit stainless steel shims.*

Each of the ten slit-shim squares shown in Figure 3.14(a) is fitted into one hole of the air-damper as shown in Figure 3.14(b). A suitable characteristics for the flow rate versus pressure relationship is obtained through the combination of the different slit dampers as shown in the next section.

3.2.2 Calibration of the linear air-damper

The air-damper of the scale model was calibrated with the aid of an available air calibration apparatus which provided constant air-flow rate.

This rig is used for the orifice calibration experiments in the mechanical engineering laboratory and consists of an inverted heavy hollow cylindrical bell that descends with constant velocity into a tank filled with water and therefore pumps air at a constant rate to an exit tap.

The flow was calculated from the velocity of descent of the bell, derived from the measurement of its position with a cable extension transducer (Celesco PT1A). The pressure across the damper was measured with the sensor designed for the pressure measurements described in Section 3.3.4.

The experimental set-up is schematically outlined in Figure 3.15(a) and a photograph of the experimental arrangement is given in Figure 3.15(b).

Figure 3.16 shows a sample of the displacement and pressure time series signals. The velocity of descent of the bell and the pressure across the slit damper are clearly remarkably constant.

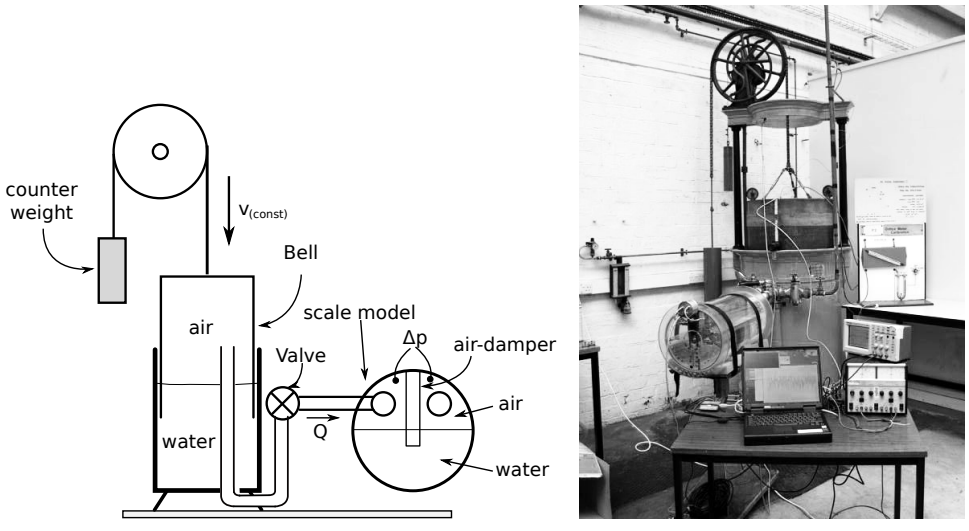

Figure 3.15: *Rig and experimental arrangement used for the calibration the air-damper of the desalination Duck scale model.*

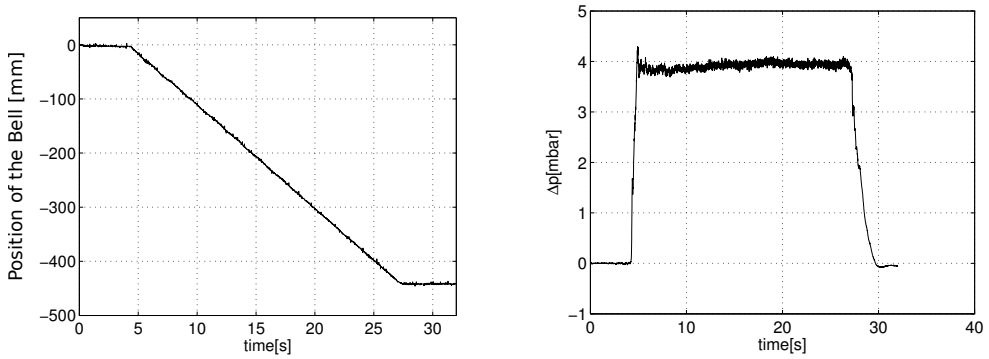

(a) (b)

Figure 3.16: *Time series signals measured during the calibration of the air-damper of the scale model of the desalination Duck. a) Position of the bell given by a cable-extension transducer. b) pressure across the damper measured with the pressure sensor developed for the pressure measurements across the damper and described on Section 3.3.4*

All measurements were performed in steady state conditions after a certain time delay so that all transients associated with the release of the bell died out and equilibrium conditions were reached. The calibration should be seen as steady state and is justified by the relative low velocities of the motion associated with the tank tests.

Because the pressure differences involved were much lower than atmospheric, flow was treated as incompressible. For this case the mass flow rate is proportional to the volume flow rate and is constant through a cross section of the air path of the experiment.

The volume flow rate (Q) is given by:

$$Q = v_b S_b \tag{3.1}$$

where $S_b = 0.355 \pm 0.0018\text{m}^2$ is the inner surface area of the base of the bell, and v_b is its decent velocity obtained though the measurement of position with a cable-extension transducer.

One of the sides of the damper bulkhead was connected to the rig through a pipe of constant cross section and the pressure differential across it was measured for different combinations of shim dampers.

By combining the shim dampers with different profiles it was possible to obtain different overall calibration characteristics across the damper.

Table 3.3 shows a configuration table that relates to the scale-model air-damper. Each column corresponds to one hole in the damper bulkhead and the labels to the slit-shim

	Hole number in the damper (left (p-) / right (p+))											
Configuration #	**1**	**2**	**3**	**4**	**5**	**6**	**7**	**8**	**9**	**10**	**11**	**12**
0	X	X	X	X	X	X	X	X	X	X	X	X
01	I1	I2	I3	I4	I5	I6	I7	I8	I9	I10	I11	I12
02	X	I2	I3	I4	I5	X	X	I8	I9	I10	I11	X
03	X	X	I3	I4	X	X	X	X	I9	I10	X	X
04	X	X	X	Q3	X	X	X	X	X	Q7	X	X
05	X	X	Q2	Q3	X	X	X	X	Q6	Q7	X	X
06	X	Q1	Q2	Q3	Q4	X	X	Q5	Q6	Q7	Q8	X
07	X	P1	P2	P3	P4	X	X	P5	P6	P7	P8	X
08	M1	M2	M3	M4	M5	M6	M7	M8	M9	M10	M11	M12
09	X	M2	M3	M4	M5	X	X	M8	M9	M10	M11	X
10	X	X	M3	M4	X	X	X	X	M9	M10	X	X

Table 3.3: *Configuration table for the air-damper. Each column corresponds to a hole in the damper and is labelled with a slit-shim profile. The crosses ('X') represent the holes that were closed.*

fitted in the hole. The crosses ('X') indicate the holes which were closed completely. Each slit-shim was labelled with a profile letter and number that corresponds to its position in the damper with the holes numbered from the front to back on each side. The four different profile letters used were 'I', 'M', 'Q', 'P'. and the correspondent profile design is shown in Figure F.1.

The calibration relationship is given for four different configurations in Figure 3.17. Figure C.1 in Appendix C presents the individual calibration relations for nine different configurations schematically represented in Table 3.3.

Configuration #	k_0 $\times 10^3$ [Pa/(m^3/s)]	δk_0	k_1 $\times 10^0$ [Pa]	δk_1
0	409.42	0.912	-26.03	0.146
01	29.95	0.042	-3.65	0.032
02	43.28	0.073	-4.84	0.052
03	71.57	0.120	-3.49	0.063
04	363.68	0.676	-45.15	0.236
05	236.43	0.434	-21.15	0.118
06	198.10	0.277	-29.62	0.135
07	173.35	0.330	-27.68	0.140
08	83.92	0.140	-21.72	0.110
09	112.83	0.162	-18.53	0.087
10	180.15	0.257	-19.16	0.095

Table 3.4: *Calibration table for the air damper. The calibration constants and errors were obtained through standard linear fit regression procedure, with the calibration relation given by $\Delta p = k_0 Q + k_1$. The values of the standard error or uncertainty associated with the slope and intersection with the abscissa are given respectively by δk_0 and δk_1.*

The plot shows that the characteristics of the air-damper is as intended approximately linear for the lower flow rates. For reference, the curve associated with the damper when

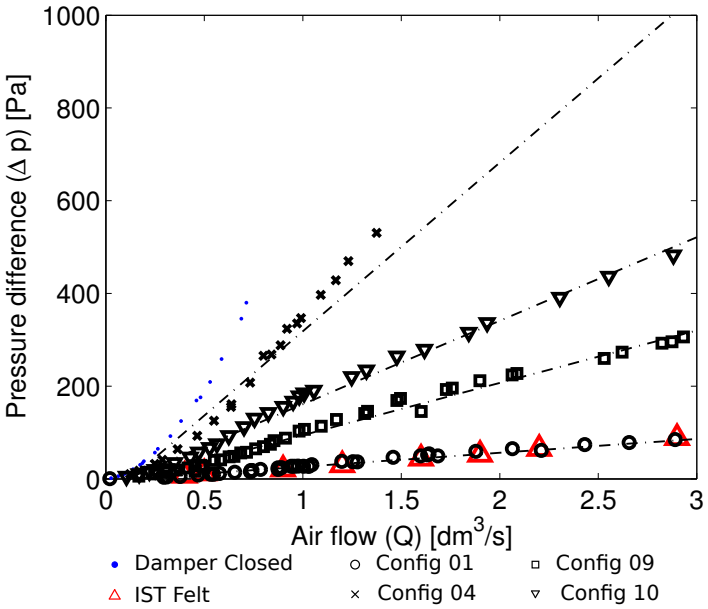

Figure 3.17: *Calibration of the linear air-damper: Flow rate versus pressure across the linear air-damper for four different configurations. For comparison, a curve obtained with a complete closure of the damper and the relationship for the first damper which used a pre-calibrated material (provided by IST) are also shown. See Figure C.1 for the individual calibration relations for each configuration.*

all air passages are closed is also given by the blue dots. As expected for this particular case, the pressure is a quadratic function of the flow rate and follows the law of flow through small orifices. This relationship gives a measure of the small leakages that are still present in the damper and which are very difficult to eliminate completely without a major change in the design. The air-flow pressure relationship for the pre-calibrated 'dry-felt' material when fitted in the damper during the initial tank tests is also shown in the plot by the red triangles and it shows a very close characteristics to configuration number '01'.

The associated calibration constants and errors where obtained through standard linear fit regression procedure and are given in Table 3.4.

Given the close to linear calibration curves, the relationship between air-flow rate and pressure across the damper can be reasonably expressed in the form:

$$\Delta p = k_0 Q + k_1 \tag{3.2}$$

and the *pneumatic power*, which is also the power available for mechanical conversion is a quadratic function of the pressure and is measured through this variable:

$$P_{abs} = \Delta p\, Q = \frac{1}{k_0}\Delta p^2 - \frac{k_1}{k_0}\Delta p \approx \frac{1}{k_0}\Delta p^2 \tag{3.3}$$

where $Q = (\Delta p - k_1)/k_0$ obtained from Equation (3.2) was introduced and the approximation $k_1/k_0 \approx 0$ taken into account as $k_1 \ll k_0$ (see Table 3.4).

The *mechanical damping* defined as the ratio between torque (τ) to the angular velocity ($\dot{\theta}$) and with units of Nms, is obtained by multiplying the pneumatic damping by the area of the air-damper (S_d) the vertical distance from the axis of oscillation to the centre of the damper (d) and the internal volume of one partition (V_p)

$$K_0 = \left(S_d\, d\, V_p\right) k_0 \tag{3.4}$$

This relation is obtained by observing that the torque at the off-centred axis is proportional to the pressure across the damper, given by: $\tau = \Delta p\, S_d\, d$, and the flow rate proportional to the angular velocity: $Q = V_p\, \dot{\theta}$. Substituting the above relations into the mechanical damping constant:

$$K_0 = \frac{\tau}{\dot{\theta}} = \frac{\Delta p\, S_d\, d}{Q/V_p} = \left(S_d\, d\, V_p\right)\frac{\Delta p}{Q} = \left(S_d\, d\, V_p\right) k_0$$

3.3 Instrumentation

In this section, the instrumentation used during the tank tests and the corresponding calibration procedures are described.

For each tank test with the scale model, a time series of nine different quantities were acquired with at 32 Hz 16-bit analogue to digital conversion acquisition card.

Each measurement started after a certain time-delay defined by a triggering signal associated with the start-up of the tank wave-paddles. This time delay was chosen to be equal to 32 s as it was sufficient to achieve stable wave conditions such that all transiences die out.

The good repeatability conditions found in the Edinburgh tank allows the values of wave energy and power associated with each test to be measured in separate tests with the scale model removed. Even so, an accurate measure of the power in the waves in a multi-directional wave-basin is intrinsically difficult, as reflections from the solid boundaries walls propagate and interfere with the generated waves, resulting in general in a non-uniform wave field. As it is not easy to improve the wave field inside the tank the only procedure that can be used to improve the accuracy of an estimation is to increase the number of individual measurements.

3.3.1 Wave probes

The wave probes used to measure the free-surface elevation were of the conductivity type. They consist of two parallel rods partially immersed in the water and placed close together such that the conductance between them is proportional to the depth of immersion and conductivity of the water. A high frequency ac-voltage signal is used to energise the gauges and prevent polarisation effects, and a time division multiplex system allows the use of very closely spaced probes without cross-talk between them. The wave-probes electronics were developed by Edinburgh designs Ltd. and more details can be found in their manual [Rogers, 1997].

Because the conductivity of water depends on temperature and ion concentration its value changes from day to day and even hour to hour. It is therefore necessary to repeat the probes calibration before and after any measurements. For the same reason, before the first calibration, it is helpful to run quite vigorous waves in the tank in order to mix the surface water to help ensure that uniform water conductivity is attained.

The calibration of a wave-gauge consists on determining the relationship between the output voltage signal from its electronic conditioning circuit and the depth of immersion of the vertical parallel rods. This process can be performed for several depths and a linear fit determined. A dynamic process which uses the vertical motion of the probes to establish the linear relationship is preferred instead. The procedure currently used in the curved-tank is described in Cruz et al. [2006] and Pascal et al. [2009]. The main advantage of this method is that it can calibrate more than one wave probe simultaneously.

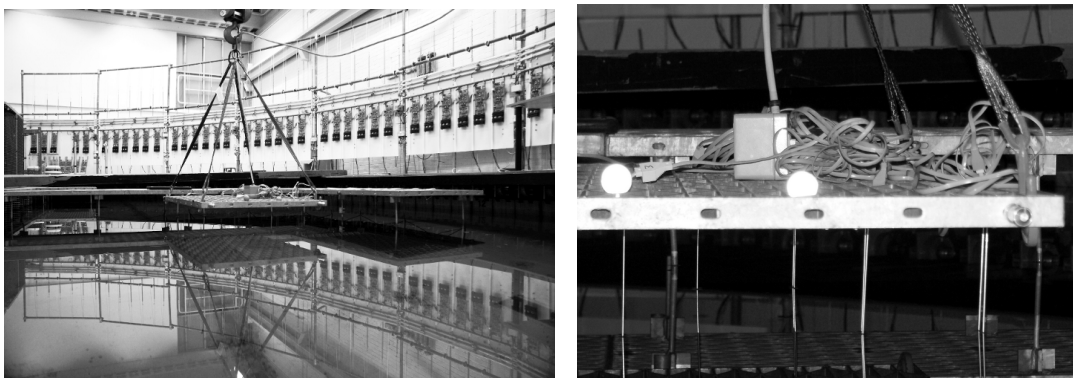

(a) (b)

Figure 3.18: *Procedure currently in use in the curved wave tank to measure the waves. Multiple conductivity wave probes are fitted into the horizontal frame shown in the centre of photograph (a), which is suspended from a motorised crane. The main advantage of this procedure is to allow the measurements in all the area of the tank. (b) Detail of horizontal frame with the wave-probes, note the glowing reflective balls used with the Qualisys motion capture system (see Section 3.3.2).*

The wave probes are fixed to a horizontal frame which is suspended from the hook of the five tonne overhead crane of the curved-tank. The crane is electrically driven with slow and fast horizontal an vertical motions conveniently controlled by a wireless keypad. This methodology ensures that all the areas in the tank can be covered and measurement made in a fast and easy procedure.

The calibration process consists of recording the vertical motion of the frame and voltage time-series of the probes as the frame is slowly lifted, to cover the likely range of vertical distance the probes will operate. The vertical motion is measured through the Qualisys system described in the next section (see the reflective balls in Figure 3.18(b)). The analysis of normal probability plots of the data residuals ensures the acceptance of a good calibration.

Because of the non-uniform wave field that develops in the tank due to interference with reflected waves it is important to make several measurements of wave amplitude around

the test area in order to estimate more accurately the average power per unit of frontage width.

The suspended frame enables the use of many probes to simultaneously measure the wave amplitude at different locations. A methodology used to measure the incident and reflected wave field based on Mansard and Funke [1980] method was briefly described in Section 3.1.1. For this method, six wave probes are used and placed in two parallel lines at distances chosen such as to avoid singularities. These distances depend on the wavelength of the measured wave and are given in Table 3.5. For the best accuracy and avoidance of singularities, Mansard and Funke [1980] recommend that the distance satisfy the following conditions:

$$x_{12} = \lambda/10; \quad \lambda/6 < x_{13} < \lambda/3$$
$$x_{12} \neq \lambda/5; \quad x_{13} \neq 3/10\lambda$$

where x_{12} and x_{13} are the distances from the first to the middle probe and from the first to the last probe relative to the direction of the incident wave respectively. The method can be also used with mixed seas with optimum distances between the probes depending on the peak frequency.

	Wave range		Distance [mm]	
	Period (s)	Wavelength [m]	1st to 2nd probe	1st to 3rd probe
long waves	2.67 – 1.33	8.1 – 2.8	525	1352
short waves	1.33 – 0.67	2.8 – 0.69	175	524

Table 3.5: *Distance between the three probes used in the reflection analysis method given by Mansard and Funke [1980]. Note that the wavelength is corrected to the curve-tank depth of 1.2 m, and the six probes are positioned in two lines at the same relative distances.*

3.3.2 Qualisys

The motion of the scale model during the tank tests was recorded through a video motion tracking system developed by Qualysis AB. This system can use up to sixteen infra-red sensitive cameras, but only two are currently installed in the curved tank. The cameras are located just above the observation glass window and were set-up to cover the measurement area under their field of view. A close look at the photograph of Figure 3.1 shows the location for these cameras.

The presence of reflective ball markers attached to the scale model (also visible attached to the frame of Figure 3.18(b)) are detected in the field of view of each camera and processed independently as 2D measurements of their position. By combining the information from both cameras, the system provides 3D measurements for the spatial position of the centres of any number of reflective balls.

The frame rate can be set as high as 1 kHz and the measurements can be accurate to better than a millimetre, but this depends on the calibration of the system.

By attaching a group of markers to the scale model and identifying them in the system software it is possible to process the position of the model in terms of the six independent degrees of freedom associated with a rigid body: surge, heave, sway, roll, pitch and yaw.

The major advantage of the use of Qualisys in marine related tests is to allow accurate measurements of position, and (by differentiation) velocity and acceleration without direct contact with the scale models being tested and so not interfering with its motion.

For the present work, an external digital-to-analogue conversion card connected to the Qualisys desktop computer was used such to stream the measured model position as a real-time continuous analogue signal, which could be recorded synchronously with the mooring force and pressure signals by the main curved wave tank data acquisition system.

For more detailed information on Qualisys AB the reader is refereed to the manual of the system [Qualisys, 2006].

3.3.3 Force sensor

The desalination Duck is conceived of as being connected to the sea-floor through the rigid struts and part of the forces that are transmitted to the device will be transferred to the attachment point at the sea-floor. Large mooring forces are thus expected as larger waves pass through the device.

A correct estimation of the order of magnitude of these forces is very important to design a full-scale prototype mooring system. Due to their intrinsic non-linear character, the best way to establish these forces is to measure them directly in carefully designed wave-tank experiments with scale models.

A load cell which is able to measure the mooring forces in both the horizontal and vertical directions was specially designed to be used in the experiments with the desalination Duck scale model.

The design was based on the load cells previously developed by the wave-power-group of the University of Edinburgh to measure the mooring forces on Duck-strings. This type consists of a square bar with fitted strain gauges that measure the bending strain of the bar which is proportional to the applied force. However the scale of those experiments was much smaller (1:150) and the sensors could not be used for the present experiments as their range was too small.

The dimensions of the square bar were selected such as to accommodate a maximum force (F) of 250 N. The design took into account a rule of thumb for the maximum acceptable strain such to keep the bar within linear elasticity limits – it should always be less than or equal to 1000 micro-strain. A square bar of aluminium-alloy with a length of 400 mm and width (W) of 3/4 in ($\approx$ 20 mm) was used and the eight strain gauges were placed at approximately (L) 300 mm from the loading point giving a maximum bending strain (ε) of about 800 micro-strain ($\varepsilon = \frac{6FL}{EW^3}$, with E = 7000 MPa the Young's modulus for aluminium).

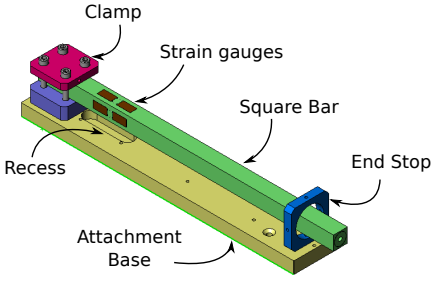

Figure 3.19: *Perspective view of the force sensor used to measure mooring forces.*

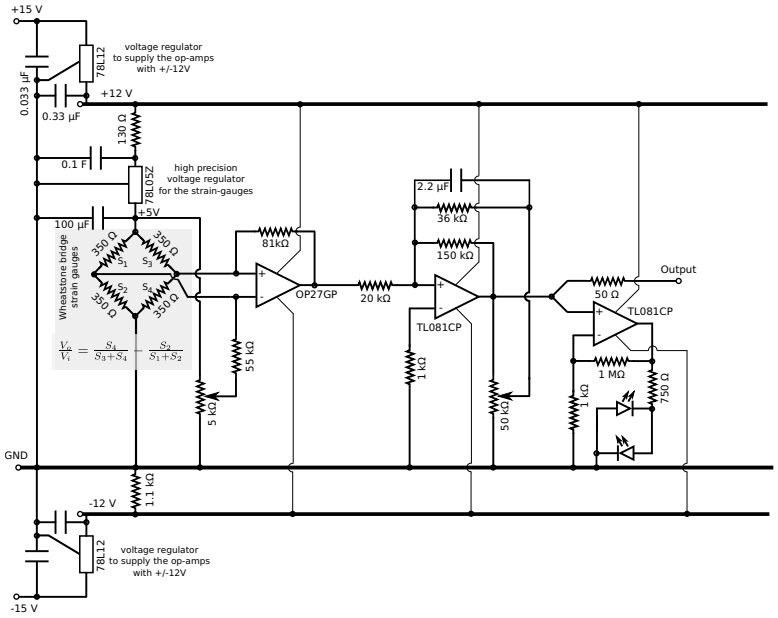

Figure 3.20: *Conditioning circuit to amplify the small voltages from the 'Wheatstone-bridge' of strain gauges fitted in the force cell sensor.*

Figure 3.19 shows a perspective view of the 3D solid model of the force sensor. The square bar is clamped to an attachment base which is fixed to the tank floor. An end stop is set such to prevent excessive bending which would compromise the linear elasticity characteristics. All parts were made of anodised aluminium to prevent oxidation due to the long contact with water. Dimensioned drawings are given in Figure F.4 in Appendix F.

A pair of 350 Ω strain gauges (*HBM-LY13-10/350 Y Series*) was placed on each of the four faces of the bar and connected as two balanced 'Wheatstone bridge' circuits on the opposing faces. This circuit is used to measure minute changes in resistance which are proportional to the variations of strain in the bar. One 'Wheatstone bridge' circuit is shown schematically in Figure 3.20 (shadowed grey area).

The output voltage is zero volts when there is no net force applied to the bar and in such case the resistance of all strain gauges is the same. When a net force is applied to the bar and is slightly bend it strains occurring very small changes in the resistance of the gauges. The 'Wheatstone bridge' in this case is unbalanced and a small voltage is produced. This small voltage is then amplified through a differential amplifier. The conditioning circuit was based in a circuit presented in Jeffrey et al. [1976, pp. 24.10] and is shown in Figure 3.20.

A key factor in the overall process was the bonding of strain gauges onto the anodised aluminium bar. A two component adhesive ('*HBM-EP310S*') was used which required a special thermal cure to ensure a long life for the sensor.

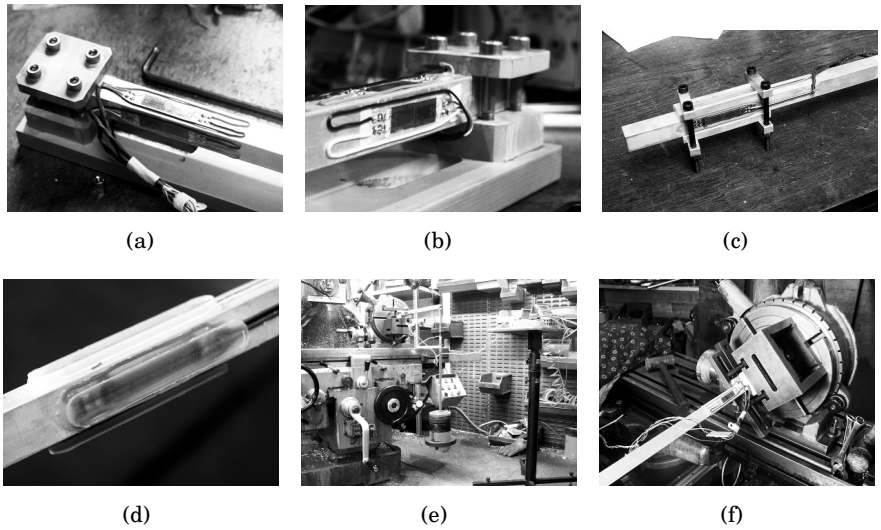

(a) (b) (c)

(d) (e) (f)

Figure 3.21: *(a) (b) Different views of the assembled force sensor before waterproofing, (c) (d) waterproofing through non-acetic silicon-rubber (e) (f) calibration process.*

Another important factor during the manufacturing and which was difficult to achieve due the relatively large areas of the sensor, was the waterproofing. The best solution found was to use a very thick layer of non-acetic silicon-rubber sealant to enclose all the electronic elements i.e. the strain gauges in the bar and the bridge connections in the base (see Figures 3.21(e), 3.21(f)). In the final assemblage an additional layer of a heat-shrink sleeving was placed around the strain-gauges to ensure mechanical protection.

Some photos of the process are presented in Figure 3.21. The last two photographs show the sensor during the calibration process. The sensor was fixed to a dividing head of a milling machine such to provide a stable fixation base which could be rotated through a precise angle. Known weights were hanged from the end of the bar for each 30° over 360° arc and the output voltage recorded. The measurements associated with the horizontal and vertical direction are shown in Figure 3.22 and which correspond to measurements for the angles equal to 0, 90, 180, 275 and 360° respectively. In this plot it can be identified a very small and negligible value of cross-talk for the axis perpendicular to the hanging weigh.

The calibration constants and associated uncertainties (A, B, δA and δB) such that the linear relationship is represented by $Y = A + BX$, were computed through a standard linear regression least square fit and are presented in Table 3.6.

Figure 3.23 shows measured forces in the horizontal (X) and vertical (Z) directions for each 30°angle in a 360° arc.

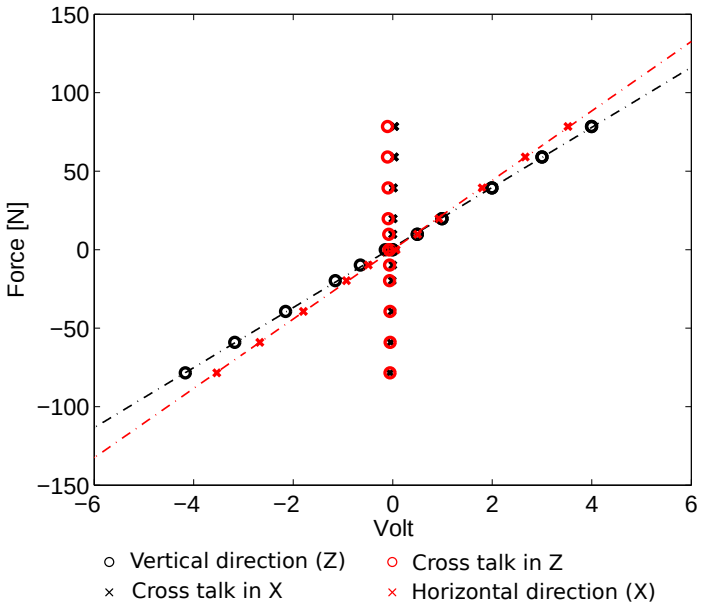

Figure 3.22: *Force sensor calibration curves for the horizontal and vertical directions (see Table 3.6).*

Direction:	B **[N/V]**	δB **[N/V]**	A **[N]**	δA **[N]**
Vertical (Z) dir.	19.13	0.002	1.376	0.005
Horizontal (X) dir.	22.09	0.004	0.006	0.007

Table 3.6: *Force sensor calibration table.*

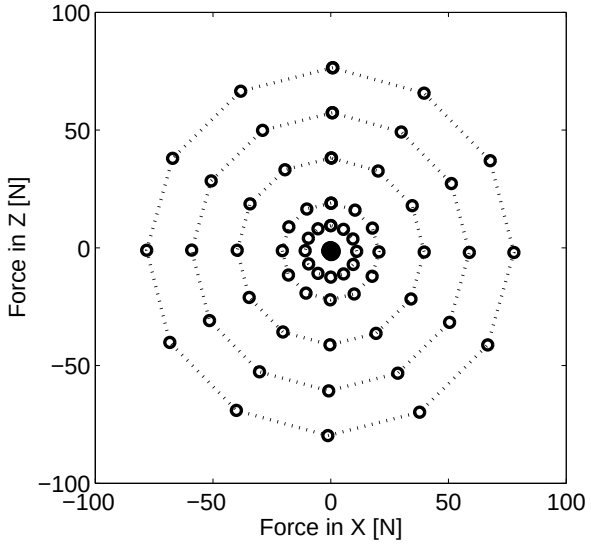

Figure 3.23: *Measured forces for a 360°arc for corresponding weights of ≈ 1, 2, 4, 6 and 8 kg.*

3.3.4 Pressure sensor

The sensor which was used to measure the pressure across the air-damper was housed in a water-proof casing box fixed to the top of the front end-plate of the scale model. The photograph shown in Figure 3.24(a) shows this box in place. The water-proof box was designed to stay dry during the tank tests and it was found to work even during the tests which fully submerged the scale model presented in Lucas et al. [2008].

The initial design considered two sensors '*Honeywell DUXL01D*' and '*DUXL05D*' which measured different ranges of pressures and were kept both with the conditioning circuit inside the water-proof box. The main idea behind this option was to obtain sensitive readings of pressure for both small and larger motions of the scale model when excited by the waves. Figure 3.24(b) shows the pressure sensor box with the conditioning circuitry before being assembled.

(a) (b)

Figure 3.24: *(a) Pressure sensor water-proof casing box fixed to the end plate of the scale model during the calibration of the air damper. (b) Detail of the pressure sensor water-proof casing box when opened, showing the conditioning circuit kept inside the box. Afterwards this initial design was modified such to keep the conditioning circuit outside the box.*

In September 2008, due to a failure in both sensors, the design was modified and the sensor '*Honeywell 26PCAFA6D*' was used instead. Its data-sheet is presented for reference in Figure F.5 (Appendix F). This sensor has a much larger pressure range, $\pm$ 1 psi, and its sensitivity to the smaller pressures had to be increased through the amplification of its output signal. This was made to saturate (at 10 V) above 2000 Pa. The conditioning circuit was kept outside the box and it was based on the circuit designed for the force sensor. In this design, a potentiometer and 'plus' and 'minus' LEDs were included such to reset the signal to zero volts before each experiment and correct the drift which was found to occur in the previous circuit conditioning design.

The sensor was calibrated with a portable pressure indicator and calibrator (‘*Druck DPI 601*’). This instrument provides a volume adjuster which allows very fine and precise changes in the input pressure. The pressure versus voltage measurements for the calibration of this sensor are shown in Figure 3.25. The relationship is linear ($Y = A + BX$) with the respective calibration coefficients given in Table 3.7.

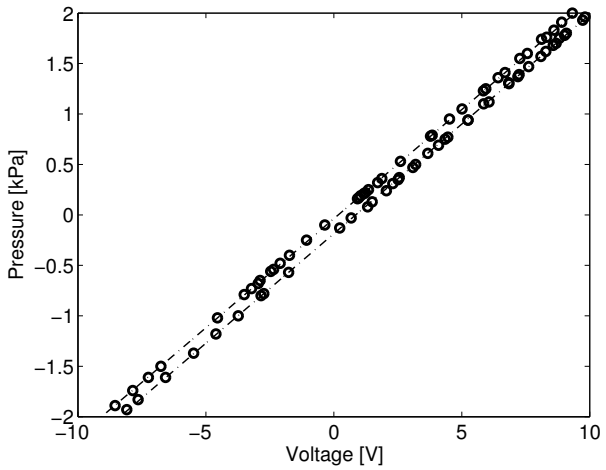

Figure 3.25: *Pressure sensor calibration relation. The two lines correspond to distinct calibrations (see Table 3.7).*

Calibration date	B **[Pa/V]**	δB **[Pa/V]**	A**[Pa]**	δA**[Pa]**
09-Sep-2008	217.2	0.29	-185.9	1.77
07-Jun-2010	216.2	0.30	-37.7	1.61

Table 3.7: *Pressure sensor calibration table.*

3.4 Experimental tests with the desalination Duck scale model

This section presents the results of the experimental tests obtained with the desalination Duck scale model performed at the curved-tank of the university of Edinburgh and which followed the re-design of the air-damper described in Section 3.2.1. Most of these experiments were already described in Lucas et al. [2007] and Lucas et al. [2008], but the use of the new air-damper justified a re-evaluation of those results. These will also be used in Section 5.3 to validate a dynamic multi-body model described and developed in Chapter 5.

3.4.1 Tank tests with regular waves

The tests were carried out for a draft of $H/D = 0.66$ with the scale model submerged at approximately 70% of its total volume and with its oscillation axis located at a distance to the centre of the cylinder of $l_0 = 110$ mm and at an angle to the still water plane of $\alpha_0 = 55^\circ$ (see Figure 3.26).

The geometry associated with these tests is sketched in Figure 3.26 and a summary of the most important parameters is given in Table 3.8. The geometry associated with these tests is approximately the same as the geometry of the tests reported in Lucas et al. [2007, 2008], Cruz [2009], and so the results obtained here can be directly related.

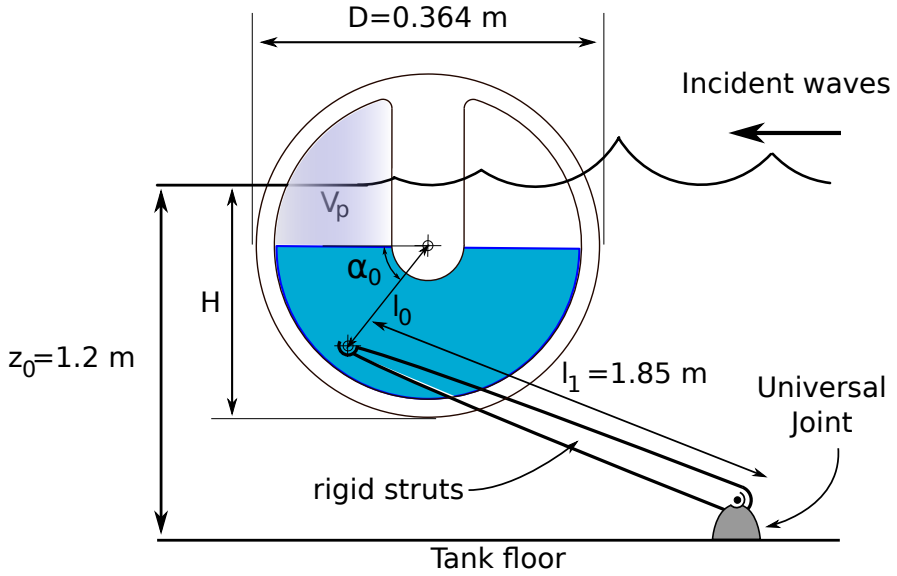

Figure 3.26: *Schematic drawing for the scale model layout used in the tank experiments.*

Scale model geometry:		
Diameter of the cylinder hull [mm]	D	364
Width of the cylinder hull [mm]	W	643
Volume of the cylinder hull [m^3]	V	0.0669
Draft with no water pendulum [mm]	H_0	156
Draft with water pendulum [mm]	H	242
Total mass without water pendulum [kg]	m_H	27.0
Total mass with water pendulum [kg]	m	46.6
Mass of water inside the model [kg]	m_W	19.6
Moment of inertia of the hull at the principal axis (*) [kgm^2]	$(I_H)_{11}, (I_H)_{22}, (I_H)_{33}$	$1.52, 0.47, 1.36$
Moment of inertia of the water pendulum at the principal axis (*) [kgm^2]	$(I_W)_{11}, (I_W)_{22}, (I_W)_{33}$	$0.727, 0.150, 0.646$
Centre of mass of the hull measured from the centre of the cylinder (*)[mm]	$\overrightarrow{\mathscr{C}\mathscr{H}}$	$0, 0, -32$
Centre of mass of the the water pendulum measured from the centre of the cylinder (*) [mm]	$\overrightarrow{\mathscr{C}\mathscr{W}}$	$0, 0, -57$
Total submerged volume percentage [%]	$\forall/V_0 \times 100$	70.6
Draft to cylinder diameter ratio	H/D	0.66
Width to cylinder diameter ratio	W/D	1.77
Angle between the horizontal plane and the plane that contains the off-centred axis and the central axis of a horizontal cylinder [°].	α_0	55
Distance from the off-centred axis to the centre of the cylinder [mm]	l_0	110.0
Length of the rigid struts [m]	l_1	1.85
Area of the damper [m^2]	S_d	8.53×10^{-2}
Internal volume of each partition [m^3]	V_p	8.07×10^{-3}
Vertical distance to the damper horizontal centre line [mm]	d	158

(*) Values from Solid Works solid model.

Table 3.8: *Value of some parameters associated with the geometric configuration of the scale model used in the tank experiments.*

The tank experimental layout was similar to that described in Section 3.1.1. Two additional beaches were placed inside the tank at the same location as shown in Figure 3.4 and the six furthermost wave-makers were only used to absorb energy from the reflected waves. The transfer function of the tank was set to the optimised function obtained through the methodology described in Section 3.1.1.

A total of eleven regular waves were used with periods between 0.8 s to 2.67 s and height of approximately 10 mm. The wave periods were chosen to be an integer number of the repeat time which was set to be equal to 16 s.

The waves were measured just before the experiments and without the scale model in tank. The methodology used to measure the wave height is described in Section 3.3.1. Six

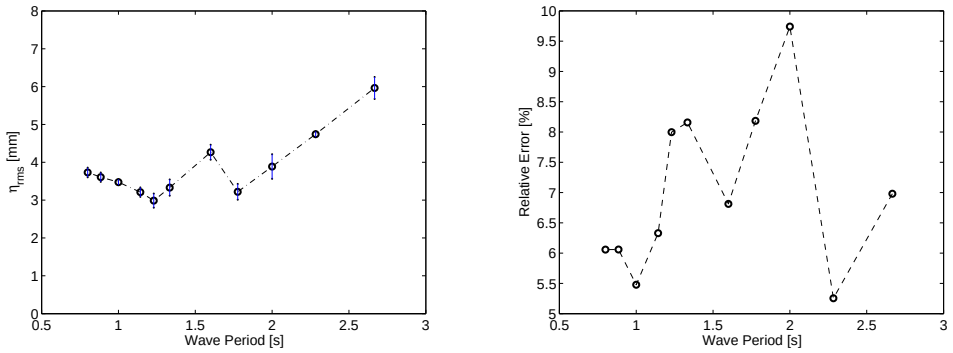

(a) (b)

Figure 3.27: *(a) Measured η_{rms}. The error bars are relative to the standard error $\delta\eta = s_\eta/\sqrt{N}$ obtained for a total of at least eighteen independent measurements in the test area. (b) Relative errors associated with the normalised amplitudes assuming a maximum error of 5% in the measurements ($(\delta x/\overline{x})^2 = (\delta y/\overline{y})^2 + \left(\delta\eta/\overline{\eta_{rms}}\right)^2$).*

conductivity wave gauges fixed to a metallic frame were used and the frame was placed in at least two distinct locations of the working area so that a total of at least twelve different wave elevations were available to estimate the height of the waves.

A total of eight different damping settings were used in these experiments. The mechanical damping values are shown in Table 3.9 which are related to the pneumatic damping given in Table 3.3 through the relationship (3.4) for a particular geometry of off-centred axis.

The *time series signal responses* for the motion of the scale model, pressure across the damper and mooring forces associated with three different waves with periods equal to 2.0 s, 1.3 s, 1.0 s and height of about 10 mm, when three different values of damping were applied, is shown in Figure 3.28.

The small wave heights were intended to keep the linearity and sinusoidal character of the responses. However, even for small incident waves, the mooring forces signals show

Configuration #	**Pneumatic damping** (k_0) $\times 10^3$ **[Pa/(m^3/s)]**		**Mechanical damping** (K_0) **[Nms]**	
01	29.95	0.042	3.26	0.01
02	43.28	0.073	4.71	0.01
03	71.57	0.120	7.79	0.01
04	363.68	0.676	39.57	0.07
05	236.43	0.434	25.73	0.05
06	198.10	0.277	21.56	0.03
09	112.83	0.162	12.28	0.02
10	180.15	0.257	19.60	0.03

Table 3.9: *Pneumatic to Mechanical damping constant conversion for the geometrical configuration under study and based on relation* (3.4) *($K_0 = \left(S_d\, d\, V_p\right) k_0$, with $\left(S_d\, d\, V_p\right) = 1.09 \times 10^{-4}$).*

higher order harmonics which are kept small. Note, in Figure 3.28(f), the non-sinusoidal shape of the mooring forces for the steepest wave with period equal to 1.0 s. The almost triangular shape of the signal gives evidence of the *snatching loads* identified for the solo-Duck with tension leg mooring cables and for which the pre-tensioned concrete rigid struts solution aims to solve.

Close to resonance when the excitation wave period is equal to $T = 2.0$ s (Figures 3.28(a) and 3.28(b)), the amplitude of all responses increase and the phase shifts for increasing values of damping.

For the other frequencies this behaviour is less evident or simply does not occur. For a wave period equal to 1.34 s (Figures 3.28(c) and 3.28(d)), an increase in the amplitude and phase shift of the signal response with increased damping can be identified for the pressure but not for pitch.

Figure 3.29 shows for six incident wave periods, the variation of the amplitude response for the motions (surge, heave, pitch), pressure and mooring forces with applied damping. All plots show that near resonance, at a wave period of $T = 2.0$ s all amplitudes responses, except surge (Figure 3.29(a)), increase with increasing values of damping. For all other wave periods, the amplitudes of pitch and the mooring forces do not change appreciably with damping. Figure 3.29(d), shows that the pressure for the all wave periods except resonance increases slightly to about 100 Pa when damping equals 19.6 Nms. At resonance ($T = 2.0$ s) and for the same damping setting, pressure has an amplitude close to the absolute maximum measured value and is equal to approximately 300 Pa. Figure 3.29(b), shows that a maximum in the heave amplitude for all frequencies except at resonance $T = 2.0$ s is reached for a lower damping value equal to 12.3 Nms.

Figure 3.30 show the phase differences between pitch and pressure response signals for different damping settings and wave periods. The top plot shows a small dependence on damping except when it is set to be equal to 19.6 Nms. This can be also observed in the bottom plot. For all other damping settings the variation of the phase difference between pitch and pressure has an almost linear dependency with the incident wave period.

For the present experiments only one measurement of the responses (motion, pressure and mooring forces) was made. Based on previous experiments an upper bound of a relative error equal to 5% is considered ($\delta y/\overline{y}$). The incident wave amplitude was estimated through at least twelve independent measurements in the test area of the free surface elevation 'RMS' (η_{rms}). As shown in Section 3.1.1 these can be used to estimate the incident wave amplitude to an accuracy less than 5%. Figure 3.27(a)

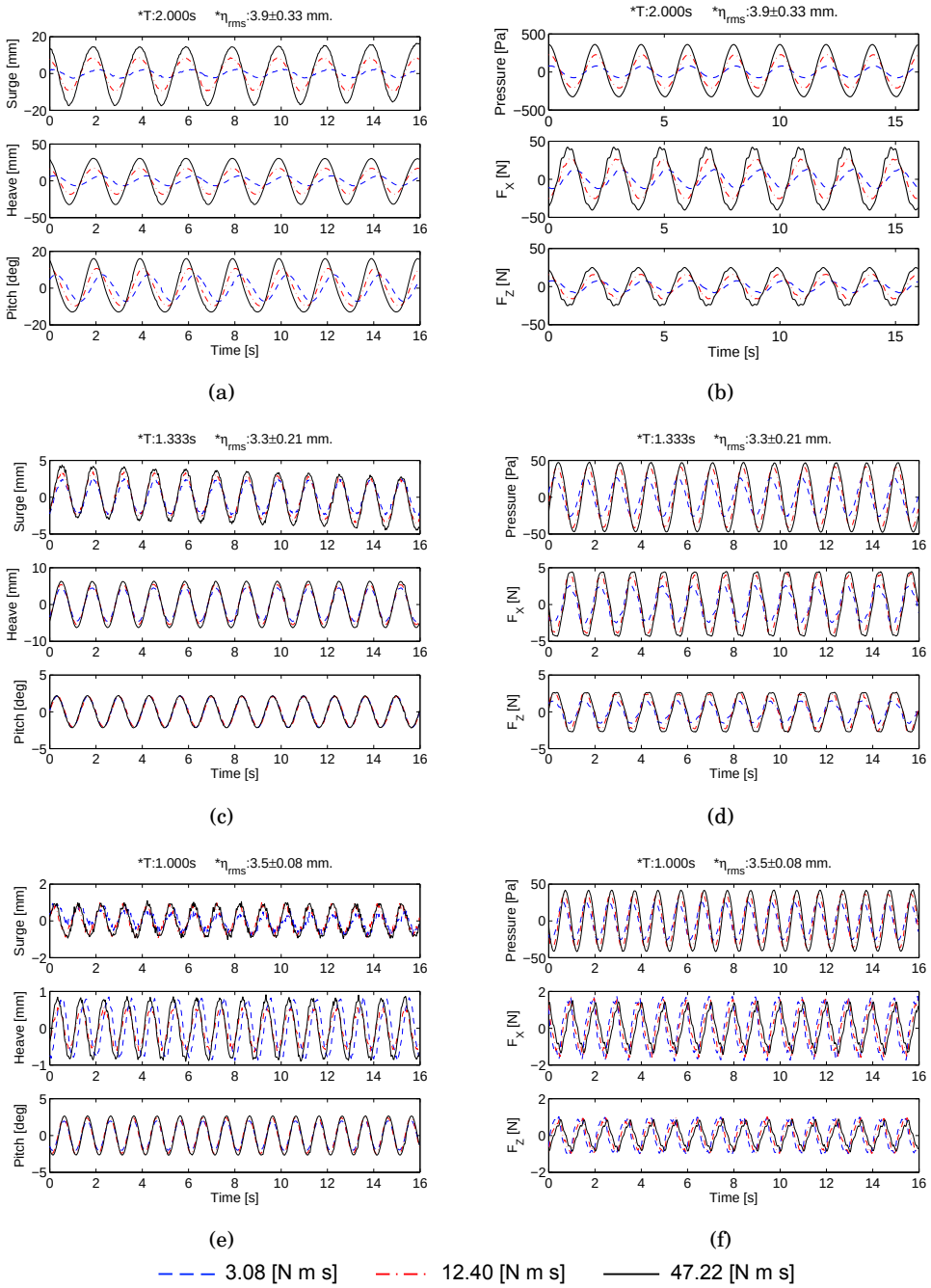

Figure 3.28: *Time series signal response for three incident regular waves with periods equal to 2 s (a), (b), 1.3s (c), (d) and 1.0s (e), (f) and wave height of about 10 mm and for three different values of applied damping.*

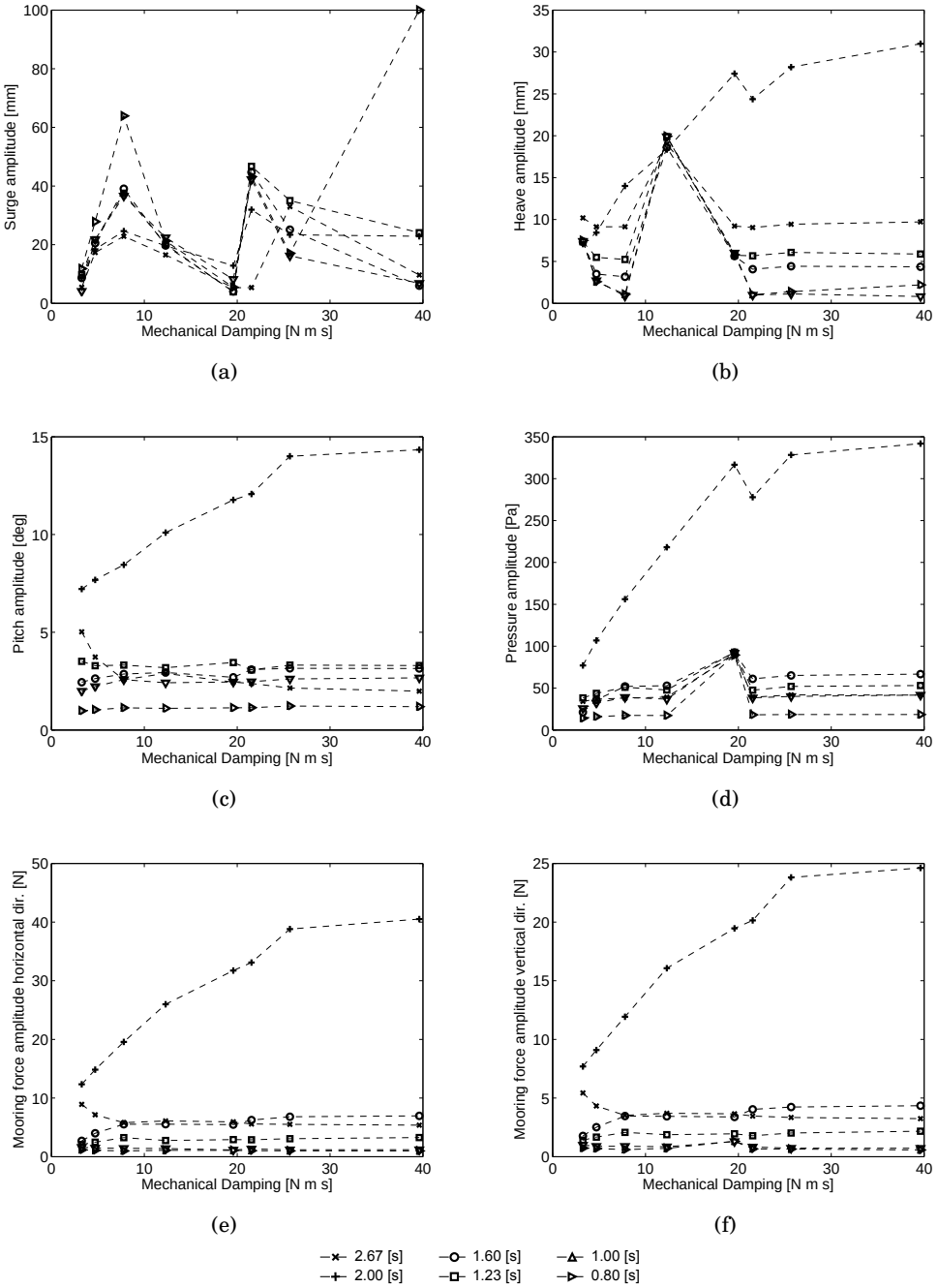

Figure 3.29: *Dependency of several quantities with applied damping for different incident regular wave periods: (a) surge amplitude, (c) heave amplitude, (c) pitch amplitude, (d) pressure across the damper amplitude, (e) mooring force in the horizontal direction and f) in the vertical direction.*

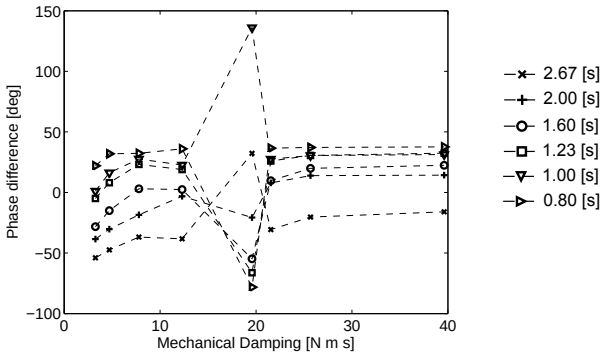

(a)

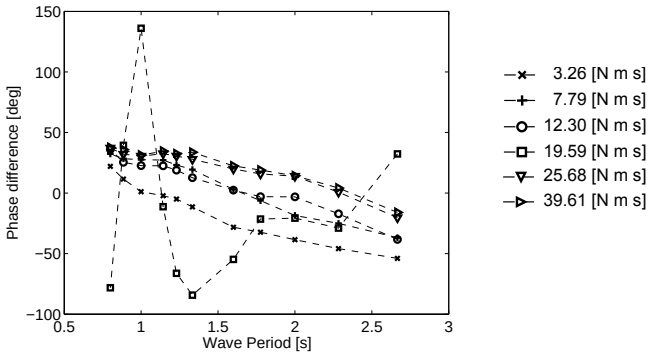

(b)

Figure 3.30: *Phase differences between pitch and pressure response signals: (a) variation with applied damping for six wave periods, (b) variation with wave period for six damping settings.*

shows the estimated values of η_{rms} in which the error bars represent the standard error or uncertainty associated with the estimation ($\delta\eta = s_\eta/\sqrt{N}$). Figure 3.27(b) show the relative errors associated with the estimation of the normalised amplitudes which are given by: $(\delta x/\overline{x})^2 = (\delta y/\overline{y})^2 + \left(\delta\eta/\overline{\eta_{rms}}\right)^2$. The plot shows that the maximum measured error was less than 10%.

Figure 3.32 show the *normalised amplitudes* of the responses for the motions, pressure and mooring forces and its variation with the wave period for different applied damping settings. These operators are obtained by dividing the response of the scale model by the incident wave amplitude.

The normalised amplitudes for surge, heave and pitch shown in Figures 3.32(a), 3.32(b) and 3.32(c) were obtained by dividing the 'RMS' value of the respective quantity by $\overline{\eta_{rms}}$. For heave and surge, this quantity is non-dimensional and is defined in a similar way as the *response amplitude operator* of the motion, whereas for pitch this quantity has units of rad/m.

The normalised amplitude of the pressure response is non-dimensional and was obtained by dividing the 'RMS' value of the pressure across the damper ($\overline{\Delta p_{rms}}$) by $\overline{\eta_{rms}}$, by the density of water (ρ) and the by acceleration of gravity (g): $\Delta\hat{p} = \overline{\Delta p_{rms}}/\left(\rho\, g\, \overline{\eta_{rms}}\right)$.

In a similar way, the normalised amplitude for the mooring forces is non-dimensional and was obtained by dividing the 'RMS' value of the mooring forces ($\overline{F_{rms}}$) by $\overline{\eta_{rms}}$, by the diameter (D) and width (W) of the cylinder, and by $\left(\rho\, g\right)$: $\hat{F} = \overline{F_{rms}}/\left(\rho\, g\, D\, W\, \overline{\eta_{rms}}\right)$.

All plots of Figure 3.32 show again within the range of resonance (at T = 2.0 s and T = 1.8 s), an increase in the amplitudes response with increasing values of damping. Except for the mooring forces, the amplitude responses show a second peak at about T = 1.14 s and of lower amplitude than the first. Between the two peaks there is a steep valley with the amplitudes of the responses decreasing considerably.

The maximum values of the normalised amplitudes for surge, heave and pitch are respectively approximately equal to 3.0, 6.0 and 46 rad/m. For example, for these values if a wave is incident with a period equal to 2.0 s and amplitude of 10 mm, and if the damping setting is kept the same, the amplitude of the response would be equal to approximately 30 mm in surge, 60 mm in heave and to 26° for pitch. The maximum measured normalised pressure amplitude is equal to 6.4 corresponding to a pressure amplitude of 628 Pa for an incident wave with amplitude equal to 10 mm. A maximum resultant normalised mooring force equal to 3.8 was measured for these experiments

Mechanical Damping setting [Nms]:	Normalised Surge:	Resonance peak (T=2.0 s)	Second peak (T=1.14 s)
	3.3	0.4	0.6
	19.6	2.3	0.9
	39.6	2.9	1.1
	Heave:		
	3.3	1.2	0.7
	19.6	5.1	1.1
	39.6	5.6	1.4
	Pitch:		
	3.3	22.9	14.7
	19.6	37.6	19.0
	39.6	45.9	18.1
	Pressure:		
	3.3	1.4	1.0
	19.6	5.9	2.4
	39.6	6.4	1.7
	FX:		
	3.3	1.0	0.3
	19.6	2.7	0.3
	39.6	3.3	0.3
	FZ:		
	3.3	0.6	0.2
	19.6	1.6	0.2
	39.6	1.9	0.2
	RCW:		
	3.3	0.6	0.6
	19.6	1.6	0.6
	39.6	0.9	0.1

Table 3.10: *Measured normalised responses at the peaks for surge, heave, pitch, pressure, mooring forces in surge (Fx) and heave (Fz) and relative capture width (RCW).*

which for an incident wave with amplitude equal to 10 mm, corresponds to a force equal to 86.0 N. The values of the normalised amplitudes at the peaks are presented in Table 3.10.

The *relative capture width* (RCW) is a quantity commonly used by wave energy engineers to quantify the performance of a device, and refers to the ratio of the power captured by the device to that incident upon its width. This quantity was defined in Section 2.5 by Equation (2.3b) and was computed for the ranges of wave periods and damping settings used in this experiment, and is given in Figure 3.31.

The mean absorbed power ($\overline{P_{abs}}$) is obtained by averaging over an integer number of wave periods the instantaneous absorbed power given by Equation (3.3):

$$\overline{P_{abs}} = \frac{1}{T}\int_0^T P_{abs}\,dt = \frac{1}{k_0}\overline{\Delta p^2} \tag{3.5}$$

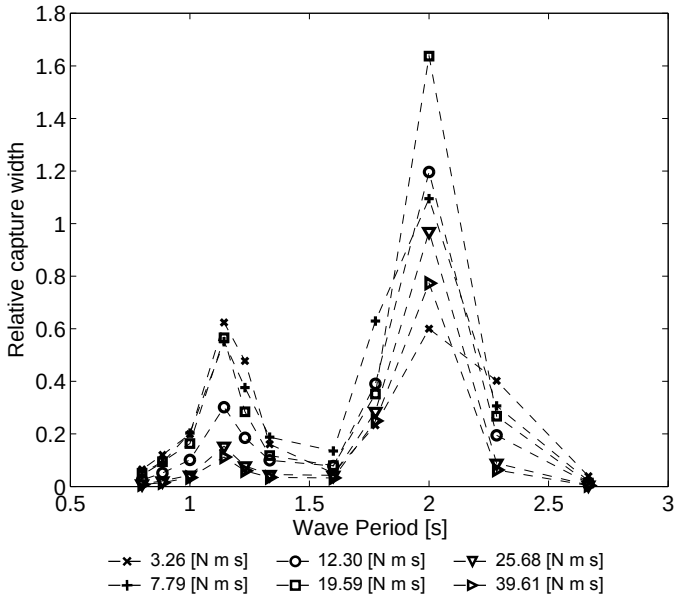

Figure 3.31: *Relative capture width for different settings of applied damping.*

3.4.2 Tests with mixed seas

In this section the results obtained with the scale model for a set of mixed seas based on a two dimensional *Bretschneider spectra* are presented. This spectra is characterised by the significant wave height (H_{m_0}) and peak frequency (f_p) and has the same shape as a more commonly used spectrum known as *Pierson-Moskowitz* which depends only on the wind speed and is representative of full developed seas.

These spectral parameters were chosen to match sea-state occurrences at Lanzarote, Canaries Islands (30°N, 12°W) and were scaled down for the tank tests, with the same scale as the experimental model (1:33), using a Froude similarity law. This location was selected because it presents a good wave resource and these islands are known to have a need for freshwater and so it could be a candidate place to operate the desalination Duck.

The spectral data was obtained from Wave Atlas - WAM (1987 – 1994) and is reproduced in Table 3.11.

Ideally, an overall assessment of the annual average performance of the desalination Duck for this location would require tests in each of the mixed seas represented in Table 3.11. Unfortunately, serious limitations on the selection of these were imposed by the scale for the tests (1:33). The generation of longer waves with higher amplitudes require longer strokes of the wave-paddles which are limited by finite end-stops. Thus, the operation of the tank within the safe limits is limited to the less energetic sea states.

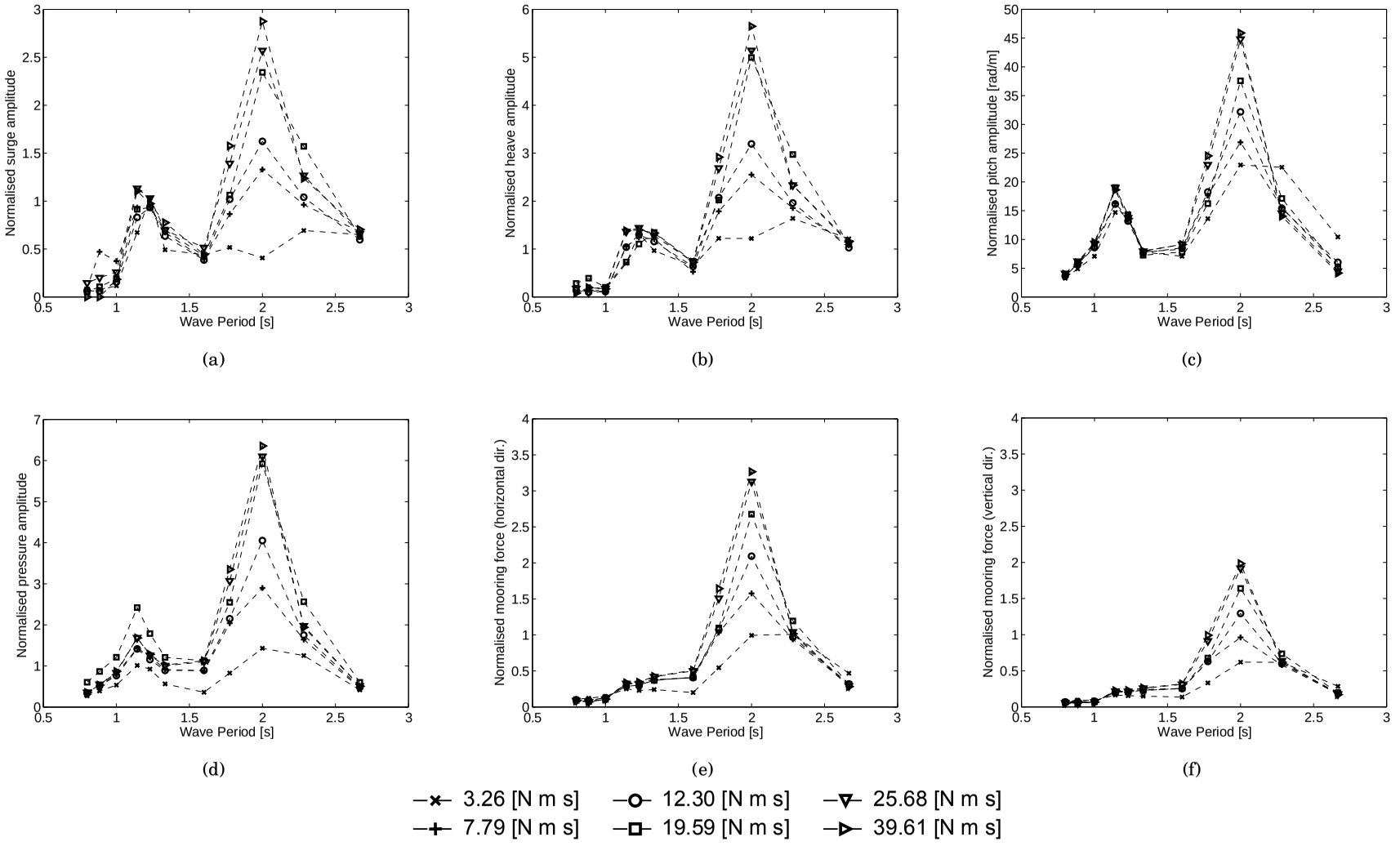

Figure 3.32: *Period response of several quantities and its variation with applied damping: Normalised amplitudes in a) surge, b) heave and c) pitch, d) pressure e) mooring force in horizontal and f) vertical direction.*

A total of eleven different sea states were chosen and are marked in Table 3.11 by the shadowed grey cells. These mixed sea states were generated with a repeat time of 128 s and all measurements were made over the same time interval.

	Te											
Hs	**5 - 6**	**6 -7**	**7 - 8**	**8 - 9**	**9 - 10**	**10 - 11**	**11 - 12**	**12 - 13**	**13 - 14**	**14 - 15**	**15 - 18**	
5.5 - 6.0	0	0	0	0	0	1	0	0	1	1	1	**4**
5.0 - 5.5	0	0	0	0	1	1	0	1	0	1	0	**4**
4.5 - 5.0	0	0	0	1	2	1	1	1	1	1	1	**9**
4.0 - 4.5	0	0	0	2	3	3	2	2	2	1	2	**17**
3.5 - 4.0	0	0	2	9	6	5	4	3	4	3	1	**37**
3.0 - 3.5	0	0	11	14	12	8	8	8	9	5	0	**75**
2.5 - 3.0	0	10	27	19	16	16	15	15	12	2	0	**132**
2.0 - 2.5	1	44	39	29	29	36	33	16	3	0	0	**230**
1.5 - 2.0	19	72	47	48	46	38	18	3	0	0	0	**291**
1.0 - 1.5	22	48	44	41	21	7	1	0	0	0	0	**184**
0.5 - 1.0	1	6	8	1	0	0	0	0	0	0	0	**16**
Total	**43**	**180**	**178**	**164**	**136**	**116**	**82**	**49**	**32**	**14**	**5**	**1000**

Table 3.11: *Bivariate frequency table (H_s,T_e) for Lanzarote.*

The tests were performed with the scale model piercing the free-surface with a draft of 242 mm ($H/D = 0.66$), corresponding to a submergence level ratio of about 70% and with a low value of fixed pneumatic damping equal to 3.0×10^4 Nm^{-5}s which corresponds to configuration number 1 in Table 3.4.

Two distinct locations of the off-centred axis were tested, corresponding to an angle to the horizontal plane and distance to the centre of the cylinder equal to (see Figure 3.26 for reference):

(a) $\alpha_0 = 55°$, $l_0 = 110$ mm $[l_0/(D/2) = 0.60]$;

(b) $\alpha_0 = 5°$, $l_0 = 90$ mm $[l_0/(D/2) = 0.49]$.

Figure 3.33 show the time series signals recorded for the motions, pressure, mooring forces and converted power for a mixed sea generated with a significant wave height of 53 mm and energy period of 1.16 s which correspond to a full scale sea with $H_{m_0} = 1.8$ m and $T_e = 6.7$ s.

The time-series show the continuous response of the scale model to this mixed sea spectra and the instantaneous and average converted power are shown in Figure 3.33(c). This figure demonstrates the peaky character of the instantaneous power typically associated with sea waves. The maximum recorded peak value for this sea was equal to 1.46 W. The average converted power is much lower and is equal to about 0.24 W. Full scale values for power can be obtained through Froude scaling, multiplying the model scale values by a factor equal to $sf = (33)^{3.5}$, giving 301.4 kW for the maximum peak and 49.5 kW for the average converted power.

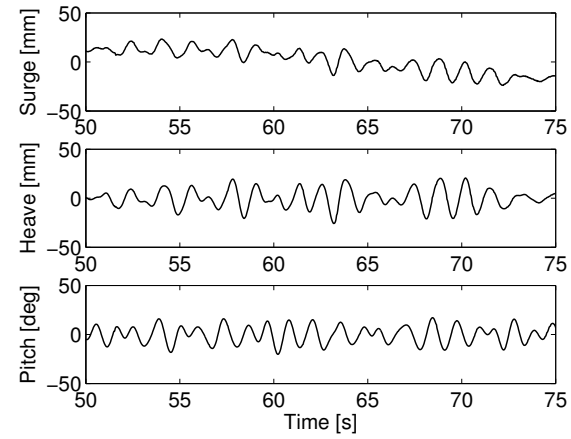

(a)

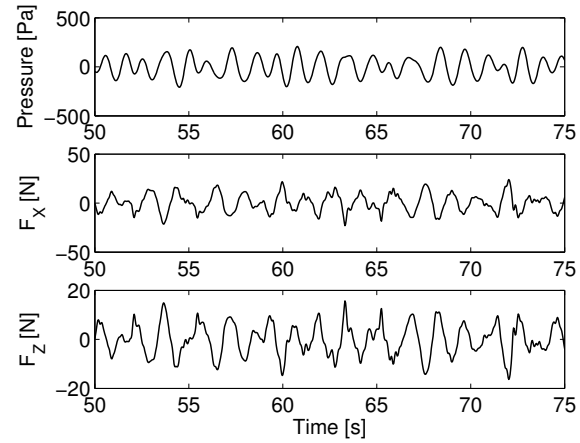

(b)

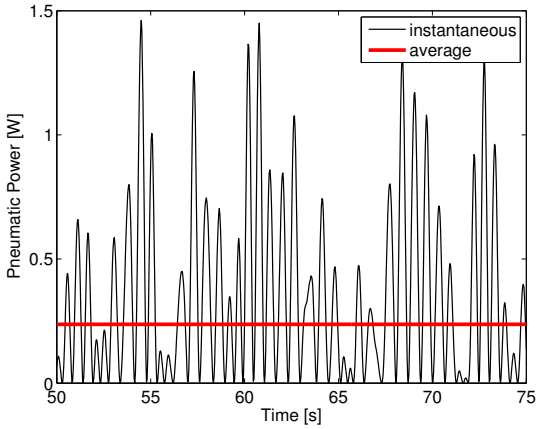

(c)

Figure 3.33: *Time series signal response for a modified Pierson-Moskowitz sea generated with* $H_{m_0} = 53\ mm$ *and* $T_e = 1.16\ s$*. The scale model is submerged at* $H/D = 0.66$ *with the off-centred axis located at* $\alpha_0 = 55\ ^\circ$ *and* $l_0/(D/2) = 0.60$ *(see Figure 3.26) and with fixed damping set to 3.26 Nms. (a) motions in surge, heave and pitch, (b) pressure and mooring forces in the horizontal and vertical direction, (c) instantaneous and average converted power.*

The maximum peak mooring force (resultant) observed during all tests was equal to 99.9 N. This force would correspond to a full scale value of about 3.6 MN ($sf = (33)^3$). The very large forces observed at the attachment point suggest that those large forces can be further used to generate energy through a power-take-off system located either at the mooring attachment point or in the rigid struts.

Figure 3.34 show the normalised values of the resultant mooring force computed using its 'RMS' and maximum peak values. These were obtained in a similar way as in the previous section, for the regular waves, by substituting η_{rms} by the significant wave height (H_{m_0}) and the force term by the max peak or 'RMS' value. The normalisation formulas are given by: $\hat{F}^{sea}_{rms} = F^{sea}_{rms}/\left(\rho\, g\, D\, W\, H_{m0}\right)$ and $\hat{F}^{sea}_{peak} = F^{sea}_{max}/\left(\rho\, g\, D\, W\, H_{m0}\right)$.

Both configurations with the different locations of the off-centred axis are represented in this plot for all tested mixed seas. The configuration represented by the red crosses, with $\alpha_0 = 55°$ and $l_0/(D/2) = 0.60$ show lower mooring forces. These are in the same range of values as the observed for the regular waves tests when a comparable configuration and value of damping was used (shown in Figures 3.32(e) and 3.32(f) for the damping condition equal to 3.26 Nms). Note the linear trend between the 'RMS' value of the mooring forces and the significant wave height which results from the agglomeration of the points for the lower energetic sea states with the same energy period and different significant wave heights.

Figure 3.35 show the relative capture width obtained during these tests for the two configurations with different locations of the off-centred axis and for the eleven tested mixed seas. A dashed line is shown to help to distinguish tests which used comparable values of the significant wave height. The dispersion of the performance values at comparable energy periods show that in general performance decreases with increasing wave height giving evidence of the non-linearities that are present in the system. Figure 3.36 shows this trend more clearly.

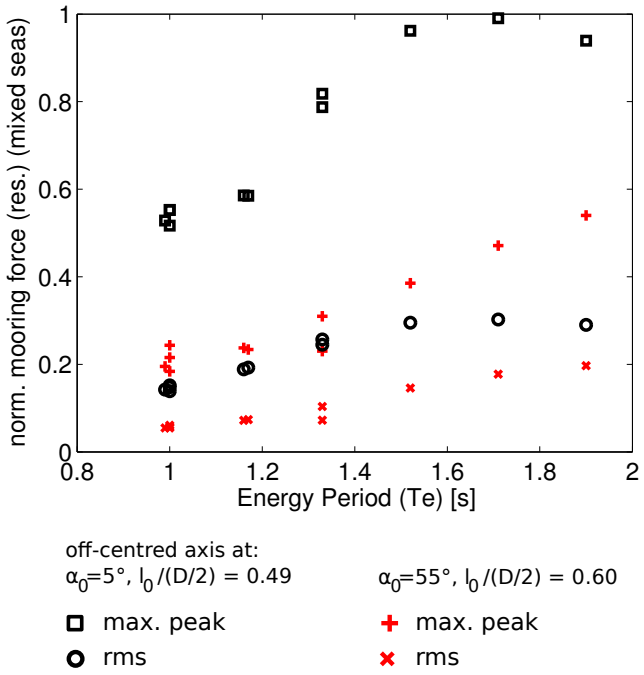

Figure 3.34: *Normalised resultant mooring force computed from the vertical and horizontal components:* $F_{\chi}^{sea}/\left(\rho\, g\, D\, W\, H_{m0}\right)$*, with* χ *corresponding to maximum peak or 'RMS' values.*

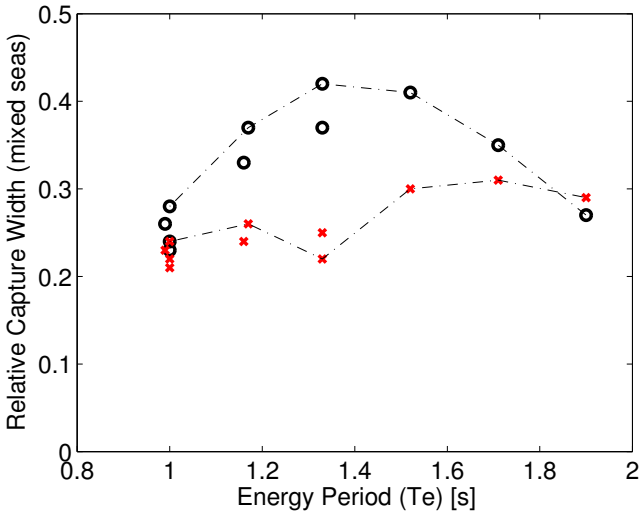

Figure 3.35: *Measured relative capture width of the scale model of the desalination Duck for the eleven mixed seas run in the tank tests and for two positions of the off-centred axis. Circles correspond to the configuration with* $\alpha_0 = 5°$ *and* $l_0/(D/2) = 0.49$*. Crosses correspond to the configuration with* $\alpha_0 = 55°$ *and* $l_0/(D/2) = 0.60$*.*

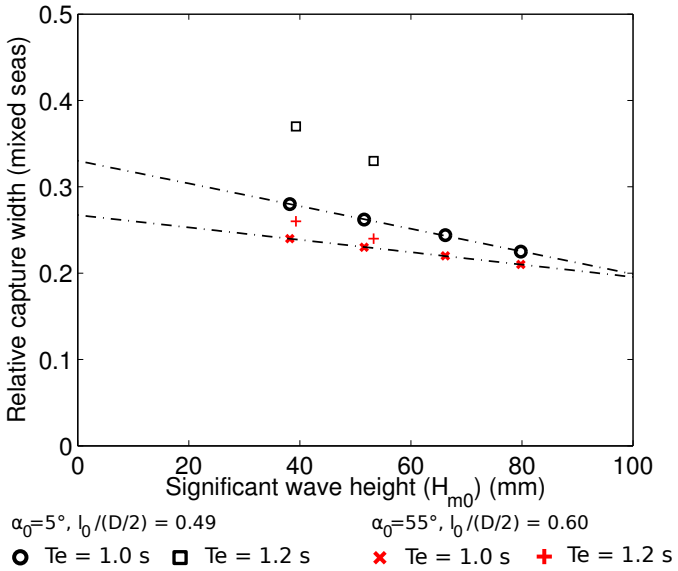

Figure 3.36: *Variation of the relative capture width with the significant wave height for four tests with similar energy period. The colour 'black' is associated with the configuration with* $\alpha_0 = 5°$ *and* $l_0/(D/2) = 0.49$ *and 'red' with the configuration with* $\alpha_0 = 55°$ *and* $l_0/(D/2) = 0.60$.

The non-linearities are thought to be mainly associated with friction losses, either in the mechanical part of the system (friction losses in the bearings, pressure losses in the damper, etc.) or in the fluid (viscous losses). An improvement in the design which would soften all the sharp edges of the scale model is expected to increase considerably the performance. Visual observations of the tests gave account for the large vortexes created by these sharp edges and corners of the scale model and the consequent dissipation of energy in the fluid.

The values of relative capture width measured for this tests are in the range between 0.2 to 0.4 with the maximum measured value equal to 0.42. The configuration with $\alpha_0 = 5°$, $l_0/(D/2) = 0.49$ is shown to perform better, but as seen in Figure 3.34 presents higher mooring forces.

Table 3.12 summaries the measurements obtained during the mixed seas tests and Table 3.11(b) shows the measured values scaled to prototype size by using a Froude similarity law. Following these values, if a prototype was deployed at a location near Lanzarote, for a total of 2821 operational hours (which is about 32% of a year) it would be expected to produce a total of about 172 MWh of pneumatic power.

(a) results from the tank tests.

	scale model seas			$\alpha_0 = 5°$; $l_0/(D/2) = 0.49$							$\alpha_0 = 55°$; $l_0/(D/2) = 0.60$						
				mooring forces (N)				pneumatic power (W)			mooring forces (N)				pneumatic power (W)		
n	Hm_0 (mm)	Te (s)	$\overline{P_w}$ (W/m)	max. peak (X-Z)		rms (X-Z)		max. peak	$\overline{P_{abs}}$	RCW	max. peak (X-Z)		rms (X-Z)		max. peak	$\overline{P_{abs}}$	RCW
1	38.2 (0.23)	1.00 (0.003)	0.698 (0.0072)	30.8 (0.20)	32.4 (0.09)	9.5 (0.01)	7.3 (0.003)	0.83 (0.003)	0.124 (0.0001)	0.28 (0.003)	12.9	9.3	2.7	3.9	0.750	0.107	0.24
2	51.6 (0.25)	0.99 (0.002)	1.268 (0.0117)	44.4 (0.10)	42.9 (0.38)	13.2 (0.04)	10.1 (0.02)	1.34 (0.013)	0.211 (0.0005)	0.26 (0.003)	19.2	12.3	3.6	5.3	1.218	0.182	0.23
3	66.2 (0.31)	1.00 (0.003)	2.093 (0.0188)	64.9 (0.29)	51.4 (0.76)	17.6 (0.06)	13.5 (0.04)	1.97 (0.008)	0.324 (0.0006)	0.24 (0.002)	27.0	17.7	4.9	7.1	1.909	0.288	0.22
4	79.8 (0.41)	1.00 (0.003)	3.062 (0.0324)	77.8 (0.72)	62.6 (0.30)	21.8 (0.02)	16.7 (0.01)	2.62 (0.017)	0.437 (0.0008)	0.23 (0.002)	36.2	25.0	6.1	9.1	2.809	0.404	0.21
5	39.3 (0.27)	1.17 (0.004)	0.864 (0.0122)	36.6	37.0	13.6	10.4	1.51	0.200	0.37	17.6	11.1	3.7	5.4	0.884	0.140	0.26
6	53.3 (0.34)	1.16 (0.003)	1.582 (0.0234)	48.4	51.5	18.1	13.8	2.56	0.335	0.33	24.0	15.7	5.0	7.1	1.461	0.237	0.24
7	39.9 (0.36)	1.33 (0.005)	1.021 (0.0212)	52.0	52.5	18.5	14.0	2.09	0.272	0.42	17.6	11.1	3.7	5.4	0.884	0.140	0.22
8	54.2 (0.47)	1.33 (0.004)	1.877 (0.0371)	65.3	71.2	23.9	18.2	3.69	0.445	0.37	31.5	21.3	7.2	10.5	2.207	0.295	0.25
9	40.7 (0.44)	1.52 (0.004)	1.202 (0.0284)	61.5	63.8	21.7	16.4	2.65	0.311	0.41	29.8	19.3	7.6	11.1	1.884	0.229	0.30
10	41.5 (0.39)	1.71 (0.004)	1.411 (0.0247)	65.6	66.0	22.7	17.1	2.94	0.309	0.35	37.0	24.3	13.8	9.4	2.399	0.277	0.31
11	42.3 (0.25)	1.90 (0.010)	1.626 (0.0149)	64.5	62.7	22.2	16.7	2.85	0.279	0.27	44.3	26.7	15.6	10.6	2.573	0.302	0.29

(b) full scale using Froude similarity law.

	full scale seas					$\alpha_0 = 5°$; $l_0/(D/2) = 0.49$							$\alpha_0 = 55°$; $l_0/(D/2) = 0.60$						
						mooring forces (MN)				pneumatic power (kW)			mooring forces (MN)				pneumatic power (kW)		
n	Hm_0 (m)	T_e (s)	‰	h/y	$\overline{P_w}$ (kW/m)	max. peak (X-Z)		rms (X-Z)		max. peak	$\overline{P_{abs}}$	(MWh)	max. peak (X-Z)		rms (X-Z)		max. peak	$\overline{P_{abs}}$	(MWh)
1	1.26	5.74	22	192.7	4.4	1.11	1.16	0.26	0.34	171.6	25.6	4.9	0.46	0.34	0.10	0.14	154.8	22.1	4.3
2	1.70	5.69	19	166.4	7.9	1.60	1.54	0.36	0.47	276.8	43.6	7.3	0.69	0.44	0.13	0.19	251.4	37.6	6.3
3	2.18	5.74	1	8.8	13.1	2.33	1.85	0.48	0.63	406.9	66.9	0.6	0.97	0.64	0.17	0.26	394.1	59.5	0.5
4	2.63	5.74	0	0.0	19.2	2.80	2.25	0.60	0.78	540.3	90.2	0.0	1.30	0.90	0.22	0.33	579.9	83.4	0.0
5	1.30	6.72	48	420.5	5.4	1.31	1.33	0.38	0.49	312.6	41.3	17.4	0.63	0.40	0.13	0.19	182.5	28.9	12.2
6	1.76	6.66	72	630.7	9.9	1.74	1.85	0.50	0.65	528.5	69.2	44.6	0.86	0.56	0.18	0.26	301.6	48.9	30.9
7	1.32	7.64	44	385.4	6.4	1.87	1.89	0.50	0.66	430.6	56.2	21.6	0.63	0.40	0.13	0.19	182.5	28.9	11.1
8	1.79	7.64	47	411.7	11.7	2.35	2.56	0.65	0.86	762.0	91.9	37.8	1.13	0.77	0.26	0.38	455.6	60.9	25.1
9	1.34	8.73	41	359.2	7.5	2.21	2.29	0.59	0.78	546.7	64.2	23.1	1.07	0.69	0.27	0.40	388.9	47.3	17.0
10	1.37	9.82	21	184.0	8.8	2.36	2.37	0.62	0.82	605.9	63.8	11.7	1.33	0.87	0.34	0.50	495.3	57.2	10.5
11	1.40	10.91	7	61.3	10.2	2.32	2.26	0.60	0.80	588.2	57.6	3.5	1.59	0.96	0.38	0.56	531.2	62.3	3.8

Table 3.12: *Summary of the results obtained in the tank tests with a scale model of the desalination Duck in mixed seas. The seas are characterised by H_m0 and T_e. Two different positions of the off-centred axis were tested with $\alpha_0 = 5°$, $l_0 = 90$ mmand $\alpha_0 = 55°$, $l_0 = 110$ mm (see Figure 3.26). The pneumatic damping was fixed and equal to 3.0×10^4 $Nm^{-5}s$.*

$\overline{P_w}$ – average power per unit front length in mixed seas (in deep water).
$\overline{P_{abs}}$ – average converted power (given by Equation (3.5)).
(The values in parenthesis are the associated uncertainties.)

Chapter 4
The dynamics of a horizontal cylinder excited by waves.

The hydrodynamic behaviour of a wave energy converter which consists of a horizontal cylinder oscillating around an off-centred axis is presented in this chapter.

The linear hydrodynamic forces associated with such system are discussed. The characteristics of these forces change substantially whether the cylinder is fully submerged or piercing the free surface. Both cases are analysed.

Following previous studies by McIver and Evans [1984] and Greenhow and Ahn [1988], the hydrodynamic coefficients and excitation forces of a horizontal cylinder, associated with different submerged levels are considered and extended to a cylinder of finite width and for different water depths. The hydrodynamic forces were then computed at an off-centred location of the axis of oscillation throughout a set of formulas presented subsequently. These were then used to derive a one degree of freedom equation of motion for the cylinder and an analysis which regards the influence of the off-centred axis and the mass distribution in the performance of the device is presented.

All hydrodynamic forces associated with the horizontal cylinder were computed numerically throughout a commercial software package called *WAMIT*. A brief description of this software and the main underlying assumptions associated with it are described in the following section.

4.1 *WAMIT*

Wave Analysis MIT also known as *WAMIT* is a commercial software that provides tools for the analysis of the interaction between waves and floating bodies in the frequency domain. The first version was developed in 1987 by the Massachusetts Institute of Technology (MIT) and its first release dates back to 1999. Since then it has been increasingly recognised for its high degree of accuracy and efficiency and is becoming a standard in both industry and research organisations.

WAMIT is a three dimensional free surface panel program based on linear potential flow theory that solves the velocity potential of the fluid through an integral equation method on the submerged surface of the bodies.

Several hydrodynamic parameters are derived from the velocity potential as the hydrodynamic coefficients, radiation and excitation forces, response-amplitude operators, pressure, fluid velocity and the mean drift forces and moments. The more advanced versions include also a second order module capable of evaluating second order non-linear hydrodynamic forces, but this feature is not included in the version 6.03, released in 2002, which is the only version available at present at the University of Edinburgh.

WAMIT was developed in response to the need of more accurate and efficient programs to solve the free-surface source potential and special algorithms were implemented for this purpose.

Since the first versions it is characterised by a very efficient code that allows the computation of the velocity potential with lower computational burden and consequently the possibility to achieve more accurate solutions through the refinement of the geometrical description. First versions were based on a low-order panel method and its main features can be found in Newman and Sclavounos [1988].

It is beyond the scope of the present work to give a detailed description of the use of *WAMIT* to model wave energy converters. More detail on that topic can be found in Payne [2005] which describes the use of *WAMIT* to model the sloped IPS buoy. Nevertheless, it is important to briefly outline the main underlying assumptions associated with linear potential flow theory and *WAMIT*.

4.1.1 Main assumptions

Detailed descriptions on the subject of free-surface linear potential flow can be found in many sources and it is not the purpose of the present work to go through this theory in detail. Only a brief overview is given and the reader is invited to investigate the more detailed and extensive works presented by, for example, Newman [1977], Falnes [2002], Faltinsen [1990], Mei [1989], and Wehausen and Laitone [1960].

In linear potential flow, the fluid is assumed to be incompressible, inviscid and with negligible surface tension. The flow is irrotational and so the Laplace equation for the velocity potential is required to be satisfied throughout all the fluid domain and

special boundary conditions must be also satisfied to obtain a meaningful solution of the problem.

A kinematic boundary condition is applied to all solid boundaries. As there is no fluid going through the solid, it requires that the normal velocities of the fluid and solid to be equal at the boundary.

A dynamic boundary condition is applied to the free surface interface requiring that the air pressure equals the fluid pressure. It is implicit in this formulation that capillary forces are not taken into account as surface tension is neglected. This boundary condition has a quadratic term in the velocity which is neglected by assuming small values for the velocity of the fluid and for all dynamic variables and their derivatives that result from a linearisation process.

Another kinematic boundary condition is required at the water-air interface to impose that a particle from the boundary stays at the boundary.

Finally a radiation condition at infinite is required to be satisfied to guarantee that the waves are outgoing with a proper amplitude behaviour.

Table 4.1 summarises the fundamental assumptions, equations and boundary conditions of linear potential flow theory.

The hydrodynamic forces and moments that result from the interaction of the fluid with a body are computed by taking the integral of the fluid pressure over the wet surface of the body with the pressure given in terms of velocity potential through the Bernoulli equation.

$$\vec{f}_h = \iint\limits_{S_b} p\,\vec{n}\,dS = -\rho \iint\limits_{S_b} \left(\frac{\partial \phi}{\partial t} + g\,x_3\right)\vec{n}\,dS \tag{4.1a}$$

$$\vec{m}_h = \iint\limits_{S_b} p\,(\vec{r}\times\vec{n})\,dS = -\rho \iint\limits_{S_b} \left(\frac{\partial \phi}{\partial t} + g\,x_3\right)(\vec{r}\times\vec{n})\,dS \tag{4.1b}$$

where the normal $\vec{n}$ to the wet surface of the floating structure is defined to be positive when point out of the fluid volume (i.e. towards the body).

It should be pointed out that in *WAMIT* all motions that result from the hydrodynamic interaction are considered to be harmonic in time and with small amplitudes compared with the wavelength.

Two right hand Cartesian coordinate systems coincident when the body is in (hypothetical) still water are defined. The first is considered in an inertial frame

Linear potential flow assumptions:

1 - fluid incompressible: $\frac{\partial \rho}{\partial t} = 0$

2 - inviscid: $\nu = 0$

3 - and with negligible surface tension: $\gamma \approx 0$

4 - flow is irrotational: $\nabla \times \vec{v} = 0 \Rightarrow \exists \phi : \vec{v} = \vec{\nabla}\phi$

5 - small harmonic motions: $\vec{\xi} = Re\{\hat{\vec{\xi}} e^{(-i\omega t)}\}$

6 - only gravity as applied external force: $\vec{f} = \vec{g}$

Fundamental equations:

7 - continuity equation: $\frac{\partial \rho}{\partial t} + \nabla\left(\rho \vec{v}\right) = 0 \Rightarrow (1) \Rightarrow \nabla \vec{v} = 0$

8 - Euler equation: $\frac{\partial \vec{v}}{\partial t} + \left(\vec{v} \cdot \vec{\nabla}\right)\vec{v} = \frac{1}{\rho}\left(\vec{\nabla} p + \vec{f}\right)$

9 - Bernoulli Equations (steady): $p = -\frac{1}{2}\rho v^2 - \rho g x_3 + C$

10 -(unsteady): $\frac{\partial \phi}{\partial t} + \frac{v^2}{2} + \frac{p}{\rho} + g x_3 = C(t)$

11 - Laplace equation: (4) and (7) $\Rightarrow \nabla^2 \phi = 0$

Boundary conditions:

12 - Kinematic BC at solid body: $\vec{n} \cdot \vec{v} = \vec{n} \cdot \vec{u} \Rightarrow (4) \Rightarrow u_n = \frac{\partial \phi}{\partial n}$

13 - Kinematic at the interface: $\frac{d}{dt}(x_3 - \eta)\Big|_{x_3=0} = 0 \Rightarrow (5) \Rightarrow \frac{\partial \eta}{\partial t} = \frac{\partial \phi}{\partial x_3}$ at $x_3 = 0$

14 - Dynamic BC at the interface: $\eta = -\frac{1}{g}\left(\frac{\partial \phi}{\partial t} + \frac{1}{2}\vec{\nabla}\phi \cdot \vec{\nabla}\phi\right) \Rightarrow (5) \Rightarrow \eta = -\frac{1}{g}\frac{\partial \phi}{\partial t}$

15 - Radiation condition: for constant depth (finite or infinite), both radiation and diffraction potentials (ϕ_R, ϕ_S) should satisfy: $\lim_{R\to\infty} \sqrt{R}\left(\varphi - i\,k\,\varphi\right)$, with R the radial distance from the radiation source and φ the complex amplitude of the potential (ϕ_R or ϕ_S) .

16 - Dispersion relation: $\omega^2 = k\,g\tanh(k\,h)$

Green function (source potential):

17 - Infinite water depth: $G(\vec{x};\vec{\sigma}) = \frac{1}{r} + \frac{1}{r'} + \frac{2\omega^2}{g\pi}\int_0^\infty \frac{\exp(k(x_3+\sigma_3))}{k-\omega^2/g} J_0(kR)\,dk$

$r^2 = (x_1-\sigma_1)^2 + (x_2-\sigma_2)^2 + (x_3-\sigma_3)^2$;

$r'^2 = (x_1-\sigma_1)^2 + (x_2-\sigma_2)^2 + (x_3+\sigma_3)^2$;

$\vec{\sigma} = (\sigma_1, \sigma_2, \sigma_3)$ - position of the source of strength 4π; $J_0(x)$ - Bessel function of zero order;

Integral equations:

18 - radiation velocity potential: $2\pi\phi_k(\vec{x}) + \iint_{S_b} \phi_k(\vec{\sigma})\frac{\partial G(\vec{\sigma};\vec{x})}{\partial n_\sigma} dS_\sigma = \iint_{S_b} n_k\, G(\vec{\sigma};\vec{x})\, dS_\sigma$

19 - diffraction velocity potential: $2\pi\phi_X(\vec{x}) + \iint_{S_b} \phi_X(\vec{\sigma})\frac{\partial G(\vec{\sigma};\vec{x})}{\partial n_\sigma} dS_\sigma = 4\pi\phi_0(\vec{x})$

Discretised integral equations for the high order method (final system of linear equations):

20 - radiation potential: $2\pi d_{ik}^H \left(\phi_j\right)_k + \sum_{k=1}^{N} D_{ik}^H \left(\phi_j\right)_k = S_i^H$

21 - diffraction potential: $2\pi d_{ik}^H \left(\phi_X\right)_k + \sum_{k=1}^{N} D_{ik}^H \left(\phi_X\right)_k = I_i^H$ where: $\left(\phi_j\right)_k$ and $\left(\phi_X\right)_k$ are unknown coefficients of the basis functions for the radiation and diffraction potentials.

$d_{ik}^H = \iint \tilde{U}_i\left(\tilde{w}_f\right)\tilde{U}_k\left(\tilde{w}_f\right) d\tilde{w}_f$

$D_{ik}^H = \iint \tilde{U}_i\left(\tilde{w}_f\right)\left(\iint \tilde{U}_k(\tilde{w})\frac{\partial G(\tilde{w};\tilde{w}_f)}{\partial n(\tilde{w})} J(\tilde{w})\, d\tilde{w}\right) d\tilde{w}_f$

$S_{ik}^H = \iint \tilde{U}_i\left(\tilde{w}_f\right)\left(\iint \frac{\partial \phi_j}{\partial n}(\tilde{w})\, G\left(\tilde{w};\tilde{w}_f\right) J(\tilde{w})\, d\tilde{w}\right) d\tilde{w}_f$

$I_i^H = \iint \tilde{U}_i\left(\tilde{w}_f\right)\phi_0\left(\tilde{w}_f\right) d\tilde{w}_f$

with: $\tilde{U}_k = U_l(w_1)V_m(w_2)$, $\iint d\tilde{w} = \int_{-1}^{1}\int_{-1}^{1} dw_1\, dw_2$ and $J(\tilde{w})$ is the Jacobian.

N refers to the number of patches and $\vec{x} = (x_1, x_2, x_3)$ are the Cartesian coordinates of a point in the physical space to which corresponds the parametric coordinate $\tilde{w} = (w_1, w_2)$.

Table 4.1: *Summary of the fundamental assumptions equations and boundary conditions in linear potential flow theory and WAMIT.*

of reference $(O,\vec{e}_1,\vec{e}_2,\vec{e}_3)$ with $\vec{e}_3$ pointing up in the vertical direction. The second $\left(O',\vec{b}_1,\vec{b}_2,\vec{b}_3\right)$ is fixed with respect to the body.

The translational and rotational harmonic displacements between these two coordinate systems correspond to the surge, sway, heave, roll, pitch and yaw modes. Following the notation used in *WAMIT*, those are represented as a 6 component vector: $\vec{\xi} = [\xi_1,\xi_2,\xi_3,\xi_4,\xi_5,\xi_6]$. The components of the linear and angular velocities and accelerations are given respectively by:

$$\xi_k = Re\left\{\hat{\xi}_k\, e^{i\omega t}\right\} \tag{4.2}$$

$$\dot{\xi}_k = i\,\omega\,\xi_k = Re\left\{U_k\, e^{i\omega t}\right\} = u_k \tag{4.3}$$

$$\ddot{\xi}_k = -\omega^2\,\xi_k = \dot{u}_k \tag{4.4}$$

with $k = 1,...,6$.

Physically two distinct interactions take place between a wave front and a floating body. One, that the waves diffract and scatter in all directions. The other, that the same waves will set the body into motion and generate additional waves which will radiate in all directions. These separate problems, commonly refereed as the diffraction and radiation problems, correspond respectively to: 1) the study of the interactions of the incident waves with the body held fixed and 2) the study of the interactions due to forced motions of the body in calm water.

The velocity potential in Equation (4.1) is subdivided into these different contributions and is considered to be harmonic with the same frequency as the incident excitation wave.

$$\phi = \phi_0 + \phi_S + \phi_R \tag{4.5}$$

A description of the methods to solve for the velocity potential due to these different contributions can be found for example in Wehausen and Laitone [1960, §18, 19].

The outline of the method used in *WAMIT* is detailed in, for example, Newman and Sclavounos [1988] or in *WAMIT* manual [WAM, 2000]. It is based on the solution of integral equations computed on the wet surface of the body developed by applying the Green theorem to source potentials defined as Green functions..

The potential for a unit source in the absence of the body defines the Green function G [Wehausen and Laitone, 1960, §7] (17 in Table 4.1) and this function through the Green

theorem defines an integral equation for the velocity potential on the wet surface S_b of the body. The integral equations are then solved for the velocity potentials of the radiation and diffraction problems associated with Equation (4.5). For reference, these are given in Table 4.1.

The low-order method was the first to be developed. The integral equations are discretised by dividing the wet surface of the body into an ensemble of flat quadrilateral panels assuming in each a constant velocity potential and velocity normal.

Many of the advantages of the first versions of *WAMIT* were related with the way the integrations were performed through the use of efficient algorithms. An example of such algorithms is described in Newman [1985]. All approximations are enforced to be accurate to six digits ensuring a high degree of precision for the ultimate solution. The dominant numerical errors are associated with the discretisation of the body surface and can be lowered by increasing the number of panels that describe the geometry of the body.

An alternative to obtain more accurate solutions without increasing the number of panels can be achieved by increasing the accuracy of the description of both the geometry of the body and the distribution of source potentials in its surface. This is usually performed by higher-order panel methods. *WAMIT* uses a higher order method based on '*HIPAN*' which was developed by Maniar [1995] and uses B-spline functions to describe the velocity potential. This method has been implemented in *WAMIT* since version 6.0.

In the present study the high-order method is used to compute all hydrodynamic quantities and as such it justifies a more detailed overview.

4.1.2 Higher-order method

The higher-order method uses B-spline functions to represent more accurately the velocity potential as a continuous function over the surface of a body.

The representation of the geometry of the wet surface of the body and of velocity potential are independent. This is most advantageous in comparison with the low-order method as it allows an increased accuracy of the representation of the velocity potential without the need to change the geometry description. Another advantage is that the velocity field in the body surface can be obtained through direct analytical differentiation.

Lee et al. [1996] and Lee et al. [1998] describe the application of this method to various case studies benchmarking the comparisons with the low-order method. They found that

in general faster convergence and higher accuracy can be achieved when comparable discretisations are used.

A B-Spline is a smooth and continuous function, parametrised and piecewise defined. It uses a set of control points and base polynomials to represent complex curves in a efficient way. It is defined recursively and an example of a B-spline is presented in Figure 4.1.

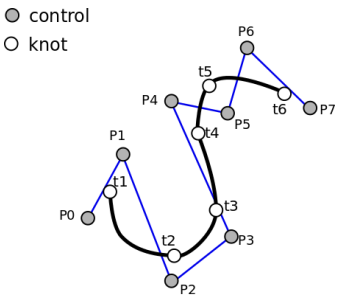

Figure 4.1: *An example of B-Spline curve.*

In the higher-order method the body geometry is represented by an ensemble of smooth continuous surfaces called patches. The patches are parametrised by a pair of normalised coordinates (w_1, w_2) (with $|w_1, w_2| \leq 1$) and the correspondence between parametric space and physical space is done through mapping functions. Representing the coordinates in the parametric space by (w_1, w_2) and the coordinates of the physical space by (x_1, x_2, x_3) , the mapping functions for a patch are given generically by:

$$x_1 = X(w_1, w_2); \qquad x_2 = Y(w_1, w_2); \qquad x_3 = Z(w_1, w_2) \tag{4.6}$$

In higher order method, *WAMIT* allows the representation of the geometry through three distinct possibilities: 1) flat panels, as in the low order method which can be useful for simple geometries; 2) parametrised B-Splines surfaces which allows a very accurate approximation of the geometry; and 3) through an analytical function that parametrises the geometry which has the great advantage to represent the geometry in an exact manner.

The last option was chosen in the present work to represent the geometry of both a fully submerged and a surface piercing horizontal cylinder. This implementation requires the analytic function to be coded into a '*FORTRAN*' subroutine. This procedure is very advantageous because it allows to input relevant body dimensions and parameters in the geometry file without modifying the code.

Furthermore, each patch is subdivided in the parametric space into a rectangular mesh and with each element of the mesh is called panel. In the parametric space a panel is a flat quadrilateral which can in general correspond to a curved surface in the physical space depending on the mapping function.

In the high order method, the panels are associated with the representation of the velocity potential whereas the patches are related with the representation of the geometry of the body wet surface.

On each patch the velocity potential is smoothly and continuously represented using B-Splines, through a tensor product of B-Spline basis functions ($W_1(w_1)$ and $W_2(w_2)$):

$$\phi(w_1,w_2) = \sum_{k=1}^{M_{w_2}} \sum_{j=1}^{M_{w_1}} \phi_{jk} W_{1j}(w_1) W_{2k}(w_2) \tag{4.7}$$

where M_{w_1} and M_{w_2} are the number of basis functions and ϕ_{ik} are to be determined when substituted in the integral equation for the velocity potential.

The accuracy of the representation of the velocity potential in the body surface depends on the order (K_{w_1},K_{w_2}) and the number of basis functions (M_{w_1},M_{w_2}). The order of the basis functions (K_{w_1},K_{w_2}) is given by the order of the polynomial + 1 and the number of basis functions is given by

$$M_{w_1} = N_{w_1} + K_{w_1} - 1 \qquad M_{w_2} = N_{w_2} + K_{w_2} - 1$$

where N_{w_1} and N_{w_2} are the number of panel subdivisions (called 'knots').

WAMIT does not allow the direct control of the number of basis functions by the user, instead it only permits to input the number of panel subdivisions and the order of those functions.

The manual recommends the use of order number values (K_{w_1}, K_{w_2}) equal to 3 for problems with a relatively complex body shape and 4 when the body is smooth and continuous.

An alternative option permits to automatically subdivide the patches into panels by specifying a parameter called 'PANEL_SIZE' so that the maximum length of each panel is approximately equal to the value of this parameter in dimensional units (i.e. m). In this process the value of the order of base functions is set to be equal to 3 and the values of panel subdivisions are assigned in a way to achieve the specified panel size.

The discretised integral equations for the radiation and diffraction problems are obtained by substituting the velocity potential from Equation (4.7) into the respective integral equations in parametric space. These are given for reference in Table 4.1.

The solutions of the integral equations are obtained by applying a Galerkin procedure and a final set of linear equations is obtained. In these equations the unknowns are the coefficients of basis functions for the radiation and diffraction potentials. For more details see WAM [2000, §12] and Maniar [1995].

The integrations are carried out in the parametric space for each patch and over each panel. Those relative to the field point are refereed as '*outer integrations*'. The others associated with a point on the patch are carried out for each abscissa of the outer integral and are refereed as the '*inner integrations*'.

The inner integration involves additional algorithms to solve inherent singularities that arise from the source potential (Green function). These algorithms involve a continuous iterative subdivision of the panels where the singularities arise into smaller domains until a certain threshold and evaluating analytically the singularities. In the 'regular' panels where no singularities are identified, the integrations are performed using Gauss-Legendre quadrature algorithm.

Lee et al. [1996] reports that most significant errors are associated with the order of the Gauss-Legendre rule for the outer integration and the limitations of the B-Spline approximation. Secondary sources of errors are related with the truncated normal derivative expansion, the amplification of errors in the solution due to ill-conditioned linear system of equations, inaccuracies in the B-Spline surface patches and lack of continuity across the patches.

4.1.3 Output quantities from *WAMIT*

The evaluation of the velocity potential (4.5) and derivatives allows the computation of several hydrodynamic quantities which are available as outputs from *WAMIT*. Most of these quantities are presented in Table 4.2.

In what follows, special attention is given towards the derivation of the equations of motion for a body which is in motion when excited by small harmonic incident waves. With this assumption it is supposed that the body is oscillating for a sufficiently long time so that all transients have died out.

1. Hydrostatic coefficients:

$C_{33} = \rho g S_{00}$
$C_{34} = \rho g S_{01}$
$C_{35} = -\rho g S_{10}$
$C_{44} = \rho g S_{02} + \rho g \forall z_b - m g z_g$
$C_{45} = -\rho g S_{11}$
$C_{46} = -\rho g \forall x_b + m g x_g$
$C_{55} = \rho g S_{20} + \rho g \forall z_b - m g z_g$
$C_{56} = -\rho g \forall y_b + m g y_g$
with:
$\vec{r}_b = (x_b, y_b, z_b) = \iiint_{V_0} \vec{r}\, dV$ (centre of buoyancy)
$\vec{r}_g = (x_g, y_g, z_g)$ (centre of mass)
$S_{ij} = \iint_{S_0} x_1^i x_2^j dx_1 dx_2$ (waterplane area and moments(*)).

2. Added mass (A) and hydrodynamic damping (B):

$\omega^2 A_{lm} - i\omega B_{lm} = -\rho \iint_{S_b} \frac{\partial \phi_l}{\partial n} \phi_m \, dS$.

3. Excitation forces from Haskind relations:

$X_i = -i\omega\rho \iint_{S_b} \left(\frac{\partial \phi_i}{\partial n} \phi_0 - \phi_i \frac{\partial \phi_0}{\partial n} \right) dS$.

4. Excitation forces from pressure integration:

$X_i = -i\omega\rho \iint_{S_b} \frac{\partial \phi_i}{\partial n} \phi_D \, dS$.

5. Response amplitude operator:

$\xi_m / a = \sum_{m=1}^{6} \left[-\omega^2 \left(M_{lm} + M_{lm}^E + A_{lm} \right) + i\omega \left(B_{lm} + B_{lm}^E \right) + \left(C_{lm} + C_{lm}^E \right) \right]^{-1} X_l$.

5. Hydrodynamic pressure on the body boundary:

$p = -\rho \frac{\partial \phi}{\partial t}$.

6. Free-surface elevation:

$\eta = -\frac{1}{g} \left(\frac{\partial \phi}{\partial t} \right)_{z=0}$.

(*) see note on 'about notation'.

Table 4.2: *List of hydrodynamic quantities derived from the velocity potential and derivatives which are outputs from WAMIT.*

The hydrodynamic forces acting on the body are given by the integral of the fluid pressure on the wet surface of the body (S_b) as in Equation (4.1). In this equation $\vec{n}$ is a unit vector, normal to the body surface and positive when pointing out of the fluid (i.e into the body).

The second term in Equation (4.1) is the contribution of the hydrostatic pressure to the total applied force. The hydrostatic force and moment are thus given in the most fundamental way as:

$$\vec{f}_C = -\rho g \iint_{S_b} x_3 \vec{n} \, dS \tag{4.8a}$$

$$\vec{m}_C = -\rho g \iint_{S_b} x_3 (\vec{r} \times \vec{n}) \, dS \tag{4.8b}$$

Following Newman [1977, §6.16] and Newman [1978], the Green theorem is applied to the above integrals and the integrations are performed over the instantaneous displaced volume of fluid. Subsequently these integrals are evaluated in terms of the body-fixed coordinates for which the instantaneous volume is decomposed into the a static volume beneath the still water plane and the thin layer bounded by the planes between the body-fixed and inertial coordinate systems (with $z = 0$). The linear hydrostatic force and moment are given in the most general form as:

$$\vec{f}_C = \rho g \left(\forall - S_{00}\xi_3 - S_{01}\xi_4 + S_{10}\xi_5\right)\vec{e}_3 \tag{4.8c}$$

$$\begin{aligned}\vec{m}_C = &\rho g \left[\forall y_b - \forall z_b \xi_1 + S_{01}\xi_3 + S_{02}\xi_4 - S_{11}\xi_5 + \forall x_b \xi_6\right]\vec{e}_1 \\ &- \rho g \left[\forall x_b + S_{10}\xi_3 + S_{11}\xi_4 + \forall z_b \xi_5 - S_{20}\xi_5 - \forall y_b \xi_6\right]\vec{e}_2\end{aligned} \tag{4.8d}$$

with $\forall$ the volume of displaced water, $\vec{r}_b = (x_b, y_b, z_b)$ the centre of buoyancy and S_{ij} the water-plane area and moments given in Table 4.2.

The non-vanishing moments are given by Newman [1977], Wehausen [1971] and the final expressions for the hydrostatic force and moment are further simplified by adding the gravitational force and moment due to the weight of the body and assuming equilibrium when the unsteady motions vanish so that the weight is perfectly balanced by the buoyancy force and the horizontal coordinates of the centre of mass are coincident with the centre of buoyancy ($x_g = x_b$ and $y_g = y_b$):

$$\left(\vec{f}_C\right)_3 = -\rho g \left(S_{00}\xi_3 - S_{10}\xi_5\right) \tag{4.8e}$$

$$(\vec{m}_C)_1 = -\rho g \left(S_{02} + \forall \left(z_b - z_g\right)\right)\xi_4 \tag{4.8f}$$

$$(\vec{m}_C)_2 = \rho g \left[S_{10}\xi_3 - \left(S_{20} + \forall \left(z_b - z_g\right)\right)\xi_5\right] \tag{4.8g}$$

The velocity potential (ϕ) in Equation (4.1) is separated into the contributions from the radiation and diffraction problems accordingly to Equation (4.5).

The radiation component is further described as a sum of the contributions due to a unit amplitude displacement of the rigid-body (ξ_k) ($k = 1,..,6$) in the absence of incident waves.

$$\phi_R = Re\left\{\sum_{k=1}^{6} \phi_k \xi_k e^{i\omega t}\right\} \tag{4.9}$$

Applying the solid body kinematic boundary condition for unit amplitude motion in one direction:

$$u_n = \frac{\partial \phi_j}{\partial n} = \vec{u}\cdot\vec{n} = i\omega\vec{\xi}\cdot\vec{n} = i\omega\vec{\xi}\cdot\vec{n} = i\omega n_j \tag{4.10}$$

where the vectors associated with the velocity of the body ($\vec{u}$) displacements ($\vec{\xi}$) and normal to its surface ($\vec{n}$) are extended to the six components which include both the linear and angular terms ($n_k = (\vec{r} \times \vec{n})_{(k-3)}$ for $k = 4,5,6$).

Substituting the time derivative of the radiation potential and (4.10) into Equation (4.1), the components of the force and moment associated with the forced motion of the body can be written as:

$$\left(\vec{f}_R\right)_k = Re\left\{\xi_l \, e^{i\omega t} f_{kl}\right\} \tag{4.11}$$

where f_{kl} is the complex force due to the fluid pressure in k direction due to a sinusoidal motion of unit amplitude in the direction l and is given by:

$$f_{kl} = -\rho \iint_{S_b} \frac{\partial \phi_k}{\partial n} \phi_l \, dS = \omega^2 A_{kl} - i\,\omega B_{kl} \tag{4.12}$$

where A_{kl} and B_{kl} are the components of the added mass and hydrodynamic mass matrices respectively.

The diffraction potential $\phi_X = \phi_0 + \phi_S$ is written as being proportional to the amplitude of the incident wave (a), i.e:

$$\phi_X = Re\left\{a\left(\phi_0 + \phi_S\right) e^{i\omega t}\right\} \tag{4.13}$$

Substituting into Equation (4.1) and taking into account the boundary condition given by Equation (4.10) the components of the excitation force and moments can be written as:

$$\left(\vec{f}_X\right)_j = Re\left\{a\, e^{i\omega t} X_j\right\} \tag{4.14}$$

with:

$$X_j = -\rho \iint_{S_b} \left(\phi_0 + \phi_S\right) \frac{\partial \phi_j}{\partial n} \, dS \tag{4.15}$$

Following Newman [1977, §6.19], defining the six components of the inertial force and moments of an unrestrained body and with the assumption of linearised motions:

$$\left(\vec{f}_m\right)_j = \sum_{j=1}^{6} M_{jk}\, \dot{u}_k = -\omega^2 \sum_{j=1}^{6} M_{jk}\, \xi_k \tag{4.16}$$

where:

$$M = \begin{bmatrix} m & 0 & 0 & 0 & m z_g & -m y_g \\ 0 & m & 0 & -m z_g & 0 & m x_g \\ 0 & 0 & m & m y_g & -m x_g & 0 \\ 0 & -m z_g & m y_g & J_{11} & J_{12} & J_{13} \\ m z_g & 0 & -m x_g & J_{21} & J_{22} & J_{23} \\ -m y_b & m x_g & 0 & J_{31} & J_{32} & J_{33} \end{bmatrix} \tag{4.17}$$

and in which J_{jk} are the components of the inertia matrix of the body.

Substituting Equations (4.16), (4.8e), (4.11),(4.14) into $\vec{f}_m = \vec{f}_C + \vec{f}_R + \vec{f}_X$ the final system of six equations of motion is obtained:

$$\sum_{m=1}^{6} \left[-\omega^2 (M_{lm} + A_{lm}) + i\,\omega B_{lm} + C_{lm} \right] \xi_m = a\, X_l \tag{4.18a}$$

WAMIT allows the inclusion of external force terms to restrain the motion of the system. Introducing an external damping $\mathbf{B}^E$ and stiffness $\mathbf{C}^E$ matrices, the final system of equations of motion is written as:

$$\sum_{m=1}^{6} \left[-\omega^2 (M_{lm} + A_{lm}) + i\,\omega \left(B_{lm} + B^E_{lm} \right) + \left(C_{lm} + C^E_{lm} \right) \right] \xi_m = a\, X_l \tag{4.18b}$$

4.1.4 Parametric definition of the geometry

As mentioned previously in Section 4.1.2, *WAMIT* allows an exact representation of the wet surface of a body through the definition of an analytical function. For this purpose, the function is coded in a specific '*FORTRAN*' subroutine file ('*GEOMXACT.F*') and compiled as dynamic-library link ('*DLL*').

This option is very advantageous as it provides a flexible way to change the geometry through the variation of input parameters with no need to modify the code. An obvious advantage of this methodology is the possibility to execute efficiently systematic studies evaluating different geometries associated with a defined body.

The present work is concerned with two distinct hydrodynamic interactions cases associated with a horizontal cylinder, namely when 1) it is fully submerged at a certain distance from the still free-surface and 2) when it is piercing the free-surface with a certain draft. To represent these situations two different analytic functions are required to be defined.

For both cases, two patches are need: one for the ends (patch 2) and the other for the side (patch 1). Planes of symmetry at $x = 0$ and $y = 0$ can be exploited to reduce the number of panels and the computational burden. These patches are shown in Figure 4.2.

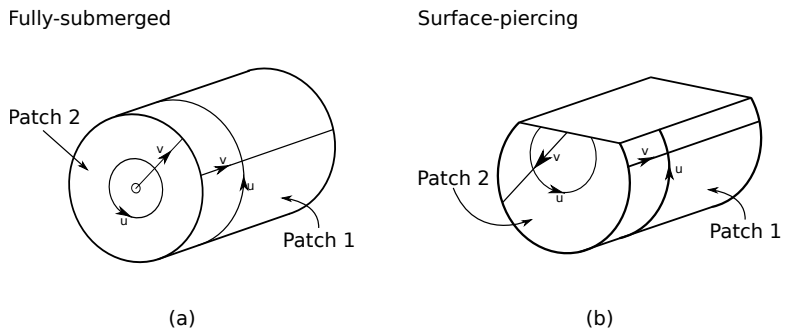

Figure 4.2: *Parametric definition of the horizontal cylinder (a) totally submerged (b) piercing the water surface.*

As it is indicated in Figure 4.2, the origin of the parametrisations for the end of the cylinder are different. The fully submerged cylinder has its origin at its the geometrical centre whereas the free-surface piercing cylinder has its origin at the free-surface.

The parametrisation for the totally submerged cylinder is based in a $2\,cos\theta$ law. With this definition a larger number of B-Spline 'knots' and panels are attributed to the region near the free-surface and a better representation of the velocity potential is achieved.

The implementation of the analytical functions for both cases is defined below and the '*FORTRAN*' subroutine coding is presented in Appendix D. The parametric variables w_1 and w_2 have values in the interval $[-1,1]$. The radius of the cylinder is $D/2$ and its width is W. The draft is H.

1. Parametric definition for the fully-submerged horizontal cylinder :

patch 1 (side):

$$x_1 = \frac{D}{2}\cos(\vartheta_1(w_1)); \quad x_2 = -\frac{W}{4}(w_2+1); \quad x_3 = \frac{D}{2}\sin(\vartheta_1(w_1)) \tag{4.19a}$$

patch 2 (base):

$$x_1 = \varphi_1(v)\cos(\vartheta_1(w_1)); \quad x_2 = -\frac{W}{2}; \quad x_3 = \varphi_1(w_2)\sin(\vartheta_1(w_1)) \tag{4.19b}$$

with:

$$\vartheta_1(w_1) = \frac{\pi}{2}\left[2\cos\left(\frac{\pi}{4}(w_1+1)\right)-1\right] \tag{4.19c}$$

$$\varphi_1(v) = \frac{D}{4}\left[1+2\cos\left(\frac{\pi}{4}(w_2+1)\right)-1\right] \tag{4.19d}$$

2. For the horizontal cylinder piercing the free surface:

patch 1 (side):

$$x_1 = \frac{D}{2}\cos(\vartheta_2(w_1)) - x_b; \quad x_2 = \frac{W}{4}(w_2+1) - y_b; \quad x_3 = \frac{D}{2}\sin(\vartheta_2(w_1)) - H - z_b \tag{4.19e}$$

patch 2 (base):

$$x_1 = \varphi_2(w_2)\cos(\vartheta_2(w_1)) - x_b; \quad x_2 = -\frac{W}{2} - y_b; \quad x_3 = \varphi_2(w_2)(\sin(\vartheta_2(w_1))) - z_b \tag{4.19f}$$

with:

$$\vartheta_2(w_1) = -\left(\arcsin\left(\frac{H}{D/2}\right) + \frac{\pi}{2}\right) w_1 - \frac{\pi}{2} \tag{4.19g}$$

$$\varphi_2(w_2) = \frac{D}{4}(1 - w_2) \tag{4.19h}$$

The partial derivatives of these functions are also required to be stated in the '*FORTRAN*' subroutine to derive the kinematic boundary condition and to compute the hydrodynamic loads from pressure integration.

4.1.5 Mesh and error evaluation

This section is concern with the evaluation of the errors associated with the discretisation of the velocity potential and precedes the section where the results for the hydrodynamic forces of a horizontal cylinder are discussed.

Cruz [2009] presented a study based on Richardson extrapolation method to justify the use of a mesh that presents the most accurate numerical results for the case of a horizontal cylinder piercing the free-surface. The methodology considered grid triplets arrangements of fine, medium and coarse meshes and evaluates the error associated with the numerical prediction, grid convergence ratio and uncertainty. The study concludes that a spider web arrangement showed most consistent and accurate results and the finest discretisations with panel sizes equal to 0.02 and 0.01, resulted in most acceptable values for the error norm.

In the present study, a very large number of different geometric configurations are taken into consideration and a larger panel size equal to 0.05 was used to reduce the computational time associated with each configuration. An assessment of the convergence and errors related with the coarser mesh is thus necessary and justified. The hydrodynamic forces are computed systematically for cylinders with different widths, at different drafts and submerged levels and for the cases of shallow, medium and deep water levels. A more rigorous study would require the systematic evaluation of

Fully-submerged

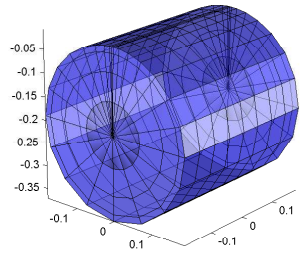

(a) coarse mesh (0.05)

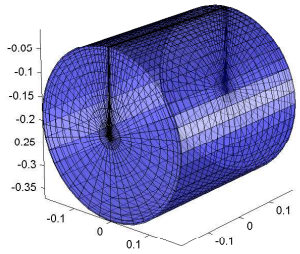

(b) fine mesh (0.02)

Surface-piercing

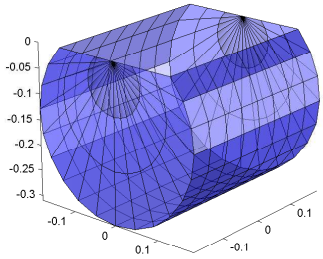

(c) coarse mesh (0.05)

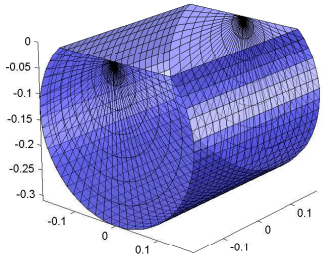

(d) fine mesh (0.02)

Figure 4.3: *Example of meshes used in the convergence studies. The cylinder width ratio is equal to* $W/D = 1$*. The fully submerged cylinder with submergence ratio of* $H/D = 1.02$ *is represented with a) panel size of 0.05 and b) panel size of 0.02. The cylinder piercing the free-surface at a draft ratio equal to* $H/D = 0.85$ *is represented with c) panel size of 0.05 and d) panel size of 0.02*

the errors associated with each configuration. However such study would be very time consuming and the advantages of the use of a coarser mesh diluted.

In the end, only two distinct cases were analysed. They are believed to be representative worst case scenarios. They correspond to the cylinder fully submerged and placed very close to the free surface, and to the surface piercing cylinder almost completely submerged.

A cylinder with a width ratio equal to $W/D = 1$ was selected for ten successive refinements of the mesh. The submergence level for the fully submerged cylinder was set at $H/D = 1.02$ and the hydrodynamic coefficients and excitation forces evaluated at five different wave periods. The second case considers a cylinder piercing the free surface at a draft of $H/D = 0.85$ and a total of ten wave periods were evaluated. Figure 4.3 shows distinct refinements of the mesh for the two case studies considered.

Figures 4.4 and 4.5 show the absolute relative errors to the finer mesh found on each hydrodynamic quantity for different wave periods and for the cases of the fully-submerged and free-surface piercing cylinder.

Table 4.3 summaries the errors observed for the coarse mesh (panel size of 0.05) when compared with the finer mesh (panel size of 0.01). The absolute mean value for the error and standard deviation were computed for the range of wave periods considered. The maximum value and the wave period at which occurs is also given. The mean relative errors are much lower than the maximum errors that in general are less than 1% except for two cases where the value of the quantity is very small.

	Fully submerged cylinder				Surface piercing cylinder			
	$\overline{Err}$ [%]	σ_{Err} [%]	max(Err) [%]	at T [s]	$\overline{Err}$ [%]	σ_{Err} [%]	max(Err) [%]	at T [s]
A_{11}	0.24	0.34	0.84	0.75	0.21	0.17	0.67	0.75
A_{33}	0.45	0.81	1.90	0.75	0.18	0.02	0.20	1.50
B_{11}	0.11	0.03	0.16	1.00	0.15	0.06	0.30	0.50
B_{33}	0.15	0.16	0.42	0.75	0.13	0.11	0.38	1.25
ReX_1	0.11	0.05	0.19	1.00	0.21	0.26	0.93	0.50
ImX_1	0.10	0.10	0.27	0.50	0.09	0.02	0.11	0.75
ReX_3	0.19	0.24	0.61	0.50	0.56	1.47	4.75	1.00
ImX_3	0.16	0.15	0.42	0.75	0.12	0.11	0.35	1.00

Table 4.3: *Absolute relative errors of the hydrodynamic quantities computed by WAMIT associated with a coarse mesh (panel size of 0.05) when compared to a finer mesh (panel size equal to 0.01). The mean relative error ($\overline{Err}$) and standard deviation (σ_{Err}) are computed for the wave periods considered for the convergence tests: five for the fully-submerged cylinder and ten for the free-surface piercing cylinder. The maximum error (max(Err)) observed is given for the associated wave period (T).*

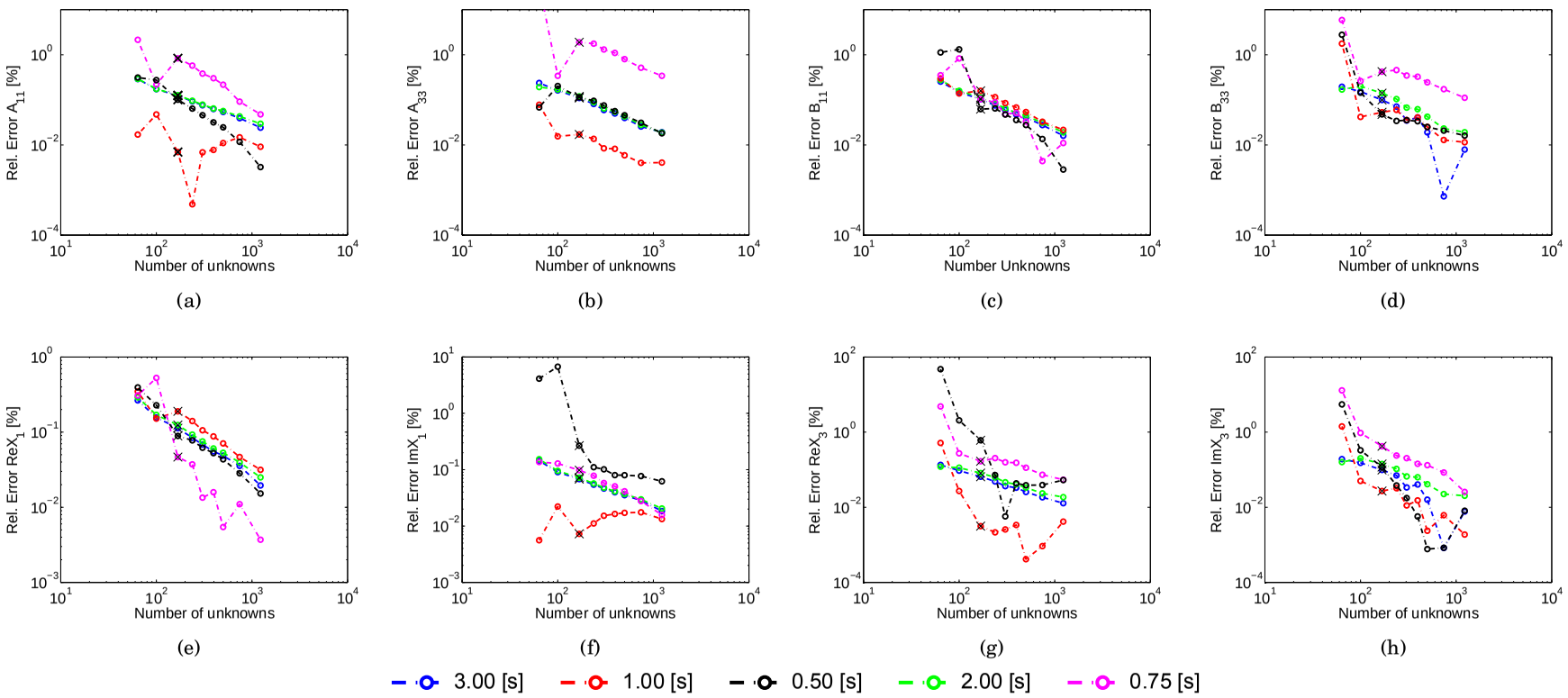

Figure 4.4: *Absolute relative errors associated with the hydrodynamic coefficients and excitation forces at different wave periods when a coarser mesh is compared with a finer with panel size equal to 0.01. The number of unknowns is associated with the discretisation (mesh). The geometry is for the* ***fully submerged cylinder*** *with a width ratio of* $W/D = 1$ *at a submergence ratio of* $H/D = 1.02$*. The different curves are associated different wave periods.*

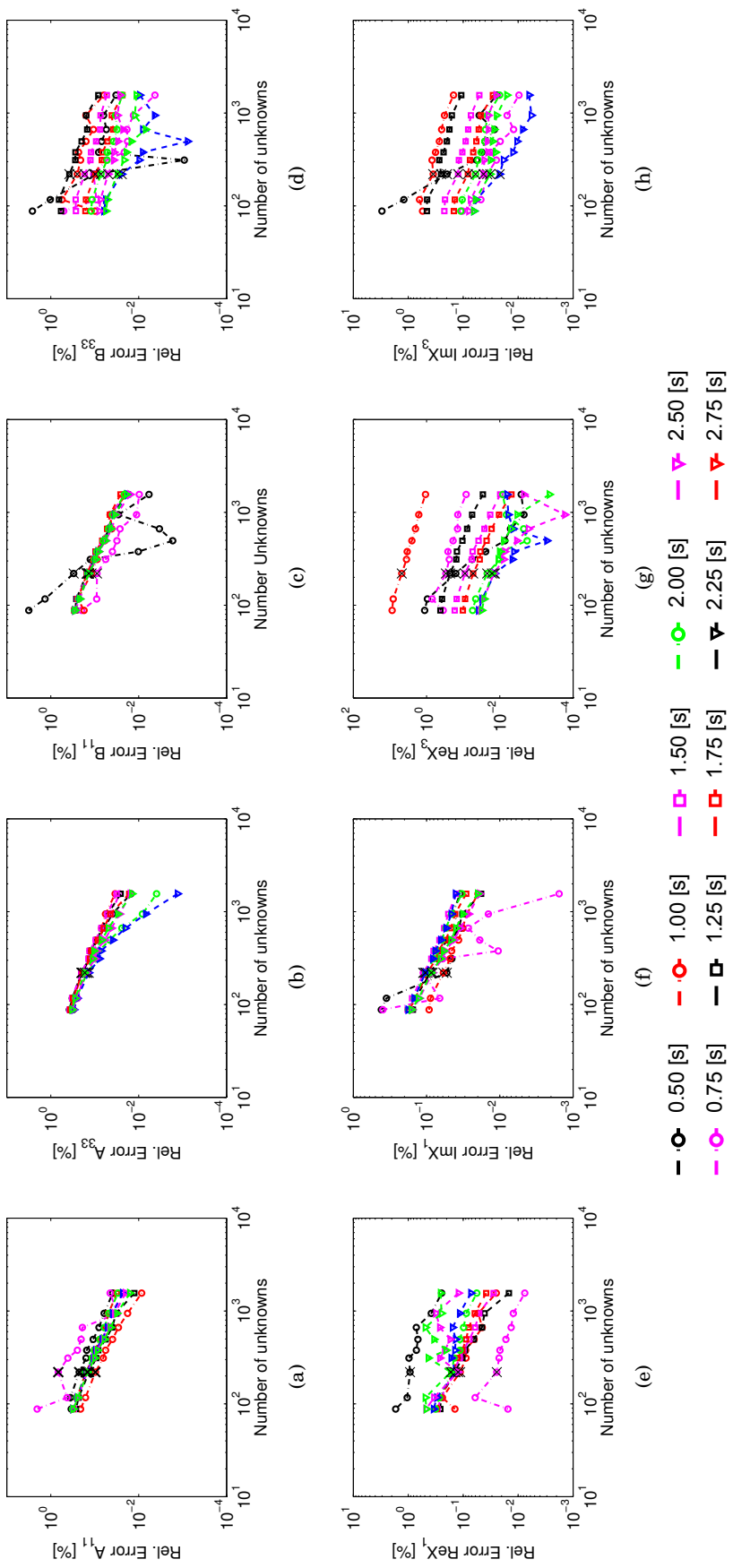

Figure 4.5: *Absolute relative errors associated with the hydrodynamic coefficients and excitation forces at different wave periods when a coarser mesh is compared with a finer with panel size equal to 0.01. The number of unknowns is associated with the discretisation (mesh). The geometry is for the* ***cylinder piercing the free-surface*** *with a width ratio of $W/D = 1$ and a draft of $H/D = 0.85$. The different curves are associated different wave periods.*

4.2 Hydrodynamic forces of a horizontal cylinder - extended study

This section is devoted to the study of the hydrodynamic forces in horizontal cylinders and extends previous studies by looking into the influence of variables which were previously disregarded .

The effect of water depth and width of the cylinder are investigated for different drafts and submergence levels and extended to the case of an a horizontal cylinder with an off-centred axis of oscillation.

Cruz [2009] has shown that the hydrodynamic forces are extremely dependent on the draft ratio and location of the off-centred axis, and thus by choosing an appropriate geometry, the performance of a cylindrical-Duck can be adjusted to closely match that of the the 'classic' solo Duck when operated with an equivalent power-take-off system.

In the present study an alternative approach to Cruz [2009] which computes the hydrodynamic forces and moments at the off-centred axis of oscillation is used. Instead the hydrodynamic forces and moments are computed at the geometrical centre of the cylinder and transformed through analytical functions to those at the off-centred axis of oscillation.

It is assumed a two dimensional description of the motion of a cylinder which moves in surge, heave and rotates in turn of its central axis. For such case, the only radiation impedance matrix components to consider are in heave (Z_{11}) and surge (Z_{33}). This is justified by the geometry and symmetry of the cylinder.

Each term of the radiation impedance matrix is measured in calm water, by forcing a small oscillatory motion in only one direction and measuring the force on the cylinder due to the radiated wave in all directions. Thus, the components of the radiation impedance matrix are written as:

$$Z_{kl} = -\frac{F_{R_k}}{U_l}$$

where U_l and F_{Rk} are the complex amplitudes of the excitation velocity in the direction l and measured force in direction k respectively.

The radiation force results from the integration of the pressure along all submerged area of the cylinder. If the cylinder oscillates around of its own axis no wave is radiated. The pressure integration results in a null force and because of the symmetry of the radiation impedance: $Z_{15} = Z_{35} = Z_{55} = Z_{51} = Z_{53} = 0$. If the cylinder oscillates in heave (direction

3) the wave radiated will be symmetric, and so due to the symmetry of the cylinder only a force in heave will be measurable. Surge oscillations radiate an anti-symmetrical wave and so only a force in surge is measurable: $Z_{13} = Z_{31} = 0$.

The radiation impedance matrix terms can be written as a function of the hydrodynamic coefficients, added mass (A_{kl}) and hydrodynamic damping (B_{kl}) as:

$$Z_{kl} = i\,\omega A_{kl} + B_{kl} \tag{4.20}$$

thus, $A_{ik} = 0$, $B_{ik} = 0$ for $i \neq k = 1,3,5$ and $i = k = 5$ and only the components with $i,k = 1$ or 3 are of interest.

The cases of a fully submerged and surface piercing cylinder are examined separately and should be compared with the results presented by Greenhow and Ahn [1988] (see Figures 2.6 and 2.7).

WAMIT was used to compute the hydrodynamic coefficients and excitation forces. The geometrical dimensions of the scale model cylinder served as a base for the definition of the geometry inputs, thus D = 0.364 m. All computations considered wave periods between 0.5 to 2.975 s spaced by 0.025 s. Three water depths equal to 0.5, 1.2 and 5.0 m representative of shallow, intermediate and deep water conditions were used for nine cylinder widths and sixteen submergence level ratios in a total of 432 different configurations. A schematic drawing of the geometry is presented in Figure 4.6.

In what follows non-dimensional quantities are used. A special note should be drawn to the non-dimensional wave length for deep water which is proportional to the square of the wave period and was used to represent the wave period dependency of the hydrodynamic forces. This quantity is defined as:

$$\lambda_d/D = \frac{g}{2\pi}\frac{T^2}{D} \tag{4.21}$$

The added mass, hydrodynamic damping and excitation force in heave and surge are non-dimensionalised by dividing its actual value by $(\rho\forall)$, $(\rho\forall\omega)$ and $(\rho a g\forall/W)$ respectively.

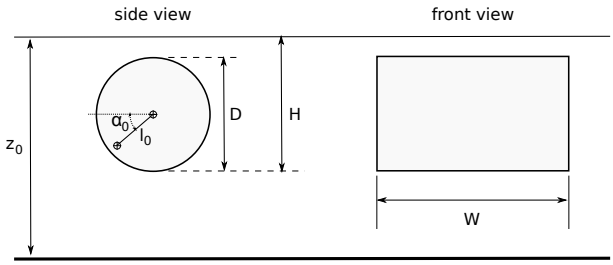

Figure 4.6: *Schematic drawing for the geometry.*

4.2.1 Influence of the width of the cylinder

The hydrodynamic properties of two dimensional fully-submerged horizontal cylinders were studied by Greenhow and Ahn [1988] and are reproduced in Figure 2.6. It is known since Ogilvie [1963] that both added mass and hydrodynamic damping are equal in the surge (horizontal) and heave (vertical) modes for all wave periods.

Figure 4.7 shows the variation of these hydrodynamic coefficients and the excitation forces for a three dimensional cylinder with different widths. The submergence level ratio is fixed and equal to $H/D = 1.10$ and only the deep water case is considered (with $z_0/D = 14$). For reference, the corresponding curves obtained by Greenhow are also shown (blue continuous line).

For cylinders with small widths the hydrodynamic coefficients in surge and heave modes are not equal. However, these are closer to the values given by Greenhow as width increases and they should converge to the same value as $W/D \gg 10$. The modulus of the excitation forces in surge and heave present the same tendency to converge towards the same curve as the width of the cylinder increases and the phases for surge and heave are shifted by about 90°.

Figure 4.8 shows the corresponding results for the free-surface piercing cylinder with a fixed draft ratio of $H/D = 0.90$ in deep water ($z_0/D = 14$) and for the same width ratios. As in the previous case the hydrodynamic coefficients converge towards the two dimensional solutions presented by Greenhow as the width of the cylinder increases.

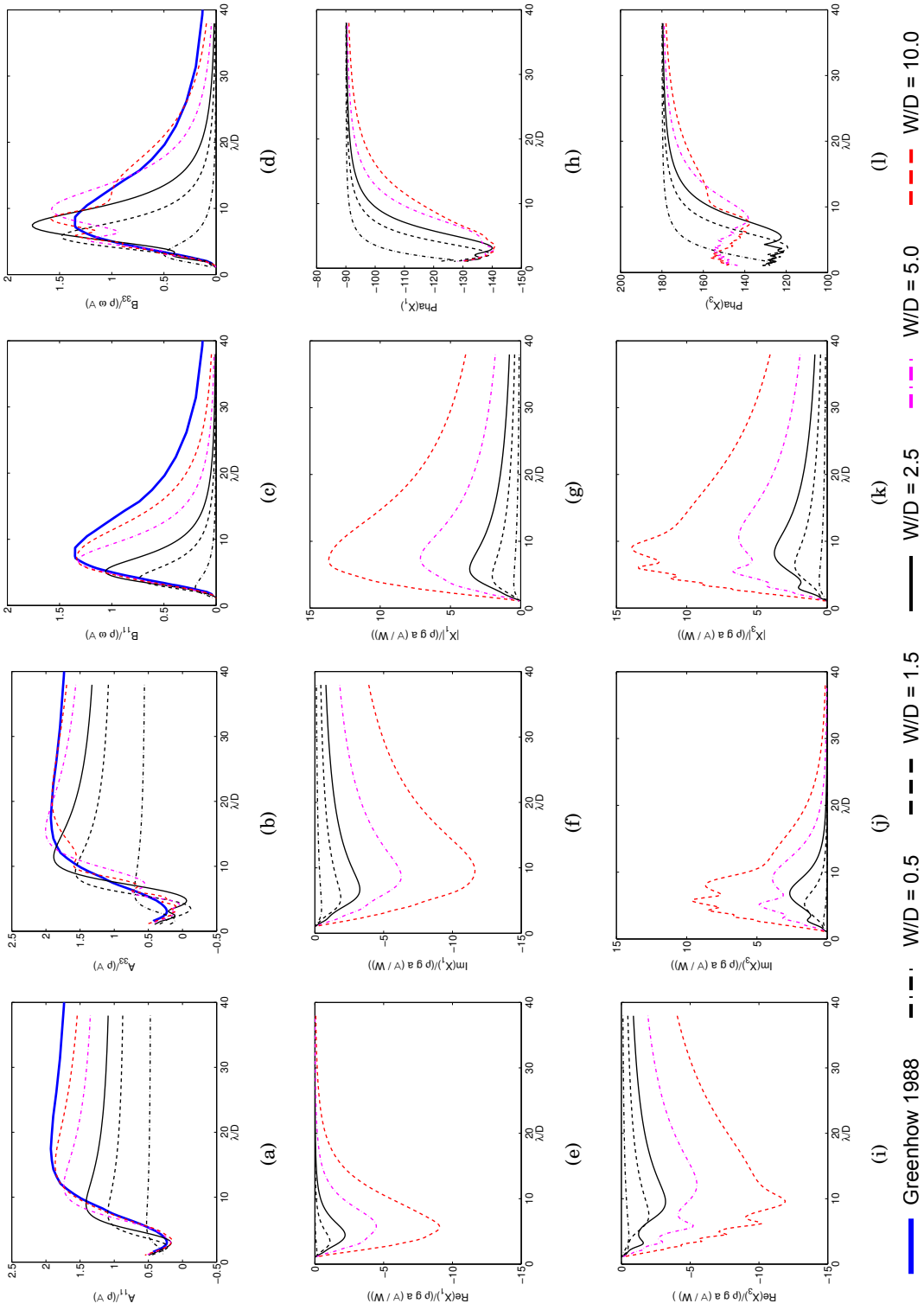

Figure 4.7: *Variation of the hydrodynamic coefficients and excitation forces with the non-dimensional wavelength (λ/D) for the* ***fully-submerged horizontal cylinder*** *(in deep water). Dependence of the width ratio W/D for a fixed submergence level ratio H/D = 1.10. (a) Added mass in surge (b) in heave (c) hydrodynamic damping in surge (d) in heave (e) excitation force in surge, real part (f) imaginary part (g) modulus (h) phase (i) excitation force in heave, real part (j) imaginary part (k) modulus (l) phase.*

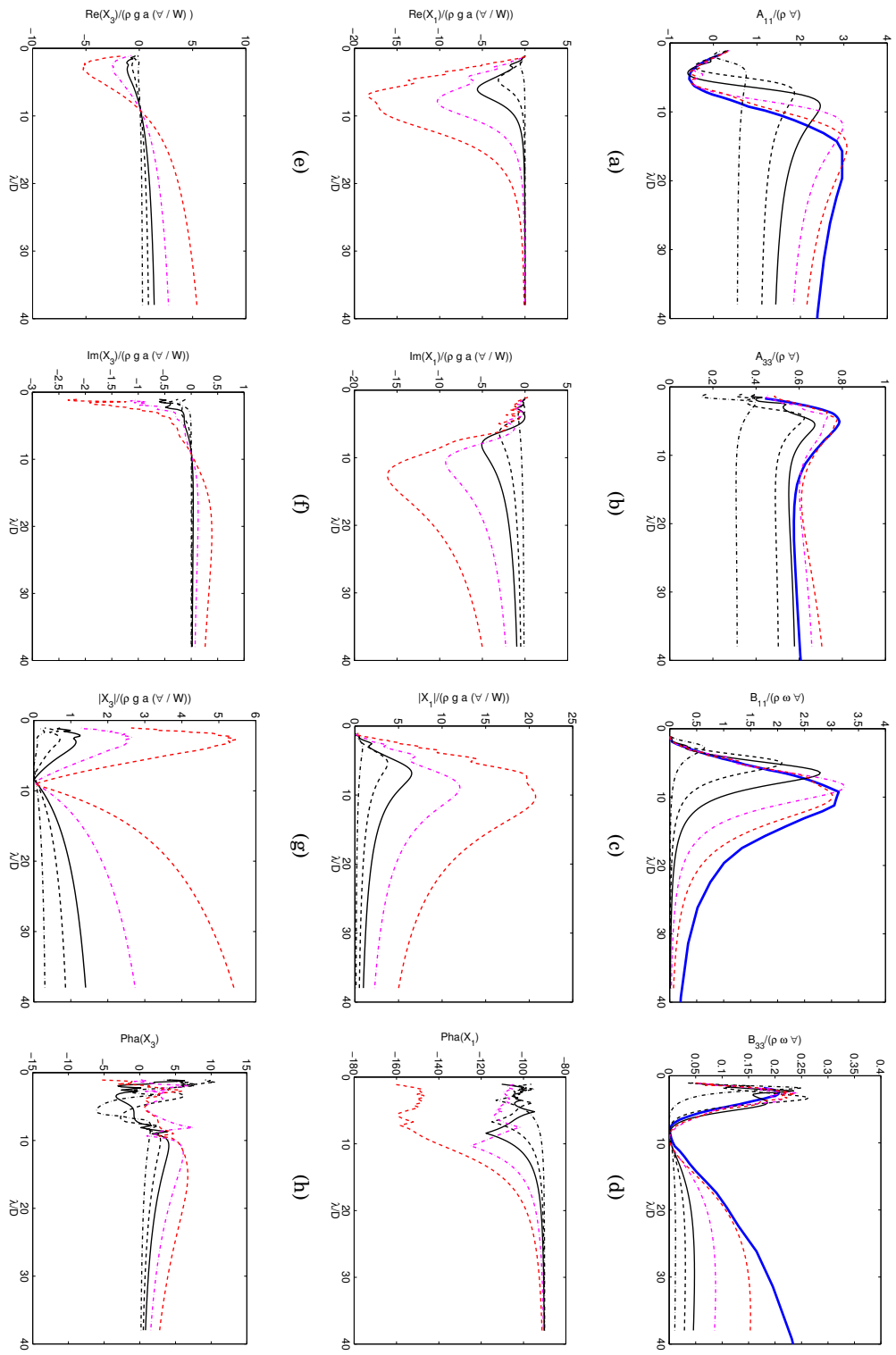

Figure 4.8: *Variation of the hydrodynamic coefficients and excitation forces with the non-dimensional wavelength (λ/D) for the* ***horizontal cylinder piercing the free-surface*** *(in deep water). Dependence of the width ratio W/D for a fixed draft ratio H/D = 0.90. (a) Added mass in surge (b) in heave (c) hydrodynamic damping in surge (d) in heave (e) excitation force in surge, real part (f) imaginary part (g) modulus (h) phase (i) excitation force in heave, real part (j) imaginary part (k) modulus (l) phase.*

4.2.2 Influence of the draft and submergence level

The dependence of the hydrodynamic coefficients and excitation forces with the draft and submergence level ratio (H/D) for a fully-submerged and free-surface piercing cylinder with a fixed width ratio equal to $W/D = 2.5$ when in deep water ($z_0/D = 14$), is shown in Figures 4.9 and 4.10 respectively.

As pointed out in Section 4.2.1, for a fully submerged cylinder with finite width ratio of $W/D < 10$, the hydrodynamic coefficients are different in heave and surge modes. In heave, the hydrodynamic coefficients tend to have higher peak values than in surge and exhibit the same trend as in Greenhow and Ahn [1988].

The hydrodynamic damping vanishes at the shortest and longest wavelengths, when λ_d/D tend to zero and when is greater than 40 (see Figure 4.9(c) and 4.9(d)). A maximum occurs when the incident wavelength is about 5 to 10 times the diameter of the cylinder and increases as the cylinder is closer to the free-surface. When very close to the free-surface ($H/D < 1.1$), its value increases rapidly and fluctuations that look like 'spikes' are identified, specially for heave (Figure 4.9(d)).

The origin of this 'spikes' in not entirely clear. Initially it was though that these were related with the mesh. Consecutive refinements at the top of the cylinder, closer to the free-surface were performed, but the same spikes remained. Evans and Porter [2007] give a close account of singularities that occur in the hydrodynamic damping for certain frequencies when a fully-submerged horizontal cylinder is placed very close to the free-surface, confirming to a high degree of accuracy that the 'hydrodynamic damping does indeed vanish at certain frequencies'. In the present study, the frequency resolution used in the computations is too low to show these singularities, but the 'spikes' give a testimony of this phenomena.

The added mass and excitation forces are related to the hydrodynamic damping through the Kramers-Kroning and Haskind relations respectively. Thus these quantities reflect the wavelength dependencies of the hydrodynamic damping and specifically the 'spikes' identified for the hydrodynamic damping when the cylinder is very close to the free-surface are also present for these quantities.

The added mass tend to finite values at both short and long wavelengths, and attains a minimum and maximum at the wavelengths in between (see Figures 4.9(a) and 4.9(b)). At the longest wavelengths it increases as it is closer to the free-surface. When the cylinder is placed very close to the free-surface, the well known phenomena of negative

added mass is observed as pointed out by many authors [McIver and Evans, 1984, Greenhow and Ahn, 1988].

The modulus of the excitation force vanishes as the wavelength tends to zero and attains a finite value for the very long wavelengths. Between these limits it reaches a maximum which increases as the cylinder is closer to the free-surface (see Figures 4.9(g) and 4.9(k)).

For the free-surface piercing cylinder moving in surge, the hydrodynamic damping shows the same trend characteristic curve as for the fully-submerged cylinder, but with higher peak values for higher drafts ratios ($H/D > 0.70$). The maximum value of the non-dimensional damping in surge is between 0.4 to 4.0 and is attained for wavelengths between 3 to 5 times the diameter of the cylinder, increasing with the draft. For higher drafts ratios ($H/D > 0.90$) the 'spikes' phenomena is also identified as for the fully-submerged cylinder (see Figure 4.10(c)). The added mass in surge is related with the hydrodynamic damping through the Kramers-Kroning relations and as such a similar trend as for the fully-submerged cylinder is found. Negative values of added mass were identified for drafts ratios greater than 0.80 (see Figure 4.10(a)).

The hydrodynamic damping in heave for the surface-piercing cylinder is distinct as found previously for surge or for the fully-submerged case (see Figure 4.10(d)). For drafts ratios less than half ($H/D < 0.5$), at the longer wavelengths it decreases very slowly and attains higher values for lower draft ratios, and tends to vanish as the wavelength tend to zero. For drafts ratios greater than half ($H/D > 0.5$) at the long wavelengths it follows the same asymptotic behaviour as for $H/D < 0.5$, whereas the asymptotic behaviour at shorter wavelengths ($\lambda_d \rightarrow 0$) it is not very clear, as if it tends to a finite value or zero. An important feature of these curves that can be seen for draft ratios greater than 0.70 is a singularity of the hydrodynamic damping that occurs for certain wavelengths and which depends on the draft ratio. The nature of these singularities seams to be different from the 'spikes' phenomena, also found at drafts close to the fully-submergence, as for these the hydrodynamic damping vanishes in a smoothly and continuously way whereas for the 'spikes' it present a very fast and abrupt variations.

Trough the Kramers-Kroning and Haskind relations the added mass and excitation force in heave reflect the remarks given for the hydrodynamic damping. For drafts ratios less than half, the added mass decreases consistently with the increasing draft showing a minimum value at short wavelengths ($\lambda_d/D < 3$). At draft ratios greater than 0.80, the added mass attains a local minimum and maximum showing a closer trend to the surge and fully submerged cylinder. No negative added mass values were observed.

The absolute value of the excitation force for draft ratios less than 0.60, show a 'logarithmic like' trend. For draft ratios greater than 0.7 a singularity occurs for different wavelengths which depend on the draft.

4.2.3 Influence of the water depth

The dependences of the hydrodynamic coefficients and excitation forces with the water depth (z_0) for a cylinder with a fixed width ratio equal to W/D = 2.5, when fully-submerged and piercing the free-surface, are plotted for three different submergence levels (H/D) in Figures 4.11 and 4.12 respectively.

In linear theory the shallow and deep water approximations depend on the ratio between depth and the wavelength. Deep water conditions apply when the water depth is larger than half the wavelength and shallow water conditions apply when is less than 1/20 of the wavelength. For consistency with the results from the previous sections, the dependence of the hydrodynamic coefficients and excitation force with the wave period is given in terms of the deep water wavelength (λ_d/D) which is proportional to the square of the wave period. It should be noted that in general λ_d is larger than the actual wavelength when intermediate and shallow water conditions apply. Three water depths (z_0) equal to 0.5, 1.2 and 5 m were considered in the present study, corresponding to water depth to diameter ratios (z_0/D) equal to 1.4, 3.3 and 14.0 respectively. Three different drafts and submergences were taken into account. For the fully submerged cylinder, these are equal to H/D = 1.02, 1.10 and 1.20, whereas for the free-surface piercing cylinder these are equal to H/D = 0.5 (half submerged), 0.7 and 0.85.

The hydrodynamic damping in surge (Figure 4.11(c)) for a water depth ratio equal to z_0/D = 3.3 is very close to the values associated with deeper water with z_0/D = 14.0. For the shallower water with z_0/D = 1.4, the damping has a slower variation and at the longer wavelengths it tends to a finite value. The added mass and the absolute value of the excitation force in surge reflect the behaviour of the hydrodynamic damping. As such the added mass for the shallower water depths (z_0/D = 1.4) shows comparatively higher values at the longer wavelengths (Figure 4.11(a)). The absolute value of the excitation force for the shallower water depths ($z0/D$ = 3.3 and 1.4) tend to higher values at the longer wavelengths (Figure 4.11(g)).

The hydrodynamic damping in heave for all water depths vanishes at both very small and very large wavelengths and it exhibits smaller values of damping for the shallower water depths (Figure 4.11(d)). The added mass in heave tends to the same value at

sorter and longer wavelengths regardless of the water depth (Figure 4.11(b)), whereas the absolute value of the excitation force in heave has the same value at the smaller wavelengths tending to very close values at the longer wavelengths exhibiting smaller values for shallower water depths (Figure 4.11(k)).

For the free-surface piercing cylinder, the variation of the hydrodynamic damping in surge with water depth is similar to that of a fully-submerged cylinder and as such the same remarks apply (Figure 4.12(c)). These also apply to the added damping and absolute value of the excitation force (Figures 4.12(a) and 4.12(g)). In heave, the hydrodynamic damping shows a slower variation for the shallower water depths and so at these it presents higher values (Figure 4.12(d)). The added mass and absolute value of the excitation force does not present such high discrepancies and at the longer and shorter wavelengths present close values for the different water depths (Figures 4.12(b) and 4.12(k)).

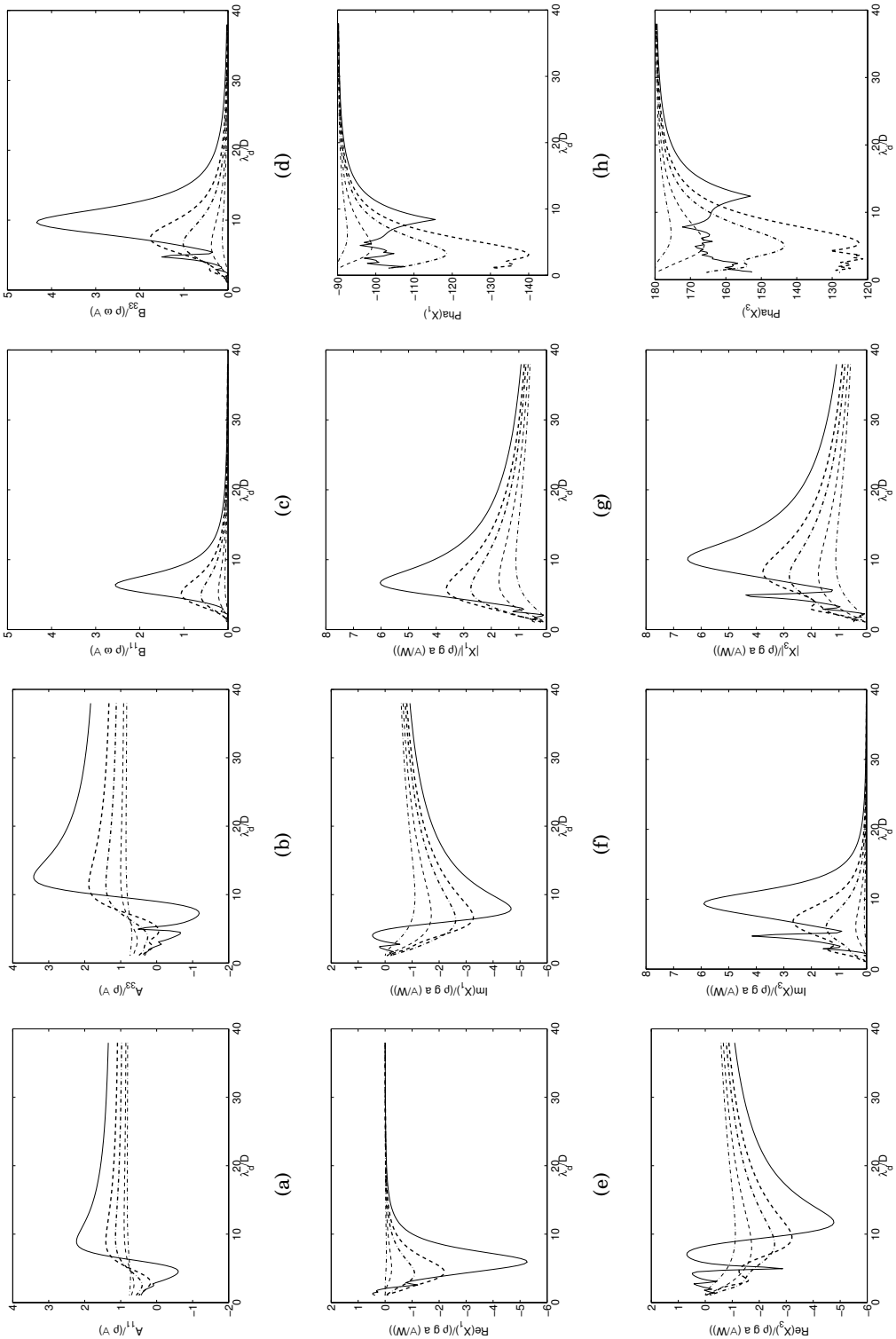

Figure 4.9: *Variation of the hydrodynamic coefficients and excitation forces with the non-dimensional wavelength (λ_d/D) for the* ***fully-submerged horizontal cylinder*** *with a fixed width ratio equal to $W/D = 2.5$ (in deep water). Dependence on the submergence ratio H/D . (a) Added mass in surge (b) in heave (c) hydrodynamic damping in surge (d) in heave (e) excitation force in surge, real part (f) imaginary part (g) modulus (h) phase (i) excitation force in heave, real part (j) imaginary part (k) modulus (l) phase.*

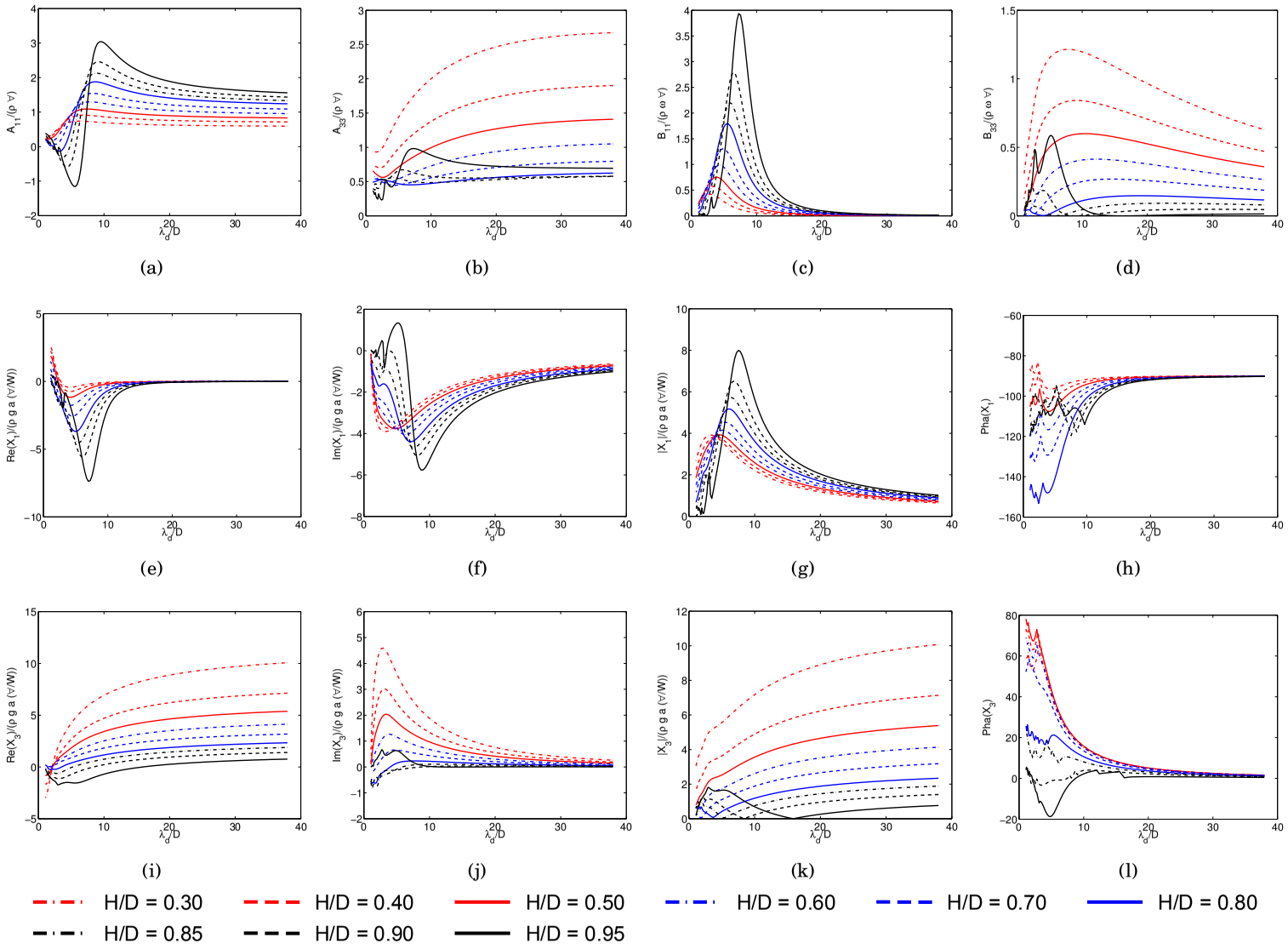

Figure 4.10: *Variation of the hydrodynamic coefficients and excitation forces with the non-dimensional wavelength (λ_d/D) for the* ***horizontal cylinder piercing the free-surface*** *with a fixed width ratio equal to $W/D = 2.5$ (in deep water). Dependence on submergence ratios H/D. (a) Added mass in surge (b) in heave (c) hydrodynamic damping in surge (d) in heave (e) excitation force in surge, real part (f) imaginary part (g) modulus (h) phase (i) excitation force in heave, real part (j) imaginary part (k) modulus (l) phase.*

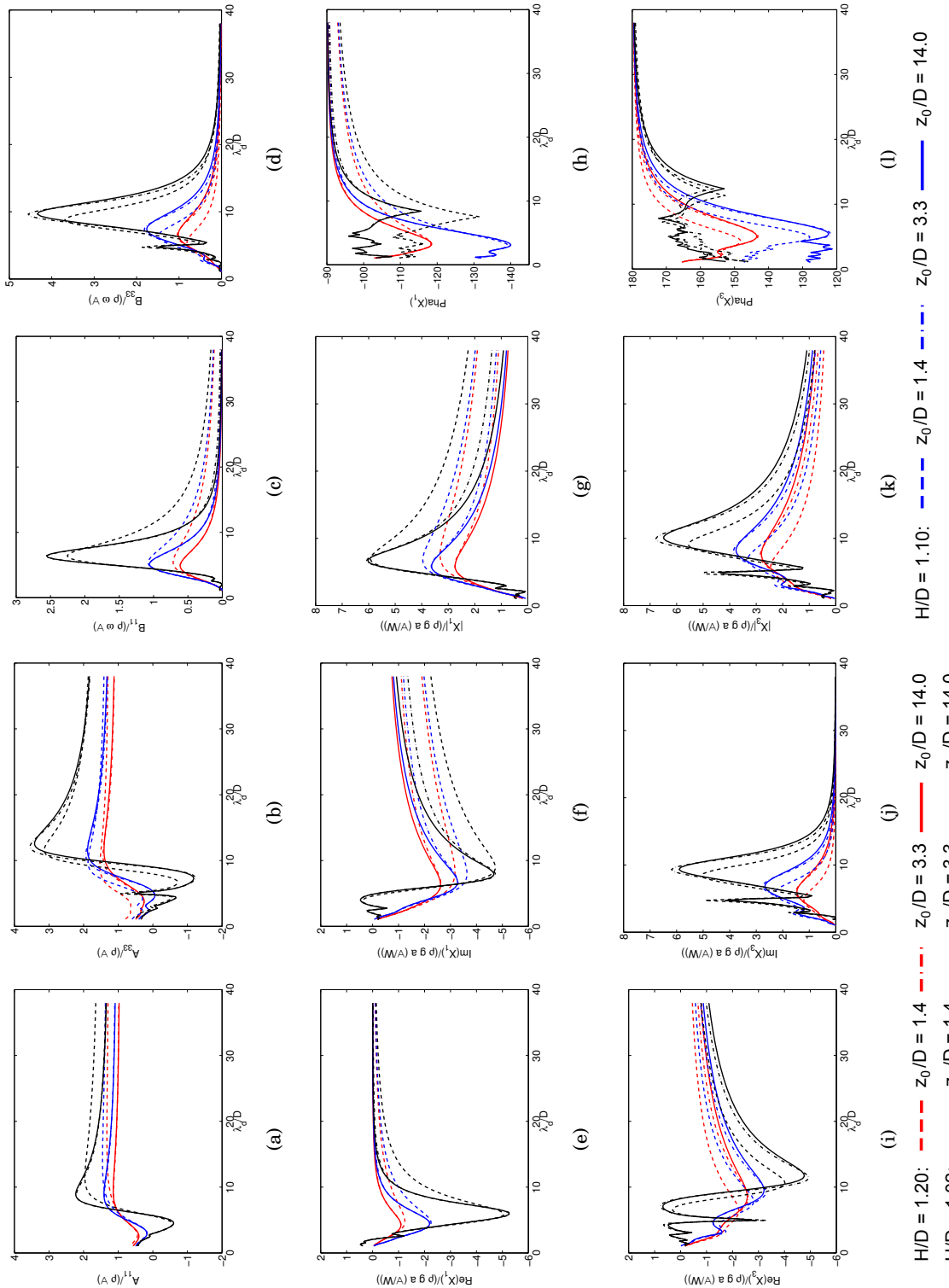

Figure 4.11: *Variation of the hydrodynamic coefficients and excitation forces with non-dimensional wavelength in deep water (λ_d/D) for the* ***fully-submerged horizontal cylinder*** *with a fixed length ratio of $W/D = 2.5$. Dependence on the water depth ratio Z_0/D for three submergence ratios $H/D = 1.20, 1.10, 1.02$. (a) Added mass in surge (b) in heave (c) hydrodynamic damping in surge (d) in heave (e) excitation force in surge, real part (f) imaginary part (g) modulus (h) phase (i) excitation force in heave, real part (j) imaginary part (k) modulus (l) phase.*

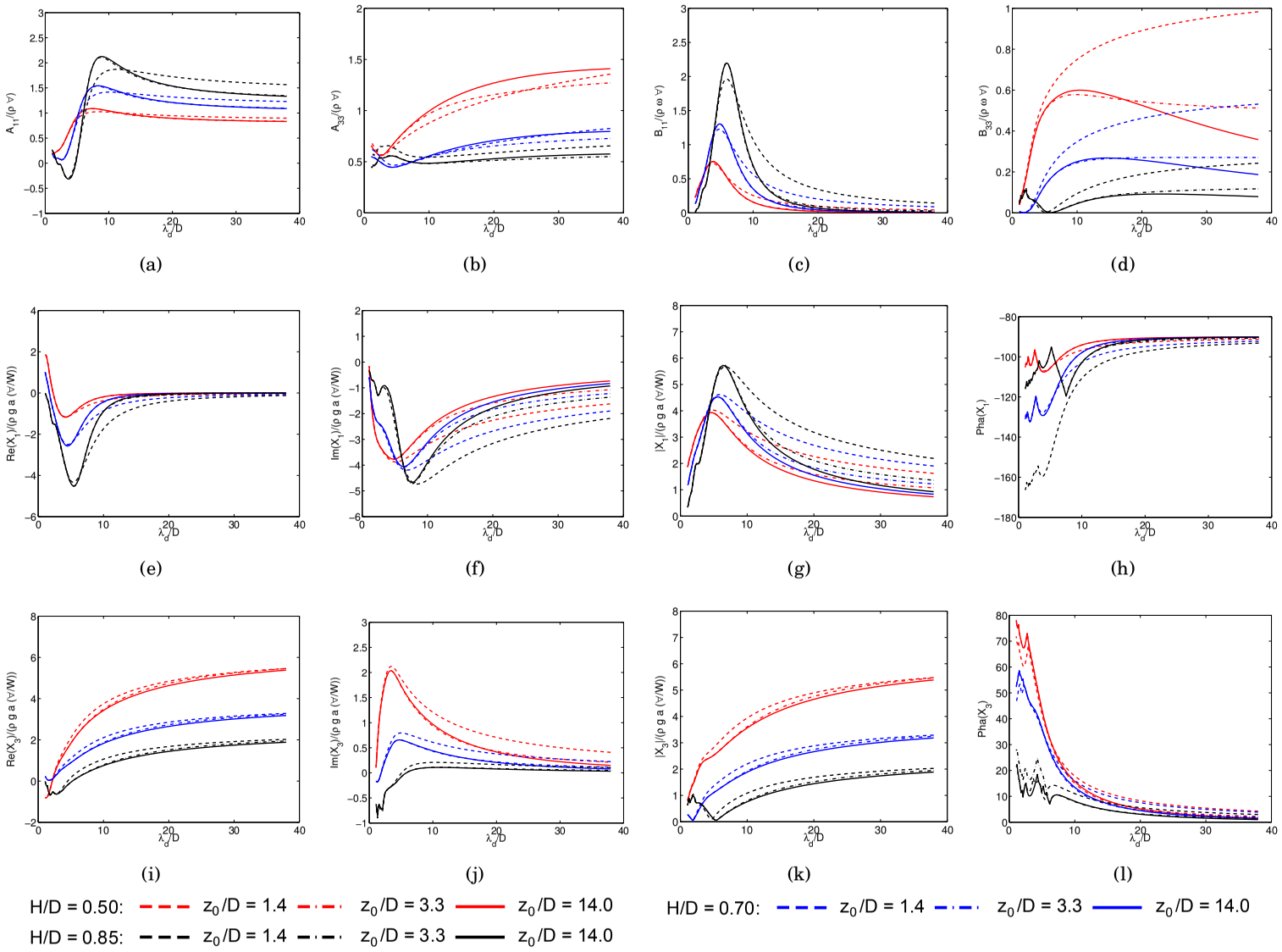

Figure 4.12: *Variation of the hydrodynamic coefficients and excitation forces with the non-dimensional wavelength in deep water (λ_d/D) for the* ***horizontal cylinder piercing the free-surface*** *with a fixed width ratio of $W/D = 2.5$. Dependence on the water depth ratio Z_0/D for three submergence ratios $H/D = 0.50, 0.70, 0.85$. (a) Added mass in surge (b) in heave (c) hydrodynamic damping in surge (d) in heave (e) excitation force in surge, real part (f) imaginary part (g) modulus (h) phase (i) excitation force in heave, real part (j) imaginary part (k) modulus (l) phase.*

4.3 Hydrodynamic forces on an off-centred horizontal cylinder

The hydrodynamic forces experienced by a horizontal cylinder piercing the water surface with an off-centred axis of oscillation were studied in detail by Cruz and Salter [2006]. It was shown that the hydrodynamic coefficients, both added mass and hydrodynamic damping and the excitation force are extremely dependent on the configuration chosen, i.e on the draft and location of the off-centred axis.

The approach taken here is rather different. Instead of using *WAMIT* to compute directly the hydrodynamic forces at the off-centred axis, the knowledge of these forces at the centre of the cylinder is used to derive the forces and moments at an off-centred location of the axis. This formulation takes into account general transformation formulas which relate the forces and moments at two different origins in the body. The formulas are derived in Appendix A and presented in its final form applied to the specific case of the off-centred cylinder in Table 4.4.

Added Mass at R:	**Hydro. Damping at R:**	**Hydro. Stiffness at R:**	**Excitation Force at R:**
$A'_{11} = A_{11}$	$B'_{11} = B_{11}$		$X'_1 = X_1$
$A'_{15} = l_0 \sin\alpha_0 A_{11}$	$B'_{15} = l_0 \sin\alpha_0 B_{11}$		$X'_3 = X_3$
$A'_{33} = A_{33}$	$B'_{33} = B_{33}$	$C'_{33} = C_{33}$	$X'_5 = l_0 \sin\alpha_0 X_1 - l_0 cos\alpha_0 X_3$
$A'_{35} = -l_0 \cos\alpha_0 A_{33}$	$B'_{35} = -l_0 \cos\alpha_0 B_{33}$	$C'_{35} = C_{35} + l_0 \cos\alpha_0 C_{33}$	
$A'_{55} = l_0^2 \sin^2\alpha_0 A_{11} + l_0^2 \cos^2\alpha_0 A_{33}$	$B'_{55} = l_0^2 \sin^2\alpha_0 B_{11} + l_0^2 \cos^2\alpha_0 B_{33}$	$C'_{55} = 2l_0 \cos\alpha_0 C_{35} + l_0^2 \cos^2\alpha_0 C_{33} + C_{55}$	

Table 4.4: *Transformation formulas for the horizontal cylinder that relate the hydrodynamic forces at its geometric centre with the forces and moments at an off-centred axis of oscillation.*

Figure 4.13 shows a comparison for the added mass, damping and absolute value of the excitation wave force in pitch at an off-centred axis obtained with both approaches, through direct calculation with *WAMIT* and by using the formulas in Table 4.4. For the three plots, the two curves are perfectly superimposed showing that the two approaches are indistinct.

In what follows, the position of the off-centred axis is described by the radial distance to its centre l_0 and the angle between the horizontal plane and the plane that contains the off-centred axis and the axis of the cylinder α_0, as shown in Figure 4.6.

The hydrodynamic coefficients and excitation forces for different locations of the off-centred axis are plotted for the fully-submerged and surface piercing cylinders in

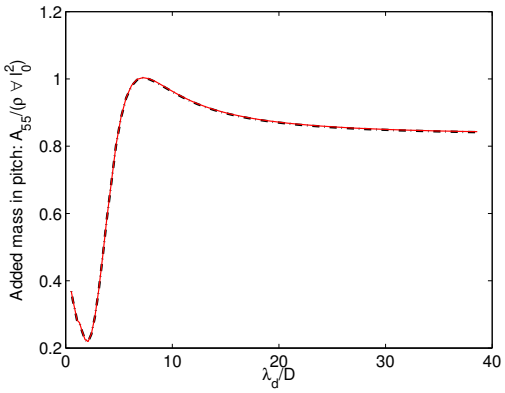

(a)

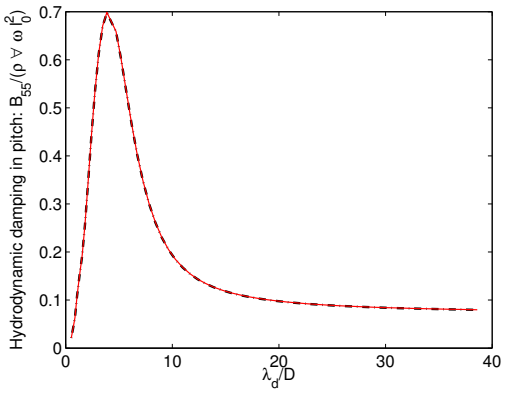

(b)

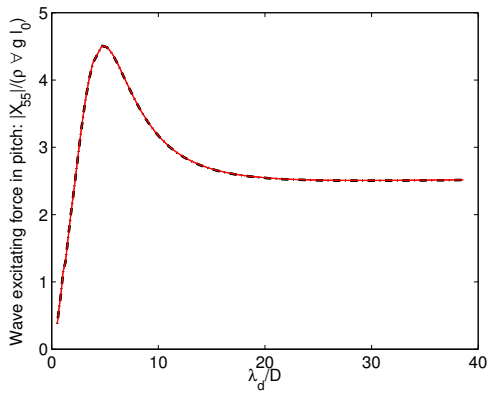

(c)

Figure 4.13: *(a) Added mass, (b) hydrodynamic damping and (c) wave excitation force in pitch at an off-centred axis located at* $\alpha_0 = 55°$, $l_0/(D/2) = 0.60$ *computed directly at the axis (black discontinuous line) and computed at the centre of the cylinder and transform to the same location through the formulas in Table 4.4 (red continuous line).*

Figures 4.14 and 4.15. All plots refer to a water depth ratio of $z_0/D = 14$, for a cylinder with fixed width ratio equal to $W/D = 2.5$. The submergence level ratios are equal to $H/D = 1.10$ and $H/D = 0.85$ for the fully-submerged and surface piercing cylinder respectively.

All quantities in the plots are non-dimensional. The added mass, hydrodynamic damping and excitation force in pitch are non-dimensionalised by dividing the actual value by $(\rho \forall l_0^2)$, $(\rho \forall \omega l_0^2)$ and $(\rho g a \forall / W l_0)$ and for the added mass and damping crossed terms by $(\rho \forall l_0)$, $(\rho \forall \omega l_0)$ respectively. At the off-centred axis, the non-dimensional quantities do not depend on the distance to the centre of the cylinder (l_0) and only depend on the angle α_0 (as can be seen in the formulas of Table 4.4).

All plots present complex dependencies in α_0 and the behaviour for the curves of the fully-submerged and free-surface piercing cylinder are very different. In what follows, the attention is focused in the pitch mode at the off-centred axis of the cylinder.

For the fully-submerged cylinder, the hydrodynamic damping curve vanishes for the smallest and larger wavelengths and has a maximum at wavelengths between 5 to 7.5 times the diameter of the cylinder, increasing and shifting towards larger wavelengths with decreasing α_0(Figure 4.14(f)). The absolute value of the excitation force vanishes at the smallest wavelengths and converges for a finite value at the largest wavelength regardless of the angle α_0 reaching a maximum at wavelengths six to eight times the diameter of the cylinder and which depend on the angle α_0 (Figure 4.14(i)). The added mass in pitch at the off-centred axis has a minimum and a maximum and depends on the angle α_0 (Figure 4.14(c)).

The hydrodynamic damping in pitch for the free-surface piercing cylinder is shown in Figure 4.15(f). It vanishes at the shortest wavelengths and converges towards zero for the very largest wavelengths. It has a maximum at about six times the diameter of the cylinder which decreases with decreasing values of the angle α_0 vanishing as this angle tends towards zero. The excitation moment is zero at the wavelength which tends towards zero and has finite value for the longest wavelengths. It has a maximum when wavelength of the incident wave is about six times the diameter of the cylinder. This maximum decreases with decreasing values of the angle α_0 and minimum is attain at very small wavelengths which shifts towards the larger with decreasing values of α_0 (Figure 4.15(i)). The added mass in pitch is shown in Figure 4.15(c). It converges towards a finite value at both ends of the wavelength range and has a minimum and a maximum other than for the very small angles α_0.

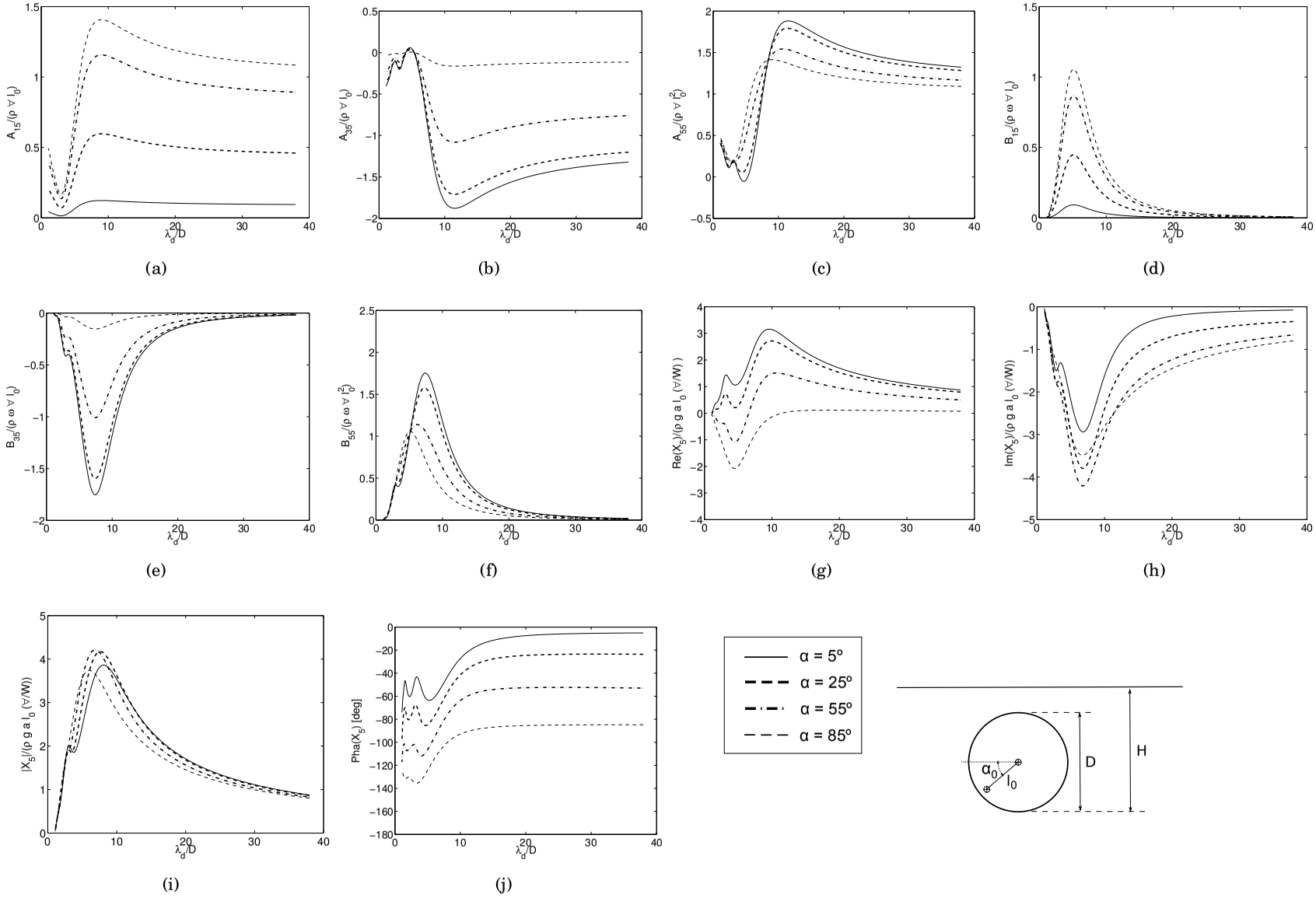

Figure 4.14: *Variation of the hydrodynamic coefficients and excitation forces with the non-dimensional wavelength (λ_d/D) for the* ***fully-submerged horizontal cylinder*** *with an off-centred axis of oscillation. The plots refer to deep water for a fixed submergence level and cylinder width ratio equal to $H/D = 1.10$ and $W/D = 2.5$ respectively.*

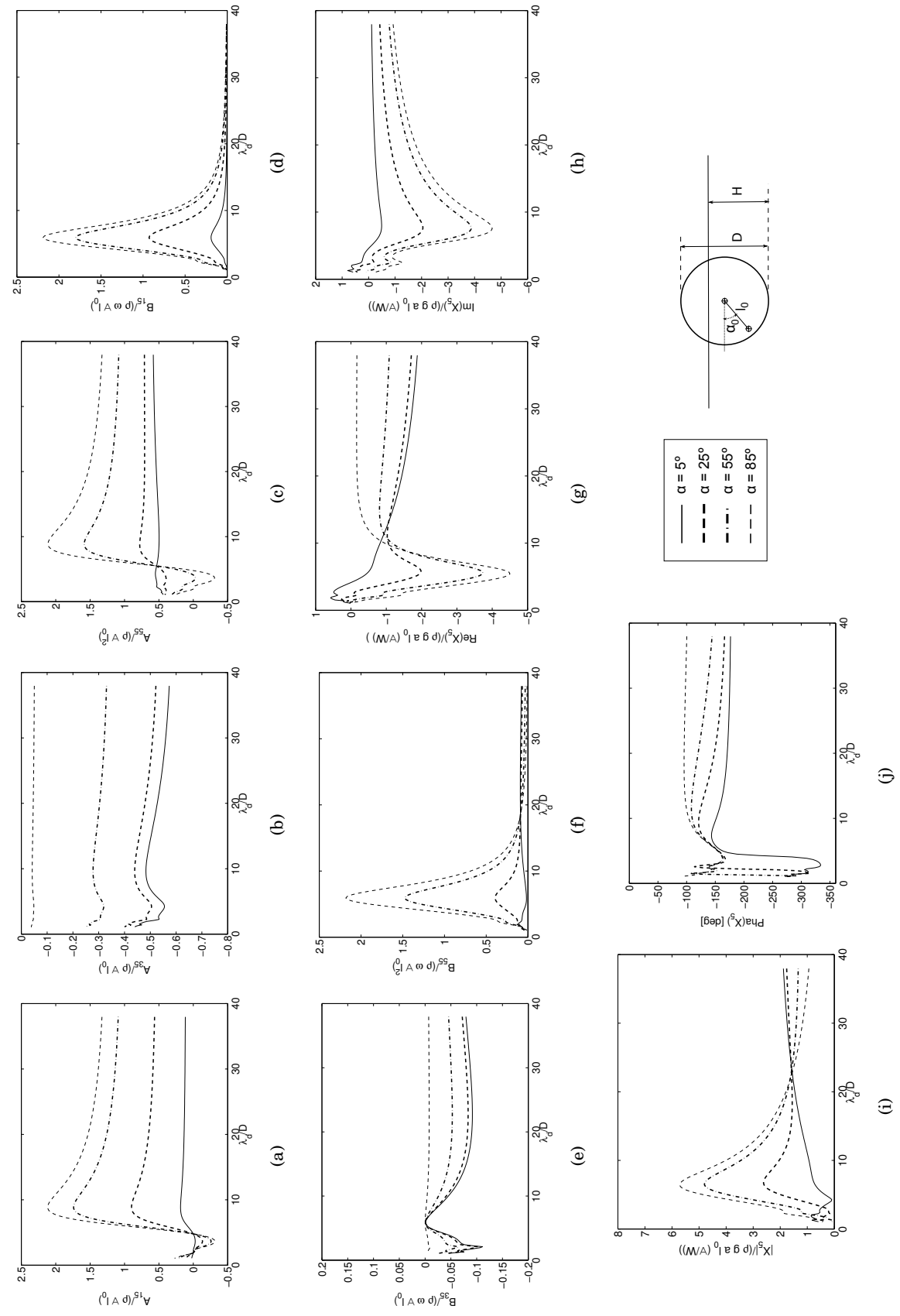

Figure 4.15: *Variation of the hydrodynamic coefficients and excitation forces with λ_d/D for the* ***cylinder piercing the free-surface*** *with an off-centred axis of oscillation. All plots are for deep water with a fixed submergence level ratio and width ratio equal to $H/D = 0.85$ and $W/D = 2.5$ respectively.*

4.4 One degree of freedom model

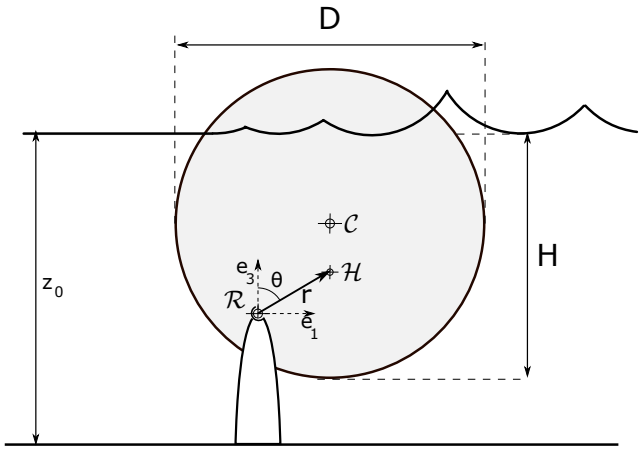

Figure 4.16: *Schematic drawing for the one degree of freedom model.*

In this section the hydrodynamic forces computed in the previous section are used to derive the equations of motion for a horizontal cylinder which oscillates about an off-centred axis.

This system is represented in Figure 4.16. It is assumed that the cylinder with a diameter of D and width of W is submerged at a certain draft H and oscillates with small harmonic motion in turn of an axis that passes through point $\mathscr{R}$. The system has only one degree of freedom and energy is taken through a linear power-take-off. The linear potential flow theory assumptions associated with the hydrodynamic forces discussed in Section 4.1.1 apply as well to this case.

WAMIT has incorporated a solver to compute directly the motions of a system under hydrodynamic interaction in a fluid domain with a free-surface condition. This was described in Section 4.1.3 for the special case of an unrestrained body. Six equations of motion associated with each of the six degrees-of-freedom are solved and the linear and angular displacements obtained. For the specific case of a system restrained to move in only one degree-of-freedom, only one equation is required to be solved and the direct solver of *WAMIT* requires the specification of the mode of motion of interest. In the present case only pitch at the off-centred axis.

However, in this work the equation of motion is solved separately by equating the inertial to the applied moments. The solution can then be verified with the one obtained by *WAMIT*.

The moment along the off-centred axis is given by $(\vec{m})_2 = J_{22}\ddot{\theta}(t)$, where J_{22} is the moment of inertia at the axis and $\ddot{\theta}(t) = \dot{u}_5 = \ddot{\xi}_5$ the angular acceleration.

The equation of motion in time domain for such system can be written as:

$$J_{22}\ddot{\theta}(t) = m_d + m_h \tag{4.22a}$$

where:

$$m_d = -K\dot{\theta} = -K\dot{\xi}_5 \tag{4.22b}$$

$$m_h = \left(\vec{f}_h\right)_5 = \left[\vec{f}_R + \vec{f}_X + \vec{f}_C\right]_5 \tag{4.22c}$$

are the linear control torque of the power take off (m_d) and the hydrodynamic moment in pitch along the the off-centred axis (m_h), given by Equations (4.11), (4.14) and (4.8e) respectively.

Considering small harmonic motions in the pitch mode, the angular displacements, velocity and acceleration are given by Equation (4.2), and substituting into the equation of motion (4.22a), the frequency domain equation is obtained:

$$(Z_{55} + K)\,U_5 = a\,X_5 \tag{4.23a}$$

where Z_{55} is the radiation impedance in pitch mode given by:

$$Z_{55} = i\,\omega\left(J_{22} + A_{55} - \frac{C_{55}}{\omega^2}\right) + B_{55} \tag{4.23b}$$

and U_5 is the complex amplitude of the velocity $U_5 = i\,\omega\,\hat{\xi}_5$.

Following Evans and Linton [1993] the mean power absorbed by the device over an integer number of wave cycles is given by Equation (2.1d):

$$\begin{aligned}\overline{P_{abs}} &= -\frac{1}{T}\int_0^T f_d(t)\,u_5(t)dt = -\frac{1}{2}Re\left\{{F_d}^*\,U_5\right\} = \frac{1}{4}\left(K + K^*\right)|U_5|^2 \\ &= \frac{a^2\,|X_5|^2}{8B_{55}}\left(1 - \frac{|K - Z_{55}^*|^2}{|K + Z_{55}|^2}\right)\end{aligned} \tag{4.24}$$

The maximum mean absorbed power ($\overline{P_{max}}$) is achieved at resonance for a particular wavelength, or for a range of wavelengths if a particular control function is imposed to the motion through the use of a sophisticated power-take-off. To achieve this, it

is required the control term of the force (K) to be equal to the complex conjugate of the radiation damping ($K = Z_{55}^*$) for all the incoming waves. Such control strategy is commonly referred as complex conjugate control and it implies the constant adjustment of control term to match the hydrodynamic added mass and damping which are strongly dependent on the wave period. $\overline{P_{max}}$ is then given by Equation (2.1b):

$$\overline{P_{max}} = \frac{|X_5|^2}{8B_{55}}$$

If the control force consists only on pure damping, K is a real number and the mean absorbed power is given by Equation (2.2a):

$$\overline{P_{abs}} = \frac{|X_5|^2}{4(B_{55}+|Z_{55}|)}\left(1-\frac{(K-|Z_{55}|)^2}{|K+Z_{55}|^2}\right)$$

The maximum absorbed power is then achieved when the control term is equal to the absolute value of the radiation impedance ($K = |Z_{55}|$), and is given by Equation (2.2c):

$$\overline{P_{max}} = \frac{|X_5|^2}{4(B_{55}+|Z_{55}|)}$$

4.5 Optimisation in one degree of freedom

This section gives an insight on the optimisation of the design for the horizontal cylinder with off-centred axis. This analysis is restricted to cylinders which only move in pitch (one degree of freedom system) and the attention is focused at cylinders with widths ratios equal to $W/D = 2.5$ and to water depths ratios of $z_0/D = 14$. Nevertheless, this study can be extended to cylinders of different widths and water depths by taking into account the associated hydrodynamic forces.

Both cases of a fully-submerged and surface-piercing cylinder are considered. The optimisation variables that enter into this analysis are: the diameter of the cylinder (D), the draft or submergence ratio (H/D), the location of the off-centred axis (α_0 and l_0) and the mass distribution.

The maximum average power that a wave-energy-converter can absorb from regular waves is given by Equation (2.1b) ($\overline{P_{max}} = |X_5|^2/(8B_{55})$) and is achieved when the velocity of the device is exactly in phase with the excitation force with an optimum amplitude equal to half of the ratio of the excitation force by the hydrodynamic damping (Equation (2.1c): $U_O = 1/2\,X_5/B_{55}$).

Taking the hydrodynamic coefficients and excitation forces in heave and surge at the centre of the horizontal cylinder, computed in Section 4.2, these are converted to the off-centred axis through the formulas given in Table 4.4. Recalling those relationships, the excitation force and hydrodynamic damping at the off-centred axis are given by:

$$X_5' = l_0 \sin\alpha_0 X_1 - l_0 \cos\alpha_0 X_3 \tag{4.25a}$$

$$B_{55}' = l_0^2 \sin^2\alpha_0 B_{11} + l_0^2 \cos^2\alpha_0 B_{33} \tag{4.25b}$$

Substituting Equation (4.25) into (2.1b) and (2.1c), the maximum mean absorbed power and optimum velocity amplitude of the device are given as:

$$\overline{P_{max}} = \frac{\sin^2\alpha_0 X_1^2 + \cos^2\alpha_0 X_3^2 - 2\cos\alpha_0 \sin\alpha_0 X_1 X_3}{8\left(\sin^2\alpha_0 B_{11} + \cos^2\alpha_0 B_{33}\right)} \tag{4.26a}$$

$$U_O = i\,\omega\,\xi = \frac{1}{2\,l_0}\,\frac{\cos\alpha_0 X_3 - \sin\alpha_0 X_1}{\sin^2\alpha_0 B_{11} + \cos^2\alpha_0 B_{33}} \tag{4.26b}$$

The above expressions show that the distance at which the off-centred axis is placed (l_0) is not important regarding the maximum average absorbed power and theoretically this value can be achieved for every distance. However, as this distance decreases, higher velocity amplitudes of oscillation are required imposing a practical limit to the value that l_0 can take.

The above expressions also show that the angle at which the off-centred axis is placed relative to the horizontal plane (α_0) controls the contribution of the heave and surge modes of motion to the maximum mean absorbed power. If the angle is equal to zero, only heave is contributing to the mean absorbed power, whereas if the angle is equal to 90° only the surge mode contribute instead.

The value of the optimum angle for the location of the off-centred axis (α_O) which maximizes the mean absorbed power is obtained by solving the equation in α_0: $\partial\overline{P_{max}}/\partial\alpha_0 = 0$. However, the result of this is a transcendental equation which can be solved by numerical methods provided a good initial guess for α_O is given.

As the hydrodynamic forces, the value of α_O also depends on the wave period of the incident wave. Figure 4.17 shows the variation of α_O with the wavelength ratio (λ_d/D) for both cases of a fully-submerged and free-surface piercing horizontal cylinder and taking into account a width ratio of $W/D = 2.5$ and a water depth ratio of $z_0/D = 14$.

An argument that was used to provide an initial estimation for the value of α_0, in order to solve for the root of the transcendental equation is as follows:

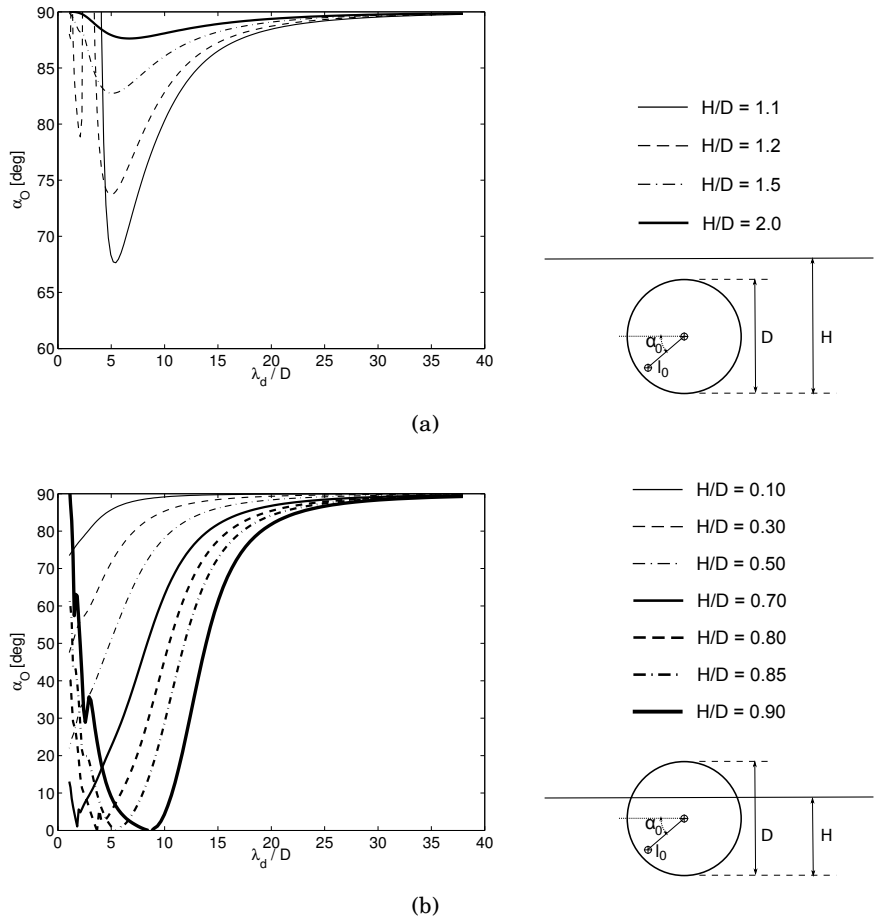

Figure 4.17: *Optimum value of α_0 to ensure maximum mean absorbed power given by Equation* (4.26) *for different drafts and submergence levels of an horizontal cylinder with width ratio of $W/D = 2.5$ and water depth ratio of $z_0/D \approx 14$: (a) fully-submerged and (b) free-surface piercing case.*

As it is understood since Evans [1976], a good wave energy absorber should have the ability to generate waves in only one direction. The hydrodynamic damping is related with the amplitudes of the waves at both sides in the far-field by the two-dimensional Haskind relation: $B = \frac{1}{2}\rho\omega\left(|a^+|^2 + |a^-|^2\right)W$. For a cylinder (which is axi-symmetric), heave oscillation generate symmetric waves whereas surge oscillations generate anti-symmetric waves and so a suitable combination of these motions in a particular proportion should generate waves in only one direction.

To ensure that the amplitudes of the symmetric and anti-symmetric waves generated in the far-field have the same amplitudes it is necessary to have both contributions from heave and surge modes being the same. This can be achieved by choosing a value for α_0

such that both terms in Equation (4.25b) are equal, giving:

$$\sin^2\alpha_0 B_{11} = \cos^2\alpha_0 B_{33} \Rightarrow \frac{B_{33}}{B_{11}} = \tan^2\alpha_0 \tag{4.27}$$

The above argument, however, does not ensure that both heave and surge contributions for the motion of the cylinder have opposite phases and so it is not used to compute the final value α_O.

The plots on Figure 4.17 show values of α_0 which maximise the maximum average absorbed power given by Equation (4.26b) for the incident wavelengths ratios (λ_d/D) and submergence ratios (H/D). For the very long waves the optimum angle α_O tends asymptotically to 90°. At this angle the contributions from the heave mode vanish and only surge is of importance and $\overline{P_{max}} = X_1^2/(8B_{11})$. However this result should be treated carefully as for these wavelengths $\overline{P_{max}}$ is mostly impractical to achieve as it requires very large velocity amplitudes ($|U_O| = |X_1|/(2l_0B_{11})$). Moreover, the theoretical high values of $\overline{P_{max}}$ at the longer wavelengths are mostly related with the low values of the hydrodynamic damping which tend asymptotically to zero faster than the square of the excitation force. This can be confirmed in the plots of Figures 4.9(c), 4.9(g) and Figures 4.10(c) and 4.10(g). At smaller wavelengths the values α_O varies considerably with the draft and submergence ratios. Particularly interesting is the behaviour of α_O for the case of the free-surface piercing cylinder for draft ratios greater than 0.70 ($H/D > 0.70$). At wavelength ratios $\lambda_d/D < 10$, α_O has a minimum equal to 0° which is related with the occurrence of the singularities in the hydrodynamic damping in heave mode associated with these drafts and wavelength ratios (see Figure 4.10(d)).

The angle α_0 is thus an important variable to take into account in the design of the cylindrical-Duck. It controls the contribution of the hydrodynamic forces in heave or surge modes to the torque at the off-centred axis, and by choosing this angle appropriately is possible to further improve the performance of the device. An ideal design might even consider a mechanism to automatically change this angle to adapt the device to changing sea conditions.

However, in the present work and in what follows, the value of α_0 is chosen to be fixed such to accommodate a maximum performance of the device at a particular deployment location. As in section 3.4.2 the bivariate histogram at Lanzarote (Canaries Islands) is considered. The average available energy in a year by energy period for this location is shown in Figure 4.18.

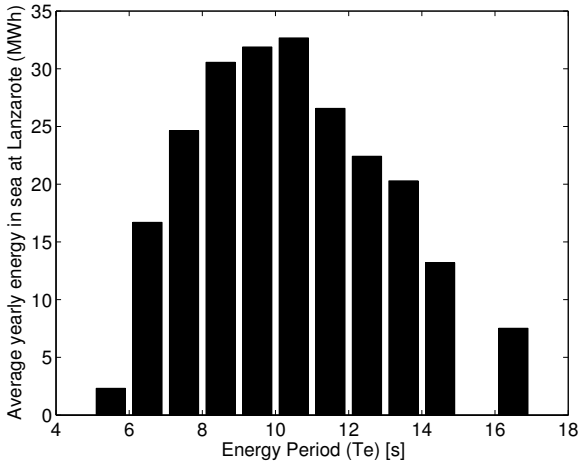

Figure 4.18: *Average energy in a year by energy period at Lanzarote, Canaries Islands (30°N, 12°W), correspondent to the histogram of Table 3.11.*

The design wave period is chosen at around 9 s (T_p) which corresponds to a wavelength (in deep water) of about 120 m.

Following Count [1978], a sensible design philosophy which aims to achieve a broad bandwidth of energy absorption would be to choose an external damping close to the maximum value of the hydrodynamic damping and adjust the spring and mass terms so to provide resonance at that wavelength.

The plots in Figures 4.14(f) and 4.15(f) show that the maximum values of hydrodynamic damping (B_{55}) for the case of $H/D = 0.85$ and $H/D = 1.10$ occur at about $\lambda_d/D = 6$. If the geometrical dimensions of the cylinder are chosen such that it resonates for waves with 9 s wave period or equivalently to wavelengths of about 120 m, the diameter of the cylinder should be of about 20 m. In what follows, the design cases corresponding to smaller cylinders with diameters equal to 12 m and 6 m are also investigated. For these cylinders to resonate at 9 s waves, the resonant wavelength ratios are respectively equal to $\lambda_d/D = 10$ and $\lambda_d/D = 20$.

At each of these design cases, with the cylinder diameters equal to 20, 12 and 6 m, the value of α_O which maximises the average absorbed power is chosen at the correspondent resonant wavelengths ratio ($\lambda_d/D = 6$, 10 and 12) for each draft and submergence ratio of the fully-submerged and free-surface piercing cylinder. The maximum performances obtained for these three design cases are shown in Figures 4.19(a), 4.19(b) and 4.19(c) with the blue lines associated with the fully-submerged cylinder and the black lines to the surface-piercing cylinder.

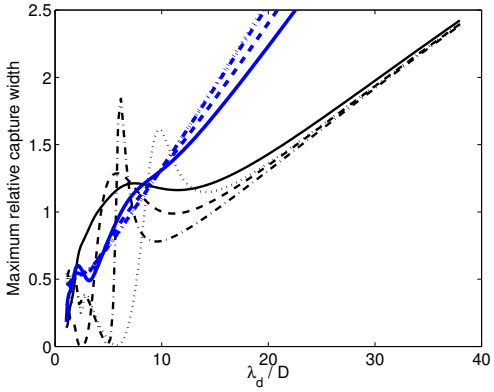

(a) Cylinder diameter of $D = 20$ m which corresponds to a resonance wavelength of $\lambda/D = 6$.

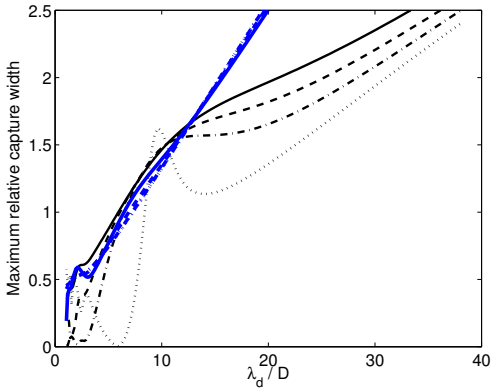

(b) Cylinder diameter of $D = 12$ m which corresponds to a resonance wavelength of $\lambda/D = 10$.

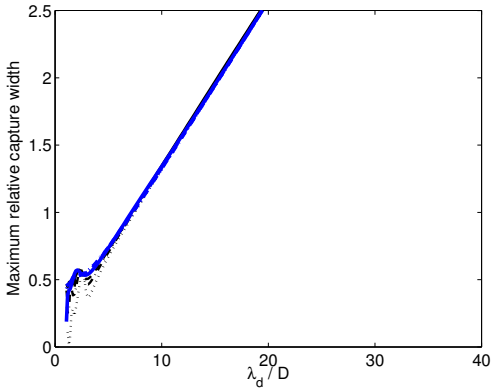

(c) Cylinder diameter of $D = 6$ m which corresponds to a resonance wavelength of $\lambda/D = 20$.

Figure 4.19: *Maximum performances obtained for the the three design cases with cylinder diameters equal to (a) 20 m, (b) 12 m and (c) 6 m. The angle of the off-centred axis (α_0) is chosen such to maximise performance at resonance wavelength ratios $\lambda_d/D = 6$, 10 and 20 respectively, for each draft and submergence ratios (H/D) of the surface-piercing (black) and fully-submerged cylinder (blue).*

The maximum performances for the fully-submerged and surface-piercing cylinder are very different. The fully-submerged cylinder depends less on the submergence ratio than the free-surface piercing cylinder. The blue and black continuous lines associated with submergence ratios equal to H/D = 1.10 and 0.70 show an overall best performance for the three design cases and these submergence ratios were chosen in what follows.

Such maximum performances require the implementation of a linear complex conjugate power-take-off which remains mostly theoretical. To achieve the maximum average absorbed power away from resonance it requires the input of large amounts of reactive power. A more practical implementation of a controller uses only pure damping. The control force is set to be proportional to the velocity of the device and so the control term (K) is a real number.

The average absorbed power obtained with a pure damping controller is given by Equation (2.2a):

$$\overline{P_{abs}} = \frac{1}{4}\frac{|X|^2}{(B+|Z|)}\left(1-\frac{(K-|Z|)^2}{|K+Z|^2}\right)$$

which achieves a maximum when the control damping is equal to the absolute value of the radiation impedance ($K = |Z|$), given by Equation (2.2c):

$$\overline{P_{max}} = \frac{1}{4}\frac{|X|^2}{(B+|Z|)}$$

At resonance, which occurs for a particular wave period ($T_0 = 1/(2\pi\omega_0)$),

$$J + A_{55}(\omega_0) - \frac{C_{55}}{\omega_0^2} = 0 \tag{4.28}$$

the average absorbed power is maximum and independent of the controller and the pure damping controller achieves as good performance as a complex conjugate controller.

To achieve resonance at a particular wavelength, the controller should be designed with a spring term that balances the total inertia (of the device plus the added mass) and hydrostatic stiffness. Alternatively, resonance can be achieved at a particular wavelength through a careful distribution of the mass of the device such to obtain an inertia that balances both the added mass and hydrostatic stiffness.

4.5.1 Mass redistribution

In what follows the second option is considered and the analysis extends the work presented in Lucas et al. [2009]. It is shown how to optimise the performance of a cylindrical-Duck such to achieve resonance at a certain wavelength by redistributing its mass whilst maintaining its total value constant.

It is convenient to separate the total mass into structural mass and 'ballast'. Ballast is defined here as dead weight placed inside the structure to sink it to a certain draft and distributed such to achieve a particular inertia, so changes in the inertia of the system can be made by altering the positions of discrete masses that form the ballast of the device.

The total mass is kept constant and the structural mass, referred to as the mass of the hull (m_H), is assumed to be symmetrically distributed in order to simplify the analysis. For such case the centre of mass of the hull lies at the geometrical centre of the cylinder ($Z_H = 0$) and the mass of the hull is assumed to be a fraction of the mass of the ballast: $m_H = x\, m_B$. The total mass is then given by:

$$m = m_H + m_B = (1+x)\, m_B = \forall\, \rho = cte. \tag{4.29}$$

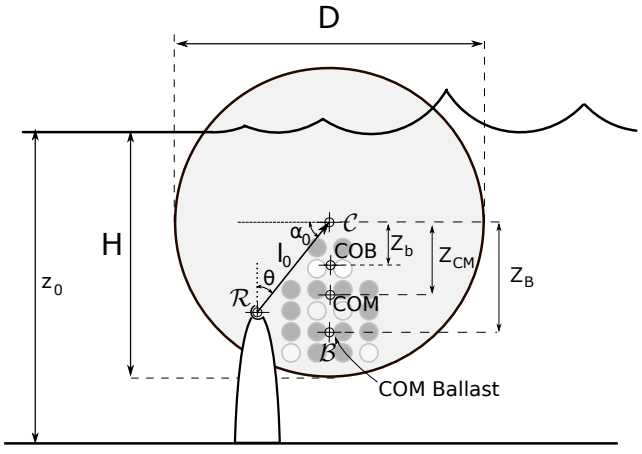

Figure 4.20: *Schematic drawing. The small circles inside the cylinder represent the ballast arrangement. The total mass is kept constant. The moment of inertia of the system can vary by redistributing the ballast. In the drawing this is possible by a permutation of the small circles. $\mathcal{B}$ represents the centre of mass of the ballast. COM the centre of mass of the system. COB the centre of buoyancy.*

The inertia of the device at the off-centred axis (J) is expressed as the sum of the contributions from the hull (J_H) and ballast (J_B) at this location:

$$J = J_H + J_B \tag{4.30a}$$

Through the parallel axis theorem, these can be rewritten in terms of the inertias at the centres of mass of the hull and ballast (I_H and I_B):

$$J_H = I_H + m_H l_H^2 = I_H + x m_B l_0^2 \tag{4.30b}$$

$$J_B = I_B + m_B l_B^2 \tag{4.30c}$$

with $l_H = l_0$ and $l_B = \sqrt{(l_0 \sin\alpha_0 - Z_B)^2 + (l_0 \cos\alpha_0)^2}$, the distances from the centre of the cylinder to the off-centred axis and the centre of mass of the ballast respectively, and Z_B representing the vertical distance from the centre of the cylinder to the centre of mass of the ballast.

The centre of mass of the system, measured from the centre of the cylinder is given by:

$$Z_{CM} = \frac{m_B Z_B}{m} = \frac{Z_B}{1+x} \tag{4.31}$$

(note that it was assumed $Z_H = 0$ and the relation (4.29) was taken into account).

The added mass at the off-centred axis is related to the added mass in surge and heave modes at the centre of the cylinder through the formulas given in Table 4.4, thus:

$$A'_{55} = l_0^2 \sin^2\alpha_0 A_{11} + l_0^2 \cos^2\alpha_0 A_{33} \tag{4.32}$$

The same table gives the expression for the hydrostatic stiffness at the off-centred axis in terms of those measured at the centre of the cylinder:

$$C'_{55} = 2 l_0 \cos\alpha_0 C_{35} + l_0^2 \cos^2\alpha_0 C_{33} + C_{55} = l_0^2 \cos^2\alpha_0 C_{33} \tag{4.33a}$$

Note that in the above expression, the coefficients C_{35} and C_{55} are given at the centre of the cylinder assuming that the centre of mass is located at the centre of the cylinder, and so, these do not contribute to the hydrostatic stiffness moment at the off-centred axis (C'_{55}). However, C'_{55} depend on the centre of mass and this should be accounted for in the above expression. Table 4.2 gives C'_{55} in terms of its fundamental definition, which depends on the water-plane area, moments (S_{ij}) and vertical coordinate of the centres of

buoyancy (z_b) and mass (z_g):

$$C'_{55} = \rho\, g \left(S_{20} + \forall\, z_b - \forall\, z_g\right) = \rho\, g \left(S_{20} - \forall\, Z_b\right) + \rho \forall\, g\, Z_{CM} \tag{4.33b}$$

In the above expression, the values of z_b and z_g are refereed to the off-centred axis, which relate with their values measured at the centre of the cylinder (Z_b and Z_g) through the relations: $z_g = l_0 \sin\alpha_0 - Z_{CM}$ and $z_b = l_0 \sin\alpha_0 - Z_b$. In Equation (4.33b) the first term remains constant, and equal to (4.33a) when the centre of mass is at the centre of the cylinder ($Z_{CM} = 0$). Thus, the final expression of C'_{55} which accounts for any location of the centre of mass of the system is given by:

$$C'_{55} = l_0^2 \cos^2\alpha_0\, C_{33} + m\, g\, Z_{CM} = l_0^2 \cos^2\alpha_0\, C_{33} + m_B\, g\, Z_B \tag{4.33c}$$

For the special case of a fully-submerged cylinder, the water-plane area and moments are zero and the centre of buoyancy is located at the geometrical centre of the cylinder, and so the above expression is simplified accordingly ($C_{33} = 0$).

Substituting Equations (4.30a), (4.32) and (4.33c) into the resonance condition (4.28) a quadratic expression in Z_B is obtained whose solution gives the location for the centre of mass of ballast such to achieve resonance at a certain wave period. So:

$$a_2 Z_B^2 + a_1 Z_B + a_0 = 0 \tag{4.34a}$$

with:

$$a_2 = m_B \tag{4.34b}$$

$$a_1 = -\left(\frac{g}{\omega^2} + 2 l_0 \sin(\alpha_0)\right) m_B \tag{4.34c}$$

$$a_0 = +I_H + I_B + (x+1)\, l_0^2 m_B + l_0^2 \sin^2\alpha_0 A_{11} + l_0^2 \cos^2\alpha_0 A_{33} - \frac{l_0^2 \cos^2\alpha_0\, C_{33}}{\omega^2} \tag{4.34d}$$

The quadratic Equation (4.34a) has two solutions given by:

$$Z_B = \frac{-a_1 \pm \sqrt{a_1^2 - 4 a_2 a_0}}{2 a_2} \tag{4.34e}$$

which are real provided that $\Delta = a_1^2 - 4 a_2 a_1 \geq 0$.

The above expression provides a relationship for the value of the inertia of the ballast (I_B) such as to satisfy resonance and provide real solutions for Z_B. In general terms, I_B can be defined in terms of its radius of gyration (K_B): $I_B = m_B K_B^2$.

Some generic numbers can be worked out so as to evaluate the feasibility of this assumption. As an example, if the ballast is made of a solid cylinder, its inertia would be equal to $I_B = (m_B/2)(D_B/2)^2$, with D_B its diameter. Choosing K_B as a fraction of the radius of the hull: $K_B = y(D/2)$, the diameter of the ballast (D_B) is then given by: $D_B = y\sqrt{2}D$. For example, if $y = 0.3$, which satisfies $\Delta \geq 0$ for most wavelengths, $D_B = 0.4D$.

Figure 4.21 shows different solutions for Equation (4.34a), in terms of the optimum relative location of the centre of mass of the ballast ($Z_B/(D/2)$) to make the device resonate at a particular wavelength. It corresponds to the design case of a free-surface piercing cylinder of 12 m diameter, with a draft ratio of $H/D = 0.70$ and with the off-centred axis located at an angle $\alpha_0 = 63°$ such to maximise the maximum average absorbed power at $\lambda_d/D = 10$. The different curves in the plot correspond to different distances of the off-centred axis from the centre of the cylinder (l_0). It shows that Z_B depends on l_0, and that for each value of l_0, there is an optimum placement of the ballast (Z_B) to make the device resonate at a particular wavelength.

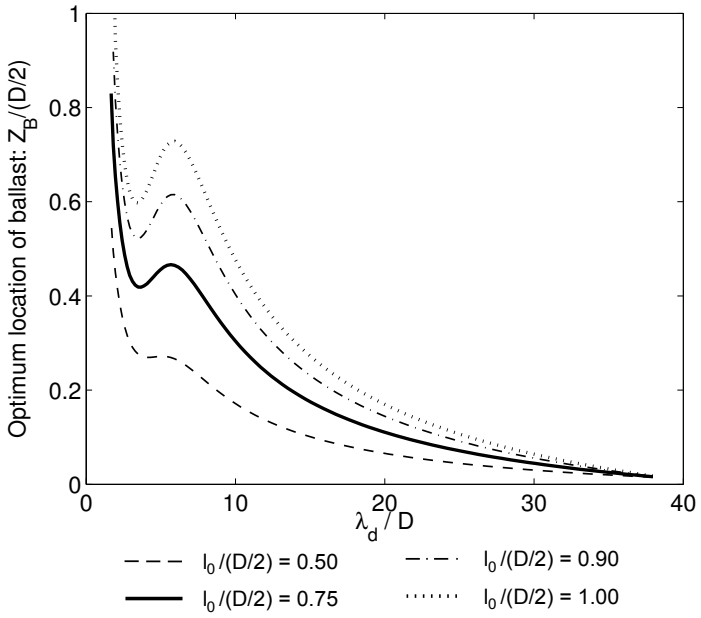

Figure 4.21: *Optimum position for the ballast such to satisfy resonance condition at a specified wavelengths for different distances of the off-centred axis to the centre of the cylinder (l_0).*

Furthermore, Figure 4.22 shows a comparison of the maximum performance obtained with a optimum pure damping controller for different locations of the off-centred axis (l_0). The design case is the same as previously ($D = 12$ m, $H/D = 0.70$, $\alpha_0 = 63°$) with Z_B

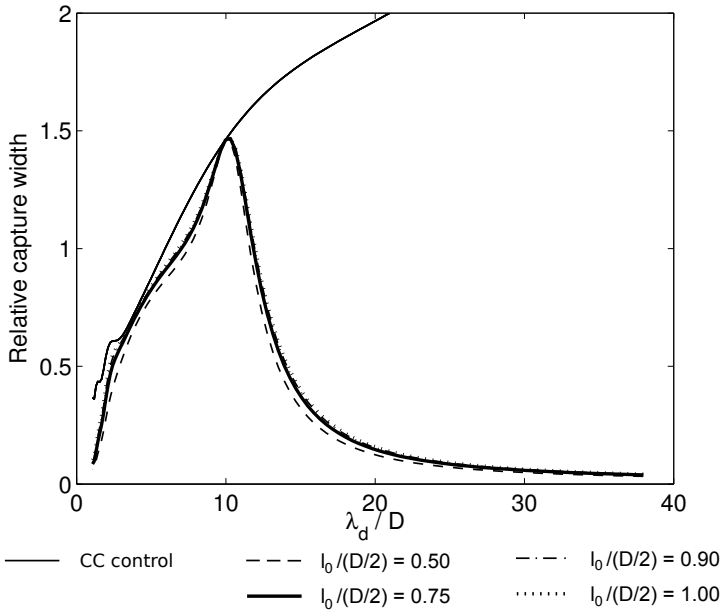

Figure 4.22: *Relative capture width (RCW) obtained with an optimum pure damping controller associated with different lengths of attachment (l_0) for which the ballast was placed optimally such to make the device resonate at $\lambda_d/D = 10$. The RCW associated with a complex conjugate controller with no amplitude constrain is also shown for comparison (thin continuous line). The design case corresponds to a free-surface piercing cylinder of diameter equal to 12 m, with a draft ratio of $H/D = 0.70$ and with the angle of attachment α_0 at 63°such to achieve a maximum performance at $\lambda_d/D = 10$.*

chosen for each l_0 such to make the device resonate at $\lambda_d/D = 10$. The performance curve correspondent to a complex conjugate controller is also shown for comparison. This plot shows that the performance obtained with an optimum pure damping controller depends only slightly on l_0 provided that the ballast is positioned optimally.

In what follows, the distance at which the off-centred axis is positioned is taken as equal to $l_0/(D/2) = 0.75$ and the ballast positioned optimally (Z_{B_o}) to satisfy resonance for the specified wavelength ($\lambda_d/D = 6$, 10 or 20 depending on the design case).

The simplest linear controller that can be used forces the control force to be proportional to the velocity of the device ($F_d = -K_0 U$) by using a fixed value of damping ($K_0 = cte.$). Following Count [1978], the broadest bandwidth response for the performance of wave energy converter which uses a fixed damping controller is achieved when damping (K_0) is approximately equal to the maximum of the hydrodynamic damping.

The previous design cases are investigated for fixed damping value equal to $K_0 = 0.9 B_{55}$ at $\lambda_d/D = 6$. The performances associated with the three controllers: complex conjugate (theoretical), pure damping and fixed damping are plotted in Figure 4.23. The values of

α_O, Z_{B_O} and full scale fixed damping (K_0) used to compute the plots in Figure 4.23 are given for reference in Table 4.5. Figure 4.24 re-plots the curves in Figure 4.23 associated with fixed damping for the six design cases considered.

H/D	D [m]	α_O [°]	$Z_{B_O}/(D/2)$	K_O [MNms]
0.7	6	87	0.20	1.93×10^0
	12	63	0.31	4.13×10^1
	20	29	0.21	1.72×10^2
1.10	6	89	0.20	2.22×10^0
	12	80	0.39	5.82×10^1
	20	69	0.50	6.06×10^3

Table 4.5: *Values of the parameters used to compute the performances shown in Figures 4.23 and 4.24. For all the design cases, the off-centred axis is placed at a distance to the centre of the cylinder equal to* $l_0/(D/2) = 0.75$. *The angle of the off-centred axis with the horizontal plane* (α_0) *and the location of the centre of mass of the ballast* ($Z_B/(D/2)$) *were chosen such to obtain resonance at 9 s waves for cylinders with diameters equal to 6, 12 and 20 m. Fixed full-scale damping* K_0 *chosen to be equal to* $0.9B_{55}(\lambda_d/D = 6)$.

The cylinder with a diameter equal to 6 m shows the poorest performance with a maximum value of relative capture width (RCW) of about 0.5. However it presents a large bandwidth with $RCW > 0.4$ for the range of wavelengths between 13 to 90 m which correspond to 3.0 to 7.6 s wave periods. The fully-submerged cylinder presents a slightly improved performance for the longer wavelengths.

The best performances are obtained for the 12 m diameter cylinders. The surface piercing cylinder presents a slightly better performance for the shorter waves but both performances are almost identical at medium and larger waves. The maximum relative capture width associated with this design case is of about 1.1 and is over 0.8 for wavelengths between 60 to 140 m which correspond to a wave-period range between 6.3 to 9.6 s.

The performance of the 20 m cylinder is better at longer waves. For this design case the fully-submerged cylinder performs better achieving a larger bandwidth. The maximum capture width is of about 1.14 being higher than 0.8 for wavelengths between 100 to 215 m corresponding to wave-periods between 8 to 11.7 s.

In mixed seas, the relative capture width (RWC_{sea}) should be computed instead as given by Equation (2.11).

Figure 4.25 show the theoretical relative capture width for the above configurations associated with a mixed sea with modified Pierson-Moskowitz spectrum for energy periods (T_e) between 6 to 16 s.

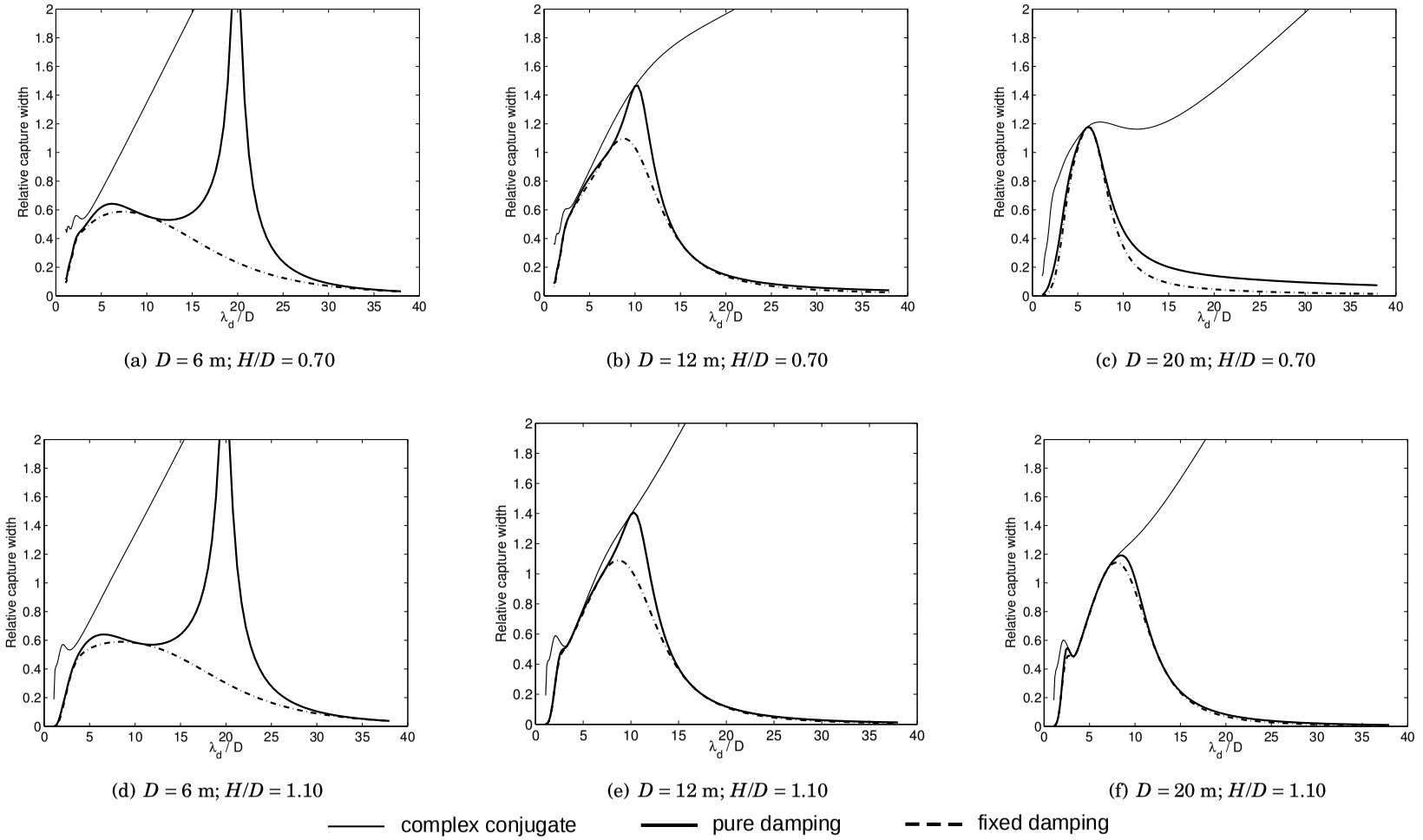

Figure 4.23: *Comparison of performances in regular waves obtained with three different linear controllers: complex conjugate, pure damping and fixed damping. The plots are associated with design cases with cylinder diameters equal to 6, 12 and 20 m, with the off-centred axis located at a distance ratio equal to* $l_0/(D/2) = 0.75$ *and with an angle* α_0 *and placement of the ballast* Z_B *chosen to achieve resonance for 9 s waves (see Table 4.5). Top plots (a), (b) and (c) are associated with a free-surface piercing cylinder with a draft ratio equal to* $H/D = 0.7$*, whereas the bottom plots (d), (e) and (f) are associated with a fully-submerged cylinder at a submergence ratio equal to* $H/D = 1.1$.

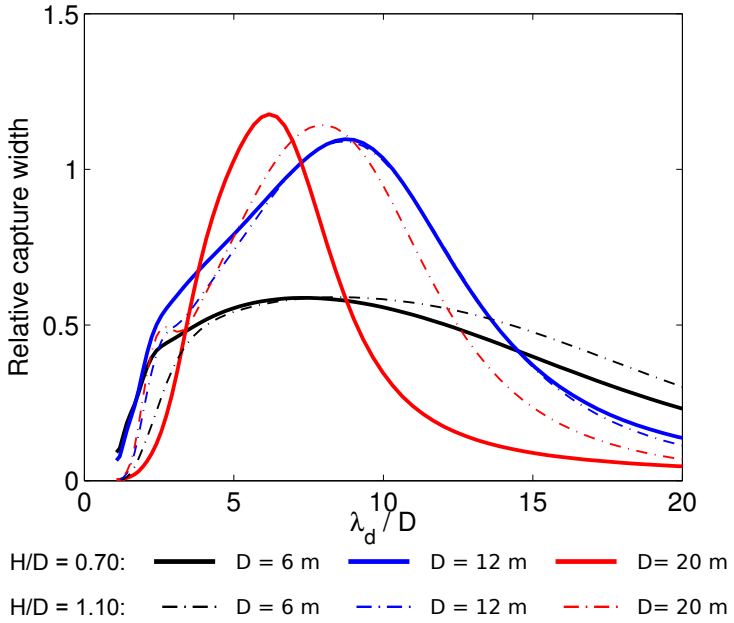

Figure 4.24: *Performance in regular waves obtained with a fixed damping controller for the six design cases described in Table 4.5.*

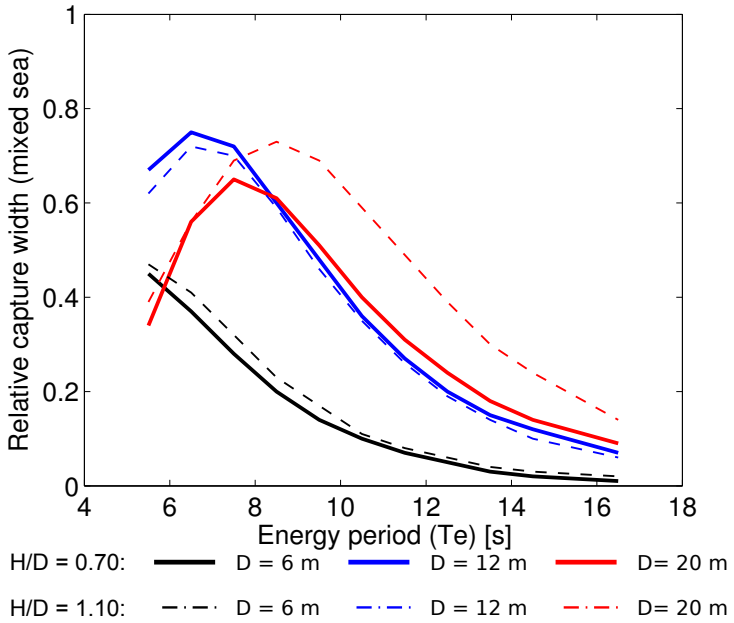

Figure 4.25: *Theoretical relative capture width for mixed seas (modified Pierson-Moskowitz) obtained for a cylinder piercing the free-surface at a draft equal to $H/D = 0.70$ and a fully-submerged cylinder near the free-surface at a level $H/D = 1.10$ for the three design cases which consider cylinder diameters equal to 6, 12 and 20 m and fixed damping and with the other parameters as given by Table 4.5.*

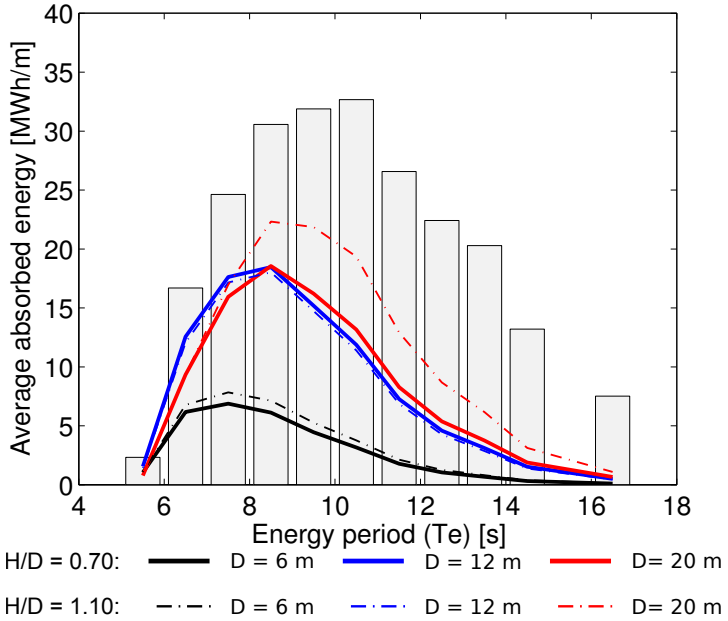

Figure 4.26: *Average absorbed energy over one year as compared with the available in the sea at a sea near Lanzarote for a cylinder piercing the free-surface at a draft equal to H/D = 0.70 and a fully-submerged cylinder near the free-surface at a level H/D = 1.10 for the three design cases which consider cylinder diameters equal to 6, 12 and 20 m and fixed damping and with the design parameters as given by Table 4.5. The bars in the graph represent the average energy density available in one year at Lanzarote (as in Figure 4.18).*

As expected the maximum achieved relative capture width in mixed seas is lower than the value obtained for regular waves. This maximum is equal to 0.75 and is obtained for the 12 m piercing cylinder. These results are in general agreement with the obtained for regular waves. The cylinder of 6 m have its best performance for the short waves in the spectrum, whereas the 12 m cylinder performs well up to seas with T_e = 10 s and the 20 m fully-submerged cylinder achieving a better performance at the longer waves. It is also apparent that there is no advantage in using a 20 m diameter cylinder piercing the free-surface as its performance at longer waves is comparable to the obtained with a 12 m diameter cylinder and which performs better at shorter waves.

Figure 4.26 presents an estimate of the average energy production over the year as compared with the available for each of the design case considered above. These numbers should be considered carefully as they are based on a linear model which does not account with any of the losses expected to occur and also does not consider the effects of directionality of the sea waves, which are expected to be important in the present system with only one degree of freedom.

The average energy absorbed over a year which corresponds to the sum of the energy in all bins of Figure 4.26 for each of the design cases considered previously is given in Table 4.6.

The area and volume of the cylinders are also given in Table 4.6 as these can give an indication of the relative capital cost associated with each design case. For the free-surface piercing cylinder, doubling the diameter of the cylinder from 6 to 12 m, maintaining the same width ratio ($W/D = 2.5$), would result in almost six times increase of the average absorbed energy over a year, whereas the area would increase four times and the volume eight. If the diameter was 20 m, comparing with a cylinder of 12 m, the average absorbed energy over the year would increase at the same rate as the width (≈ 1.7). The area would increase almost three times and the volume almost five times. A similar analysis can be made for the fully-submerged design cases. Doubling the diameter from 6 to 12 m would increase the average absorbed energy over the year in about five times, whereas increasing the diameter to 20 m would further increase the energy absorption in about twice.

Full scale cylinder				Free-surf. piercing ($H/D = 0.70$)		Fully-submerged ($H/D = 1.10$)	
Diameter	Width	Area	Volume	Average absorbed energy		Average absorbed energy	
m	m	$\times 10^3$ m^2	$\times 10^3$ m^3	MWh/m	GWh	MWh/m	GWh
6	15	0.3	0.4	31.7	0.5	36.5	0.5
12	30	1.4	3.4	94.3	2.8	90.6	2.7
20	50	3.8	15.7	93.9	4.7	122.7	6.1

Table 4.6: *Total absorbed energy over the year for the design cases which consider a cylinder piercing the free-surface at a draft equal to $H/D = 0.70$ and a fully-submerged cylinder near the free-surface at a level $H/D = 1.10$ for the three design cases which consider cylinder diameters equal to 6, 12 and 20 m and fixed damping and with the design parameters as given by Table 4.5.*

4.5.2 Mooring forces

This section concludes with the calculation of the mooring forces at the attachment point for the one-degree-of-freedom model. Figure 4.27 shows a schematic drawing which is followed for this analysis.

The only applied forces and moments for this system are the hydrodynamic force and the power take off control torque. Power is extracted through a fixed value of damping which ensures that torque is proportional to the angular velocity.

The cylinder is free to rotate about its off-centred axis which is constrained to move in the horizontal and vertical directions. Thus, the mooring forces at the attachment point,

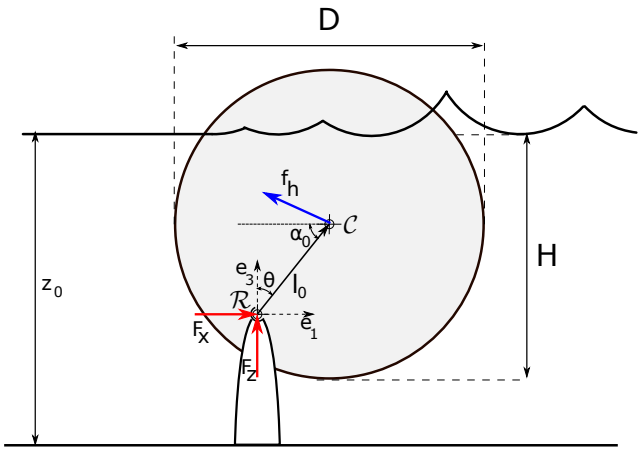

Figure 4.27: *Schematic drawing for the one degree of freedom model used to compute the mooring forces.*

in the vertical and horizontal directions are required to balance the hydrodynamic force:

$$F_x = -\left(\vec{f}_h\right)_1 = -\left(\vec{f}_A + \vec{f}_B + \vec{f}_C + \vec{f}_X\right)_1 \tag{4.35a}$$

$$F_z = -\left(\vec{f}_h\right)_3 = -\left(\vec{f}_A + \vec{f}_B + \vec{f}_C + \vec{f}_X\right)_3 \tag{4.35b}$$

These vertical and horizontal forces are the same as the forces applied at the centre of the cylinder, thus:

$$F_x = A_{11}\ddot{\xi}_1 + B_{11}\dot{\xi}_1 + X_1 \tag{4.35c}$$

$$F_z = A_{33}\ddot{\xi}_3 + B_{33}\dot{\xi}_3 + C_{33}\xi_3 + X_3 \tag{4.35d}$$

where A_{jj}, B_{jj}, C_{jj} $(j = 1,3)$ are the added mass, hydrodynamic damping and hydrostatic stiffness in surge and heave at the centre of the cylinder (note that the hydrostatic stiffness in surge is null: $C_{11} = 0$) and ξ_j $(j = 1,3)$ the surge and heave displacements. These are related with the angular displacement ξ_5, obtained by solving the equation of motion of the system (4.23a): $(Z_{55} + K)\,\dot{\xi}_5 = X_5$. The displacements at the centre of the cylinder are expressed in terms of the angular displacement through the relationship:

$$\xi_1 = \Delta r_1 = l_0(\sin\theta - \sin\theta_0) \approx l_0 \cos(\alpha_0 - \pi/2)\xi_5 \tag{4.36a}$$

$$\xi_3 = \Delta r_3 = l_0(\cos\theta - \cos\theta_0) \approx -l_0 \sin(\alpha_0 - \pi/2)\xi_5 \tag{4.36b}$$

with l_0 and α_0 the usual distance from the off-centred axis to the centre of the cylinder and angle with the horizontal plane respectively. These relations are obtained by considering the angular displacement: $\xi_5 = \Delta\theta = \theta - \theta_0$, with θ_0 the angle subtended to the vertical axis when in still water, which is given also in terms of the usual α_0 as $\theta_0 = \alpha_0 - \pi/2$. The first order approximations for the sine and cosine functions around the still position where also considered (for the sine: $\sin\theta = \sin\theta_0 + \cos\theta_0\,(\theta - \theta_0)$, see Equation (5.8a)). The velocities and accelerations in heave and surge are then derived by assuming harmonic motions, i.e.: $u_j = \dot{\xi}_j = i\,\omega\,\xi_j$ and $\dot{u}_j = \ddot{\xi}_j = -\omega^2\,\xi_j$. Note that, in the mooring forces (4.35) the control force of the power take off is accounted indirectly though its influence in the motion of the device.

Figure 4.28 shows the normalised pitch amplitude obtained by solving the equation of motion (4.23a) for the design cases considered previously.

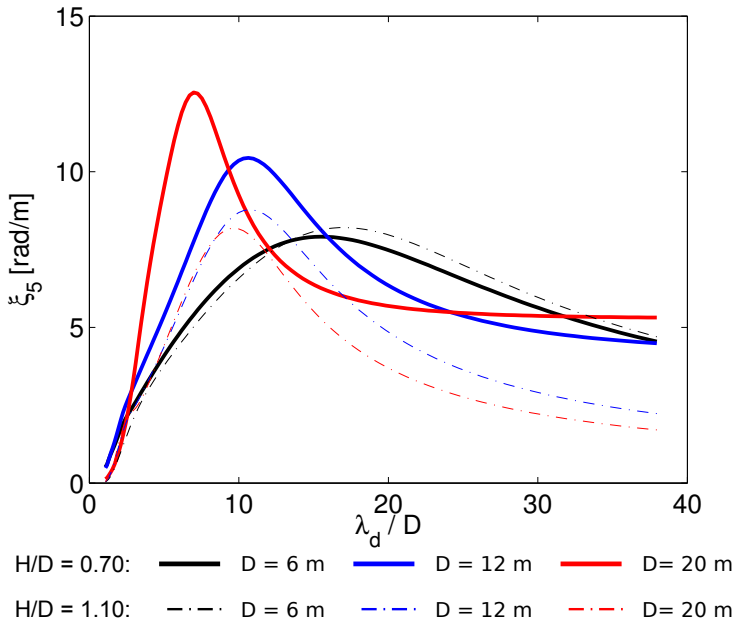

Figure 4.28: *Normalised pitch amplitude in regular waves for a cylinder piercing the free-surface at a draft equal to $H/D = 0.70$ and a fully-submerged cylinder near the free-surface at a level $H/D = 1.10$ for the three design cases which consider cylinder diameters equal to 6, 12 and 20 m and fixed damping and with the design parameters as given by Table 4.5.*

Figure 4.29 show the normalised amplitudes of the mooring forces in the horizontal and vertical directions for the previous design cases which consider a surface piercing cylinder ($H/D = 0.7$) and full-submerged ($H/D = 1.10$) with diameters equal to 6, 12 and 20 m. The normalised mooring forces where computed in a similar way as in Section 3.4.1: $\hat{F}_j = F_j/(\rho\,g\,D\,W\,a)$, with F_j $(j = x,z)$, the mooring force as given by

Equation (4.35) divided by the density of water (ρ), the constant of gravity (g), the diameter (D) and width (W) of the cylinder and the amplitude of the wave (a).

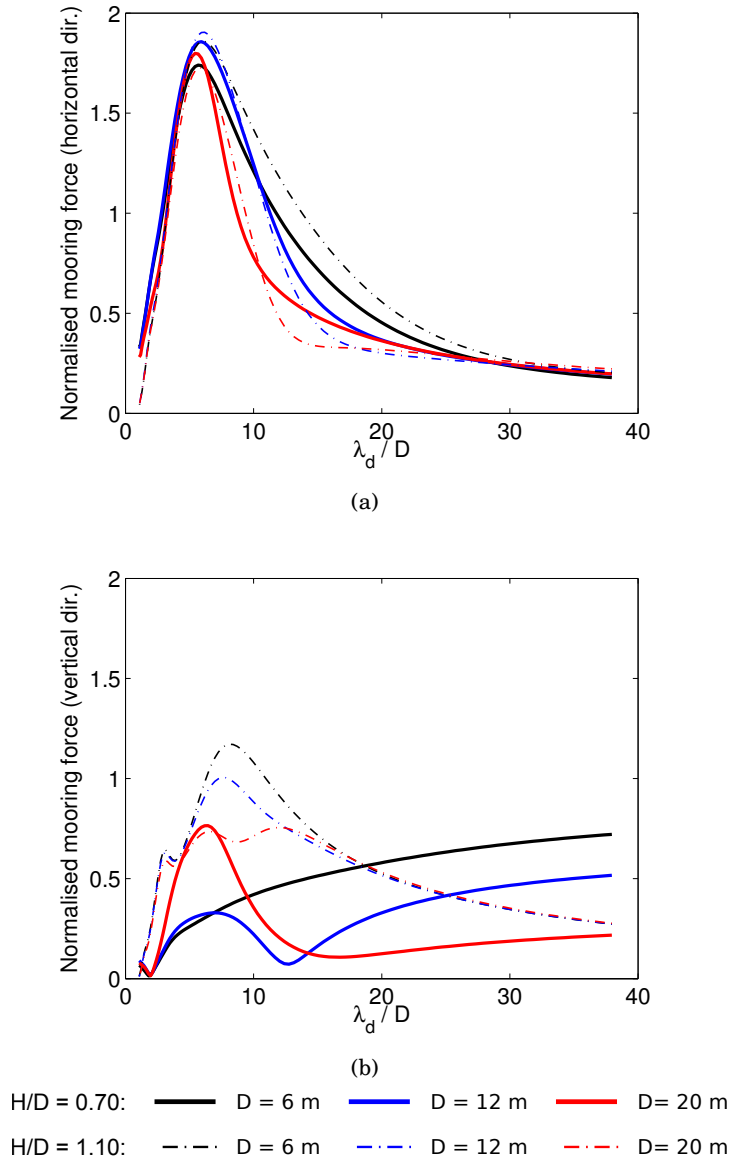

Figure 4.29: *Normalised (a) horizontal mooring force and (b) vertical mooring force in regular waves for a cylinder piercing the free-surface at a draft equal to $H/D = 0.70$ and a fully-submerged cylinder near the free-surface at a level $H/D = 1.10$ for the three design cases which consider cylinder diameters equal to 6, 12 and 20 m and fixed damping and with the other parameters as given by lable 4.5.*

For all the design cases the normalised mooring forces in the horizontal direction (surge) show similar curves with a maximum between 1.7 to 1.9 at a wavelength of approximately six times the diameter of the cylinder. These decrease to lower values than 0.5 for the very short wavelengths ($\lambda_d/D < 2$) and for wavelength ratios greater than 20. The normalised mooring force in the vertical direction (heave) shows

different dependencies for the fully-submerged and surface piercing cylinder. For the fully-submerged case it has a maximum between 0.7 to 1.2 at wavelengths of six to eight times the diameter of the cylinder, decreasing to lower values than 0.5 for wavelength ratios lower than 2 and greater than 20. The free-surface piercing cylinder shows lower values of the normalised mooring force in the vertical direction when compared with the fully-submerged case, for wavelengths ratios lower than 20, but increasing for the longer wavelengths.

Table 4.7 shows full scale values of the mooring forces associated with normalised values for the different design cases.

Normalised force	Full-scale force [MN/m]		
	(D = 6 m)	(D = 12 m)	(D = 20 m)
0.2	0.18	0.71	1.96
0.6	0.53	2.12	5.89
1.0	0.88	3.53	9.81
1.4	1.24	4.94	13.73
1.8	1.59	6.36	17.66

Table 4.7: *Correspondence between the normalised mooring forces and full scale forces for the design cases which consider cylinders with diameters equal to 6, 12 and 20 m and a width ratio of* $W/D = 2.5$.

Chapter 5
The hydrodynamics of the desalination Duck

This chapter presents a mathematical model for the dynamics of the desalination Duck.

The equations of motion associated to any system can be derived through different methodologies. Two of such applied to a horizontal cylinder under the influence of incident regular waves are presented. A Newton-Euler approach solves six equations of motion for each body with the constraint forces included as part of the problem. This approach is intuitive and preserves explicitly the physical significance of all terms in the equations. Nevertheless its complexity increases substantially with the number of bodies and constraints.

An alternative approach which may be convenient for more complex systems is based on the derivation of the equations of motion through a Lagrangian approach. The position of the components of the system are represented trough a set of independent generalised coordinates which are of the same number as the degrees of freedom of the system. The dynamics is then solved for such coordinates requiring a minimum number of equations equal to the number of degrees of freedom of the system. In the equations of motion, the external forces are written as a function of the generalised coordinates and the inertial forces are obtained through differentiation of the total kinetic and potential energy relative to the generalised coordinates and velocities. The hydrodynamic forces are included in this formulation as a function of the generalised coordinates. The process to obtain them as generalised forces is shown in detail for a simpler system with only one degree of freedom. This method to obtain the equations of motion is compared with Newton-Euler approach and both are validated with scale model measurements in the wave tank.

The dynamics of the desalination Duck is subsequently derived through this approach by extending this model to three degrees of freedom with the inclusion of the effects from the rigid struts and inner water-pendulum. The desalination process is modelled with a fixed value of damping between the relative motion of the hull and water-pendulum.

5.1 The equations of motion: Newton-Euler versus Lagrangian approach

For single body the equations of motion are conveniently expressed in a Newton-Euler formulation, as a system of six equations in which three describe the translation and the other three the rotation. This approach retains the physical meaning of each term in the equations, which in an inertial frame of reference are expressed as:

$$\left(\frac{d\,\vec{p}}{d\,t}\right)_{inertial} = m\,\dot{\vec{u}} = \vec{f} \tag{5.1a}$$

$$\left(\frac{d\vec{L}}{d\,t}\right)_{inertial} = \left(\frac{d\vec{L}}{d\,t}\right)_{body} + \vec{\Omega}\times\vec{L} = \vec{m} \tag{5.1b}$$

In an inertial frame of reference, the variation of linear momentum ($\vec{p}$) is proportional to the acceleration of the centre of mass $\dot{\vec{u}}$ and equal to the external forces applied to the system ($\vec{f}$). The variation of the angular momentum ($\vec{L}$) relative to any pivot point is equal to the external applied torque ($\vec{m}$) about the same point. In this approach, the constraint forces must be included in the equations of motion and are obtained as part of the solution.

The angular momentum in the body coordinate system can be written as $\vec{L} = \mathbf{I}\vec{\Omega}$ and if its axis are parallel to the principal axis of inertia, the components of (5.1b) are expressed in indicial notation as:

$$(\vec{m})_i = I_i\,\dot{\Omega}_i + \Omega_j\,\Omega_k\left(\varepsilon_{ijk}\,I_k + \varepsilon_{ikj}I_j\right) \tag{5.2}$$

This expression uses the summation convention (sum of repeated axis) and the antisymmetric symbol (also known as Levi-Civita) (ε_{ijk}) which are useful to represent the components of the cross product (see note about notation). **NB:** Because $\Omega_j\,\Omega_k$ is of second order, the linearisation of equation (5.2) gives $\vec{m}_i \approx I_i\,\dot{\Omega}_i$ and inertia matrix (3x3) is included in the mass matrix **M** as explained in Newman [1977].

WAMIT solves a linear system of equations using this approach, and as described in section 4.1.3 the six linear equations of motion in the frequency domain are represented by:

$$\sum_{j}^{6}\left[-\omega^2\left(M_{ij}+M^E_{ij}+A_{ij}\right)+i\,\omega\left(B_{ij}+B^E_{ij}\right)+\left(C_{ij}+C^E_{ij}\right)\right]\xi_i = X_i$$

For complex multi-body systems, the number of equations to solve increase drastically with the number of bodies to include (six per body) and the definition and inclusion of the constraint forces may be difficult to evaluate.

For such cases, it is convenient to use a Lagrangian approach. It is shown (see for example Goldstein et al. [2000], Landau and Lifshitz [1987]) that the Lagrangian equations are derived from very fundamental principles of mechanics such as the virtual work or the Hamilton principle.

In this approach, a system is described through any set of independent parameters which define completely its position at a particular instant. These independent parameters are called generalised coordinates and its number is uniquely determined, constituting the degrees of freedom. The generalised coordinates are normally conveniently chosen such to simplify the mathematical description of the system.

The Lagrangian equations of motion for a system with n degrees of freedom are obtained by solving the n equations associated with n independent generalised coordinates q_k ($k = 1, ..., n$):

$$\frac{d}{dt}\left(\frac{\partial \mathscr{L}}{\partial \dot{q}_k}\right) - \frac{\partial \mathscr{L}}{\partial q_k} - Q_k = 0 \tag{5.3}$$

where $\dot{q}_k$ are the generalised velocities, $\mathscr{L} = \mathscr{T} - \mathscr{V}$ the Lagrangian given by the difference between the total kinetic ($\mathscr{T}$) and potential ($\mathscr{V}$) energy of the system, and Q_k the generalised applied forces.

The virtual work principle is used to derive the generalised forces. It states that for a system in static equilibrium, the work performed by the applied forces through a small virtual displacement is zero, i.e.:

$$\delta W = \sum \vec{f} \cdot \delta \vec{r} = 0 \tag{5.4a}$$

A virtual displacement ($\delta \vec{r} = \delta \vec{r}(q_1, q_2, ...q_n)$) refers to a change in the configuration of a system through an infinitesimal variation of its coordinates consistent with the forces and constrains applied at a certain time t. **NB:** The $\delta \vec{r}$ displacement does not have time dependency and is called 'virtual' to distinguish from a 'regular' displacement which is time dependent.

The generalised forces are obtained by expressing this principle in the generalised coordinates:

$$\delta W = \vec{f} \cdot \delta \vec{r} = \vec{f} \cdot \sum_j \frac{\partial \vec{r}}{\partial q_j} \delta q_j = \sum_j \left(\sum_i f_i \frac{\partial r_i}{\partial q_j} \right) \delta q_j = \sum_j Q_j \delta q_j \tag{5.4b}$$

and so the generalised force Q_j associated with the generalised coordinate q_j is given by:

$$Q_j = \sum_i f_i \frac{\partial r_i}{\partial q_j} \tag{5.4c}$$

An important observation should be made here for the case when the generalised coordinate is a rotation. For this particular case, the generalised force associated is the applied torque around the axis of rotation. It is shown that for this particular case [Goldstein et al., 2000, pp. 58]:

$$\frac{\partial \vec{r}}{\partial q_j} = \vec{n} \times \vec{r} \tag{5.5}$$

and so the generalised force is written as:

$$Q_j = \vec{f} \cdot \frac{\partial \vec{r}}{\partial q_j} = \vec{f} \cdot \vec{n} \times \vec{r} = \vec{n} \cdot \vec{r} \times \vec{f} = \vec{n} \cdot \vec{m} = m = \tau \tag{5.6}$$

.

The virtual work produced by the reaction forces in a rigid body is null because these forces are orthogonal to the virtual displacements, and one of the major advantages of using this formulation is that those forces do not need to be taken into account when deriving the equations of motion.

To illustrate the application of this formulation and the derivation of the generalised hydrodynamic forces this method is first applied to a one degree of freedom model.

5.2 One degree of freedom model: Lagrangian approach

The procedure to derive the one degree of freedom equation of motion following a Newton-Euler approach was shown in Section 4.4. The present section illustrates the application of the Lagrangian formulation. The same assumptions as considered before in Section 4.4 apply here. Namely the cylinder oscillates with small harmonic motions and energy is taken off through a linear power take off mechanism. All assumptions associated with linear potential flow and *WAMIT* apply as well. For reference, Figure 4.16 is reproduced bellow.

Referring to Figure 5.1, the position of the the centre of mass of the cylindrical hull is given by:

$$\vec{r} = [l_2 \sin\theta; 0; l_2 \cos\theta] \tag{5.7}$$

where the angle θ is taken between the vertical and $\vec{r}$. This angle is chosen as the generalised coordinate ($q_1 = \theta$).

The body fixed coordinate system defined in *WAMIT* is chosen as being attached to the centre of mass of the hull ($\mathscr{H}, \vec{b}_k$). The linear and angular harmonic displacements

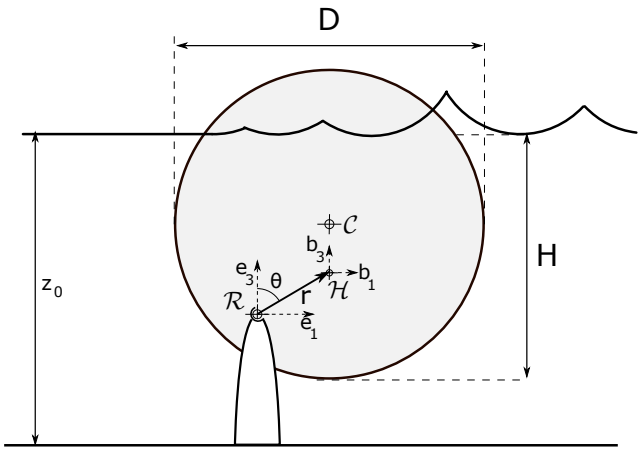

Figure 5.1: *Schematic drawing for the one degree of freedom model.*

between the inertial coordinate system and the body fixed coordinate system are:

$$\xi_5 = \Delta\theta = \theta - \theta_0 \tag{5.8a}$$

$$\xi_1 = \Delta r_1 = \left[\vec{r} - \vec{r}_0\right]_1 = l_2\,(\sin\theta - \sin\theta_0) \tag{5.8b}$$

$$\xi_3 = \Delta r_3 = \left[\vec{r} - \vec{r}_0\right]_3 = l_2\,(\cos\theta - \cos\theta_0) \tag{5.8c}$$

The velocity and acceleration associated to the displacements are given by $\vec{u} = [\dot{\xi}_1, \dot{\xi}_3, \dot{\xi}_5] = [\dot{\vec{r}}, \dot{\theta}]$ and $\dot{\vec{u}} = [\ddot{\xi}_1, \ddot{\xi}_3, \ddot{\xi}_5] = [\ddot{\vec{r}}, \ddot{\theta}]$.

The previous assumption of harmonic motions allow to represent the Cartesian hydrodynamic forces and moments given by (4.11), (4.14) and (4.8e) in the time-domain as:

$$\vec{f}_A = \mathbf{A}\,\dot{\vec{u}} \tag{5.9a}$$

$$\vec{f}_B = \mathbf{B}\,\vec{u} \tag{5.9b}$$

$$\vec{f}_X = a\,\vec{X} \tag{5.9c}$$

$$\vec{f}_C = [0;\, \rho\, g \forall;\, -\rho\, g \forall\, x_b]^T - \mathbf{C}[\Delta\vec{r};\, \Delta\theta]^T \tag{5.9d}$$

where the forces and moments due to the radiation problem are separated into the added mass and damping components ($\vec{f}_R = \vec{f}_A + \vec{f}_B$).

The generalised forces Q_θ are obtained by applying the virtual work principle given by (5.4b). For this simple model, the only external forces and moments to consider are the hydrodynamic given by (5.9) and the power-take-off moment: $m_d = -K\,\dot{\theta}$.

In what follows, the forces and moments in (5.9) are explicitly separated and represented respectively by $\vec{f}_h$ and m_h.

The virtual work principle is written as:

$$\delta W = \vec{f}_h \cdot \delta\vec{r} + m_h\,\delta\theta + m_d\,\delta\theta = \left(\vec{f}_h \cdot \frac{\partial\vec{r}}{\partial\theta} + m_h - K\dot{\theta}\right)\delta\theta \tag{5.10}$$

and so the generalised forces are:

$$Q_\theta = Q_h + Q_d = \vec{f}_h \cdot \frac{\partial\vec{r}}{\partial\theta} + m_{h_2} - K\dot{\theta} \tag{5.11}$$

with $Q_h = Q_X + Q_A + Q_B + Q_C$ given by the sum of the contributions from the radiation and diffraction problems and hydrostatic stiffness.

Using the summation convention (i.e. sum of the repeated indexes) and with $j,k = 1,3$, the generalised components of the radiation force due to the contributions of the added mass and hydrodynamic damping are given by:

$$Q_A = \vec{f}_A \cdot \frac{\partial\vec{r}}{\partial\theta} + m_A = -A_{jk}\,\ddot{r}_k\,\frac{\partial r_j}{\partial\theta} - A_{j5}\,\ddot{\theta}\,\frac{\partial r_j}{\partial\theta} - A_{5k}\,\ddot{r}_k - A_{55}\,\ddot{\theta} \tag{5.12a}$$

$$Q_B = \vec{f}_B \cdot \frac{\partial\vec{r}}{\partial\theta} + m_B = -B_{jk}\,\dot{r}_k\,\frac{\partial r_j}{\partial\theta} - B_{j5}\,\dot{\theta}\,\frac{\partial r_j}{\partial\theta} - B_{5k}\,\dot{r}_k - B_{55}\,\dot{\theta} \tag{5.12b}$$

The full expression for the generalised force associated to the added mass, obtained by substituting the components of $\dot{\vec{u}} = [\ddot{\vec{r}}, \ddot{\theta}]$ into (5.12a) is:

$$\begin{aligned} Q_A = {} & \left(-A_{11}\,l_2^2\cos^2\theta + 2A_{13}\,l_2^2\cos\theta\sin\theta - 2A_{15}\,l_2\cos\theta - A_{33}\,l_2^2\sin^2\theta + 2A_{35}\,l_2\sin\theta - A_{55}\right)\ddot{\theta} \\ & + \left(A_{11}\,l_2^2\cos\theta\sin\theta - A_{13}\,l_2^2\left(\sin^2\theta - \cos^2\theta\right) + A_{15}\,l_2\sin\theta - A_{33}\,l_2^2\cos\theta\sin\theta + A_{35}\,l_2\cos\theta\right)\dot{\theta}^2 \end{aligned}$$

A similar expression is obtained for the hydrodynamic damping by substituting $\vec{u} = [\dot{\vec{r}}, \dot{\theta}]$ into (5.12b).

These equations are linearised by neglecting the smaller second order terms in $\dot{\theta}^2$ and by considering the first order Taylor expansion for the trigonometric functions around an initial angle (θ_0), subtended when the system is in still water:

$$\sin\theta = \sin\theta_0 + \cos\theta_0\,(\theta - \theta_0) + \ldots \approx \sin\theta_0 + \cos\theta_0\,\Delta\theta \tag{5.13a}$$

$$\cos\theta = \cos\theta_0 - \sin\theta_0\,(\theta - \theta_0) + \ldots \approx \cos\theta_0 - \sin\theta_0\,\Delta\theta \tag{5.13b}$$

The linear form of the generalised radiation force is as follows:

$$Q_A \approx -A_\theta\,\ddot{\theta} \tag{5.14a}$$

$$Q_B \approx -B_\theta\,\dot{\theta} \tag{5.14b}$$

with:

$$A_\theta = A_{11} l_2^2 \cos^2\theta_0 - 2A_{13} l_2^2 \cos\theta_0 \sin\theta_0 + 2A_{15} l_2 \cos\theta_0 + A_{33} l_2^2 \sin^2\theta_0 - 2A_{35} l_2 \sin\theta_0 + A_{55} \quad (5.14c)$$

$$B_\theta = B_{11} l_2^2 \cos^2\theta_0 - 2B_{13} l_2^2 \cos\theta_0 \sin\theta_0 + 2B_{15} l_2 \cos\theta_0 + B_{33} l_2^2 \sin^2\theta_0 - 2B_{35} l_2 \sin\theta_0 + B_{55} \quad (5.14d)$$

The generalised component of the wave excitation force is given by:

$$Q_X = \vec{f}_X \cdot \frac{\partial \vec{r}}{\partial \theta} + m_X \quad (5.15)$$

Substituting $\vec{f}_X$ given by (4.14) and $\frac{\partial \vec{r}}{\partial \theta}$, after linearisation, one obtains:

$$Q_X \approx A X_\theta e^{i\omega t} - A l_2 (\cos\theta_0 X_3 + \sin\theta_0 X_1) \Delta\theta e^{i\omega t} \quad (5.16a)$$

with:

$$X_\theta = X_5 - l_2 \sin\theta_0 X_3 + l_2 \cos\theta_0 X_1 \quad (5.16b)$$

The hydrostatic force and moment, given by (4.8e) is rewritten in terms of the displacements of the centre of mass as:

$$\left(\vec{f}_C\right)_1 = 0 \quad (5.17a)$$

$$\left(\vec{f}_C\right)_3 = \rho g \forall - \rho g S_{00} \xi_3 + \rho g S_{10} \xi_5 = \rho g \forall - C_{33} \Delta r_3 - C_{35} \Delta\theta \quad (5.17b)$$

$$m_C = -\rho g \forall x_b + \rho g S_{10} \xi_3 - \rho g (S_{20} + \forall z_b) \xi_5 = -\rho g \forall x_b - C_{53} \Delta r_3 - C_{55} \Delta\theta \quad (5.17c)$$

The linear form of the generalised hydrostatic force is obtained by considering (5.13a) and (5.13b) and by neglecting the small terms in $\Delta\theta^2$:

$$Q_C = \vec{f}_C \cdot \frac{\partial \vec{r}}{\partial \theta} + m_C \approx -\Delta\theta \left(g l_2 \cos\theta_0 \rho \forall + C_\theta\right) - \rho \forall g (x_b + l_2 \sin\theta_0) \quad (5.18a)$$

with:

$$C_\theta = +C_{33} l_2^2 \sin^2\theta_0 - 2C_{35} l_2 \sin\theta_0 + C_{55} \quad (5.18b)$$

The Lagrangian associated with this simple system is by definition the difference between the total kinetic ($\mathcal{T}$) energy and potential energy ($\mathcal{V}$).

The linear velocity of the centre of mass is obtained from (5.7) and is given by: $\dot{\vec{r}} = u = \left[l_2 \dot{\theta} \cos\theta; 0; -l_2 \dot{\theta} \sin\theta\right]$, and the square of the velocity by: $\dot{\vec{r}}^2 = u^2 = l_2^2 \dot{\theta}^2$.

The total kinetic energy is given by the sum of the translational and rotational kinetic energies computed at the centre of mass of the cylinder (point $\mathscr{H}$):

$$\mathscr{T} = \mathscr{T}_{tr} + \mathscr{T}_r = \frac{1}{2}\left(I_H + m\,l_2^2\right)\dot{\theta}^2 \tag{5.19a}$$

with: $\mathscr{T}_{tr} = \frac{1}{2}\,m\,\dot{\vec{r}}^2 = \frac{1}{2}\,m\,l_2^2\,\dot{\theta}^2$ and $\mathscr{T}_r = \frac{1}{2}\,I_H\,\Omega^2 = \frac{1}{2}\,I_H\,\dot{\theta}^2$.

The potential energy is given by:

$$\mathscr{V} = m\,g\,(\vec{r})_3 = m\,g\,l_2\cos\theta \tag{5.19b}$$

The Lagrangian of the system ($\mathscr{L}$) is:

$$\mathscr{L} = \mathscr{T} - \mathscr{V} = \frac{1}{2}\left(I_H + l_2^2 m\right)\dot{\theta}^2 - m\,g\,l_2\cos\theta \tag{5.20}$$

The equation of motion is obtained by solving (5.3) relative to the generalised coordinate θ, with the generalised forces (Q_θ) given by (5.11):

$$\frac{d}{d\,t}\left(\frac{\partial\mathscr{L}}{\partial\dot{\theta}}\right) - \frac{\partial\mathscr{L}}{\partial\theta} - Q_\theta = 0 \tag{5.21}$$

Substituting (5.20), the above equation is re-written as:

$$\ddot{\theta}\left(I_H + l_2^2 m\right) - g\,m\,l_2\sin\theta - Q_\theta = 0 \tag{5.22}$$

The final linear equation of motion in time domain which is only valid for small harmonic motions is obtained through the substitution of the linear generalised forces (Q_θ) and the linearisation of $\sin\theta$ as in (5.13):

$$\left(I_H + m\,l_2^2 + A_\theta\right)\ddot{\theta} + \left(B_\theta + K\right)\dot{\theta} + C_\theta\,\Delta\theta + a\,l_2\left(X_3\cos\theta_0 + X_1\sin\theta_0\right)\Delta\theta\,e^{i\,\omega\,t} - a\,X_\theta\,e^{i\,\omega\,t} + g\,m\,x_b = 0 \tag{5.23}$$

To obtain the above equation in the frequency domain, it is necessary to substitute the expressions for the harmonic displacements, their velocities and accelerations: $\Delta\theta = \xi_5 = \theta - \theta_0 = \Theta\exp(i\,\omega\,t)$, $\dot{\theta} = i\,\omega\,\Delta\theta$ and $\ddot{\theta} = -\omega^2\,\Delta\theta$ and where Θ is the complex amplitude associated with the angle θ.

The final equation is written as:

$$a_1\,e^{2\,i\,\omega\,t} + a_2\,e^{i\,\omega\,t} + a_3 = 0 \tag{5.24a}$$

with:

$$a_1 = a\,\Theta\,l_2(\cos\theta_0 X_3 + \sin\theta_0 X_1) \tag{5.24b}$$

$$a_2 = \Theta\left[-\omega^2\left(I_H + m\,l_2^2 + A_\theta - \frac{C_\theta}{\omega^2}\right) + i\,\omega(B_\theta + K)\right] - a\,X_\theta \tag{5.24c}$$

$$a_3 = +g\,m\,x_b \tag{5.24d}$$

The functions $\exp(n\,i\,\omega\,t)$, with $n = 0,1,2$ in (5.24a) are independent, and so the coefficients a_1, a_2 and a_3 should be zero.

Condition, $a_2 = 0$, allows the equation of motion to be rewritten as:

$$(Z_\theta + K)\,U_\theta = X_\theta \tag{5.25a}$$

with the complex amplitude of the velocity, $U_\theta = i\,\omega\,\Theta$, and Z_θ being interpreted as a generalised radiation impedance in the angle θ:

$$Z_\theta = i\,\omega\left(I_H + m\,l_2^2 + A_\theta - \frac{C_\theta}{\omega^2}\right) + B_\theta \tag{5.25b}$$

An expression for the mean absorbed power can be obtain through an analogy to equation (4.24):

$$\overline{P_{abs}} = \frac{|X_\theta|^2}{8B_\theta}\left(1 - \frac{|K - Z_\theta^*|^2}{|K + Z_\theta|^2}\right) \tag{5.26}$$

The maximum mean absorbed power is obtained when $K = Z_\theta^*$, and is given by:

$$\overline{P_{max}} = \frac{|X_\theta|^2}{8B_\theta} \tag{5.27}$$

If the control force is only pure damping, the mean absorbed power is given instead by:

$$\overline{P_{abs}} = \frac{|X_\theta|^2}{4(B_\theta + |Z_\theta|)}\left(1 - \frac{(K - |Z_\theta|)^2}{|K + Z_\theta|^2}\right) \tag{5.28}$$

and the maximum absorbed power is obtained when $K = |Z_\theta|$ and is equal to:

$$\overline{P_{max}} = \frac{|X_\theta|^2}{4(B_\theta + |Z_\theta|)} \tag{5.29}$$

5.2.1 Verification and Validation.

To verify the results obtained from the Lagrangian approach just described, the response amplitude operator for the angular displacement obtained through this approach was compared with that obtained through the direct solver from *WAMIT*. Figure 5.2 show two lines associated with these approaches which are almost coincident for most of the wave periods, showing a close agreement of less than 10% for the worst case around the resonant peak.

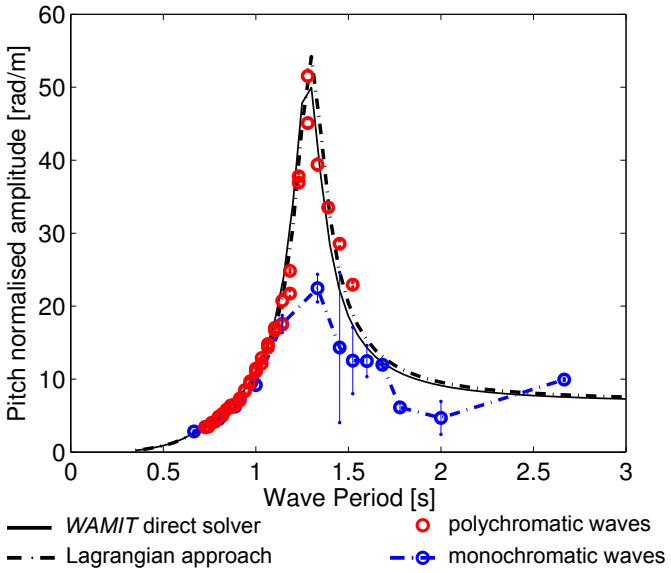

Figure 5.2: *Verification and validation of the one degree of freedom model.*

To validate this simple model and built some confidence in the computation of the hydrodynamic coefficients, some additional tank tests were performed.

The scale model was empty of the inner water and so the air-damper was inoperative. The draft was of $H/D = 0.41$ (see Figure 5.1). The rigid struts were not connected and the position of the axis of rotation was fixed using an external structure.

Two different experiments were performed. The first used a set of 14 regular (or monochromatic) waves with periods between 0.67 s to 2.67 s. It was found that the motion recorded for the different waves was strongly dependent on the location of the model in the tank. That was interpreted as an effect of the non-homogeneous wave field established in the tank due to the interferences with the reflected waves. The validity of the linear assumption require the use of small wave amplitudes and in these experiments waves about 5 mm were used. As shown in Figure 3.7 of section 3.1.1, waves of smaller amplitude are associated with higher reflections and so poorer wave fields. Increasing

the amplitude of the waves could improve the quality of the wave field at the expense of the validity of the linear assumption. The motions for each wave period were measured at least twice for two distinct locations of the scale model inside the tank. The mean value of the amplitude of these motions was used to compute the pitch normalised amplitude, by dividing it by the mean value of the amplitude of the incident waves obtained through a reflection analysis method given by Mansard and Funke [1980]. The standard errors plotted in Figure 5.2 include thus both the error contributions from the measurement of the motion and amplitude of the incident waves.

The second experiment used a set of five polychromatic waves, each composed with eight components with the same target amplitude equal to 3 mm, with each component equally spaced in the frequency range. The most extreme components of the different polychromatic waves were chosen to overlap. The motion was measured twice at only one location of the working area. The normalised amplitudes were obtained by dividing each component of the motion by the amplitude of the corresponding frequency component of the polychromatic incident wave. The amplitude of the motion components were obtained through a fast Fourier transform (FFT) of the measured time series and the incident wave amplitude components through a reflection analysis based on Mansard and Funke [1980] using two lines of three probes and which was described in Section 3.1.1. It should be noted that to avoid the aliasing phenomena associated with the use of a FFT, the components of the polychromatic waves were selected with frequencies such to be an integer number of the reciprocal of the repeat time ($f = n/r_{time}$).

The results are shown in Figure 5.2. For the lower periods the results from the two experiments are very close and within the estimated errors. They are also within *WAMIT* predictions. Greater differences occur at the resonance peak and for the longer waves.

As expected the experiments with monochromatic waves fail to catch the resonance peak predicted by *WAMIT*. This behaviour is found in other experiments of wave energy converters and is normally justified through the non validity of the linearity assumption for the larger amplitudes of the motion experienced that at resonance (see for example Payne [2005]). The present experiments show that these differences are also associated with the non-homogeneity of the wave field which depend on the placement of model in the tank. Only two different locations where considered and as such the associated uncertainties are high. Thus, it is expected to approximate the mean value of the measured motion to the theoretical predictions at the resonance peak as the number of measurements for different locations in the tank increase and also to diminish the associated uncertainty.

The less good agreement with the predictions for the longer waves is interpreted as a result of the deterioration of the wave field as reflections and interference with the incident waves get more important. Also for this case an increase in the number of measurements would probably approximate the measurements to the perditions. But this procedure is very time consuming and normally is not performed extensively.

As can be seen the motion associated with the polychromatic waves follows very closely *WAMIT* estimation catching surprisingly the peak of resonance. The explanation found is that because the polychromatic seas are more energetic the reflected waves are more efficiently absorbed by the wave-makers and beaches and thus their effect is less disturbing for the wave field.

These results suggest that the use of polychromatic waves in tank tests when investigating the dynamics and measuring the motion of a scale models is very advantageous as a closer agreement with predictions is obtained and experiments can be perform in a fraction of time compared with when using regular waves. As a consequence, a higher number incident wave components can be investigated increasing the resolution of the response and allowing the remain tank time to be used for more experiments. Thus, additional tank test experiments should be performed to evaluate this technique and to establish the limits and uncertainties associated with its use.

5.3 Extension to three degrees of freedom: model for the desalination Duck

The equations of motion for the desalination Duck are obtained by extending the approach described in section 5.2 to three degrees of freedom.

The water inside the model is included and considered as a rigid body hinged at the centre of the cylindrical hull. This multi-body approach allows to take into account more accurately the mass distribution for each oscillation cycle by decoupling the mass and moment of inertia of the off-centred cylinder from those of the water inside the model. The inner mass of water is distributed uniformly as half cylinder and is assumed to have a constant geometrical shape which swings around the centre of the cylindrical hull. The angles of oscillation are assumed to be small and so the errors associated with the description of the horizontal free-surface of the fluid should be also small (see Figure 5.3). It should be noted that a more accurate and realistic representation of the inner water would need to account with the instantaneous change of the water level between the two

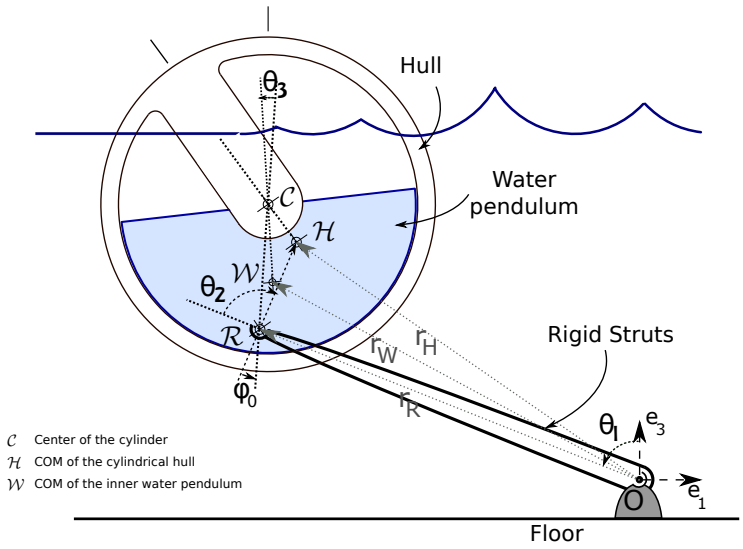

Figure 5.3: *Schematic drawing for the desalination Duck.*

sides of the partition which are proportional to the instantaneous pressure differential. There are also small changes in the mass distribution due to sloshing of the inner water not accounted in the model, whose effects are considered to be small and of second order. Sloshing was observed during tank tests for a very restricted number of wave periods, and this effect did neither affect significantly the measured motion or performance of the scale model. However, it is believed that if necessary, small changes in the design could prevent this effect to occur.

The rigid struts connecting the hull of the Duck to the sea floor are regarded as massless and with no hydrodynamic interaction. The small diameter of these structures does not scatter the incident waves and so the hydrodynamic forces in these structures are much smaller than the forces which affect the cylindrical hull. The effect of these forces is thus considered to be of second order and could be accounted in a more sophisticated model through the integration along the struts length of a modified version of the Morrison equation.

The useful power is obtained by applying a fixed value of damping between the relative motion of the hull and water-pendulum.

The equations of motion are solved for a planar geometry. For this special case, the motion of a non restrained rigid body is described by only three degrees of freedom (two translations plus one rotation). The extension to a three dimensional space which considers six degrees of freedom for each rigid body can be achieved based on the same Lagrangian approach. However this leads to longer and more complex equations.

Four distinct bodies are considered in this problem: 1) the floor, constrained in all variables, 2) the rigid struts, 3) hull and 4) water pendulum constrained for the translations. The degrees of freedom for this system (3) are given by the difference between the number of variables (12) and the total number of constraints (9).

The geometry of the problem is presented in Figure 5.3 and is comparable to a damped triple pendulum excited by an external force.

The relative angles between the bodies are chosen as the generalised coordinates: $\vec{q} = \vec{\theta} = [\theta_1, \theta_2, \theta_3]^T$.

The axis of rotation, the centre of mass of the hull and water pendulum, represented in Figure 5.3 by the points $\mathscr{R}$, $\mathscr{H}$ and $\mathscr{W}$ are given in an inertial reference-frame respectively by the position vectors:

$$\vec{r}_R = [l_1 \sin\theta_1; 0; l_1 \cos\theta_1]^T \tag{5.30a}$$

$$\vec{r}_H = \vec{r}_R + \overrightarrow{RH} \tag{5.30b}$$

$$\vec{r}_W = \vec{r}_R + \overrightarrow{RC} + \overrightarrow{CW} \tag{5.30c}$$

with:

$$\overrightarrow{RH} = [l_2 \sin(\theta_2 + \theta_1); 0; l_2 \cos(\theta_2 + \theta_1)]^T \tag{5.30d}$$

$$\overrightarrow{RC} = [l_0 \sin(\theta_2 + \theta_1 - \varphi_0); 0; l_0 \cos(\theta_2 + \theta_1 - \varphi_0)]^T \tag{5.30e}$$

$$\overrightarrow{CW} = [l_3 \sin(\theta_3 + \theta_2 + \theta_1 - \varphi_0); 0; l_3 \cos(\theta_3 + \theta_2 + \theta_1 - \varphi_0)]^T \tag{5.30f}$$

The total kinetic energies associated with the hull and water pendulum are derived from the square of the linear and angular velocities of the respective centres of mass and from the potential energy from their respective vertical position.

The Lagrangian associated with the system is defined by the difference of the total kinetic energy to the total potential energy, and is given by:

$$\begin{aligned} \mathscr{L} &= (\mathscr{T}_{tr} + \mathscr{T}_{rr})_H + (\mathscr{T}_{tr} + \mathscr{T}_{rr})_W - \mathscr{V}_H - \mathscr{V}_W \\ &= \frac{1}{2}\left(m_H \dot{\vec{r}}_H^2 + I_H \Omega_H^2 + m_W \dot{\vec{r}}_W^2 + I_W \Omega_W^2\right) - g\left(m_H r_{H_3} + m_W r_{W_3}\right) \end{aligned} \tag{5.31}$$

where the subscripts 'H' and 'W' refer to the hull of the Duck and the water pendulum respectively.

The three Lagrangian equations of motion are obtained by differentiating the Lagrangian relatively to each of the generalised coordinates and velocities and by taking the total time derivative relative to the second differentiation as given by:

$$\frac{d}{dt}\left(\frac{\partial \mathscr{L}}{\partial \dot{\theta}_k}\right) - \frac{\partial \mathscr{L}}{\partial \theta_k} - Q_k = 0 \tag{5.32}$$

with $k = 1,2,3$. The generalised forces associated with each generalised coordinate (Q_k) are obtained by considering the virtual work principle. The procedure is very similar to that described in section 5.2.

The body coordinate system is assumed to be attached to the centre of mass of the hull, and so the linear and angular displacements are given respectively by $\Delta\vec{r}_H = \vec{r}_H(t) - \vec{r}_{H_0}$ and $\Delta\beta = \beta(t) - \beta_0 = \theta_1(t) + \theta_2(t) - \theta_{0_1} + \theta_{0_2}$. Both $\vec{r}_{H_0}$ and β_0 are expressed relative to the angles subtended when the Duck is at rest in perfect still water: θ_{0_1}, θ_{0_2} and θ_{0_3}. The linear and angular velocities and accelerations are obtained by differentiating the displacements. These are represented by three component vectors which include both the linear and angular components: $\vec{u}_H = [\dot{\vec{r}}_H; \dot{\beta}]^T$ and $\dot{\vec{u}}_H = [\ddot{\vec{r}}_H; \ddot{\beta}]^T$.

The Cartesian hydrodynamic forces are obtained by substituting the displacements, velocities and accelerations in (5.9) by $\Delta\vec{r}_H$, $\Delta\beta$, $\dot{\vec{u}}_H$, $\ddot{\vec{u}}_H$.

The generalised hydrodynamic forces associated with the two generalised coordinates θ_1 and θ_2 are obtained by following the virtual work principle given by equations (5.4c) and linearised in the same way as in section 5.2.

The final expression of the generalised forces is then:

$$Q_{\theta_j} = Q_{A_{\theta_j}} + Q_{B_{\theta_j}} + Q_{C_{\theta_j}} + Q_{X_{\theta_j}} \tag{5.33a}$$

with $j = 1,2$. The generalised force associated with the relative angle θ_3 is the power-take-off moment, which is assumed to have a fixed damping value:

$$Q_{\theta_3} = -K\dot{\theta}_3. \tag{5.33b}$$

As shown in section 5.2 for the simpler case of only one generalised coordinate, the linear equations of motion in time domain are obtained from (5.32) through linearisation.

To obtain the equations of motion in the frequency domain, the angular displacements, velocities and accelerations are expressed as harmonic functions: $\Delta\theta_k = \theta_k(t) - \theta_{0_k} =$

$\Theta_k \exp(i\omega t)$, $\dot{\theta_k} = i\omega\Delta\theta_k$, $\ddot{\theta_k} = -\omega^2\Delta\theta_k$, with $k = 1,2,3$, and three equations with harmonic terms $\exp(in\omega t)$ $(n = 0,1,2)$ are obtained. These functions are orthogonal and so their coefficients should be zero. By taking the coefficients associated with $\exp(i\omega t)$ a system of three linear equations is obtained.

Rearranging these equations in terms of the complex angular velocities associated with the relative angles θ_1, θ_2 and θ_3 ($\vec{U}_\theta = i\omega[\Theta_1, \Theta_2, \Theta_3]$), an expression for a (3x3) generalised radiation impedance matrix ($\mathbf{Z}_\theta$) is obtained. As for the one degree of freedom case (5.25b), $\mathbf{Z}_\theta$ includes the masses and inertia of the hull and water pendulum and the generalised added mass, hydrodynamic damping and hydrostatic stiffness expressed as a function of the angles θ_1 and θ_2. For reference, the components of $\mathbf{Z}_\theta$ are presented in Table 5.2.

The complex amplitude of the relative angles (Θ_1, Θ_2 and Θ_3) are then obtained by solving the system of three equations represented in matrix notation by:

$$\left(\mathbf{RKR}^T + \mathbf{Z}_\theta\right)\vec{U}_\theta = \vec{X}_\theta \tag{5.34}$$

with $\vec{U}_\theta = i\omega\vec{\Theta}$ taken from the theory of maximum absorption from $m \leqq n$ modes of motion (see for example Evans and Linton [1993]). This theory assumes that only the first m components of the velocity vector of the device ($\vec{U}$) can be controlled and so the control force is written as:

$$\mathbf{F}_C = -\left(\mathbf{RKR}^T\right)\vec{U} \tag{5.35}$$

where $\mathbf{K}$ is a $m \times m$ matrix and $\mathbf{R}$ a $n \times m$ matrix with $R_{ij} = 1$ if $i = j$ and $R_{ij} = 0$ otherwise. In the present case $m = 1$ and $n = 3$, so $\mathbf{K} = [K]$ and $\mathbf{R} = [0,0,1]^T$. The mean absorbed power is then given by:

$$\overline{P_{abs}} = \frac{1}{2}Re\{\mathbf{F}_C^\dagger\vec{U}_\theta\} = \frac{1}{4}\vec{U}^\dagger\mathbf{R}^T\left(\mathbf{K} + \mathbf{K}^\dagger\right)\mathbf{R}\vec{U} \tag{5.36}$$

The performance measured as relative capture width is given by (2.3b):

$$RCW = \frac{CW}{W} = \frac{\overline{P_{abs}}}{\overline{P_w}W}$$

To finish this section a small consideration is given to the estimation of the mooring forces. The experimental tests had shown how important these forces are, and these should be taken into account in the design. However calculation of these forces where left outside the scope of present work.

Generalised linear hydrodynamic forces:
$Q_{\theta_1} = QA_{\theta_1} + QB_{\theta_1} + QC_{\theta_1} + QX_{\theta_1}$
$Q_{\theta_2} = QA_{\theta_2} + QB_{\theta_2} + QC_{\theta_2} + QX_{\theta_2}$
where:
$QA_{\theta_1} = -A_{\theta_{11}}\ddot{\theta}_1 - A_{\theta_{12}}\ddot{\theta}_2$
$QA_{\theta_2} = -A_{\theta_{21}}\ddot{\theta}_1 - A_{\theta_{22}}\ddot{\theta}_2$
$QB_{\theta_1} = -B_{\theta_{11}}\dot{\theta}_1 - B_{\theta_{12}}\dot{\theta}_2$
$QB_{\theta_2} = -B_{\theta_{21}}\dot{\theta}_1 - B_{\theta_{22}}\dot{\theta}_2$
$QC_{\theta_1} = -\Delta\theta_1\left(\rho\forall g\left(l_2\cos(\theta_{02}+\theta_{01})+l_1\cos(\theta_{01})\right)+C_{\theta_{11}}\right) - \Delta\theta_2\left(\rho\forall g\, l_2\cos(\theta_{02}+\theta_{01})+C_{\theta_{12}}\right)$ $-\rho\forall g\left(x_b + l_2\sin(\theta_{02}+\theta_{01})+l_1\sin(\theta_{01})\right)$
$QC_{\theta_2} = -\Delta\theta_1\left(-\rho\forall g\, l_2\cos(\theta_{02}+\theta_{01})+C_{\theta_{21}}\right) - \Delta\theta_2\left(\rho\forall g\, l_2\cos(\theta_{02}+\theta_{01})+C_{\theta_{22}}\right) -$ $\rho\forall g\left(x_b + l_2\sin(\theta_{02}+\theta_{01})\right)$
$QX_{\theta_1} = A\,e^{i\omega t}\left[X_{\theta_1} - (\Delta\theta_1\,(X_1\,(l_2\sin(\theta_{02}+\theta_{01})+l_1\sin(\theta_{01}))+X_3\,(l_2\cos(\theta_{02}+\theta_{01})+l_1\cos(\theta_{01})))\right.$ $\left.+\Delta\theta_2\,(X_1\,l_2\sin(\theta_{02}+\theta_{01})+X_3\,l_2\cos(\theta_{02}+\theta_{01})))\right]$
$QX_{\theta_2} = A\,e^{i\omega t}X_{\theta_2} - A\,e^{i\omega t}\,((\Delta\theta_1+\Delta\theta_2)(+X_3\,l_2\cos(\theta_{02}+\theta_{01})+X_1\,l_2\sin(\theta_{02}+\theta_{01})))$
Components of the generalised added mass matrix:
$A_{\theta_{11}} = (l_2\cos(\theta_{02}+\theta_{01}+l_1\cos(\theta_{01}))^2\,A_{11} - 2\,(l_2\cos(\theta_{02}+\theta_{01})+l_1\cos(\theta_{01}))\,(l_2\sin(\theta_{02}+\theta_{01})+l_1\sin(\theta_{01}))\,A_{13}$ $+2\,(l_2\cos(\theta_{02}+\theta_{01})+l_1\cos(\theta_{01}))\,A_{15} + (l_2\sin(\theta_{02}+\theta_{01})+l_1\sin(\theta_{01}))^2\,A_{33}$ $-2\,(l_2\sin(\theta_{02}+\theta_{01})+l_1\sin(\theta_{01}))\,A_{35} + A_{55}$
$A_{\theta_{12}} = A_{\theta_{21}} = l_2\cos(\theta_{02}+\theta_{01})\,(l_2\,cos(\theta_{02}+\theta_{01})+l_1\,cos(\theta_{01}))\,A_{11}$ $-l_2\,(2l_2\cos(\theta_{02}+\theta_{01})\sin(\theta_{02}+\theta_{01})+l_1\cos(\theta_{01})\sin(\theta_{02}+\theta_{01})+l_1\sin(\theta_{01})\cos(\theta_{02}+\theta_{01}))\,A_{13}$ $+(2l_2\cos(\theta_{02}+\theta_{01})+l_1\cos(\theta_{01}))\,A_{15} + l_2\sin(\theta_{02}+\theta_{01})\,(l_2\sin(\theta_{02}+\theta_{01})+l_1\sin(\theta_{01}))\,A_{33}$ $-(2l_2\,sin(\theta_{02}+\theta_{01})+l_1\sin(\theta_{01}))\,A_{35} + A_{55}$
$A_{\theta_{22}} = l_2^2\cos^2(\theta_{02}+\theta_{01})\,A_{11} - 2l_2^2\cos(\theta_{02}+\theta_{01})\,sin(\theta_{02}+\theta_{01})\,A_{13} + 2l_2\cos(\theta_{02}+\theta_{01})\,A_{15}$ $+l_2^2\sin^2(\theta_{02}+\theta_{01})\,A_{33} - 2l_2\sin(\theta_{02}+\theta_{01})\,A_{35} + A_{55}$
Components of the generalised hydrodynamic matrix:
$B_{\theta_{11}} = +(l_2\cos(\theta_{02}+\theta_{01})+l_1\cos(\theta_{01}))^2\,B_{11} - 2\,(l_2\cos(\theta_{02}+\theta_{01})+l_1\cos(\theta_{01}))\,(l_2\sin(\theta_{02}+\theta_{01})+l_1\sin(\theta_{01}))\,B_{13}$ $+2\,(l_2\cos(\theta_{02}+\theta_{01})+l_1\cos(\theta_{01}))\,B_{15} + (l_2\sin(\theta_{02}+\theta_{01})+l_1\sin(\theta_{01}))^2\,B_{33}$ $-2\,(l_2\sin(\theta_{02}+\theta_{01})+l_1\sin(\theta_{01}))\,B_{35} + B_{55}$
$B_{\theta_{12}} = B_{\theta_{21}} = l_2\cos(\theta_{02}+\theta_{01})\,(l_2\cos(\theta_{02}+\theta_{01})+l_1\cos(\theta_{01}))\,B_{11}$ $-l_2\,(2l_2\cos(\theta_{02}+\theta_{01})\sin(\theta_{02}+\theta_{01})+l_1\cos(\theta_{01})\sin(\theta_{02}+\theta_{01})+l_1\sin(\theta_{01})\cos(\theta_{02}+\theta_{01}))\,B_{13}$ $+(2l_2\cos(\theta_{02}+\theta_{01})+l_1\cos(\theta_{01}))\,B_{15} + l_2\sin(\theta_{02}+\theta_{01})\,(l_2\sin(\theta_{02}+\theta_{01})+l_1\sin(\theta_{01}))\,B_{33}$ $-(2l_2\sin(\theta_{02}+\theta_{01})+l_1\sin(\theta_{01}))\,B_{35} + B_{55}$
$B_{\theta_{22}} = l_2^2\cos^2(\theta_{02}+\theta_{01})\,B_{11} - 2l_2^2\cos(\theta_{02}+\theta_{01})\sin(\theta_{02}+\theta_{01})\,B_{13} + 2l_2\cos(\theta_{02}+\theta_{01})\,B_{15}$ $+l_2^2\sin^2(\theta_{02}+\theta_{01})\,B_{33} - 2l_2\sin(\theta_{02}+\theta_{01})\,B_{35} + B_{55}$
Components of the generalised hydrostatic stiffness matrix:
$C_{\theta_{11}} = +(l_2\sin(\theta_{02}+\theta_{01})+l_1\sin(\theta_{01}))^2\,C_{33} - 2\,(l_2\sin(\theta_{02}+\theta_{01})+l_1\sin(\theta_{01}))\,C_{35} + C_{55}$
$C_{\theta_{12}} = C_{\theta_{21}} = +l_2\sin(\theta_{02}+\theta_{01})\,(l_2\sin(\theta_{02}+\theta_{01})+l_1\sin(\theta_{01}))\,C_{33} - (2l_2\sin(\theta_{02}+\theta_{01})+l_1\sin(\theta_{01}))\,C_{35} +$ C_{55}
$C_{\theta_{21}} = +l_2^2\sin^2(\theta_{02}+\theta_{01})\,C_{33} - 2l_2\sin(\theta_{02}+\theta_{01})\,C_{35} + C_{55}$
Components of the generalised wave excitation force:
$X_{\theta_1} = +(l_2\cos(\theta_{02}+\theta_{01})+l_1\cos(\theta_{01}))\,X_1 - (l_2\sin(\theta_{02}+\theta_{01})+l_1\sin(\theta_{01}))\,X_3 + X_5$
$X_{\theta_2} = +l_2\,cos(\theta_{02}+\theta_{01})\,X_1 - l_2\sin(\theta_{02}+\theta_{01})\,X_3 + X_5$

Table 5.1: *Components of the generalised forces Q_{θ_j} ($j = 1,2$).*

Components of the generalised radiation impedance matrix:

$$Z_{\theta_{11}} = i\,\omega\left[I_W + I_H + m_W\left(l_0^2 + l_1^2 + l_3^2 + 2\,l_1\,l_3\cos\left(\theta_{03}+\theta_{02}-\varphi_0\right) + 2\,l_0\,l_3\cos\left(\theta_{03}\right) + 2\,l_0\,l_1\cos\left(\theta_{02}-\varphi_0\right)\right)\right.$$
$$+ m_H\left(l_1^2 + l_2^2 + 2\,l_1\,l_2\cos\left(\theta_{02}\right)\right) + \frac{1}{\omega^2}\left(m_W\,g\left(l_0\cos\left(\theta_{02}+\theta_{01}-\varphi_0\right)\right.\right. \quad -l_2\cos\left(\theta_{02}+\theta_{01}\right)$$
$$\left.\left.+ l_3\cos\left(\theta_{03}+\theta_{02}+\theta_{01}-\varphi_0\right)\right) - C_{\theta_{11}}\right) + A_{\theta_{11}}\left.\right] + B_{\theta_{11}}$$

$$Z_{\theta_{12}} = i\,\omega\left[I_W + I_H + m_W\left(l_0^2 + l_3^2 + l_1\,l_3\cos\left(\theta_{03}+\theta_{02}-\varphi_0\right) + 2\,l_0\,l_3\cos\left(\theta_{03}\right) + l_0\,l_1\cos\left(\theta_{02}-\varphi_0\right)\right)\right.$$
$$+ m_H\left(+l_2^2 + l_1\,l_2\cos\left(\theta_{02}\right)\right) + \frac{1}{\omega^2}\left(m_W\,g\left(l_0\cos\left(\theta_{02}+\theta_{01}-\varphi_0\right) - l_2\cos\left(\theta_{02}+\theta_{01}\right)\right.\right.$$
$$\left.\left.+ l_3\cos\left(\theta_{03}+\theta_{02}+\theta_{01}-\varphi_0\right)\right) - C_{\theta_{12}}\right) + A_{\theta_{12}}\left.\right] + B_{\theta_{12}}$$

$$Z_{\theta_{13}} = i\,\omega\left[I_W + m_W\left(l_3^2 + l_0\,l_3\cos\left(\theta_{03}\right) + l_1\,l_3\cos\left(\theta_{03}+\theta_{02}-\varphi_0\right) + \frac{1}{\omega^2}\,g\,l_3\cos\left(\theta_{03}+\theta_{02}+\theta_{01}-\varphi_0\right)\right)\right]$$

$$Z_{\theta_{21}} = i\,\omega\left[I_W + I_H + m_W\left(l_3^2 + l_0^2 + l_1\,l_3\cos\left(\theta_{03}+\theta_{02}-\varphi_0\right) + 2\,l_0\,l_3\cos\left(\theta_{03}\right) + l_0\,l_1\cos\left(\theta_{02}-\varphi_0\right)\right)\right.$$
$$+ m_H\left(l_2^2 + l_1\,l_2\cos\left(\theta_{02}\right)\right) + \frac{1}{\omega^2}\left(m_W\,g\left(l_0\cos\left(\theta_{02}+\theta_{01}-\varphi_0\right) - l_2\cos\left(\theta_{02}+\theta_{01}\right)\right.\right.$$
$$\left.\left.\left.+ l_3\cos\left(\theta_{03}+\theta_{02}+\theta_{01}-\varphi_0\right)\right) + A_{\theta_{21}} - C_{\theta_{21}}\right)\right] + B_{\theta_{21}}$$

$$Z_{\theta_{22}} = i\,\omega\left[I_W + I_H + m_W\left(l_3^2 + l_0^2 + 2\,l_0\,l_3\cos\left(\theta_{03}\right)\right) + m_H\,l_2^2 + \frac{1}{\omega^2}\left(m_W\,g\left(l_0\cos\left(\theta_{02}+\theta_{01}-\varphi_0\right)\right.\right.\right.$$
$$\left.\left.\left.- l_2\cos\left(\theta_{02}+\theta_{01}\right) + l_3\cos\left(\theta_{03}+\theta_{02}+\theta_{01}-\varphi_0\right)\right) - C_{\theta_{22}}\right) + A_{\theta_{22}}\left.\right] + B_{\theta_{22}}$$

$$Z_{\theta_{23}} = i\,\omega\left[I_W + m_W\left(l_3^2 + l_0\,l_3\cos\left(\theta_{03}\right) + \frac{1}{\omega^2}\,g\,l_3\cos\left(\theta_{03}+\theta_{02}+\theta_{01}-\varphi_0\right)\right)\right]$$

$$Z_{\theta_{31}} = i\,\omega\left[I_W + m_W\left(l_3^2 + l_1\,l_3\cos\left(\theta_{03}+\theta_{02}-\varphi_0\right) + l_0\,l_3\cos\left(\theta_{03}\right) + \frac{1}{\omega^2}\,g\,l_3\cos\left(\theta_{03}+\theta_{02}+\theta_{01}-\varphi_0\right)\right)\right]$$

$$Z_{\theta_{32}} = i\,\omega\left[I_W + m_W\left(l_3^2 + l_0\,l_3\cos\left(\theta_{03}\right) + \frac{1}{w^2}\,g\,l3\cos\left(\theta_{03}+\theta_{02}+\theta_{01}-\varphi_0\right)\right)\right]$$

$$Z_{\theta_{33}} = i\,\omega\left(I_W + m_W\left(l_3^2 + \frac{1}{\omega^2}\,g\,l_3\cos\left(\theta_{03}+\theta_{02}+\theta_{01}-\varphi_0\right)\right)\right)$$

Table 5.2: *Components of the generalised radiation impedance matrix ($\mathbf{Z}_\theta$).*

In the present section, the equations of motion for the desalination Duck were derived using the Lagrangian approach. One of the main advantages is the simplification of the mathematical treatment by the introduction of independent generalised coordinates. Those are sufficient to fully determine the problem and there is no need to take into account the constraint forces, as those do not produce virtual work.

However, the constraint forces can still be determined with a Lagrangian approach if 'superfluous' coordinates are introduced. The Lagrangian equations can then be re-written with these 'superfluous' coordinates regarded as if they were independent, and the forces of constraint are introduced as if were pure applied forces (see for example Goldstein et al. [2000, §2.4]).

There is still an alternative procedure that can be used to compute the constraint forces. This alternative considers the reformulation of the problem in terms of the classical Newton-Euler approach as given by equations (5.1). Then, the knowledge of the motions obtained by previously solving the problem with the Lagrangian approach can be used to solve the forces of constraint in the Newton-Euler equations.

5.3.1 Validation.

Figure 5.4 shows the comparisons between the tank measurements described in section 3.4.1 and the calculations from the multi-body semi-analytical model. In these only two values of damping are shown and a more detailed comparison for the other settings is given in Appendix C (Figures C.2, C.3, C.4, C.5, C.6, C.7).

The surge ($\hat{\xi}_1$) and heave ($\hat{\xi}_3$) normalised amplitudes are related to the amplitude of the angle of the struts (Θ_1) through the approximate relationships:

$$\hat{\xi}_1 \approx l_1 |\Theta_1| \cos\theta_{01} \tag{5.37}$$

$$\hat{\xi}_3 \approx l_1 |\Theta_1| \sin\theta_{01} \tag{5.38}$$

The pressure normalised amplitude is derived from the relative angle between the hull and water pendulum (Θ_3) by taking into account the linear damping relationship which assumes torque proportional to the angular velocity ($\tau = -K_0 \dot{\theta}$). Torque is proportional to the pressure across the damper ($\tau = \Delta p \, S_d \, d$) and the angular velocity to the angle ($\dot{\theta}_3 = i\,\omega\,\theta_3$). The final expression is given by:

$$\Delta\hat{p} = \frac{i\,\omega K_0}{S_d\, d\, \rho\, g}\,\Theta_3 \tag{5.39}$$

where S_d is the bulkhead area of the pneumatic damper and d the vertical distance from the axis of rotation to the damper horizontal centre line.

All plots in Figure 5.4 and also in Appendix C, except for the phases (Figure 5.4(f)), show a reasonable agreement between the semi-analytical model and the measured data fitting in many cases within the measurement error intervals.

The differences however can be explained through the inherent difficulties associated with the measurements in a 3D wave basin, in particular the rigorous determination of the incident wave field amplitude. The agreement is in general better for the shorter waves in the region where the wave-filed is known to have better quality and experiments to perform better. The results for the very long waves with period $T > 1.5$ s should be considered carefully as there is an inherent interference pattern in the wave field as the beaches do not absorb these waves as efficiently as the short ones.

As it was pointed out in section 5.2.1 an increase in the number of measurements of the motions with the monochromatic waves is likely to approximate the measurements to the predictions and the use of polychromatic waves to validate the motions would be beneficial to increase the wave period resolution.

The plots for the phase difference include the addition of a fixed angle equal to $\pi/2$ to the computed phases. Taking this into account, the phase differences between pitch and pressure for the lower values of applied damping show a reasonable agreement (Figures C.7 (a) to (c)) but this agreement degrades significantly for the higher values of applied damping.

At resonance ($T \approx 2.0$ s) the relative capture width increases with applied damping to reach a maximum of approximately 1.9 when damping is about 30.1 Nms. However, this maximum value is attained at the expense of the performance outside resonance and with the reduction of the absorption bandwidth as damping is increased.

Figure 5.5 show the variation with applied fixed damping of the normalised amplitudes for the motions, pressure and relative capture width associated with regular waves with nine significant periods. Equivalent plots with measured RMS amplitudes for the motions and pressures are presented in Figure 3.29.

An alternative approach to maximise the captured power would be to select the fixed value of damping which would present the best performance for the overall wave period interval of interest. Figure 5.5(e) suggest that such value would be of about 2.0 Nms for

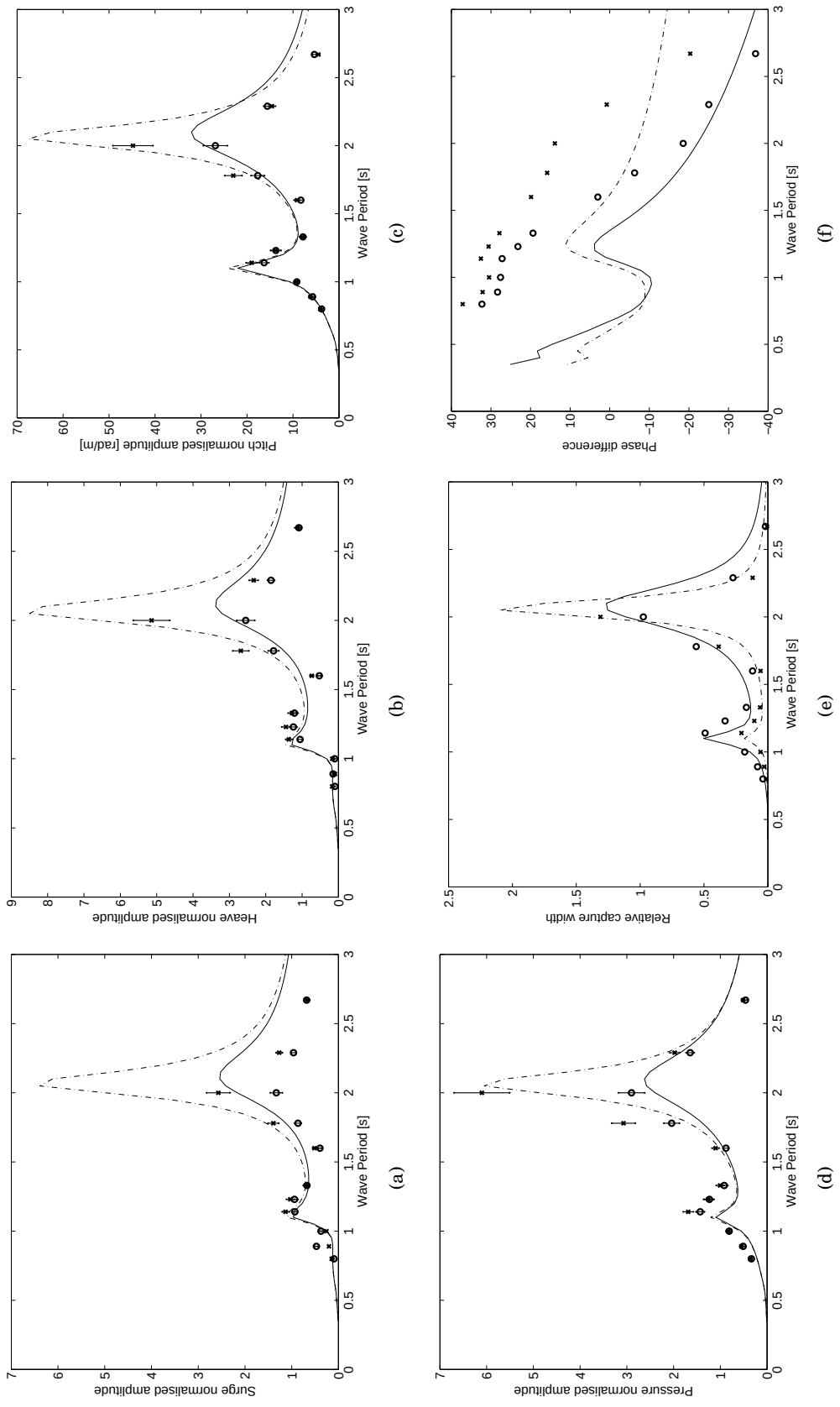

Figure 5.4: *Validation of the multi-body model for the desalination Duck. Comparison between measured and estimated quantities for two values of applied damping. The measurements were performed with a scale model and are described in section 3.4.1. The same quantities were computed with the semi-analytical model described in this section. Normalised amplitudes for a) surge b) heave c) pitch d) pressure, e) relative capture width and f) phase difference between pitch and pressure.*

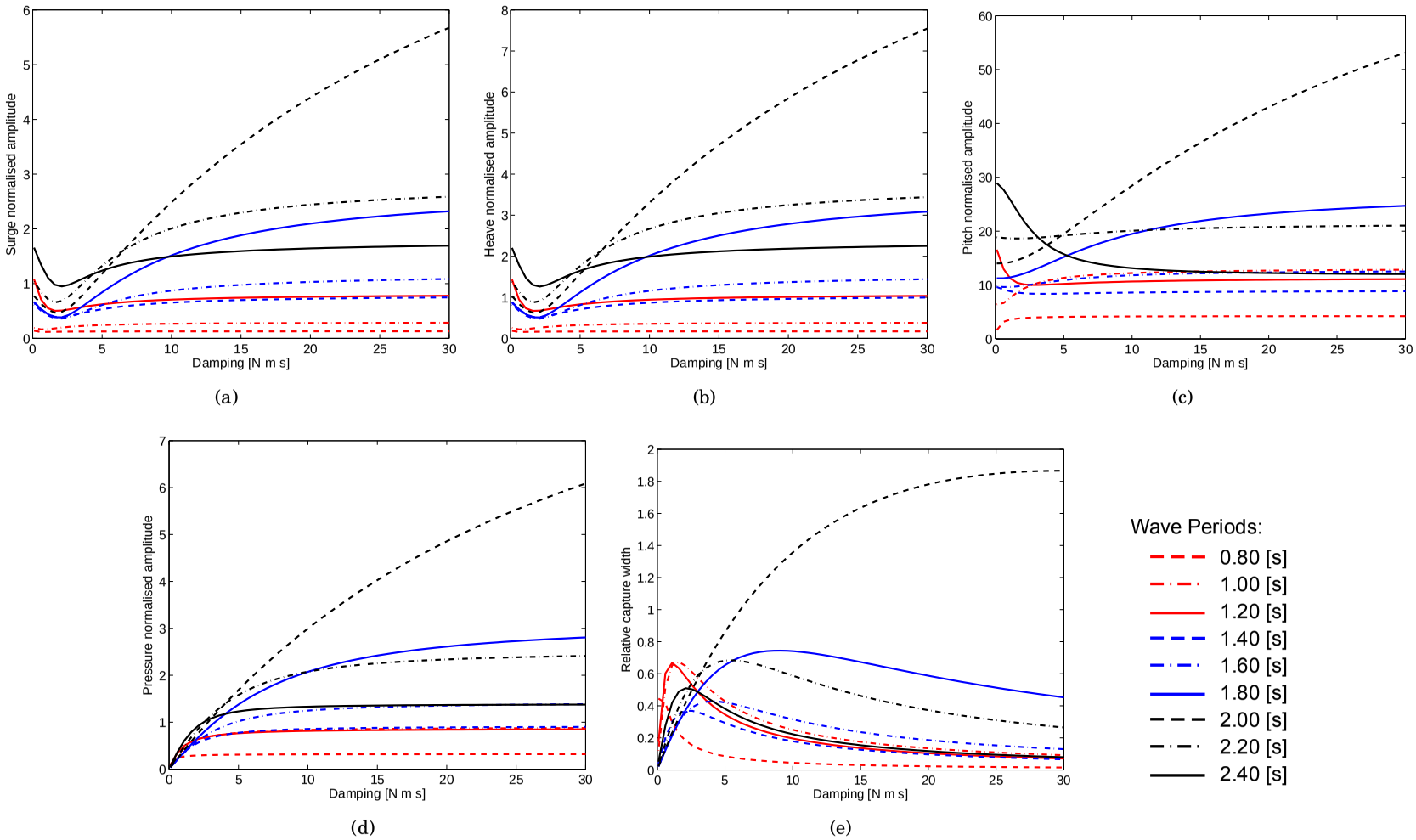

Figure 5.5: *Variation of several quantities computed by the semi-analytical model with applied damping for nine incident wave periods. a) Surge b) heave c) pitch d) pressure normalised amplitudes e) relative capture width.*

which the relative capture width would have consistent values higher than 0.35 but for most wave periods lower than 0.6.

At this point it should be stressed that relative capture width defined by expression (2.3b) is only valid when applied to monochromatic waves and can only serve as a qualitative indicator of the performance of a device in spectral seas. In mixed seas, the relative capture width should be computed instead as given by (2.11).

Figure 5.6(a) show the theoretical relative capture width for mixed seas associated with configurations of the desalination Duck with different locations of the off-centred axis and with a fixed pneumatic damping equal to 3.0×10^4 Nm^{-5} s. The spectra (modified Pierson-Moskowitz type) were chosen with energy periods between 5 to 15 s and with the same significant wave height. The curves were selected by visual inspection such to maximise the performance in these seas. The performance associated with the configuration which was used in regular waves tests, with $\alpha_0 = 55°$, $l_0/(D/2) = 0.60$ is also shown for comparison. It is apparent that this configuration is not the optimal as performance can be improved in almost all seas. The best performance curve is obtained when the off-centred axis is placed at $\alpha_0 = 5°$, $l_0/(D/2) = 0.49$. This configuration was tested in mixed seas, as shown in section 3.4.2, with better performance than the other case ($\alpha_0 = 55°$, $l_0/(D/2) = 0.60$), however, at the expense of larger mooring forces as seen in Figure 3.34.

Figure 5.6(b) show the comparison between the measured experimental performance and the expected theoretical for the two configurations tested in mixed seas (section 3.4.2). The theoretical curves and the measured values follow the same trend, but the measured performances are much lower in both configurations. This loss in performance can be justified by the non-linearities in the system and by the friction losses associated with both the mechanics (bearings, damper, etc) and the fluid. As it was pointed out in section 3.4.2, important energy losses by dissipation associated with the sharp corners and edges of the scale model are recognised in the creation of vortices at these locations. It is therefore expected an increase in performance by redesigning the scale model with soften edges and corners.

It should also be pointed out that the measured average power per unit front length for certain seas is overestimated. The formula which was used (2.9) is only valid for deep water conditions and for most wavelengths in tested mixed seas, intermediate water depths should apply.

A maximum average energy production over the year can be estimated through the theoretical relative capture width and the bi-frequency histogram given by Table 3.11. However, it should be understood that this value gives an overestimation which is well above any practical achievable value. Beyond the idealised performance curve which is based in linear theory and does not takes into account any friction losses, the histogram does not include any information on the directionality of the sea waves. It is thus expected some decrease in performance for such cases in which the prototype would not align with the incoming waves. Nevertheless such an exercise defines the maximum boundary for the expectations of energy productions over the year by deploying a desalination Duck scheme at Lanzarote. So, taking into account all these limitations the averaged energy absorbed over the year is equal to 114.0 MWh/m (of wave front) which corresponds to about half the energy available at this location which is equal to 228.8 MWh/m (and averages to 26.1 kW/m). So, taking into account all idealisations considered above, a cylindrical desalination Duck scheme with 12 m diameter by 30 m long would be able to absorb from the sea in one year the total amount of energy equal to 3.4 GWh.

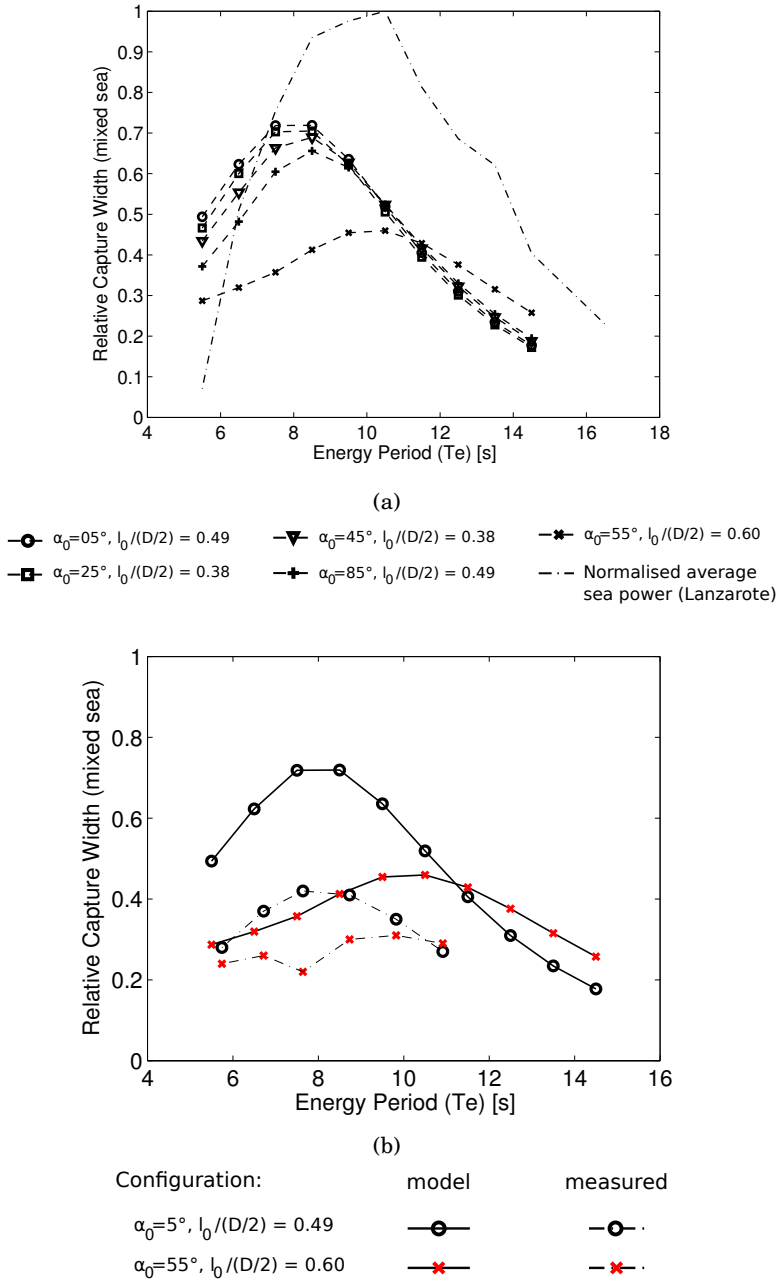

Figure 5.6: *(a) Theoretical relative capture width for mixed seas associated with different configurations of the desalination Duck. Pneumatic damping was fixed and equal to* 3.0×10^4 Nm^{-5} s. α_0 *and* l_0 *are relative to the location of the off-centred axis and given in Figure 3.26. The normalised yearly average power that occur in the sea at Lanzarote is also shown for comparison (see bi-frequency Table 3.11). (b) Comparison between the measured experimental performance and the expected theoretical for the two configurations tested in mixed seas (see section 3.4.2).*

Chapter 6
Summary of most important findings, conclusions and future work

The chapter being presented now aims to summarise and to give acquaintance of the main findings and conclusions that can be taken from the present dissertation. It also intends to describe paths which were not followed and to provide some guidance for future work.

The present work further develops the concept of a wave energy converter (WEC) that has been recently studied at the University of Edinburgh and which is known as the desalination Duck. The most recent design for this WEC evolved the asymmetric profile of the cam into a circular horizontal cylinder with an off-centred axis. The dynamics and performance associated with this device are studied both experimentally and theoretically.

Hydrodynamic properties of horizontal cylinders

The hydrodynamic properties and dynamics associated with submerged horizontal cylinders are of central concern in the present dissertation. The dynamics of an horizontal cylinder which is constraint to oscillate around an off-centred axis as a result of its interactions with water waves is studied in detail for the case of a cylinder piercing the free-surface and fully-submerged.

The hydrodynamic coefficients and excitation forces for these cylinders are computed numerically throughout a commercial software package called *WAMIT* to include cylinders with different widths and drafts at different water depths. Furthermore, these properties are extended to the case of a cylinder with an off-centred axis through the use of transformation formulas specifically derived for the effect (see Section 4.3 and Appendix A). The key findings associated with this topic (Sections 4.2 and 4.3) are summarised in the following bullet points:

- The hydrodynamic added mass and damping for a three dimensional fully-submerged cylinder of finite width are different in surge and heave. This result differs from the two dimensional cylinder considered by Evans and proposed for the Bristol cylinder WEC, for which both added mass and damping are equal in surge and heave directions. It was also found that as the width of the fully-submerged cylinder increases, the hydrodynamic coefficients in surge and heave tend to each other and to known values published for two dimensional cylinders by Greenhow and Ahn [1988].

- The characteristic curves associated with the hydrodynamic coefficients for finite width cylinders, piercing the free-surface at different drafts and fully-submerged at different levels of submergence, show a similar trend as known for the two dimensional cylinders, presented by Greenhow and Ahn [1988] (Figure 4.8).

- The phenomena of negative added mass was identified for the cases when the fully-submerged cylinder is very close to the free surface or when the free-surface piercing cylinder is almost fully submerged. For these cases, it was also identified very rapid changes in the hydrodynamic damping in the frequency dependence, specially in heave, which might be related with singularities of this quantity for certain wave frequencies as presented by Evans and Porter [2007] (trapped modes) (Figure 4.9 and 4.10).

- For the shallower water depths, and for both fully-submerged and surface piercing cylinder moving in surge mode, the hydrodynamic damping has a slower variation for the the longer wavelengths when compared with deeper water depths and thus have larger values at these wavelengths. In the heave mode, damping shows different trends for the fully-submerged and surface-piercing cylinder: for the fully submerged cylinder, damping is in general smaller for swallower water depths, whereas for the surface-piercing cylinder, the trend is complex and shows that for the longer wavelengths damping might be larger for shallower water depths (see Figure 4.11 and 4.12).

- The location of the off-centred axis is expressed as a distance to the centre (l_0) and angle to the horizontal plane (α_0) (Figure 4.6) and it is shown that the non-dimensional values of the hydrodynamic coefficients and excitation forces at the off-centred axis only depend on the variable α_0 and not on the distance l_0.

- The dependencies of the hydrodynamic coefficients and excitation forces with the angle α_0 are complex for both cylinders piercing the free-surface or

fully-submerged, as shown in Figures 4.14 and 4.15 (for cylinder with $H/D = 0.85$ and $H/D = 1.10$ for $W/D = 2.5$). The hydrodynamic damping in pitch, for the fully-submerged cylinder vanishes for the larger and smaller wavelengths, and has a maximum at λ/D between 5 to 7.5, which increases and shifts towards the larger wavelengths with decreasing α_0. For the free-surface piercing cylinder, the hydrodynamic damping in pitch, vanishes for the larger and shorter wavelengths and has a maximum at about $\lambda/D = 6$ which decreases with decreasing values of α_0 and tends to zero as α_0 approaches this value.

One degree of freedom model

In Section 4.5, the performance associated with an off-centred cylinder Duck is analysed through a linear semi-analytical model in one degree of freedom in the frequency domain. Both cases of a fully-submerged and free-surface piercing cylinder, at different drafts and submergence levels are considered. The hydrodynamic forces and moments at the off-centred axis are computed through the transformation formulas presented in Section 4.3 for a cylinder with fixed width ratio ($W/D = 2.5$) in deep water.

Three design cases, with cylinders of diameters equal to 20 m, 12 m and 6 m, were considered in a step by step optimisation of the performance associated with four variables: draft and level of submergence (H), mass distribution (J) and location of the off-centred axis (angular (α_0) and radial (l_0). These parameters were chosen to maximise the performance for an incident wave period equal to $T = 9$ s, which is close to the energy period with higher long term occurrence at a site located near Lanzarote (Canaries Islands).

The key findings associated with Section 4.5 are summarised in the following bullet points:

- The distance l_0 (from the centre of the cylinder to its off-centred axis), does not influence the maximum average absorbed power ($\overline{P_{max}}$) obtained through a complex conjugate power-take-off system. This distance is inversely proportional to the optimum velocity amplitude (U_O) required to achieve $\overline{P_{max}}$, and so l_0 is limited in practical terms to achievable amplitudes of U_O.

- The maximum average absorbed power ($\overline{P_{max}}$) depends strongly on the angle α_0. This angle also controls the contribution of heave and surge modes to $\overline{P_{max}}$: when $\alpha_0 = 0°$, only heave contributes to $\overline{P_{max}}$, whereas when $\alpha_0 = 90°$ only surge contributes.

- With α_0 selected to maximise $\overline{P_{max}}$ for a incident wave period $T = 9$ s, the draft and submergence ratios (H/D) with best performance are equal to $H/D = 0.70$ and 1.10 for the free-surface piercing and fully-submerged cylinder (see Figure 4.19).

- Considering a controller which uses only pure damping, the total mass of the device can be distributed to balance the hydrostatic stiffness and added mass terms such to make the device resonate at a certain incident wave period.

- The ideal distribution of mass to satisfy the resonance condition depends on the location of the off-centred axis. For a certain location of the off-centred axis, if the mass is distributed ideally to satisfy the resonance condition at certain incident wave period, the maximum performance achieved with an optimum damping controller does not depend much on the location of the off-centred axis (see Figure 4.21).

A comparison of the performance for regular and irregular waves is made for fully submerged and free-surface piercing cylinders (at H/D = 1.10 and H/D = 0.70 respectively), with diameters equal to 20 m, 12 m and 6 m, with its off-centred axis located at $l_0 = 0.75$ and with α_0 and the mass distributed such to maximise the absorbed power at an incident wave period equal to 9 s (and thus for wavelength ratios equal to $\lambda/D = 6$, 10 and 20 respectively, see Figure 4.23).

A fixed damping controller is also investigated and damping is selected following the recommendations given by Count [1978] to obtain an energy absorption characteristics with a large bandwidth. Thus the value of applied damping is selected as being equal to 0.9 of maximum hydrodynamic damping which occurs at a wavelength of about six times the diameter of the cylinder ($\lambda/D = 6$).

- For both regular and mixed seas it was found that the performances of the free-surface piercing and fully submerged cylinder are comparable for the diameters equal to 6 m and 12 m. For the cylinder with diameter equal to 20 m the fully submerged cylinder showed a better performance for the longer wavelengths than the free-surface piercing cylinder.

- The best performances associated with regular waves are (see Figure 4.24):

  - For the cylinder with D = 20 m: RCW_{max} = 1.1 and $RCW > 0.8$ for wave periods between 8 s to 11.7 s.

  - For the cylinder with D = 12 m RCW_{max} = 1.14 and $RCW > 0.8$ for wave periods between 6.3 s to 9.6 s.
  - For the cylinder with D = 6 m RCW_{max} = 0.5 and $RCW > 0.4$ for wave periods between 3.0 sto 7.6 s.

- For mixed seas the performances were evaluated for a Bretschneider spectra (with Te between 6 s to 16 s). The maximum value of RCW was found to be equal to 0.75 for the free-surface piercing cylinder with 12 m diameter.

- Adopting the long term bi-frequency histogram for a location near Lanzarote (Canary Islands), the average absorbed energy over a year for the *free-surface piercing cylinder* is equal to:

  - $\overline{E}$ = 4.7 GWh, for a cylinder with 20 m by 50m ($D \times W$);
  - $\overline{E}$ = 2.8 GWh, for a cylinder with 12 m by 30 m , and
  - $\overline{E}$ = 0.5 GWh, for a cylinder with 6 m by 15 m ;

  and for the *fully-submerged cylinder* is equal to:

  - $\overline{E}$ = 6.1 GWh, for a cylinder with 20 m by 50 m;
  - $\overline{E}$ = 2.7 GWh, for a cylinder with 12 m by 30 m;
  - $\overline{E}$ = 0.5 GWh, for a cylinder with 6 m by 15 m.

- The reaction forces at the off-centred axis were computed for regular waves and it was found that the non-dimensional forces in the horizontal direction are higher than in the vertical direction with a peak value of about 1.8, occurring for a wavelength close to where hydrodynamic damping has a maximum (at $\lambda/D \approx 6$). For cylinders with different diameters, this value corresponds to:

  - 1.59 MN/m (Cylinder with 6 m, by 15 m) (which is 162 tone-force/m of incident wave amplitude);
  - 6.36 MN/m (Cylinder with 12m by 30m) (which 648 tone-force/m of incident wave amplitude);
  - 17.66 MN/m (Cylinder of 20m by 50m) (which is 1800 tone-force/m of incident wave amplitude).

Desalination Duck: Multi-body model and experimental tests

The desalination Duck uses its nodding motion in the waves to directly drive a distillation process, known as vapour-compression desalination. The mechanical work required to drive this process is provided by a positive displacement double acting pump of large volume, obtained by partially filling the inside of the Duck with water, and placing a central partition to divide the remaining interior volume into two separate compartments. As the device undergoes wave-driven alternating rotations, the surface of the inner water tends to stay relatively horizontal, and the continuous variation of alternating volume of the compartments results in the pumping action. This version of the Duck is connected to the sea bed through two rigid struts, which join together at the opposite end (as a 'V'), and connect to a universal joint in the sea bed, to allow the system to automatically align to the direction of most energetic sea.

A semi-analytical model is derived to describe the dynamics of the desalination Duck. It is based on a Lagrangian formulation of the equations of motion for multiple rigid bodies, and includes both the influence of the rigid struts and the water inside the device, the later being considered as a rigid body, hinged at the centre of the cylindrical hull. Energy is taken from the system by linearly damping the relative motion of the inner water-pendulum to the cylindrical hull. The rigid struts are considered as massless and with no hydrodynamic interaction. Viscous forces are neglected and the hydrodynamic forces in the hull are considered to be the dominant applied forces to take into account.

The Lagrangian formulation as the advantage, when compared with the more usual Newton-Euler approach, to reduce the number of equations to be solved to a minimum number, equal to the number of degrees of freedom of the system. The reaction forces between the various elements in the system do not need to be included and only the external applied forces are considered.

This system as three degrees of freedom, defined by the relative angles between the rigid struts, hull and water pendulum, which are taken as the generalised coordinates. The hydrodynamic forces are considered to be the only applied forces, and are introduced as generalised forces through the principle of virtual work. A system of three equations in three the generalised coordinates (relative angles) is obtained, and by considering small harmonic motions, the equations are further linearised and converted to the frequency domain. Analogous forms of the radiation impedance, hydrodynamic coefficients and excitation forces as function of the generalised coordinates is obtained in the process, and the theory of maximum absorption from $m < n$ modes of motion is applied to calculate the absorbed power.

The process to obtain the generalised forces and to linearise the Lagrange equations of motion in the frequency domain is shown in detail for a simpler system with only one degree of freedom (Section 5.2). The results from this approach are verified and validated with direct comparisons with *WAMIT* and with scale model measurements in the wave tank. In these experiments, the scale model was restrained to move only in pitch and the inner water pendulum was not included. For this arrangement the draft was equal to $H/D = 0.41$. The tank tests considered monochromatic waves with different periods, and a set of polychromatic waves, each with eight frequency components selected with the same target amplitude. The key findings associated with these tests are summarised bellow:

- A very close agreement was found between the pitch motion obtained from the Lagrangian approach model and direct solver from *WAMIT*.
- For the test with regular waves, the agreement between the numerical models and the experiments for pitch RAO was better for the waves with lower periods (shorter waves). It was also found that the results were dependent on the location of the model in the tank. This was interpreted as a consequence of the reflections which are known to be more important for the longer waves.
- The pitch RAOs that resulted from the tests with the polychromatic waves were closer to the theoretical predictions than when regular waves were used. Those RAOs were obtained by dividing the amplitude of the motion at each bin component obtained through an FFT by the amplitude in the incident wave for the correspondent component. (Note that aliasing and inaccuracies in the FFT were avoided by selecting the frequency of the components as an integer number of the reciprocal of the repeat time).
- The tests with the polychromatic waves seem to be mostly advantageous as the tank tests can be performed faster and the results seem to be closer to the theoretical predictions. However the limits and uncertainties associated with this procedure are still to be determined and are proposed to be undertaken in future work.

The experimental tests were performed with a 1/33 scale model and took place at the curved-tank of the University of Edinburgh. This facility has a water depth equal to 1.2 m and was designed to have forty eight absorbing wave-paddles placed across a quarter of a circle with 9 m radius. On the opposite side, it has wedge shaped beaches which

together with the absorbing wave paddles cover about 70% of the total perimeter. On the remaining side, a glass window allows to directly observe the experiments, but it also reflects waves which interfere with the wave field in the working area. To improve the wave field, two additional absorbing beaches were placed along the glass window and the six furthermost wave-makes (opposite to it) were disconnected from generating waves. Furthermore, the transfer function of the tank was modified to improve quality of the waves in the working area.

The working area was evaluated in terms of measurements of the reflection coefficient in regular waves for different wave steepnesses. The method described by Mansard and Funke [1980] was followed and the measurements showed a reflection coefficient lower than 10% for the short waves (wave periods between 0.7 s to 1.0 s) and lower than 15% for the longer waves (with wave periods up to 2 s) with steepnesses ($2a/\lambda$) higher than 0.02.

The experimental model was designed to allow the variation of the location of the off-centred axis and of pneumatic damping. The linear air-damper was conceived to model the desalination unit, and to provide a pressure differential across the the inner partition proportional to the angular velocity. During the present work, it was re-designed with thin stainless steel shims with slit cuts, engineered to provide a stable linear characteristics over time. The motions of the scale model were measured with an optical tracking system (Qualisys), the pressure across the linear air-damper was recorded to estimate the pneumatic power, and the reaction forces at the attachment point to the tank floor, were measured with a force cell specially designed for the effect. All input time-series analogue signals were recorded synchronously at a trigger signal and the tests were performed for both regular waves and mixed seas.

The tests with regular waves were intended to re-evaluate the performance of the linear air-damper and to validate the semi-analytic mathematical model. A summary of the most important key findings found in these tests is given bellow:

- Only one configuration of the model was tested with the position of the off-centred axis at (see Figure 4.6): $l_0/(D/2) = 0.6$, $\alpha_0 = 55°$ and draft ratio equal to $H/D = 0.66$ for eight damping settings ranging from 3×10^4 to 36×10^4 Pa/(m^3/s). The measurements were performed for 11 different waves with periods spaced between 0.8 to 2.7 s and waves with small wave heights (of about 10 mm).

- The measurements of the motions, pressure and absorbed power from these tests showed in general a good agreement with the derived mathematical model, and in many cases the measured data fitted within the estimated error intervals (Figures 5.4, C.2, C.3, C.4, C.5, C.6, C.7). The differences might be explained due to the inherent difficulties associated with the measurements of the incident waves, the occurrence of viscous dissipation in the fluid not taken into account in the mathematical model and also the non-linearities associated with the large motion amplitudes at resonance.

- For the tested configuration, resonance occurs for waves with a period of about 2 s. A second peak with lower amplitude is observed for shorter waves at a wave period of about 1.14 s, for the motions (surge, heave and pitch), pressure and relative capture width. The mooring forces do not show evidence of this second peak. Between the two peaks there is a deep valley with low signal response.

- Near the resonance period (at T = 2 s) there is an increase in the amplitudes of all measured time series signals with increasing applied damping and also a clear change in the phase of these signals.

- The relative capture width near the resonant period (T = 2s) increases with applied damping but at the expense of narrowing the absorption peak. The mathematical model predicts a maximum of about 1.9 when damping is 30.1 Nms/rad. A maximum value equal to 1.6 was measured for a damping setting equal to 1.80×10^5 Pa/(m^3/s) (= 19.6 Nms/rad).

- The plots which show the variation of relative capture width with fixed damping (Figure 5.5(e)) suggest that a low value of damping could provide a wider bandwidth but at the expense of peak performance.

- The peak values of the mooring forces occurs for the periods close to resonance (T = 2s) and decrease with decreasing values of applied damping. For a maximum damping setting equal to 39.6 Nms/rad those are equal to:

  - F_X = 3.3 (non-dimensional) in the horizontal direction, corresponding to a full scale value of about 12 MN/m of wave amplitude (for a cylinder with D = 12 m and W = 21 m).
  - F_Z = 1.9 (non-dimensional) in the vertical direction corresponding to a full scale value equal to about 7 MN/m of wave amplitude (for a cylinder with D = 12 m and W = 21 m).

The tests with mixed seas were performed for a total of eleven different sea spectra with a Bretschneider distribution, with the significant wave height and energy period parameters selected from the long term bi-frequency histogram for a location near Lanzarote (Canaries Islands). The eleven selected sea states correspond to occurrences of about 2820 h (which is about 30% of the year). The sea spectra were selected to cover all energy period range, but were restricted to the less energetic seas compatible with the scaled seas for the wave tank.

A summary of most important the key findings is given bellow:

- The configurations had the same draft and pneumatic damping setting equal to 3×10^4 Pa/(m^3/s) and two distinct locations of the off-centred axis at:
  - $\alpha_0 = 55°$and $l_0/(D/2) = 0.6$ and,
  - $\alpha_0 = 5°$and $l_0/(D/2) = 0.4$
- The configuration with $\alpha_0 = 5°$and $l_0/(D/2) = 0.4$ was predicted and confirmed experimentally to perform better than the other which was used in the tests with regular waves.
- For the total of operational hours (2820 h) correspondent to the measured seas a full scale desalination Duck would be able to absorb a total of 172 MWh of pneumatic power.
- The maximum measured mooring force was equal to 99.9 N which corresponds to 3.6 MN.
- The RCW predicted through the theoretical model is much higher than the value measured. Some possible causes are:
  - Systematic non-identified experimental error.
  - Friction losses not accounted in the theoretical model: (bearings, losses in the fluid through visible vortex shedding, pressure losses in the air-damper).
- The estimations for the average energy absorbed over a year at Lanzarote give a total equal to 114 MWh/m which is about half of the energy available at the site (228 MWh/m) and so, a 12 m by 30 m ($D \times W$) cylindrical desalination Duck would be able to absorb about 3.4 GWh of wave energy in one year.

Some directions for future work

The present dissertation left outside its scope any simulation in the time domain. Such simulations would allow the investigation of more complex and realistic control and power-take-off strategies. In particular, the desalination process could be modelled in detail and the operation of the non-return steam valves optimised.

An extension of the dynamics to second order, such to include the effect of higher amplitude motions would be interesting to pursue. This would require the computation of second order hydrodynamic forces on horizontal cylinders and a rearrangement of the equations of motion such to include second order terms, neglected in the present model due to linearisation process.

Particularly interesting would be also to study the interaction of multiple off-centred cylinders in waves. Several configurations could be tested: 1) side-by-side as in a 'classic' Duck string arrangement, with the off-centred cylinders in the string having the axis placed at different locations such that each would be excited differently by the same wave. With this arrangement, perhaps it would be possible to achieve an inertial reference with less machines than in the 'classic' Duck string. 2) As an array of a solo machines where it would be interesting to explore the different grid spacings and the advantages of using fully-submerged and free-surface piercing off-centred cylinders at different drafts in the same array. The combination of so many wave period dependent variables would perhaps provide interesting possibilities for optimisation and to adapt the array to particular sea states.

The influence of directional mixed seas and of extreme wave events was also left outside the scope of this work. It would be interesting to investigate this effects both theoretically and experimentally.

Most important would be to consider experimental tests with a scaled off-centred cylinder with rounded edges and corners to quantify the amount of energy lost by the viscous effects.

The experimental investigation of the theoretical occurrence of singularities of hydrodynamic damping at certain frequencies in the transition to fully submergence (trapped modes) would be also very interesting to pursuit and it might be an ideal experiment to reuse and resurrect the heave, surge and pitch rig that the wave power group of the university of Edinburgh used in the early eighties to perform so many important experiments.

It would be also interesting to test a scale model with a built in automatic mechanism to re-distribute the ballast and adjust resonance at different wave periods. It would be interesting to explore the energy balance between the gains and losses of using such mechanism.

And also it should not be forgotten that would be very interesting to extend the experiments with polychromatic waves described in the present dissertation to infer about the limits and uncertainties associated with the use of such methodology.

References

AEA Energy & Environment and Sustainable Energy Ireland. Review and analysis of ocean energy systems development and supporting policies. a report by aea energy & environment on the behalf of sustainable energy ireland for the iea's implementing agreement on ocean energy systems. Technical report, International Energy Agency - Ocean Energy Systems, 2006.

M. Alves. Calibracão de uma alcatifa para introducão de perda de carga. Final report, Departamento de Eng. Mecânica, Instituto Superior Técnico, 2002.

N. Barford. *Experimental Measurements: Precision, Error and Truth*. John Wiley & Sons, 2nd edition edition, 1985.

A. Brito-Melo, T. Hofmann, A. Sarmento, A. Clément, and G. Delhommeau. Numerical modelling of OWC-shoreline devices including the effect of the surrounding coastline and non-flat bottom. In *Proc. 10th International Offshore and Polar Eng Conference*, volume 1, pages 743–748, Seatle (USA), 2000.

I. Bryden. *Long floating cylinders in three-dimensional seas.* PhD thesis, University of Edinburgh, 1983.

K. Budal and J. Falnes. A resonant point absorber of ocean-wave power. *Nature*, 256: 478–479, 1975.

K. Budal and J. Falnes. Interacting point absorbers with controlled motion. In B. Count, editor, *Power from sea waves: based on the proceedings of a conference on power from sea waves*, pages 381–399. Academic Press Inc., 1980.

K. Budal and P. M. Lillebekken. Wave forces on a horizontal submerged spinning cylinder. In D. V. Evans and A. F. d. O. Falcão, editors, *Hydrodynamics of Ocean Wave-Energy Utilization*. International Union of Theoretical and Applied Mechanics, Springer-Verlag, 1985.

A. Clément, P. McCullen, A. Falcão, A. Fiorentino, F. Gardner, K. Hammarlund, G. Lemonis, T. Lewis, K. Nielsen, S. Petroncini, M. Teresa-Pontes, P. Schild, B.-O. Sjöström, H. C. Sørensen, and T. Thorpe. Wave energy in europe: current status and perspectives. *Renewable and Sustainable Energy Reviews*, 6:405–431, 2002.

B. M. Count. On the dynamics of wave-power devices. *Proceedings of the Royal Society of London. Series A, Mathematical and Physical Sciences*, 363:559–579, 1978.

B. M. Count, editor. *Power from sea waves: based on the proceedings of a conference on power from sea waves*. The Institute of mathematics and its applications conference series: New series. Academic Press, 1980. ISBN 9780121935504.

B. M. Count and E. R. Jefferys. Wave power, the primary interface. In *13th symposium on naval hydrodynamics*, Tokio, October 1980.

A. J. Crerar. *Wave powered desalination*. PhD thesis, University of Edinburgh, 1989.

A. J. Crerar and C. L. Pritchard. Wavepowered desalination experimental and mathematical modelling. *Desalination*, 81:391–389, 1991.

A. J. Crerar, R. E. Low, and C. L. Pritchard. Wave powered desalination. *Desalination*, 67:127–137, 1987.

J. Cruz, editor. *Ocean Wave Energy: Current status and future perspectives*. Springer, 2008.

J. Cruz. *Numerical and Experimental Modelling of Offshore Wave Energy Converters*. PhD thesis, Instituto Superior Técnico, June 2009.

J. Cruz and G. Payne. Preliminary numerical studies on a modified version of the Edinburgh duck using WAMIT. In *Proc. World Maritime Technology Conference (MAREC)*, London (UK), 2006.

J. Cruz and S. H. Salter. Numerical and experimental modelling of a modified version of the Edinburgh Duck wave energy device. *Proc. IMechE Part M - Journal of Engineering for the Maritime Environment*, 220:129–147, 2006.

J. Cruz, R. Pascal, and J. Taylor. Characterisation of the wave profile in the edinburgh curved tank. In *Proceedings of OMAE2006 - 25th International Conference on Offshore Mechanics and Arctic Engineering*, Hamburg, Germany, June 2006.

M. Darwish. Thermal analysis of vapor compression desalination system. *Desalination*, 69:275–295, 1988.

M. A. Darwish and N. M. Al-Najem. Energy consumptions and costs of different desalting systems. *Desalination*, 64:83–96, 1987.

M. A. Darwish and H. El-Dessouky. The heat recovery thermal vapour-compression desalting system: A comparison with other thermal desalination processes. *Applied Thermal Engineering*, 16(6):523 – 537, 1996. ISSN 1359-4311.

P. A. Davies. Wave-powered desalination: resource assessment and review of technology. *Desalination*, 186:97–109, 2005.

W. R. Dean. On the reflection of surface waves by a submerged cylinder. *Proceedings of the Cambridge Philosophical Society*, 44:483–491, 1948.

Y. M. C. Delauré and A. Lewis. 3D hydrodynamic modelling of fixed oscillating water column wave power plant by a boundary element methods. *Ocean Engineering*, 30 (Issue 3):309–330, February 2003.

L. Duckers, N. Minns, R. Haken, and S. Watson. "a novel, compact wave energy converter". In *WREC X*, 2008.

D. V. Evans. A theory for wave-power absorption by oscillating bodies. *Journal of Fluid Mechanics*, 77:1–25, 1976.

D. V. Evans. Some theoretical aspects of three-dimensional wave energy absorbers. In *Symposium on Ocean Wave Energy Utilization*. Gothenburg, Sweden, october 1979.

D. V. Evans. Some analytic results for two and three dimensional wave-energy absorbers. In B. M. Count, editor, *Power from sea waves: based on the proceedings of a conference on power from sea waves*, pages 213–249. Academic Press Inc., 1980.

D. V. Evans. Power from water waves. *Annual reviews of fluid mechanics*, 13:157–187, 1981.

D. V. Evans. A note on the transparency of a submerged circular cylinder to the waves radiated by a pulsating line source. *IMA Journal of Applied Mathematics*, 33(2): 105–107, 1984.

D. V. Evans. The hydrodynamic efficiency of wave-energy devices. In D. Evans and A. F. d. O. Falcão, editors, *Hydrodynamics of ocean wave-energy utilization*, pages 1–34, Lisbon, Portugal, 1985. International Union of Theoretical and Applied Mechanics, Springer-Verlag.

D. V. Evans and C. M. Linton. Hydrodynamics of wave-energy devices. Technical report, University of Bristol, Department of Mathematics, June 1993.

D. V. Evans and R. Porter. Wave-free motions of isolated bodies and the existence of motion-trapped modes. *Journal of Fluid Mechanics*, 584:225–234, 2007.

D. V. Evans, D. C. Jeffrey, S. H. Salter, and J. Taylor. Submerged cylinder wave energy device: theory and experiment. *Applied Ocean Research*, 1(1):3–12, 1979.

A. F. Falcão. Modelling and control of oscillating-body wave energy converters with hydraulic power take-off and gas accumulator. *Ocean Engineering*, 34:2021–2032, 2007.

A. F. Falcão. Phase control through load control of oscillating-body wave energy converters with hydraulic pto system. *Ocean Engineering*, 35:358–366, 2008.

A. F. Falcão. Wave energy utilization: A review of the technologies. *Renewable and Sustainable Energy Reviews.*, 14:899–918, 2010.

J. Falnes. Radiation impedance matrix and optimum power absorption for interacting oscillators in surface waves. *Applied Ocean Research*, 2(2):75–80, 1980.

J. Falnes. Optimum control of oscillation of wave-energy converters. Technical report, Universitetet i Trondheim, Institutt for fysikk, NTH, 1993.

J. Falnes. On non-causal impulse response functions related to propagating water waves. *Applied Ocean Research*, 17(6):379–389, 1995.

J. Falnes. *Ocean waves and oscillating systems*. Cambridge University Press, 2002.

J. Falnes. A review of wave-energy extraction. *Marine Structures*, 20:185–201, 2007.

O. M. Faltinsen. *Sea loads on ships and offshore structures*. Cambridge University Press, 1990.

P. Fornasini. *The uncertainty in physical measurements: An introduction to data analysis in the physics laboratory.* Springer, 2008.

W. Frank. Oscillation of cylinders on or bellow the free surface of deep fluids. Technical Report Rep. no. 2375, Naval Ship Research & Development Center (N.S.R.D.C), 1967.

M. J. French. On the difficulty of inventing an economical sea wave energy converter: a personal view. *Proc. IMechE Part M - Journal of Engineering for the Maritime Environment*, 220:149–155, 2006.

C. J. Garrison and P. Y. Chow. Wave forces on submerged bodies. *Journal of the waterways, harbors and Coastal Engineering Division*, 98, 1972.

Y. Goda and Y. Suzuki. Estimation of incident and reflected waves in random wave experiments. In *Procedings of 15th Costal Engineering Conference*, volume 1, pages 828–845. American Society of Civil Engineers, 1976.

H. Goldstein, C. P. Poole, and J. Safko. *Classical Mechanics*. Addison–Wesley, 3rd edition edition, 2000.

M. Greenhow. High- and low-frequency asymptotic consequences of the kramers-kronig relations. *Journal of Engineering Mathematics*, 20:293–306, 1986.

M. Greenhow and S. I. Ahn. Added mass and damping of horizontal circular cylinder sections. *Ocean Engineering*, 15(5):495–504, 1988.

M. Greenhow and L. Yanbao. Added masses for circular cylinders near or penetrating fluid boundaries - review, extension and application to water-entry, -exit and slamming. *Ocean Engineering*, 14(4):255–358, 1987.

M. Greenhow, T. Vinje, P. Brevig, and J. R. M. Taylor. A theoretical and experimental study of the capsize of salter's duck in extreme waves. *Journal of Fluid Mechanics*, 118:221–239, 1982.

J. L. Hess. Panel methods in computational fluid dynamics. *Annual reviews of fluid mechanics*, 22:255–274, 1990.

D. C. Hicks, C. M. Pleass, G. R. Mitcheson, and J. F. Salevan. Delbuoy: Ocean wave-powered seawater reverse osmosis desalination system. *Desalination*, 73:81–94, 1989.

M. Isaacson. Measurement of regular wave reflection. *Journal of Waterway, Port, Coastal, and Ocean Engineering*, 117(6):553–569, 1991.

IWMI. Insights from the comprehensive assessment of water management in agriculture. Technical report, International Water Management Institute (IWMI), Colombo, Sri Lanka, 2006.

E. R. Jefferys. *Device Characterisation*, chapter III.8, pages 413–438. Academic Press Inc., 1980.

D. C. Jeffrey, D. J. E. Richmond, S. H. Salter, J. R. M. Taylor, and I. A. Young. Second year interim report on edinburgh wave power project: "study of mechanism to extract power from sea waves". Interim report, Wave-power project, University of Edinburgh, September 1976.

D. C. Jeffrey, G. J. Keller, D. Mollison, D. Richmond, S. H. Salter, J. R. M. Taylor, and I. Young. Fourth year report on edinburgh wave power project: Study of mechanisms for extracting power from sea waves. Technical report, Wave-power project, University of Edinburgh, 1978a.

D. C. Jeffrey, G. J. Keller, D. Mollison, D. Richmond, S. H. Salter, J. R. M. Taylor, and I. Young. Fourth year report volume 2 of 3: Slamming tests. Technical report, Wave-power project, University of Edinburgh, 1978b.

D. C. Jeffrey, G. J. Keller, D. Mollison, D. Richmond, S. H. Salter, J. R. M. Taylor, and I. Young. Fourth year report volume 3 of 3. Technical report, Wave-power project, University of Edinburgh, July 1978c.

H. Lamb. *Hydrodynamics*. Cambridge University Press, 32 East 67th Street, New York, N.Y.10022, 6th edition edition, 1975. First Edition in 1879, 6th edition in 1932, this edition in 1975.

L. D. Landau and E. M. Lifshitz. *Fluid Mechanics*, volume 6 of *Course of theoretical physics*. Pergamon Press, 2nd edition, 1987.

C.-H. Lee, H. D. Maniar, J. N. Newman, and X. Zhu. Computations of wave loads using a b-spline panel method. In *Proceedings of the 21st symposium on naval hydrodynamics*, pages 75–92, Trondheim, Norway, 1996.

C.-H. Lee, L. Farina, and J. N. Newman. A geometry-independent higher-order panel method and its application to wave-body interactions. In *Proceedings of the 3rd engineering mathematics and applications conference*, pages 303–306, Adelaide, Australia, 1998.

J. M. Leishman and G. Scobie. The development of wave power – a techno economical study. Technical Report NEL report, EAU M25, Department of Industry, 1976.

M. S. Longuet-Higgins. The mean forces exerted by waves on floating or submerged bodies with applications to sand bars and wave power machines. *Proceedings of the Royal Society of London. Series A, Mathematical and Physical Sciences*, 352(1671): 463–480, 1977.

J. Lucas, J. Cruz, S. H. Salter, J. Taylor, and I. Bryden. Update on the modelling of a 1:33 scale model of a modified edinburgh duck wec. In *Proceedings of the 7th European Wave and Tidal Energy Conference*, page 9, Porto, Portugal, September 2007.

J. Lucas, J. Cruz, S. H. Salter, J. Taylor, and I. Bryden. Update on the design of a 1:33 scale model of a modified edinburgh duck wec. In *Proceedings of Offshore Mechanics and Arctic Engineering 2008*, page 11, Estoril, Portugal, June 2008.

J. Lucas, S. H. Salter, J. Cruz, J. Taylor, and I. Bryden. Performace optimisation of a modified duck through optimal mass distribution. In *Proceedings of the 8th European Wave and Tidal Energy Conference*, page 10, Uppsala, Sweden, September 2009.

H. D. Maniar. *A three dimensional higher order panel method based on B-splines*. PhD thesis, Massachusetts Institute of Technology, 1995.

E. Mansard and E. Funke. The measurement of incident and reflected spectra using a least squares method. In *Proceedings, 17th International Conference on Coastal Engineering*, volume 1, pages 154–172, Sydney, Australia, 1980.

S. R. Masterton and C. Swan. On the accurate and efficient calibration of a 3d wave basin. *Ocean Engineering*, 35:763–773, 2008.

P. McIver and D. V. Evans. The occurence of negative added mass in free-surface problems involving submerged oscillating bodies. *Journal of engineering mathematics*, 18:7–22, 1984.

P. McIver and M. McIver. Wave radiation by a submerged circular cylinder of finite lenght. In *International workshop on water waves and floating bodies*, volume 9th, pages 173–176, Kuju, Fukuoka, Japan, April 1994.

P. McIver and M. McIver. Trapped modes in an axisymmetric water-wave problem. *Quarterly Journal of Mechanics and Applied Mathematics*, 50:165–178, 1997.

C. C. Mei. Numerical methods in water-wave difraction and radiation. *Annual reviews of fluid mechanics*, 10:393–416, 1978.

C. C. Mei. *The applied dynamics of ocean surface waves.* Advanced Series on Ocean Engineering. World Scientific., Singapore, 2nd ed. edition, 1989.

N. Minns. Calibration of slit-rubber wells turbine simulators. personal communication, 2008.

A. E. Mynett, D. D. Serman, and C. C. Mei. Characteristics of salter's cam for extracting energy from ocean waves. *Applied Ocean Research*, 1(1):13–20, 1979.

P. Nebel. Maximizing the efficiency of wave-energy plants using complex conjugate control. *Proc. IMechE Part I - Journal of systems and control engineering*, 206(4): 225–236, 1992a.

P. Nebel. Optimal control of a duck. Technical report, Department of Mechanical Engineering, University of Edinburgh, May 1992b.

D. E. Newland. *An introduction to random vibrations, spectral & wavelet analysis*. Dover Publications, Inc, Mineola, New York, 1975.

J. N. Newman. Interaction of waves with two-dimensional obstacles: a relation between the radiation and scattering problems. *Journal of Fluid Mechanics Digital Archive*, 71 (02):273–282, 1975.

J. N. Newman. The interaction of stationary vessels with regular waves. In *Proceedings of the 11th Symposium on naval hydrodynamics*, pages 491–501, London, 1976.

J. N. Newman. *Marine Hydrodynamics*. The MIT Press, 1977.

J. N. Newman. *The theory of ship motions*, volume 18 of *Advances in applied mechanics*, chapter 5, pages 221–283. Academic Press, Inc., 1978.

J. N. Newman. Algorithms for the free-surface green function. *Journal of Engineering Mathematics*, 19:57–67, 1985.

J. N. Newman. Trapping structures with linear mooring forces. In *Proc. 22nd Int. Workshop on Water Waves & Floating Bodies*, Plitvice Lakes, Croatia, April 2007.

J. N. Newman. Trapping of water waves by moored bodies. *Journal of Engineering Mathematics*, 62(4):303–314, 2008.

J. N. Newman and P. D. Sclavounos. The computation of wave loads on large offshore structures. In *"BOSS" Conference*, Trondheim, Norway, June 1988.

W. P. G. of the University of Edinburgh. Bending moments in long spines. Technical report, Wave-power project, University of Edinburgh, 1984.

W. P. G. of the University of Edinburgh. The long spine mooring. Technical report, Wave-power project, University of Edinburgh, 1986.

T. F. Ogilvie. First- and second-order forces on a cylinder submerged under a free surface. *Journal of Fluid Mechanics*, 16:451–472, 1963.

R. Pascal, J. Lucas, D. Ingram, and I. Bryden. Assessing and improving the edinburgh curved wave tank. In *Proceedings of the Nineteenth (2009) International Offshore and Polar Engineering Conference*, pages 269–275, Osaka,Japan, June 2009.

G. S. Payne. *Numerical modeling of a sloped wave energy device.* PhD thesis, The University of Edinburgh, 2005.

G. S. Payne, J. R. Taylor, T. Bruce, and P. Ì. Parkin. Assessment of boundary-element method for modelling a free-floating sloped wave energy device. part 2: Experimental validation. *Ocean Engineering*, 35:342–357, 2008a.

G. S. Payne, T. Taylor, Jamie R.M.and Bruce, and P. Ì. Parkin. Assessment of boundary-element method for modelling a free-floating sloped wave energy device. part 1: Numerical modelling. *Ocean Engineering*, 35:333–341, 2008b.

G. S. Payne, J.-B. Richon, D. Ingram, and J. Spinneken. Development and preliminary assessment of an optical wave gauge. In *Proceedings of the 8th European Wave and Tidal Energy Conference*, Uppsala, Sweden, September 2009.

D. J. Pizer. The numerical predictions of the performance of a solo duck. Technical report, University Of Edinburgh, 1992.

D. J. Pizer. Maximum wave-power absorption of point absorbers under motion constraints. *Applied Ocean Research*, 15:227–234, 1993a.

D. J. Pizer. The numerical prediction of the performance of a solo-duck. In *Proceedings of the 1993 European Wave Energy symposium.*, pages 129–137, Edinburgh, Scotland, July 1993b.

D. J. Pizer. Numerical modeling of wave energy absorbers. Numerical models, University of Edinburgh, September 1994.

R. Plu. Beaches and wave quality. preliminary investigation in the new edinburgh curved wave tank. interim report, University of Edinburgh, 2003.

R. Porter and D. Evans. Examples of trapped modes in the presence of freely floating structures. *Journal of Fluid Mechanics*, 606:189–207, 2008.

W. H. Press, S. A. Teukolsky, W. T. Vetterling, and B. P. Flannery. *Numerical Recipes 3rd Edition: The Art of Scientific Computing*. Cambridge University Press, New York, NY, USA, 2007. ISBN 0521880688.

Qualisys. *Qualisys Track Manager: User Manual.* Qualisys AB, 1.9.2xx edition, Febuary 2006.

P. J. Roache. Quantification of uncertainty in computational fluid dynamics. *Annual Review of Fluid Mechanics*, 29(1):123–160, 1997.

D. Rogers. *WG8 wavegauge manual.* Edinburgh Designs Ltd, July 1997.

D. Rogers and G. B. King. *Wave generation using 'ocean' and 'wave'*. Edinburgh Designs Ltd., 27 Ratcliffe Terrace, Edinburgh EH9 1SX, March 1997. Version 3.62.

D. Ross. *Power from the waves*. Oxford Univ. Press, 1995.

S. H. Salter. Wave power. *Nature*, 249(249):720–724, 1974.

S. H. Salter. Wave power - nodding duck wave energy extractors. In J. Kohl, editor, *Energy from the oceans fact or fantasy?*, pages 5–8, Raleigh, North Carolina, January 1976. The Center for Marine and Coastal Studies - North Carolina State University. report no. 76-1 UNC-SG-76-04.

S. H. Salter. Power conversion systems for ducks. In *International Conference on Future Energy Concepts*, pages 100–108, 1979.

S. H. Salter. Recent progress on ducks. *IEE Proceedings A: Science, Measurement & Technology*, 127(5):308–319, 1980.

S. H. Salter. Absorbing wave-makers and wide tanks. In R. L. Wiegel, editor, *Proceedings of the conference on directional wave spectra applications*. University of California, Berkeley, California, American Society of Civil Engineers, September 1981.

S. H. Salter. The use of gyros as reference frame in wave energy converters. In *The second international symposium on wave-energy utilization*, Trondheim, Norway, June 1982.

S. H. Salter. Wave powered desalination. In *In Proceedings of a conference on Energy for Rural Communities*, pages 235–241, Inverness (UK), 1985a.

S. H. Salter. Progress on edinburgh ducks. In D. V. Evans and A. F. d. O. Falcão, editors, *Hydrodynamics of Ocean Wave-Energy Utilization: IUTAM*. International Union of Theoretical and Applied Mechanics, Springer-Verlag, 1985b.

S. H. Salter. World progress in wave energy-1988. *International Journal of Ambient Energy*, 10(01):3–24, 1989.

S. H. Salter. Changes to the 1981 design of the spine-based ducks. In *Proceedings of the 1993 European Wave Energy Symposium.*, pages 295–309, Edinburgh, Scotland, UK, July 1993.

S. H. Salter. Proposals for combined wave and current tank with independent 360 deg. capability. In *Proceedings of MAREC 2001*, Newcastle, 2001. IMAREST.

S. H. Salter. High purity desalination using wave-driven vapour compression. In *Proc. World Renewable Energy Conference*, Aberdeen (UK), 2005.

S. H. Salter. A materials wish list for wet renewables. *Energy Materials*, 1(1):14–16, 2006.

S. H. Salter. *Looking back*, chapter 2, pages 7–39. Springer, 2008.

S. H. Salter, D. C. Jeffrey, and J. Taylor. First year interim report on edinburgh wave power project: "study of mechanism to extract power from sea waves". Technical report, Wave-power project, University of Edinburgh, September 1975.

S. H. Salter, D. C. Jeffrey, and J. R. Taylor. The architecture of nodding duck wave power generators. *Naval Architect*, 1(1):21–24, January 1976.

S. H. Salter, J. R. M. Taylor, and N. J. Caldwell. Power conversion mechanisms for wave energy. *Proc. IMechE Part M - Journal of Engineering for the Maritime Environment*, 216:1–27, 2002.

S. H. Salter, J. Cruz, J. Lucas, and R. Pascal. Wave powered desalination. In *International Conference on Integrated Sustainable Energy Resources in Arid Regions*, Abu Dhabi, 2007.

A. Sarmento. Wave flume experiments on two-dimensional oscillating water column wave energy devices. *Experiments in Fluids*, 12:286–292, 1992.

T. Sarpkaya and M. Isaacson. *Mechanics of wave forces on offshore structures*. Van Nostrand Reinhold Company, 1981.

H. A. Schäffer and G. Klopman. Review of multidirectional active wave absorption methods. *Journal of waterway, port, coastal, and ocean engineering*, 126(2):88–97, March / April 2000.

A. A. Shabana. *Dynamics of multibody systems*. Cambridge University Press, third edition edition, 2005.

D. Skyner. Solo duck linear analysis. Technical report, Wave-power project, University of Edinburgh, 1987.

J. Spinneken and C. Swan. Second-order wavemaker theory using force-feedback control. parti: A new theory for regular wave generation. *Ocean Engineering*, 36:539–548, 2009a.

J. Spinneken and C. Swan. Second-order wavemaker theory using force-feedback control. partii: An experimental verification of regular wave generation. *Ocean Engineering*, 36:549–555, 2009b.

M. Taylor, Jamie R, M. Rea, and D. Rogers. The edinburgh curved tank. In *5th European Wave Energy Conference*, Cork, Ireland, 2003.

T. W. Thorpe. A brief review of wave energy. Final ETSU-R120, The UK Department of Trade and Industry, May 1999.

M. J. Tucker and E. G. Pitt. *Waves in ocean engineering*. Elsevier Science Ltd., 2001.

F. Ursell. On the heaving motion of a circular cylinder on the surface of a fluid. *The Quarterly Journal of Mechanics and Applied Mathematics*, 2(2):218–231, 1949a.

F. Ursell. On the rolling motion of cylinders in the surface of a fluid. *Quarterly Journal of Mechanics and Applied Mathematics*, 2(3):335–353, 1949b.

F. Ursell. Surface waves on deep water in the presence of a submerged circular cylinder, i. *Proceedings of the Cambridge Philosophical Society*, 46:141–152, 1950a.

F. Ursell. Surface waves on deep water in the presence of a submerged circular cylinder, ii. *Proceedings of the Cambridge Philosophical Society*, 46:153–158, 1950b.

F. Ursell. Water waves generated by oscillating bodies. *Quarterly Journal of Mechanics and Applied Mathematics*, 7(4):427–437, 1954.

WAMIT - User Manual (Versions 6.0, 6.0PC, 5.3S). WAMIT, Inc., 2000. URL `www.wamit.com`.

J. V. Wehausen. The motion of floating bodies. *Annual reviews of fluid mechanics*, 3: 7–268, 1971.

J. V. Wehausen and E. V. Laitone. *Surface Waves*, volume IX of *Encyclopaedia of Physics*, pages 446–778. Springer Verlag, 1960.

R. L. Wiegel. *Oceanographical Engineering*. Prentice-Hall, Inc. / Englewood Cliffs, N.J, 1964.

J. Wittenburg. *Dynamics of Multibody Systems*. Springer, second edition edition, 2008. Originally published under: Dynamics of Systems of Rigid Bodies, in the LAMM series, Teubner 1977.

World Resources Institute (WRI). *World Resources 2005: The Wealth of the Poor – Managing Ecosystems to Fight Poverty.* World Resources Institute, 2005. World Resources Institute (WRI) in collaboration with United Nations Development Programme, United Nations Environment Programme, and World Bank.

H. E. Young and J. Pollock. Variable coefficient control of a wave-energy device. Report, Wave-power project, University of Edinburgh, March 1985.

Appendix A
Hydrodynamic coefficients and wave excitation force at different locations in the body.

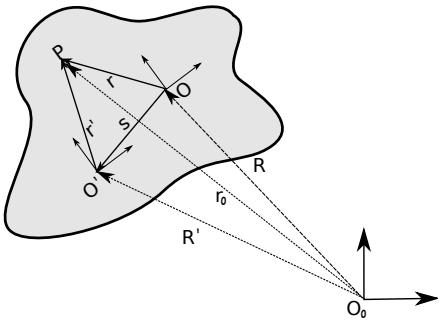

Figure A.1: *Rigid body in motion represented at an inertial frame of reference with coordinate system given by* (O_0, X_0, Y_0, Z_0)*. Two non-inertial coordinate systems fixed with the body given by* (O, X, Y, Z) *and* $\left(O, X', Y', Z'\right)$ *are also represented.*

Figure A.1 shows a rigid body in motion in an inertial frame of reference with coordinate system given by (X_0, Y_0, Z_0) located at point O_0. The position of a generic point P of the rigid body in the inertial frame of reference is represented by the vector $\vec{r_0}$. A non-inertial reference frame fixed with the body and with coordinate system (X, Y, Z) and located at point O is also considered. The position of point P in this coordinate system is given by vector $\vec{r}$. The position of the moving coordinate system (X, Y, Z, O) relative to the inertial reference frame (X_0, Y_0, Z_0, O_0) is given by the vector $\vec{R}$.

Following for example Landau and Lifshitz [1987, pp. 97], an infinitesimal displacement of point P in the inertial reference frame (X_0, Y_0, Z_0) is given by: $d\vec{r}_0 = d\vec{R} + d\vec{\phi} \times \vec{r}$, where $d\vec{\phi} \times \vec{r}$ is a displacement relative to O that results from a rotation through an infinitesimal angle $d\vec{\phi}$. The velocity of P in (X_0, Y_0, Z_0) is given by:

$$\vec{u}_0 = \vec{U} + \vec{\Omega} \times \vec{r} \tag{A.1}$$

Then it is considered a second coordinate system $\left(X', Y', Z'\right)$ also fixed with the body (to simplify) with its axis parallel with (X, Y, Z) but with a different origin at O'. In this

coordinate system, the position of point P is given by:

$$\vec{r}' = \vec{r} - \vec{s} \tag{A.2}$$

The velocity of point P in the inertial coordinate system can also be written in terms of the quantities of the second coordinate system as:

$$\vec{u_0} = \vec{U}' + \vec{\Omega} \times \vec{r}' \tag{A.3}$$

The angular velocity of the rigid body measured in the inertial frame of reference is the same: $\vec{\Omega}' = \vec{\Omega}$ and also $d\phi' = d\phi$.

Substituting (A.2) into (A.3), and taking into account (A.1), the relationship between the velocities at different points in the body is obtained, given by:

$$\vec{U} = \vec{U}' - \vec{\Omega} \times \vec{s} \tag{A.4}$$

The acceleration of point P in the inertial coordinate system is given by:

$$\dot{\vec{u}}_0 = \dot{\vec{U}} + \vec{\Omega} \times \left(\vec{\Omega} \times \vec{r}\right) + 2\vec{\Omega} \times \vec{U} + \dot{\vec{\Omega}} \times \vec{r} \tag{A.5}$$

And in terms of the vectors of the second coordinate system can be written as:

$$\dot{\vec{u}}_0 = \dot{\vec{U}}' + \vec{\Omega} \times \left(\vec{\Omega} \times \vec{r'}\right) + 2\vec{\Omega} \times \vec{U}' + \dot{\vec{\Omega}} \times \vec{r'} \tag{A.6}$$

Substituting (A.2) into (A.6), rearanging and taken into account (A.4), the relationship for the accelerations at different coordinate systems in the body can be written as:

$$\dot{\vec{U}} = \dot{\vec{U}}' + \vec{\Omega} \times \left(\vec{\Omega} \times \vec{s}\right) - \dot{\vec{\Omega}} \times \vec{s} \tag{A.7}$$

The term $\vec{\Omega} \times \left(\vec{\Omega} \times \vec{s}\right)$ is of second order provided Ω is small, and so the previous equation can be approximated to:

$$\dot{\vec{U}} \approx \dot{\vec{U}}' - \dot{\vec{\Omega}} \times \vec{s} \tag{A.8}$$

For the displacements, a similar approach is followed. Substituting (A.2) into the relation that gives the displacements relative to the primed coordinate system: $d\vec{r}_0 = d\vec{R}' + d\vec{\phi} \times \vec{r}'$, it is obtained:

$$d\vec{R} = d\vec{R}' - d\vec{\phi} \times \vec{s} \tag{A.9}$$

The forces and moments due to the radiation problem [see Newman, 1977, pp. 295] and relative to a certain point O, are written as (with $j,k = 1,...6$):

$$F_j = F_{Aj} + F_{Bj} = -\left(A_{jk}\dot{U}_k + B_{jk}U_k\right) \tag{A.10}$$

NB: 1. The summation convention (sum of repeated indexes) was used and it will be used in what follows. 2. The general force $\vec{F}$ is represented as a 6 component vector containing the force and moment components: $\vec{F} = [f_1, f_2, f_3, m_1, m_2, m_3]$, and the velocity and acceleration vectors $\vec{U}$ and $\dot{\vec{U}}$ in (A.10) include both linear and angular components: $\vec{U} = [U_1, U_2, U_3, \Omega_1, \Omega_2, \Omega_3]$ and $\dot{\vec{U}} = \left[\dot{U}_1, \dot{U}_2, \dot{U}_3, \dot{\Omega}_1, \dot{\Omega}_2, \dot{\Omega}_3\right]$.

The hydrodynamic damping component given by (A.10). At point O, is given in matrix form as:

$$\vec{F}_B = -\mathbf{B}\vec{U} \tag{A.11a}$$

(**NB:** $\vec{F}_B$ includes both forces and moments).

At a different point O' in the body, translated relatively to O by $\vec{s}$, such that (A.2) holds (see Figure A.1):

$$\vec{f}'_B = \vec{f}_B \tag{A.11b}$$

$$\vec{m}'_B = \vec{m}_B + (-\vec{s}) \times \vec{f}_B \tag{A.11c}$$

Taking into account (A.4), equation (A.11b) can be rewriten in indice notation (compact form) as:

$$f'_{B_j} = f_{B_j} = -B_{jk}U_k - B_{jk+3}\Omega_k = -B_{jk}U'_k + \varepsilon_{klm}B_{jk}\Omega_l s_m - B_{jk+3}\Omega_k \tag{A.12a}$$

and equation (A.11c) as (with $j,k,l,m,p,q,r,s,t = 1,..,3$):

$$\begin{aligned} m'_{B_j} =& m_{B_j} - \varepsilon_{jpq}s_p f_{B_q} = -B_{j+3k}U_k - B_{j+3k+3}\Omega_k + \varepsilon_{jpq}s_p\left(B_{qr}U_r + B_{qr+3}\Omega_r\right) = \\ =& -B_{j+3k}U'_k + \varepsilon_{klm}B_{j+3k}\Omega_l s_m - B_{j+3k+3}\Omega_k + \varepsilon_{jpq}s_p B_{qr}U'_r \\ & - \varepsilon_{jpq}s_p B_{qr}\varepsilon_{rst}\Omega_s s_t + \varepsilon_{jpq}s_p B_{qr+3}\Omega_r \end{aligned} \tag{A.12b}$$

If only two dimensional description in a plane is considered, the following terms vanish:

$$s_2 = B_{2k} = B_{j2} = B_{4k} = B_{j4} = B_{6k} = B_{j6} = 0$$

and equations (A.12a) and (A.12b) simplify to:

$$f'_{B_1} = -B_{11}U'_1 - B_{13}U'_3 - (-B_{11}s_3 + B_{13}s_1 + B_{15})\Omega_2 \tag{A.13a}$$

$$f'_{B_3} = -B_{31}U'_1 - B_{33}U'_3 - (-B_{31}s_3 + B_{33}s_1 + B_{35})\Omega_2 \tag{A.13b}$$

$$m'_{B_2} = -(-s_3B_{11} + s_1B_{31} + B_{51})U'_1 - (-s_3B_{13} + s_1B_{33} + B_{53})U'_3 \tag{A.13c}$$

$$-\left(s_3^2B_{11} + s_1^2B_{33} + B_{55} - 2s_3B_{15} - 2s_3s_1B_{13} + 2s_1B_{53}\right)\Omega_2 \tag{A.13d}$$

To obtain the formulas for the hydrodynamic added mass at point O' translated from point O by $\vec{s}$ a similar procedure is followed. The component of the hydrodynamic force due to the added mass is given by:

$$F_A = -A\dot{\vec{U}} \tag{A.14}$$

with $\dot{\vec{U}}$ given by (A.8) and the forces and moments transformation given similarly by:

$$\vec{f}'_A = \vec{f}_A \tag{A.15}$$

$$\vec{m}'_A = m_A + (-\vec{s}) \times \vec{f}_A \tag{A.16}$$

The final expressions which relate the hydrodynamic added mass coefficients at a different locations in the body for a planar geometry are given in Table A.1.

The *hydrostatic force* at the body fixed coordinate system located at point O is given by (see Newman [1978]):

$$\left(\vec{f}_C\right)_3 = -\rho g(S_{00}\xi_3 - S_{10}\xi_5) = -C_{33}\xi_3 - C_{35}\xi_5 \tag{A.17}$$

$$(\vec{m}_C)_1 = -\rho g\left(S_{02} + \forall\left(z_b - z_g\right)\right)\xi_4 = -C_{44}\xi_4 \tag{A.18}$$

$$(\vec{m}_C)_2 = \rho g\left[S_{10}\xi_3 - \left(S_{20} + \forall\left(z_b - z_g\right)\right)\xi_5\right] = -C_{35}\xi_3 - C_{55}\xi_5 \tag{A.19}$$

where the coordinates of the centre of buoyancy ($\vec{r}_b = (x_b, y_b, z_b)$), the water-plane area and moments S_{ij} and the hydrostatic coefficents are given in Table 4.2.

Substituting the small translational displacements by $d\vec{R} = \vec{\xi}_T = (\xi_1, \xi_2, \xi_3)$ and the angular displacements by $d\vec{\phi} = \vec{\xi}_R = (\xi_4, \xi_5, \xi_6)$ the relationship (A.9) between the displacements at point O' translated relatively to O can be re-written explicitly as:

$$\xi_1 = \xi'_1 - s_3\xi'_5 + s_2\xi'_6 \tag{A.20}$$

$$\xi_2 = \xi'_2 - s_1\xi'_6 + s_3\xi'_4 \tag{A.21}$$

$$\xi_3 = \xi'_3 - s_2\xi'_4 + s_1\xi'_5 \tag{A.22}$$

Substituting the above relations into the transformation relations for the hydrostatic force and moment at O' translated relatively to O by $\vec{s}$ and given by:

$$\vec{f}'_C = \vec{f}_C \tag{A.23a}$$

$$\vec{m}'_C = \vec{m}_C + (-\vec{s}) \times \vec{f}_C \tag{A.23b}$$

it is obtained:

$$\left(\vec{f}_C{}'\right)_3 = \left(\vec{f}_C\right)_3 = -C_{33}\,\xi_3 - C_{35}\,\xi_5 = -C_{33}\,\xi'_3 + s_2\,C_{33}\,\xi'_4 - (s_1\,C_{33} + C_{35})\,\xi'_5 \tag{A.23c}$$

$$\begin{aligned}\left(\vec{m}_C{}'\right)_1 &= (\vec{m}_C)_1 + \left((-\vec{s}) \times \vec{f}_C\right)_1 = -C_{44}\,\xi_4 - s_2\,(-C_{33}\,\xi_3 - C_{35}\,\xi_5) \\ &= s_2\,C_{33}\,\xi'_3 - \left(s_2^2\,C_{33} + C_{44}\right)\xi'_4 + (s_2\,s_1\,C_{33} + s_2\,C_{35})\,\xi'_5\end{aligned} \tag{A.23d}$$

$$\begin{aligned}\left(\vec{m}_C{}'\right)_2 &= (\vec{m}_C)_2 + \left((-\vec{s}) \times \vec{f}_C\right)_2 = -(C_{35} + s_1\,C_{33})\,\xi_3 - (s_1\,C_{35} + C_{55})\,\xi_5 \\ &= -(C_{35} + s_1\,C_{33})\,\xi'_3 + (s_2\,C_{35} + s_1\,s_2\,C_{33})\,\xi'_4 - \left(2\,s_1\,C_{35} + s_1^2\,C_{33} + C_{55}\right)\xi'_5\end{aligned} \tag{A.23e}$$

If the *excitation force* at point O is given by $\vec{F}_X = [\vec{f}_X, \vec{m}_X]$, at point O', translated by $\vec{s}$ (as in Figure A.1) is given by:

$$\vec{f}'_X = \vec{f}_X$$

$$\vec{m}'_X = \vec{m}_X + (-\vec{s}) \times \vec{f}_X$$

If for the planar geometry $\vec{F}_X = [f_{X_1}, f_{X_3}, m_{X_2}] = [X_1, X_3, X5]$, then:

$$X'_1 = X_1 \tag{A.24}$$

$$X'_3 = X_3 \tag{A.25}$$

$$X'_5 = X_5 - s_3\,X_1 + s_1\,X_3 \tag{A.26}$$

Added Mass	**Hydro. Damping**	**Hydro. Stiffness**	**Excitation Force**
$A'_{11} = A_{11}$	$B'_{11} = B_{11}$		$X'_1 = X_1$
$A'_{15} = -s_3\,A_{11} + s_1\,A_{13} + A_{15}$	$B'_{15} = -s_3\,B_{11} + s_1\,B_{13} + B_{15}$		$X'_3 = X_3$
$A'_{33} = A_{33}$	$B'_{33} = B_{33}$	$C'_{33} = C_{33}$	$X'_5 = X_5 - s_3\,X_1 + s_1\,X_3$
$A'_{35} = -s_3\,A_{31} + s_1\,A_{33} + A_{35}$	$B'_{35} = -s_3\,B_{31} + s_1\,B_{33} + B_{35}$	$C'_{35} = s_1\,C_{33} + C_{35}$	
$A'_{55} = s_3^2\,A_{11} + s_1^2\,A_{33} + A_{55} - 2s_3\,A_{15} - 2s_3\,s_1\,A_{13} + 2s_1\,A_{53}$	$B'_{55} = s_3^2\,B_{11} + s_1^2\,B_{33} + B_{55} - 2s_3\,B_{15} - 2s_3\,s_1\,B_{13} + 2s_1\,B_{53}$	$C'_{55} = 2s_1\,C_{35} + s_1^2\,C_{33} + C_{55}$	

Table A.1: *Transformation formulas for the hydrodynamic coefficients and wave excitation force at different locations in a rigid body.*

Appendix B
Additional reference tables.

This appendix presents additional tables which can be used for reference purposes.

Parameter	**power of the scale**
Wave height and lenght	1
Period	1/2
Frequency	-1/2
Nod Angle	0
Angular Velocity	-1/2
Angular Acceleration	-1
Buoyancy	3
Inertial Forces	3
Velocity Forces	3
Drift Forces	3
Torque	4
Power	3.5
Power per unit lenght	2.5
Force per unit lenght	2
Torque per unit lenght	3
Mass	3
Inertia per unit lenght	4
Buoyancy Spring per unit lenght	3
Damping per unit lenght	3.5
Heave and surge distances	1
Heave and surge velocities	1/2
Heave and surge accelerations	0
Stiffness Density	1
Compliance Density	-1
Beam Stiffness EI	5

Table B.1: *Scale factors between model and full scale.*

Appendix C
Additional data.

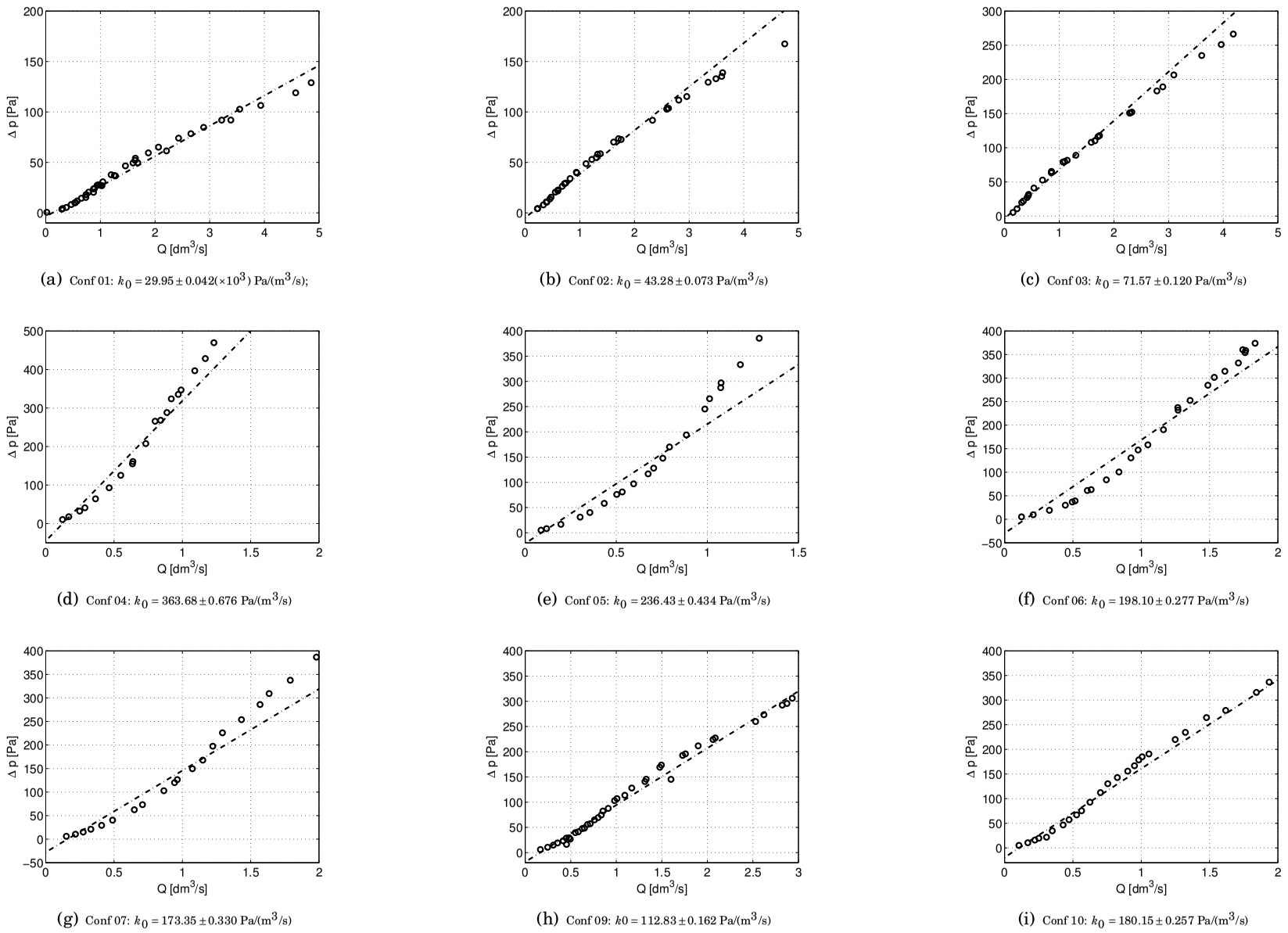

(a) Conf 01: $k_0 = 29.95 \pm 0.042 (\times 10^3)$ Pa/(m^3/s);
(b) Conf 02: $k_0 = 43.28 \pm 0.073$ Pa/(m^3/s)
(c) Conf 03: $k_0 = 71.57 \pm 0.120$ Pa/(m^3/s)
(d) Conf 04: $k_0 = 363.68 \pm 0.676$ Pa/(m^3/s)
(e) Conf 05: $k_0 = 236.43 \pm 0.434$ Pa/(m^3/s)
(f) Conf 06: $k_0 = 198.10 \pm 0.277$ Pa/(m^3/s)
(g) Conf 07: $k_0 = 173.35 \pm 0.330$ Pa/(m^3/s)
(h) Conf 09: $k0 = 112.83 \pm 0.162$ Pa/(m^3/s)
(i) Conf 10: $k_0 = 180.15 \pm 0.257$ Pa/(m^3/s)

Figure C.1: *Calibration of the linear air-damper: Flow rate versus pressure across the damper for nine different configurations. Details on the calibration are given in Section 3.2.2.*

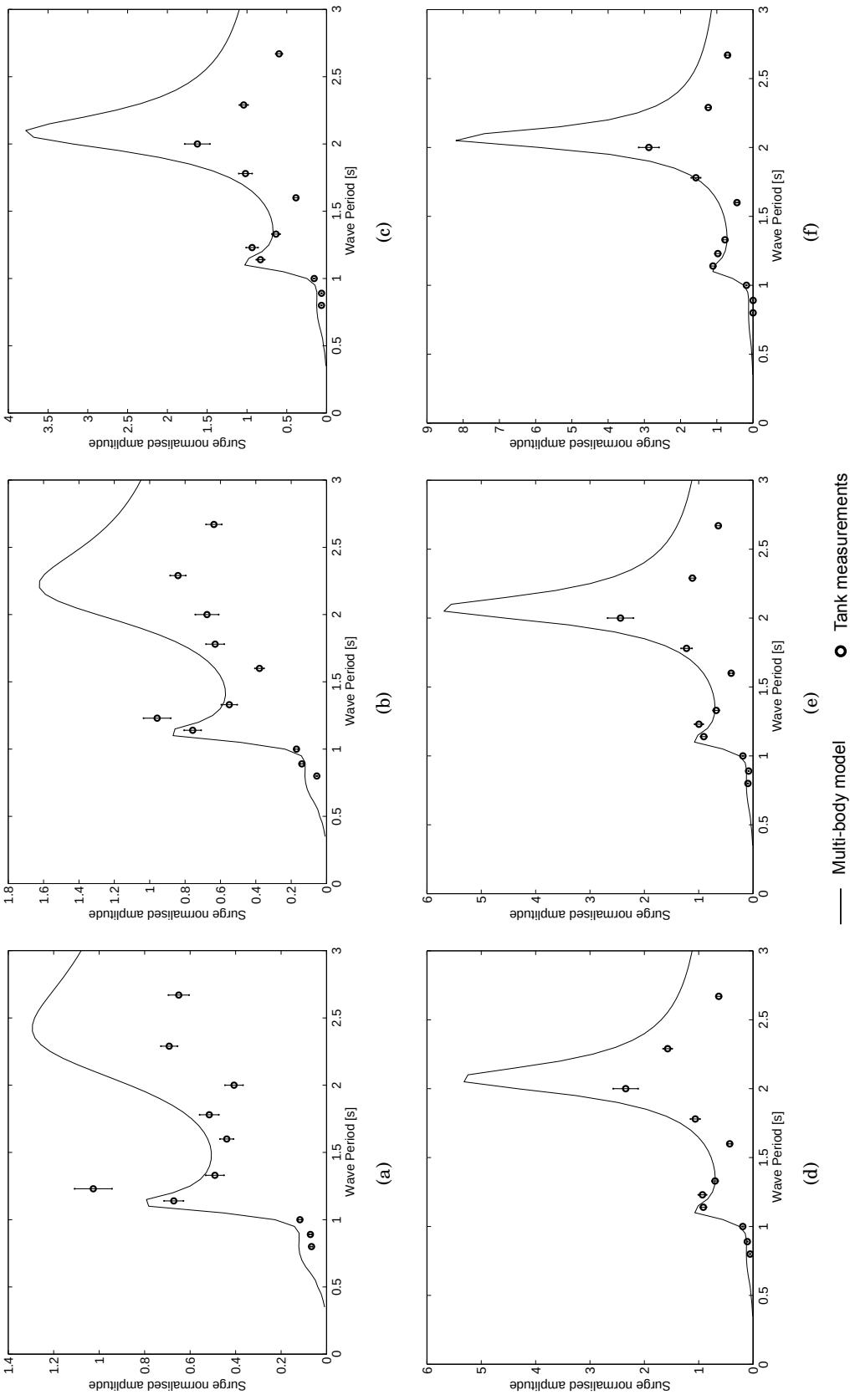

Figure C.2: *Comparison of the* ***surge normalised amplitude*** *computed through the the multi-body model for the desalination Duck with measurements with the scale model described in section 3.4.1 for different damping settings a) 3.26 Nms b) 4.71 Nms c) 12.3 Nms d) 19.59 Nms e) 21.54 Nms f) 39.61 Nms*

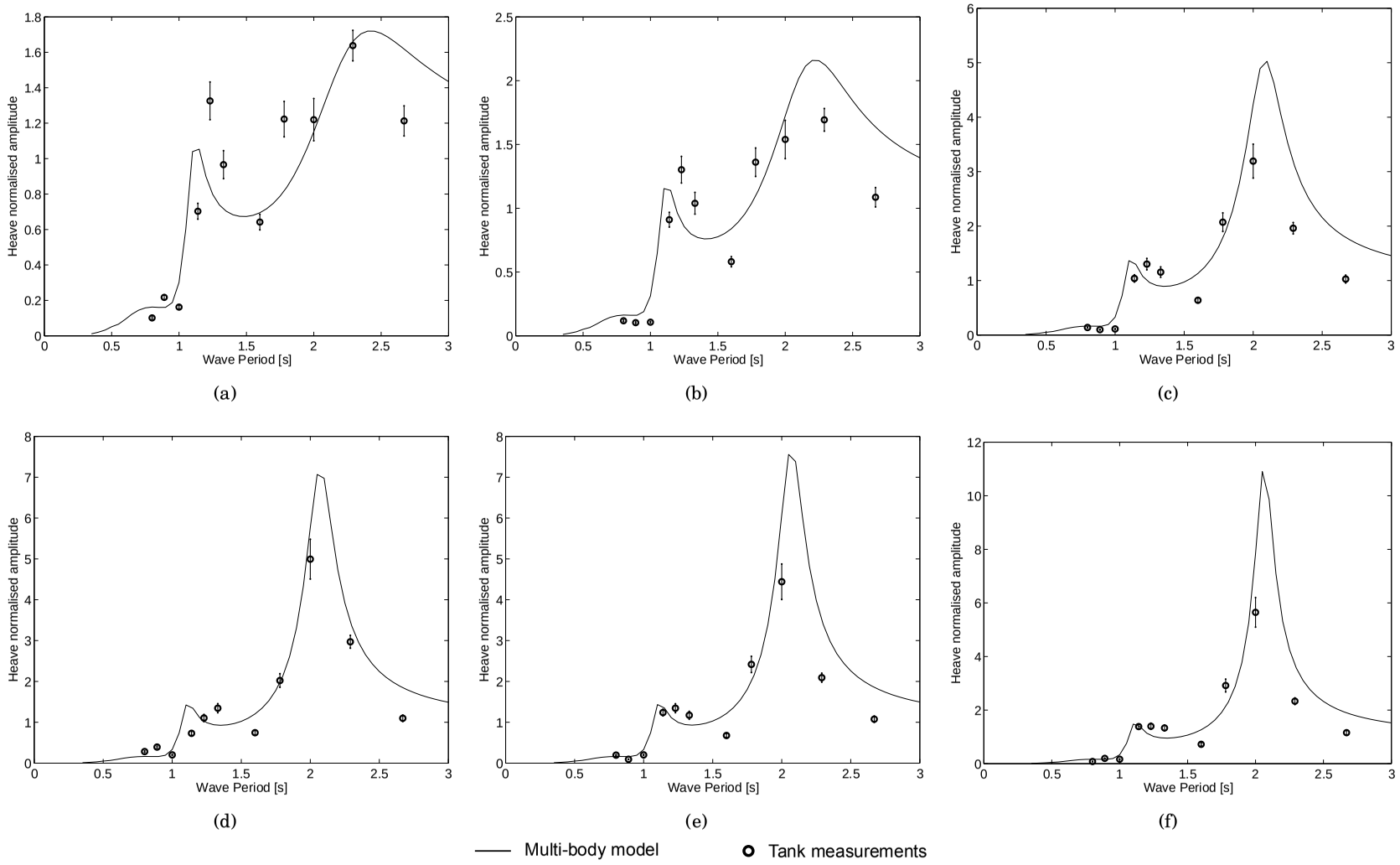

Figure C.3: *Comparison of the* ***heave normalised amplitude*** *computed through the the multi-body model for the desalination Duck with measurements with the scale model described in section 3.4.1 for different damping settings a) 3.26 Nms b) 4.71 Nms c) 12.3 Nms d) 19.59 Nms e) 21.54 Nms f) 39.61 Nms*

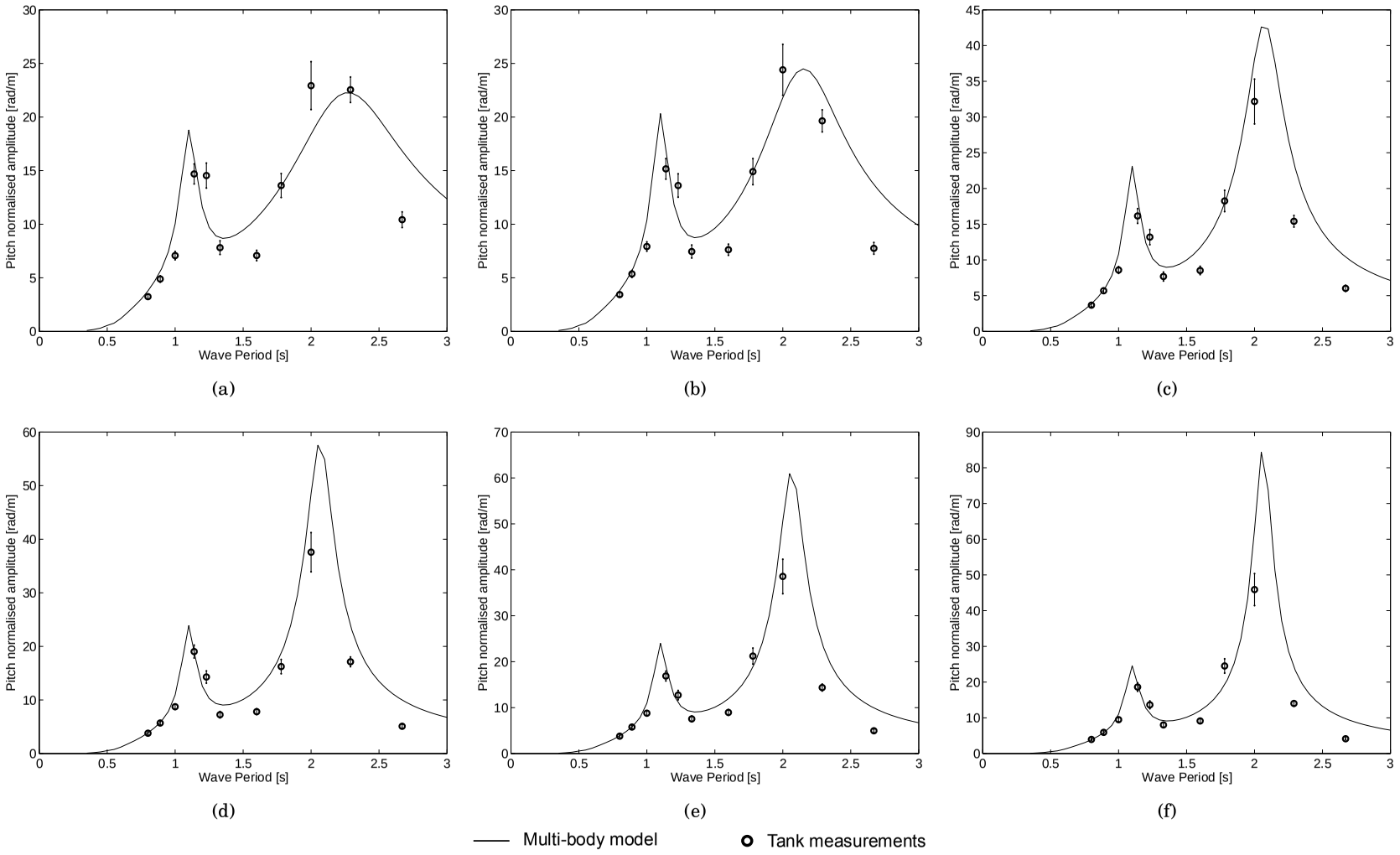

Figure C.4: *Comparison of the **pitch normalised amplitude** computed through the the multi-body model for the desalination Duck with measurements with the scale model described in section 3.4.1 for different damping settings a) 3.26 Nms b) 4.71 Nms c) 12.3 Nms d) 19.59 Nms e) 21.54 Nms f) 39.61 Nms*

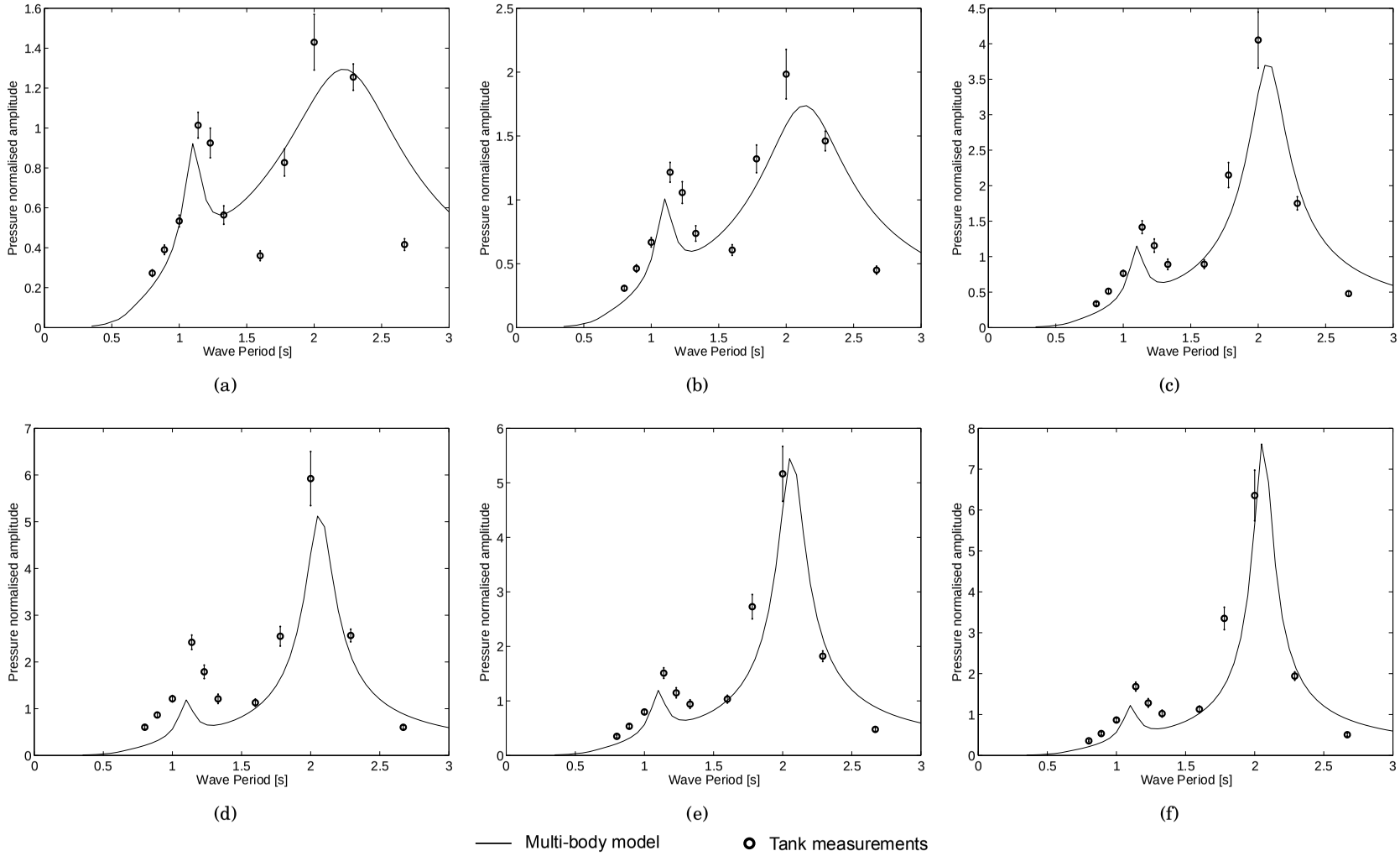

Figure C.5: *Comparison of the **pressure normalised amplitude** computed through the the multi-body model for the desalination Duck with measurements with the scale model described in section 3.4.1 for different damping settings a) 3.26 Nms b) 4.71 Nms c) 12.3 Nms d) 19.59 Nms e) 21.54 Nms f) 39.61 Nms*

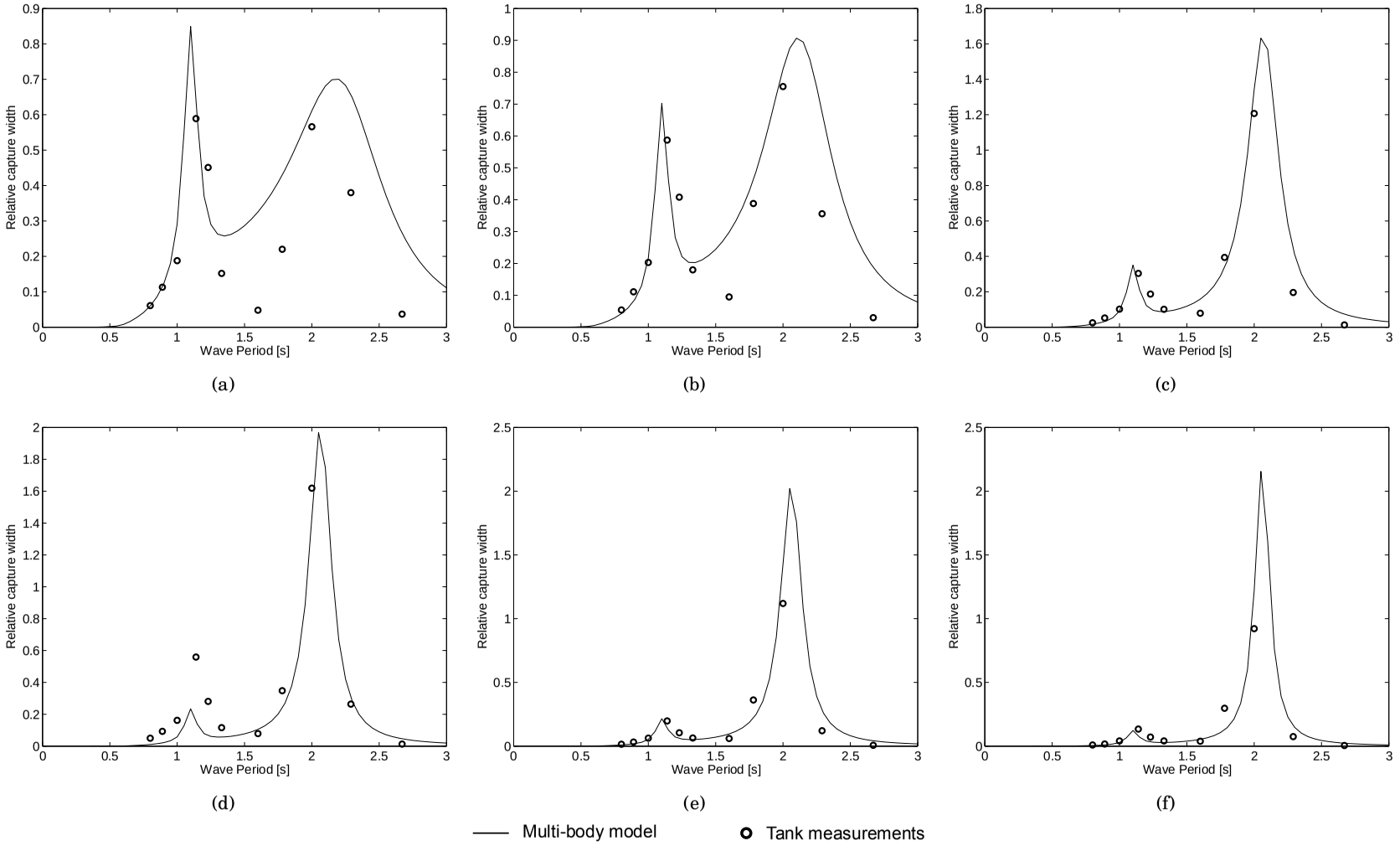

Figure C.6: *Comparison of the **relative capture width** computed through the the multi-body model for the desalination Duck with measurements with the scale model described in section 3.4.1 for different damping settings a) 3.26 Nms b) 4.71 Nms c) 12.3 Nms d) 19.59 Nms e) 21.54 Nms f) 39.61 Nms*

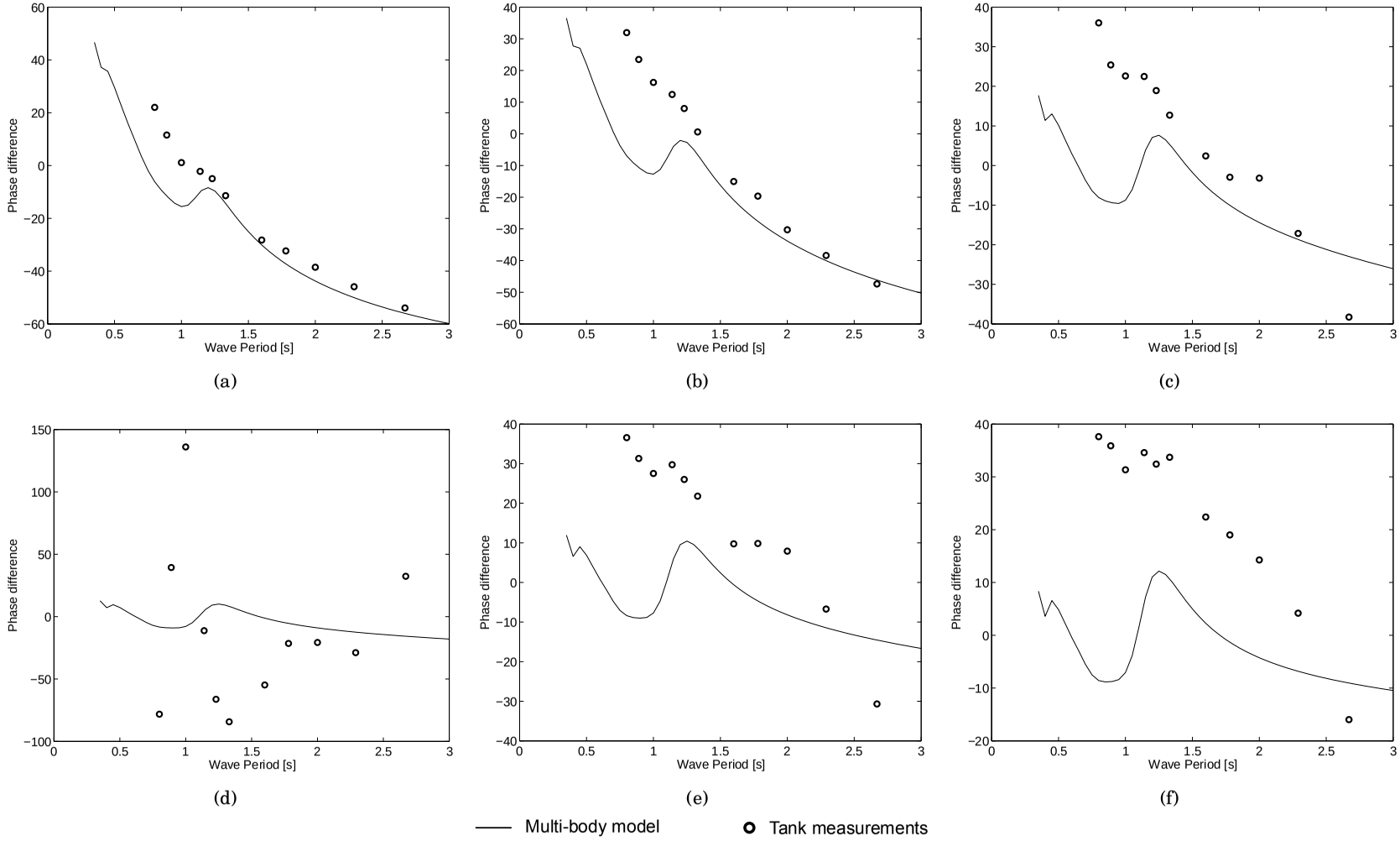

Figure C.7: *Comparison of the **phase difference** between pitch and computed through the the multi-body model for the desalination Duck with measurements with the scale model described in section 3.4.1 for different damping settings a) 3.26 Nms b) 4.71 Nms c) 12.3 Nms d) 19.59 Nms e) 21.54 Nms f) 39.61 Nms*

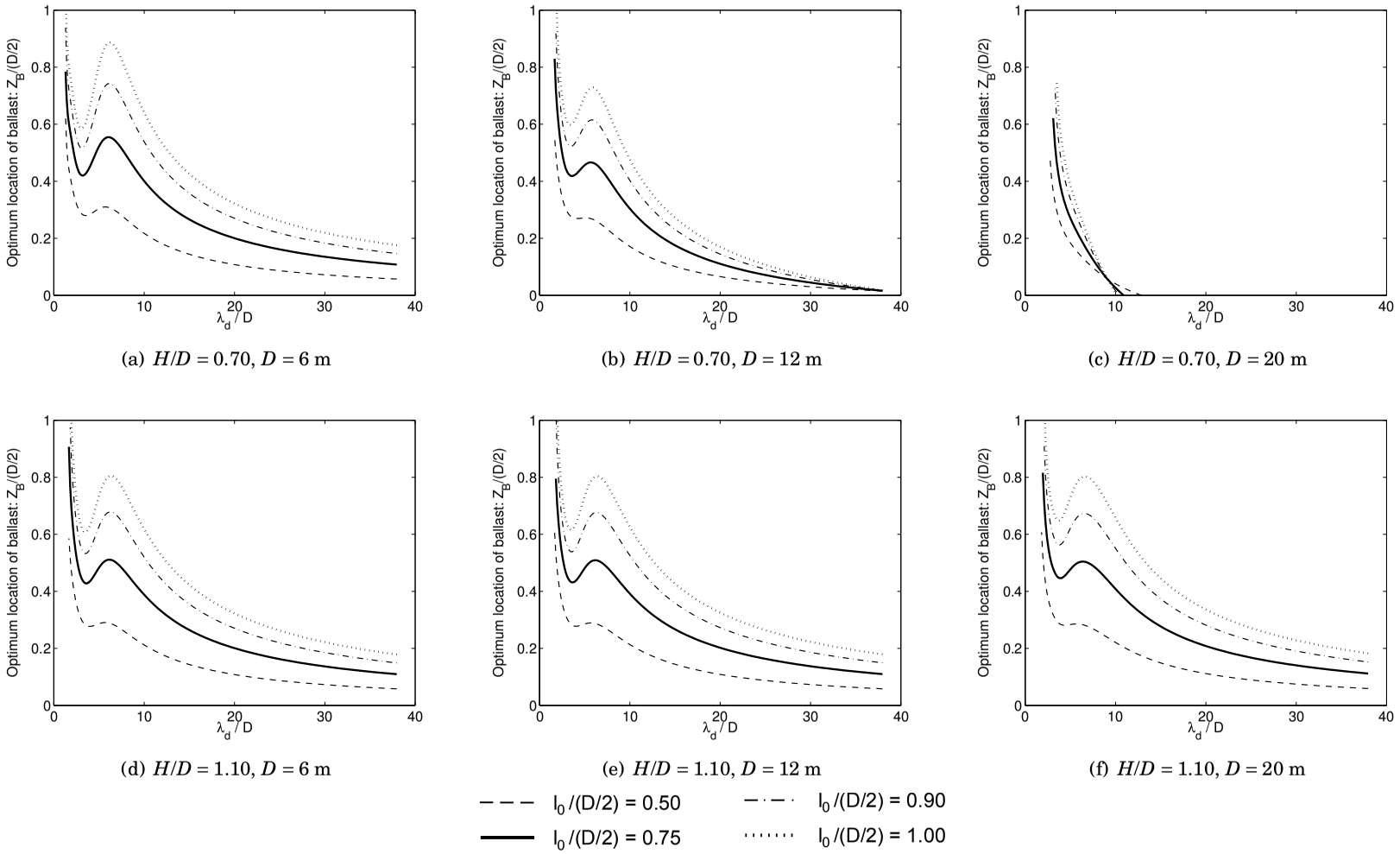

Figure C.8: *Location for the centre of mass of the ballast such to satisfy resonance at λ_d/D for different distances of the off-centred axis to the centre of the cylinder (l_0).*

Additional data.

Appendix D
Code Files

D.1 Parametric definition of the horizontal cylinder

```
      SUBROUTINE HCIRCCYL(U,V,IBI,IPI,X,XU,XV,IGDFSCRB,IER)
!-----------------------------------------------------------------------
!     jlucas 12 July 2008
!-----------------------------------------------------------------------
!     Version : 6.0
!-----------------------------------------------------------------------
!     Source-code file : GEOMXACT.FOR
!-----------------------------------------------------------------------
!     DESCRIPTION :
!     Subroutine that defines analytically the geometry of a submerged
!     horizontal circular cylinder. The geometry presents ZY(x=0)
!     and XZ(y=0) as symmetry planes(ISX=ISY=1). The body-fixed coordinate
!     system is defined relatively to the parameterisation, i.e. with the
!     origin at the middle of the cylinder on the still water plane.
!     DIAM, LEN, HEXT are read from GDF input file.
!
!     DIAM  - diameter of the base of the cylinder
!     LEN   - length of the cylinder
!     HEXT - distance from the centre of the cylinder to the still water
!
!     Patch 1: side
!     Patch 2: base
!-----------------------------------------------------------------------
      IMPLICIT NONE
      REAL X(3),XU(3),XV(3),U,V
      INTEGER IPI,IBI,IGDFSCRB,IER
!-----------------------------------------------------------------------
!  user-assigned definitions -- inputs from GDF must have SAVE attribute
!  RADIUS, HALFLEN, HALFRAD LENO4 are evaluated/saved at first call
!-----------------------------------------------------------------------
      REAL, SAVE :: DIAM,RADIUS,LENGTH,HEXT,HALFRAD,HALFLEN,LENO4,
     & HALFHEXT
      REAL THETA,CTHETA,STHETA,SR,A,B,THETA0
!-----------------------------------------------------------------------
!    PIO4=pi/4
!    PIO2=pi/2
!-----------------------------------------------------------------------
      REAL, PARAMETER :: PIO4=0.785398163397E0
      REAL, PARAMETER :: PIO2=1.570796326795E0
!-----------------------------------------------------------------------
!    On initial call read data from GDF and evaluate parameters to SAVE
!    On all subsequent calls evaluate azimuthal angle and cos/sine
!-----------------------------------------------------------------------
      IF(IPI.EQ.0) THEN
        READ (IGDFSCRB,*,IOSTAT=IER) DIAM,LENGTH,HEXT
        IF (IER.NE.0) GOTO 99
        RADIUS = 0.5E0*DIAM
        HALFLEN=0.5E0*LENGTH
        LENO4 = 0.25E0*LENGTH
        HALFRAD=0.5E0*RADIUS
        HALFHEXT=0.5E0*HEXT
      ELSE
        THETA0 = ASIN(HEXT/RADIUS);
        B = (PIO2-THETA0)/(THETA0+PIO2);
        A =(-PIO2)/(1+B);
```

```
          THETA= A*(U+B);
          CTHETA=COS(THETA)
          STHETA=SIN(THETA)
        ENDIF
!-------------------------------------------------------------------------------
!  Patch 1: side
!-------------------------------------------------------------------------------
        IF(IPI.EQ.1) THEN
          X(1)=RADIUS*CTHETA
          X(2)=-LENO4*(V+1.E0)
          X(3)=RADIUS*STHETA - HEXT
          XU(1)=-A*RADIUS*STHETA
          XU(3)= A*X(1)
          XV(2)=-LENO4
!-------------------------------------------------------------------------------
!  Patch 2: base
!-------------------------------------------------------------------------------
        ELSEIF(IPI.EQ.2) THEN
          SR=HALFRAD*(1.E0-V)
          X(1)=SR*CTHETA
          X(2)=-HALFLEN
          X(3)=SR*(STHETA - HEXT/RADIUS)
          XU(1)=-A*SR*STHETA
          XV(1)=-HALFRAD*CTHETA
          XU(3)= A*X(1)
          XV(3)=-HALFRAD*STHETA + HALFHEXT
        ENDIF
 99     RETURN
        END
```

```
      SUBROUTINE HCIRCCYL2(U,V,IBI,IPI,X,XU,XV,IGDFSCRB,IER)
!-----------------------------------------------------------------------
!     jlucas 12 July 2008
!-----------------------------------------------------------------------
!     Version : 6.0
!-----------------------------------------------------------------------
!     Source-code file : GEOMXACT.FOR
!-----------------------------------------------------------------------
!     DESCRIPTION :
!     Generalisation of HCIRCCYL subroutine to represent the geometry in
!     a given body-fixed coordinate system.
!     it defines analytically the geometry of a submerged horizontal
!     circular cylinder piercing the free water surface.
!     Unlike HCIRCCYL there is only one symmetry plane XZ(y=0), so that
!     (ISX=0,ISY=1).
!     DIAM, LENGTH, HEXT, XBODY(1) XBODY(2) XBODY(3) are read from
!     GDF input file.
!
!     DIAM  - diameter of the base of the cylinder
!     LENGTH  - length of the cylinder
!     HEXT - distance from the centre of the cylinder to the still water
!     XBODY(1), XBODY(2), XBODY(3) - XYZ origin of the body-fixed
!     coordinate system relative to the global coordinate system.
!
!     Patch 1: side
!     Patch 2: base
!-----------------------------------------------------------------------
      IMPLICIT NONE
      REAL X(3),XU(3),XV(3),XBODY(3), U,V
      INTEGER IPI,IBI,IGDFSCRB,IER
!-----------------------------------------------------------------------
!  user-assigned definitions -- inputs from GDF must have SAVE attribute
!  HALFLEN, HALFRAD are evaluated/saved at first call
!-----------------------------------------------------------------------
      REAL, SAVE :: DIAM,RADIUS,LENGTH,HEXT,HALFRAD,HALFLEN,LENO4,
     & HALFHEXT
      REAL THETA,CTHETA,STHETA,SR,A,B,THETA0,THETA1
!-----------------------------------------------------------------------
!    PIO4=pi/4
!    PIO2=pi/2
!-----------------------------------------------------------------------
      REAL, PARAMETER ::    PI=3.141592653590E0
      REAL, PARAMETER :: PIO2=1.570796326795E0
      REAL, PARAMETER :: PIO4=0.785398163397E0
!-----------------------------------------------------------------------
!    On initial call read data from GDF and evaluate parameters to SAVE
!    On all subsequent calls evaluate azimuthal angle and cos/sine
!-----------------------------------------------------------------------
      IF(IPI.EQ.0) THEN
        READ (IGDFSCRB,*,IOSTAT=IER) DIAM,LENGTH,HEXT,XBODY(1),XBODY(2),
     &  XBODY(3)
        IF (IER.NE.0) GOTO 99
        RADIUS = 0.5E0*DIAM
        HALFLEN=0.5E0*LENGTH
        LENO4 = 0.25E0*LENGTH
        HALFRAD=0.5E0*RADIUS
        HALFHEXT=0.5E0*HEXT
      ELSE
        THETA0 = ASIN(HEXT/RADIUS)
        THETA1 = -(PI+THETA0)
        B = (THETA1+THETA0)/(THETA1-THETA0);
        A =(THETA1)/(1+B);
        THETA= A*(U+B)
        CTHETA=COS(THETA)
        STHETA=SIN(THETA)
      ENDIF
!-----------------------------------------------------------------------
!  Patch 1: side
!-----------------------------------------------------------------------
      IF(IPI.EQ.1) THEN
        X(1)=RADIUS*CTHETA - XBODY(1)
```

```
          X(2)=-LENO4*(V+1.E0) - XBODY(2)
          X(3)=RADIUS*STHETA - HEXT - XBODY(3)
          XU(1)=-A*RADIUS*STHETA
          XU(3)= A*RADIUS*CTHETA
          XV(2)=-LENO4
!-------------------------------------------------------------------------
!  Patch 2: base
!-------------------------------------------------------------------------
       ELSEIF(IPI.EQ.2) THEN
          SR=HALFRAD*(1.E0-V)
          X(1)=SR*CTHETA - XBODY(1)
          X(2)=-HALFLEN  - XBODY(2)
          X(3)=SR*(STHETA - HEXT/RADIUS) - XBODY(3)
          XU(1)=-A*SR*STHETA
          XV(1)=-HALFRAD*CTHETA
          XU(3)= A*SR*CTHETA
          XV(3)=-HALFRAD*STHETA + HALFHEXT
       ENDIF
 99    RETURN
       END
```

```
      SUBROUTINE HCIRCCYL0(U,V,IBI,IPI,X,XU,XV,IGDFSCRB,IER)
!-----------------------------------------------------------------------
!     jlucas 09 October 2009
!-----------------------------------------------------------------------
!     Version : 6.0
!-----------------------------------------------------------------------
!     Source-code file : GEOMXACT.FOR
!-----------------------------------------------------------------------
!     DESCRIPTION :
!     It defines analytically the geometry of a totally submerged
!     horizontal circular cylinder. The geometry presents the symmetry
!     planes ZY(x=0) and XZ(y=0) (ISX=ISY=1).
!     The body-fixed coordinate system is defined relatively
!     to the parameterisation, i.e. with the origin at the centre
!     of the cylinder.
!     DIAM, LEN, HEXT are read from GDF input file.
!
!     DIAM  - diameter of the base of the cylinder
!     LENGTH  - length of the cylinder
!
!     Patch 1: side
!     Patch 2: base
!-----------------------------------------------------------------------
      IMPLICIT NONE
      REAL X(3),XU(3),XV(3),U,V
      INTEGER IPI,IBI,IGDFSCRB,IER
!-----------------------------------------------------------------------
!  user-assigned definitions -- inputs from GDF must have SAVE attribute
!  RADIUS, HALFLEN, HALFRAD LENO4 are evaluated/saved at first call
!-----------------------------------------------------------------------
      REAL, SAVE :: DIAM,RADIUS,LENGTH,HALFRAD,HALFLEN,LENO4
      REAL THETA,CTHETA,STHETA,SR
!-----------------------------------------------------------------------
!   PIO4=pi/4
!   PIO2=pi/2
!-----------------------------------------------------------------------
      REAL, PARAMETER :: PIO4=0.785398163397E0
      REAL, PARAMETER :: PIO2=1.570796326795E0
      REAL, PARAMETER :: PI=3.141592653590E0
!-----------------------------------------------------------------------
!   On initial call read data from GDF and evaluate parameters to SAVE
!   On all subsequent calls evaluate azimuthal angle and cos/sine
!-----------------------------------------------------------------------
      IF(IPI.EQ.0) THEN
        READ (IGDFSCRB,*,IOSTAT=IER) DIAM,LENGTH
        IF (IER.NE.0) GOTO 99
        RADIUS = 0.5E0*DIAM
        HALFLEN=0.5E0*LENGTH
        LENO4 = 0.25E0*LENGTH
        HALFRAD=0.5E0*RADIUS
      ELSE
        THETA=-PIO2*U;
        CTHETA=COS(THETA)
        STHETA=SIN(THETA)
      ENDIF
!-----------------------------------------------------------------------
!  Patch 1: side
!-----------------------------------------------------------------------
      IF(IPI.EQ.1) THEN
         X(1)= RADIUS*CTHETA
         X(2)=-LENO4*(V+1.E0)
         X(3)=RADIUS*STHETA
         XU(1)=-PIO2*RADIUS*STHETA
         XU(3)= PIO2*X(1)
         XV(2)=-LENO4
!-----------------------------------------------------------------------
!  Patch 2: base
!-----------------------------------------------------------------------
      ELSEIF(IPI.EQ.2) THEN
         SR=HALFRAD*(1.E0-V)
         X(1)=SR*CTHETA
```

```
            X(2)=-HALFLEN
            X(3)=SR*(STHETA)
            XU(1)=-PIO2*SR*STHETA
            XV(1)=-HALFRAD*CTHETA
            XU(3)= PIO2*X(1)
            XV(3)=-HALFRAD*STHETA
        ENDIF
 99     RETURN
        END
```

Appendix E
WAMIT input file

The following files are an example of the input files used by *WAMIT* to compute the hydrodynamic coefficients and wave excitation force on a horizontal cylinder width ratio of $W/D = 2.5$ with the geometry defined analytically. The cylinder is piercing the free-surface at a draft equal to $H/D = 0.70$. The body fixed coordinate system is translated relatively to the global coordinate system such to have its origin at the centre of the cylinder.

FNAMES.WAM:

```
config.wam
hcyl.gdf
model.pot
model.frc
```

CONFIG.WAM:

```
CONFIG.WAM header: HYDRODYNAMIC FORCES: CYLINDER WITH OFF-CENTRED AXIS OF ROTATION
ISOR=0
IQUAD=0
ILOG=0
IDIAG=0
IRR=0
ILOWHI=1
ISOLVE=1
MAXSCR=5770
IALTFRC=2
PANEL_SIZE=0.05
SCRATCH_PATH=N:\myhome\wamitRuns\SCRATCH
USERID_PATH=c:\WAMITv6
```

HCYL.GDF:

```
HYDRODYNAMIC FORCES: CYLINDER WITH OFF-CENTRED AXIS OF ROTATION
1.00 9.81
0 1
2 7
0.364 0.910 0.073 0.000 0.000 -0.073
```

MODEL.POT:

```
Alternative form 1 potfile , ILOWHI=1, IRR=0
1.20 0.000 0.000 -0.073 0.0
0 0
1 1 1 1 1 1
100
2.975 2.950 2.925 2.900 2.875 2.850 2.825 2.800 2.775 2.750 2.725 2.700 2.675 2.650 2.625
2.600 2.575 2.550 2.525 2.500 2.475 2.450 2.425 2.400 2.375 2.350 2.325 2.300 2.275 2.250
2.225 2.200 2.175 2.150 2.125 2.100 2.075 2.050 2.025 2.000 1.975 1.950 1.925 1.900 1.875
1.850 1.825 1.800 1.775 1.750 1.725 1.700 1.675 1.650 1.625 1.600 1.575 1.550 1.525 1.500
1.475 1.450 1.425 1.400 1.375 1.350 1.325 1.300 1.275 1.250 1.225 1.200 1.175 1.150 1.125
1.100 1.075 1.050 1.025 1.000 0.975 0.950 0.925 0.900 0.875 0.850 0.825 0.800 0.775 0.750
0.725 0.700 0.675 0.650 0.625 0.600 0.575 0.550 0.525 0.500
7
180.0 165.0 150.0 135.0 120.0 105.0 90.0
```

MODEL.FRC:

```
Alternative form 2 force file
1 1 1 0 0 0 0 0 0
1000.0
0.000 0.000 0.000
0
0
0
0
0
```

Appendix F
Technical drawings.

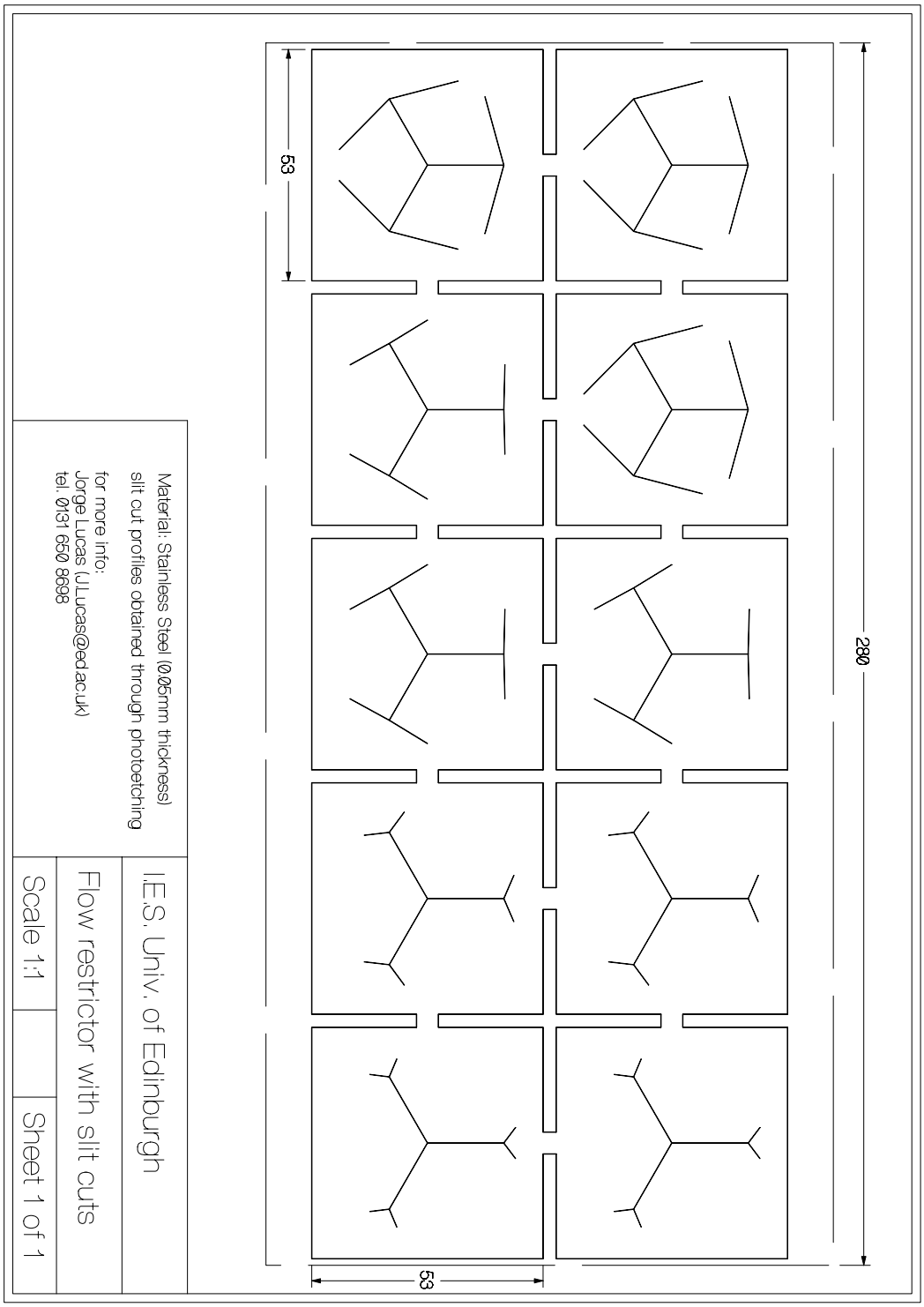

Figure F.1: *Technical drawing for the flow restrictor with slit cuts.*

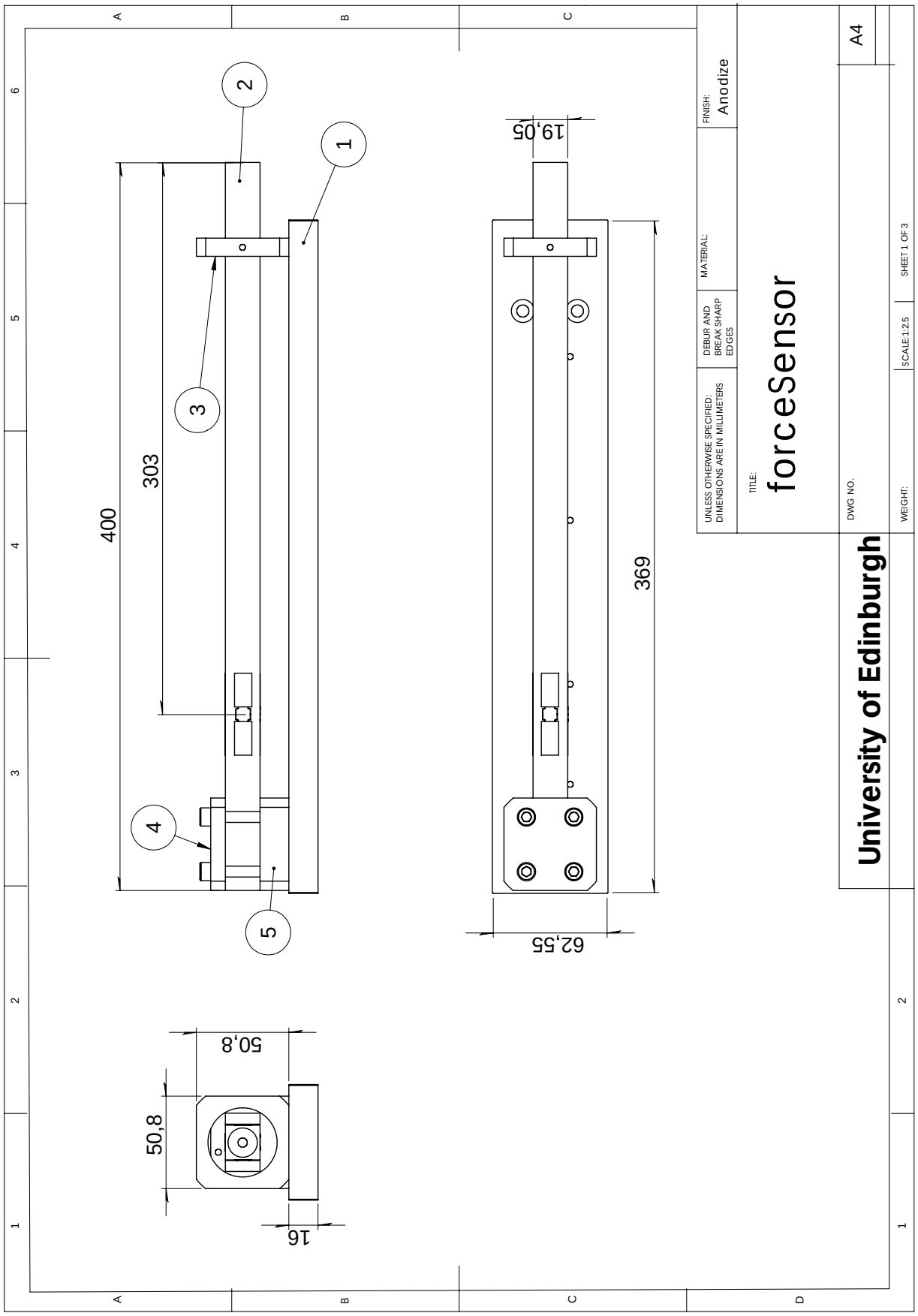

Figure F2: *Assembly drawing for the force sensor (scale 1:2.5).*

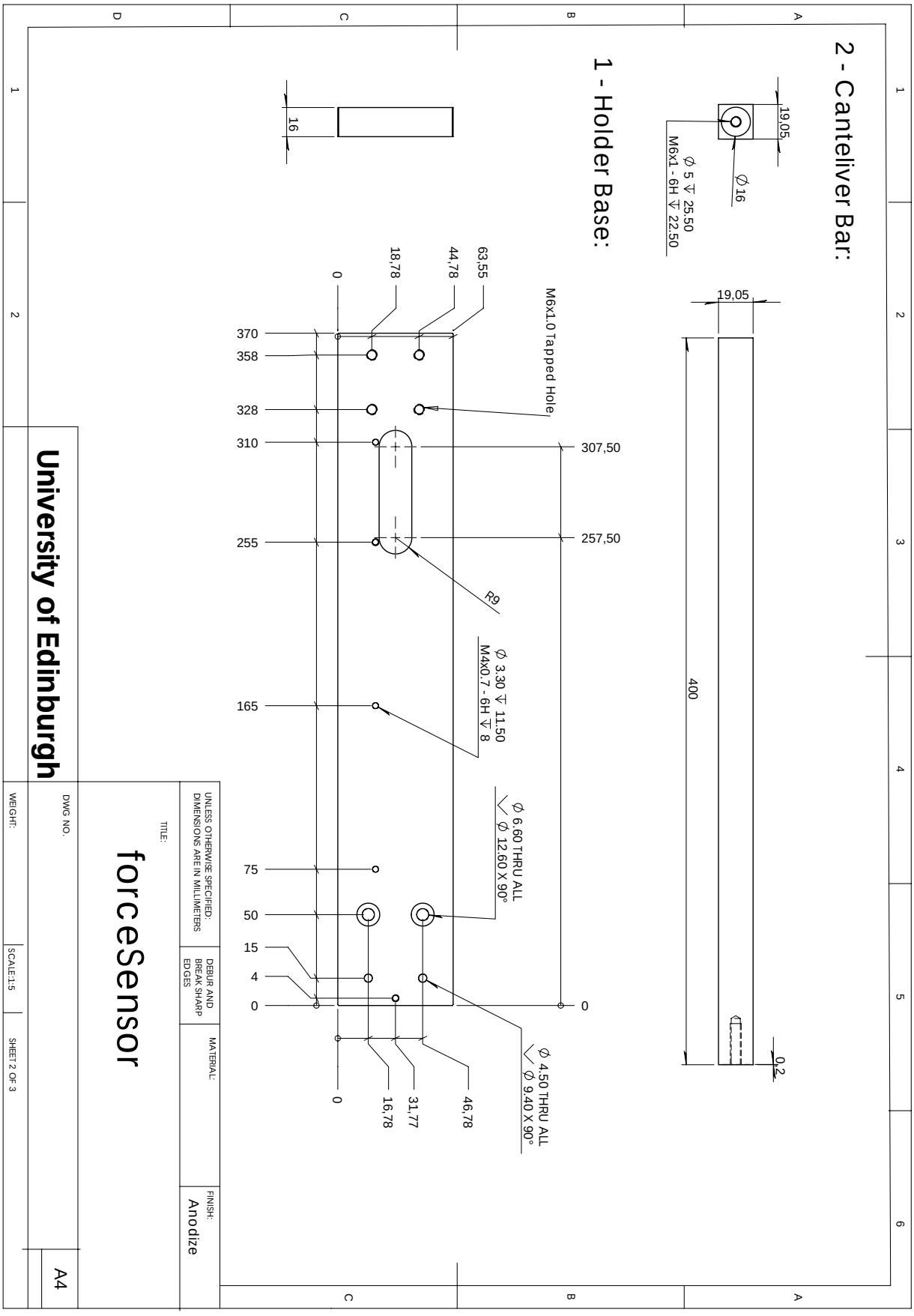

Figure F.3: *Dimensioning drawing for the holder base and cantilever bar (scale 1:2.5).*

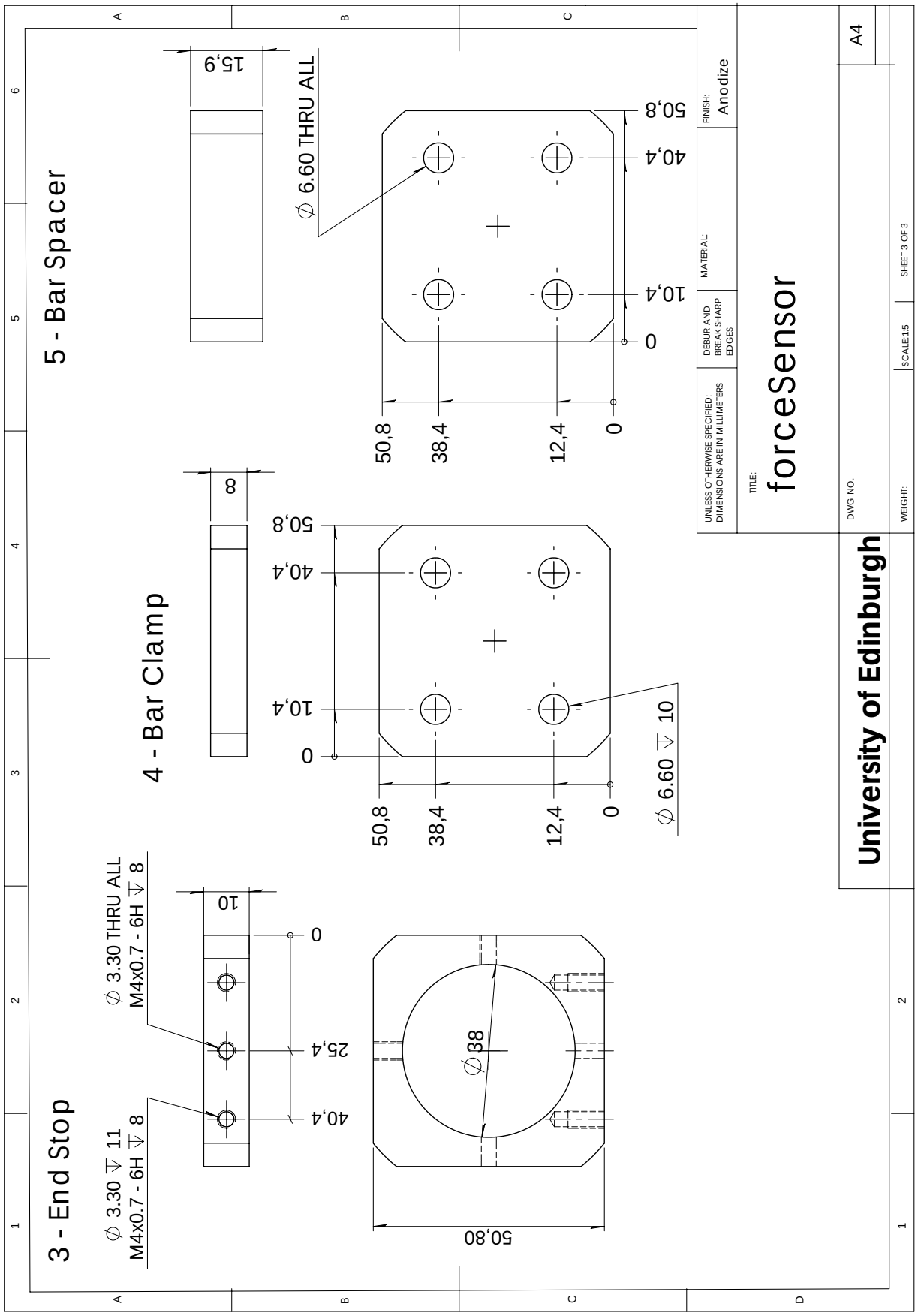

Figure F.4: *Dimensioned drawing for the end stop, the cantilever bar clamp and spacer (scale 1:1).*

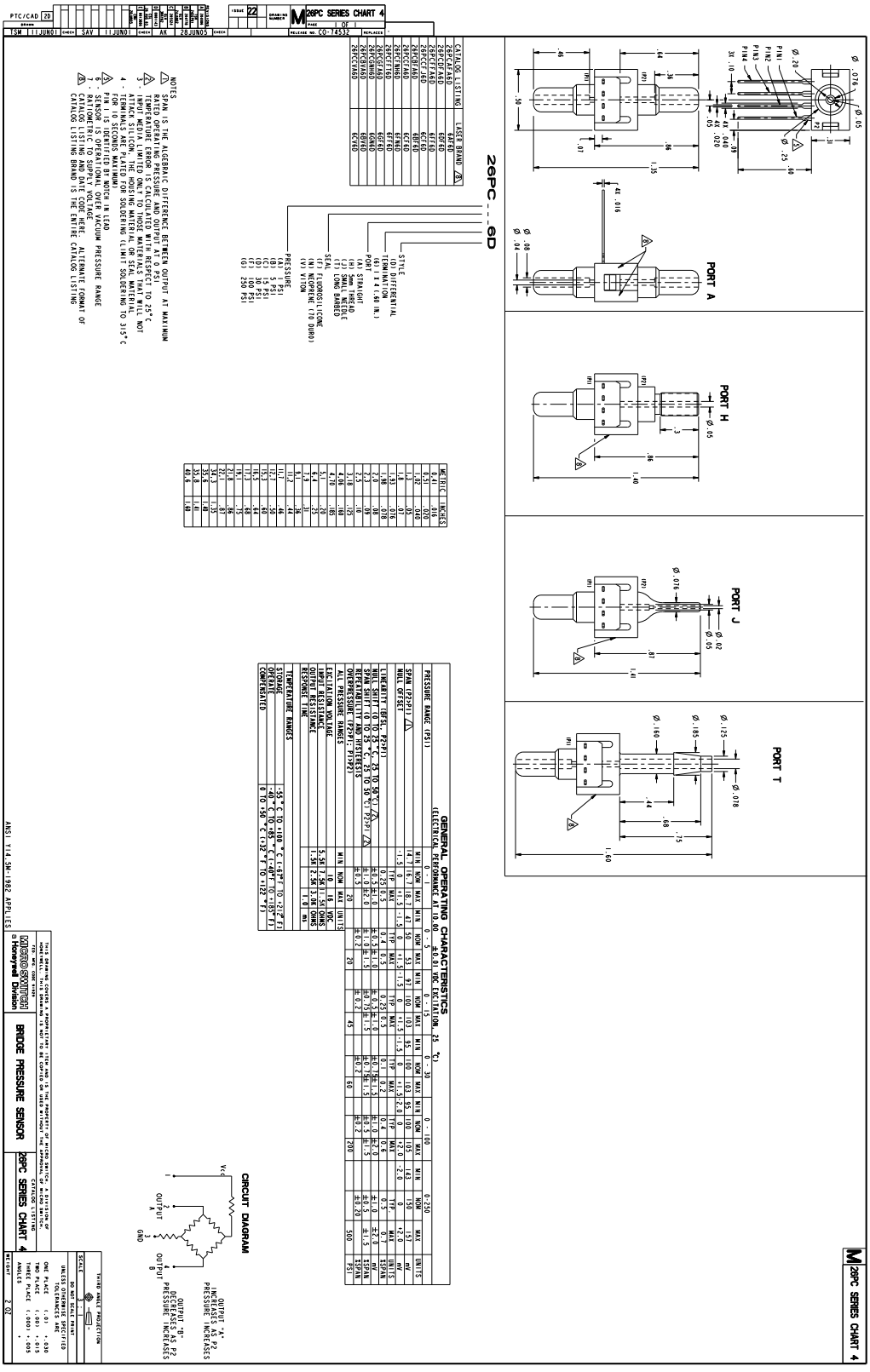

Figure F.5: *Data Sheet for the pressure sensor.*

Appendix G
Published papers